Aalborg Universitet

Turbulence Modulation by Non-Spherical Particles

Mandø, Matthias

Publication date:
2009

Document Version
Publisher's PDF, also known as Version of record

Link to publication from Aalborg University

Citation for published version (APA):
Mandø, M. (2009). *Turbulence Modulation by Non-Spherical Particles*. Aalborg Universitet.

Turbulence Modulation by Non-spherical Particles

by

Matthias Mandø

Dissertation submitted to the Faculties of Engineering, Science and
Medicine at Aalborg University in partial fulfillment of the requirements
for the degree of Doctor of Philosophy in Mechanical Engineering

Department of
ENERGY TECHNOLOGY
E.T.

AALBORG UNIVERSITY

Aalborg University
Department of Energy Technology
Pontoppidanstræde 101
DK-9220 Aalborg Øst

Printed in Denmark by Uniprint

Abstract

This study deals with the interaction between turbulence and non-spherical particles and represents an extension of the modeling framework for particle-laden flows. The effect of turbulence on particles is commonly referred to as turbulent dispersion while the effect of particles on the carrier phase turbulence is known as turbulence modulation. Whereas the former is well understood, no commonly accepted explanation has been presented for the latter. Moreover, considerations regarding the influence of shape on the experienced turbulence modulation must be considered as terra incognita. This study encompass an outlook on existing work, an experimental study, development of a numerical model and a case study advancing the modeling techniques for pulverized coal combustion to deal with larger non-spherical biomass particles.

Firstly, existing knowledge concerning the motion of non-spherical particles and turbulence modulation are outlined. A complete description of the motion of non-spherical particles is still lacking. However, evidence suggests that the equation of motion for a sphere only represent an asymptotical value for a more general, but yet unformulated, description of the motion of non-spherical particles.

Secondly, an extensive parametric study concerning the measurement of turbulence intensity in a particle-laden jet compared to that of a clear jet has been undertaken. The effect of three different sizes of spherical particles as well as two distinct non-spherical shapes is measured at different concentrations using laser-optical techniques. Emphasis is put towards developing a method to evaluate the additional influence of shape. Results suggest that non-spherical particles follow the same tendency as that observed for spheres, only with seemingly greater effect for comparable parameters. This is believed to be due to the increase in drag coefficient for increasing aspects ratios.

Thirdly, a numerical model has been theoretically derived from the governing conservation equations for fluid flow, the Navier-Stokes equations, considering the additional influence resulting from the interaction with particles. Validation, using existing measurements as well as those obtained for the particle-laden jet, demonstrate that the new model is able to predict the experimentally observed tendencies and thus represent an improvement compared to existing models. The additional effect of shape is modeled through the modification of the drag coefficient.

Finally, the acquired knowledge is synthesized into the development of techniques to predict the combustion of large non-spherical straw particles in suspension fired power plants which are to replace coal in tomorrow’s society. Although the straw particles are significantly larger than coal particles, the larger drag coefficient associated with straw particles ultimately leads to an attenuation of the carrier phase turbulence. Compared to other modeling choices the inclusion of a model for turbulence modulation is found to be influential for the correct prediction of combustion efficiency.

Acknowledgements

This work has been carried out at the Department of Energy Technology, Aalborg University in the period September 2006 to August 2009. This work has received financial support from Energinet.dk under grant PSO 2006 1 6364. The study has been carried out under the supervision of Prof. Lasse Rosendahl from Aalborg University and by Prof. Marilyn Lightstone (March to June, 2008) from McMaster University.

I would like to express my sincere gratitude to my supervisors Prof. Lasse A. Rosendahl and Prof. Marilyn F. Lightstone for their expert guidance and constructive criticism as well as being a constant source of inspiration throughout this study.

I would like to thank my colleagues Henrik Sørensen and Chungen Yin for their support and helpful comments and suggestions during the course of this study.

Grateful acknowledgements are due to Jan Christiansen, Mads Lund, Flemming B. Larsen and other support staff at Aalborg University for their assistance.

I also wish to thank my dear sister Anne-Christine Mandø for proofreading this manuscript.

Table of Contents:

Nomenclature

Latin symbols:

a	acceleration		[m/s^2]
a	semi-minor axis		[m]
A	area		[m^2]
A	pre-exponential factor		[1/s]
b	semi-major axis		[m]
d_p	particle diameter, diameter of sphere with equal volume		[m]
D	pipe diameter, nozzle diameter		[m]
D	diffusion/dispersion coefficient		[-]
E	activation energy		[J]
C	constant		[-]
C	particle concentration	$C = \tilde{\rho}_p / \tilde{\rho}_c = \alpha \rho_p$	[kg/m^3]
C_c	Cunningham's correction coefficient		[-]
C_D	drag coefficient		[-]
C_p	specific heat		[J/kg·K]
f	departure from Stokes drag	$f = \left(1 + 0.15\,\mathrm{Re}_p^{0.687}\right)$	[-]
F	force		[N]
g	gravitational acceleration	$g = 9.8$	[m/s^2]
h	convective heat transfer coefficient		[W/m^2·K]
I	moment of inertia		[kg·m^2]
k	turbulent kinetic energy	$k = 3u'^2 / 2$	[m^2/s^2]
k	kinetic rate of reaction		[1/s]
$\boldsymbol{K}$	translation matrix		[-]
l_e	characteristic length of large energy containing eddies, integral length scale		[m]
l_{int}	inter-particle spacing	$l_{\mathrm{int}} \approx \left(\pi / 6\alpha\right)^{1/3} d_p$	[m]

L	Lagrangian length scale		[m]
m	mass		[kg]
$\dot{m}$	particle mass flow		[kg/s]
M	fractional change in turbulence intensity	$M=\left(\sigma-\sigma_0\right)/\sigma_0$	[-]
M_c	molecular mass		[-]
n	number of particles		[-]
P	pressure		[Pa]
u	velocity		[m/s]
U	mean velocity, free-stream velocity		[m/s]
V	volume		[m^3]
R	universal gas constant	$R=8314.47$	[J/kmol·K]
S	source		[-]
t	time		[s]
T	temperature		[K]
T	torque		[N·m]
y^+	dimensionless wall distance		[-]
x	spatial coordinate		[m]
z	mass loading	$z=\dot{m}_p/\dot{m}_c$	[-]

Greek symbols:

α	volume fraction of particle phase	[-]
α	inclination angle	[-]
β	aspect ratio	[-]
γ	ratio of specific heats	[-]
Γ	diffusion coefficient	[-]
ε	dissipation rate	[m^2/s^3]
ε	particle emissivity	[-]

ε	small eccentricity		[m]
θ_R	radiation temperature		[K]
Θ	combustion enhancement factor	$\Theta = \left(0.3\psi + 0.7\right)/\psi$	[-]
λ	free mean path		[m]
μ	dynamic viscosity		[kg/m·s]
ν	kinematic viscosity		[m^2/s]
π	constant	$\pi = 3.1415926$	
ρ	density		[kg/m^3]
σ	turbulence intensity	$\sigma = u'/\overline{u}$	[-]
σ	Stefan-Boltzmann constant	$\sigma = 5.67040E-08$	[W/m^2· K^4]
σ	constant in k-ε model		[-]
τ_V	particle time constant	$\tau_V = \rho_p d_p^2 / 18\mu_c$	[s]
τ_p	particle response time	$\tau_p = 24\rho_p d_p^2 / 18\mu_c C_d \operatorname{Re} = f / \tau_V$	[s]
τ_e	turnover time of large eddy	$\tau_e = l_e / u'$	[s]
τ_f	characteristic time scale of flow	$\tau_f = l/U$	[s]
ϕ	transport parameter		[-]
ψ	sphericity	$\psi = \left(\pi^{1/3}\left(6V_p\right)^{2/3}\right) / A_p$	[-]
ω	angular velocity		[1/s]

Non-dimensional numbers:

Kn	Knudsen number	$Kn = 2\lambda / d_p$	[-]
Ma	Mach number		[-]
Pe	Rotational Peclet number		[-]
Re_p	particle Reynolds number	$\operatorname{Re}_p = \rho_c d_p \left\lvert \overline{u} - \overline{v} \right\rvert / \mu_c$	[-]
St	Stokes number	$St = \tau_p / \tau_f$	[-]

Abbreviations:

A/F	air-fuel ratio
CFD	computational fluid dynamics
CHP	combined heat and power
CTE	crossing trajectory effect
DNS	direct numerical simulation
GUI	graphical user interface
LES	large eddy simulation
LDA	laser Doppler anemometry
LHV	lower heating value
PA	primary air
PDF	probability density function
RANS	Reynolds averaged Navier Stokes
RMS	root mean square
RSM	Reynolds stress model
SA	secondary air
TA	tertiary air
UDF	user defined function

Superscripts:

$'$	fluctuating quantity
$-$	ensample average

Subscripts:

i,j	indices
∞	local fluid property evaluated at particle position
p	particle
u	momentum

k	turbulent kinetic energy
ε	dissipation rate
ave	average
t	turbulent
0	clear flow
V	stokes flow
c	clear flow

1. Introduction

”In recent years, new nations have entered enthusiastically into industrial production, thereby increasing their energy needs. This has led to an unprecedented race for available resources. Meanwhile, some parts of the planet remain backward and development is effectively blocked, partly because of the rise in energy prices. What will happen to those peoples?”

- Pope Benedict XVI

In the framework of multi-phase flows the influence of particles on the carrier phase turbulence is commonly known as turbulence modulation. The interaction between solid particle and gas phase turbulent flows is important for many engineering devices as well as naturally occurring processes. Examples of these are the pneumatic transport of fine powders, the combustion of pulverized solid fuels, dust storms and the pollutant dispersion in the atmosphere. In each of these cases a fundamental understanding concerning the underlying phenomena, which is responsible for the complex interaction between the particulate phase and the turbulent carrier flow, is required to advance the design of engineering devices in which these flows occur. Most research concerning particle-gas interaction has been focused on spherical particles although the vast majority of particulate flows involves non-spherical particles which flight can be significantly different than that of a sphere.

Objectives/Problem statement

The aim of this study is to improve the understanding of the governing aspects of particulate two-phase flow with particular attention to the influence of non-spherical particles on the carrier phase turbulence. This is achieved by performing measurements on a particle-laden jet with the intention to gain a better understanding of the mechanisms involved in turbulence modulation, by the development of appropriate source terms for the turbulence equations in the framework of Computational Fluids Dynamics, to account for the presence of particles, and by demonstrating the practical implementation of this model extension on a pulverized fuel burner.

Background

This PhD study is part of a larger research initiative concerning the combustion of biomass in suspension fired power plants. This work is primary funded by the grant PSO 2006 1 6364 by the Danish organization Energinet.dk which owns and maintains the energy infrastructure in Denmark[1]. The main goal of this project is to improve the understanding of the governing multiphase aspects of biomass combustion and further the development in the design of equipment for biomass applications. The aim of the Danish strategy, since the energy crisis in 1973/74, has been to reduce the dependency on foreign resources and from 1990 also to promote the use of sustainable energy sources. The motivation for using biomass in the energy supply is based on that biomass is considered CO_2-neutral, that it saves foreign currency, that it creates Danish jobs, and that it utilizes waste products from agriculture, forestry, households, trade and industry (Energistyrelsen 2002). The Danish potential for biomass resources is estimated to approximately 165 PJ/y which corresponds to 20 % of the current consumption of energy in Denmark (Energistyrelsen 2008). Currently half of the total potential for biomass energy is used for energy production in Denmark. On a global scale the potential for biomass energy production in the year 2050 have been estimated from as low as 33 EJ/y up to 1272EJ/y which corresponds to respectively 7% and 282% of the worlds current energy consumption[2] (Smeets et al. 2007), (Hoogwijk et al. 2003), (Wolf et al. 2003). Currently the category Combustible Renewable and Waste of which biomass is a part of constitutes 10.6% of the total world energy consumption (IEA 2008). Biomass are regarded as the most important and potent renewable fuel. This is due to its ability to be used directly as a substitute for fossil fuels and thereby using well proven technology and the existing infrastructure.

In Denmark two overall technologies has been utilized to combust biomass: suspension firing of pulverized biomass alone or with addition of coal-dust and burning on vibrating grates. Both technologies have advantages and drawbacks concerning their use together with biomass and can be seen as supplementary technologies rather than competitive technologies. Grate fired boilers are characterized by being able to burn almost any type of solid fuel regardless of the condition but are associated with lower efficiency compared to suspension firing. On the other hand suspension firing requires dried, pulverized solid fuels to work but performs best of all technologies used in the burning of biomass (Evald and Witt 2006). State-of-the-art facilities are demonstrated for vibrating grates by

---

[1] Energinet.dk is a non-profit organization owned by the Danish state whose income comes from fees on the transmission of electricity and natural gas. Energinet.dk supports research and development in sustainable energy production through PSO (Public Service Obligation) grants. A special PSO fee of 0.4 øre/kWh (1øre=1/100 DKK) is charged from all electricity customers in Denmark.

[2] The large discrepancy between these numbers comes from the uncertainty in the estimates of population growth and diet. As such biomass potential is essential limited by the surplus agricultural land and in the end the amount of people on earth.

Avendøre unit 2 which is the largest straw fired boiler yet built and for suspension firing by Amager unit 1 which was put into commercial operation in 2009. Biomass fuel used for suspension firing basically uses the same technology as that of firing with coal which is a well proven concept. This includes the pulverization in grinding mills, the pneumatic transport in pipe systems and the use of intricate swirling patterns inside the burner for optimal combustion. The flow pattern in the burner and inside the boiler is to be engineered in such a way that no unburnt particles escape through the top of the boiler or are deposited in the ash hopper. Although coal as all fossil fuels has the same origin as biomass fuels their structure and chemical properties are distinctly different.

Table 1: Properties of solid fuels

Quantity	Coal	Wood chips	Wood pellets	Straw
Proximate analysis (wt%)				
Moisture	1.7	45.0	7.1	13.1
Volatiles	29.4	44.6	79.0	67.6
Fixed carbon	64.4	9.9	13.5	15.5
Ash	4.5	0.6	0.5	3.8
Ultimate analysis (wt%)				
Carbon	82.9	50.0	46.2	40.4
Hydrogen	4.5	6.2	5.8	5.2
Nitrogen	1.9	0.3	<0.1	0.7
Sulfur	1.3	0.05	<0.02	0.1
Oxygen	3.3	43.0	40.4	36.6
Chorine	0.02	0.02	<0.01	0.09
High heating value (MJ/kg)	32.8	19.4	19.0	16.7
Low heating value (MJ/kg)	31.8	9.7	17.6	15.24

Coal: (Ye et al. 2004), Wood chips: (Energystyrelsen 2002), Wood pellets, Straw: (Holm et al. 2006)

One issue is the moisture content and management; coal contains very little moisture and can be stored with no shelter without absorbing excess water while biomass contains large amounts of water and needs to be dried prior to combustion. The moisture content reduces the energy content in the fuel and part of the energy is used to evaporate the water. Moisture contents in excess of 55w% makes it very difficult to maintain the combustion process. The water content also influences the time required to combust a particle and thereby acts to extent the required residence time. Biomass has a significantly large contents of volatiles compared to coal. Volatiles are released from the particle as a gas when heated and combusted when mixed with oxygen. Combustion of the gaseous volatiles is fast compared to the combustion of the solid charcoal and a high ratio of volatiles acts to decrease the residence time of particles in the furnace. The remaining charcoal particle will predominantly retain its original shape and will during burnout be reduced to ash.

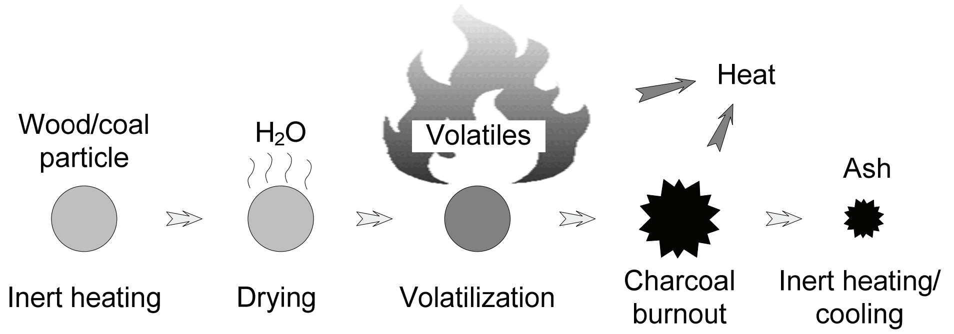

Figure 1: A particle combustion route. For a small particle this can be seen as a sequential process while large particles can support several stages simultaneously.

Depending on the mix of minerals in the fuel the ash has different properties. Ash from straw or from bark, needles and leaves contains a high amount of potassium and chlorine which causes the ash to become sticky and to be deposited on the heating surfaces, this is known as slag. Slag deteriorates the efficiency of the boiler and large pileup of slag pose a danger in operating the boiler. Pure wood contains fewer minerals than straw and its ash is not known to cause slag problems. To overcome the slagging problems of certain biomass fuels certain additives may be used and co-firing with wood help to reduce the problems (Nicolaisen et al. 2002). Another difference between biofuels and coal is the energy content. Whether this is judged on the higher or lower heating value coal has a significantly higher energy density than biomass. Thereby to maintain the nominal output of a coal fired boiler when shifting to biomass the volume load of the fuel has to be increased. Since this is not always possible often the only alternative is to downgrade the nominal load which causes the installation and operational cost of the plant to become higher compared to the output. Furthermore, the collection, transport and drying of biomass fuels also require energy and to properly make the comparison with coal. This should also be taken into consideration.

A very important issue in the combustion of solid in suspension fired boiler is the particles size and uniformity. Basically the larger the particle the longer time does it take for it to burn out and the longer time it is necessary to maintain the particle inside the furnace to fully use the energy contained in the particle. Particle size is a characteristic of the individual grinding mill and not of the fuel itself and with that in mind it is difficult to relate particle sizes and shapes as a property of the fuel. However, there are issues concerning the structure of the solid fuels which indicates a difference in their size distribution if they are grinded in the same mill. Coal has a crystalline structure which fractures when applied to pressure while biomass particles can be characterized as being soft and flexible with a composite like structure which has to be pulled apart. Biomass particles ground in a conventional coal mill has a tendency to cause excess wear on the grinding surfaces and on the machinery due to the jolting motion which results when the fibers are torn apart.

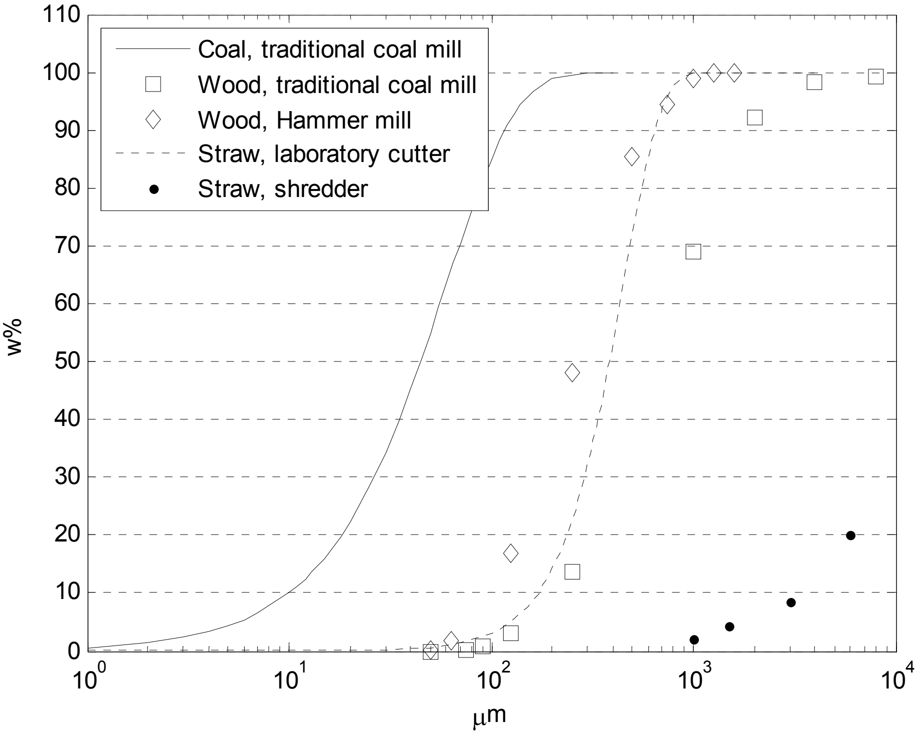

Figure 2: Particle size distribution of solid fuels when milled in similar fashion. Size is based on mesh diameter. Based on data from Holm et al. (2006), Esteban and Carrasco (2006), Damstedt (2007) and Rosendahl et al. (2007).

Using traditional coal mills to pulverize biomass pellets result in a size distribution with significant lager particles and a wider size distribution than for coal. Even when using heavy-duty laboratory equipment it is not possible to achieve sizes comparable to that of pulverized coal. Another difference between the appearances of particles produced from the milling of different solid fuels is the shape of the particles. Coal particles, due to their crystalline origin, tend to have sharp edges but otherwise be spherical in shape. Biomass particles produced from milling tend to be rounded but are often oblong and/or flat in appearance. This is especially pronounced for the largest particles which might not be abundant in numbers but due to their volume fraction can be very important for the flow and combustion processes as a whole. The shape of the biomass particles also does that the surface area to volume ratio of the particle is significant larger than for the coal particles with their spherical shape which constitutes the minimum of the surface area to volume ratio. A non-spherical particle with a larger surface area to volume ratio will combust faster then a spherical particle of equal volume due to the increased heat transfer from the larger surface area.

Figure 3: Sample of pulverized biomass (straw) (Damstedt 2007)

Of the different techniques used in commercial power plants to produce electricity, suspension firing is know to be the most effective process when measured on power output compared to the input energy of the fuel. Suspension firing has been around for many years and has been developed and optimized for the combustion of coal. In the later years the air flow inside the boiler together with the configuration of the burners has been optimized using Computation Fluid Dynamics (CFD) tools to simulate and visualize the flow patterns. However, the aerodynamic and combustion properties of biomass particles are very different from that of coal particles. Coal particles are most often modeled as being perfect spheres and as being point particles where their volumetric extend are ignored. Biomass particles modeled using CFD tools developed for coal particles are not able to accurately predict the motion of neither large non-spherical particles nor their interaction with the entraining air flow. (Yin et al. 2004)

Thesis outline

This thesis consists of four main chapters. Chapter 2 - Perspective on Non-spherical Particles and Turbulence deals with the motion of spheres, well-defined non-spherical particle shapes such as ellipsoids of revolution and arbitrary shaped particles. The effect of turbulence on the motion of particles as well as the effect of particles on the turbulence is clarified in this chapter. Chapter 3 - Measurement of Turbulence Modulation deals with an experimental parametric study of a particle laden jet. Three different sizes of spherical particles and two well defined non-spherical shapes, the disk and the prolate spheroid, are added to an air jet in different concentration. The turbulence intensity of the particle laden jet is compared with that of a clear jet to determine modulation caused by the addition of particles. Special focus has been directed towards validating existing criteria for turbulence modulation as well as developing methods to determine the additional effect of shape. Chapter 4 - Numerical Model and Validation accounts for existing models in the contexts of CFD and establishes a new basis to accurately predict particle-laden flows. The model developed is subsequently validated using existing measurements for pipe flow and the present measurements for a particle laden jet. In chapter 5 - Pulverized Straw Combustion – A Case Study the necessary steps to modify the existing methodology to deal with larger non-spherical biomass particles are scrutinized. Special attention is cast on different modeling choices effect on the combustion efficiency and evaluated side by side with the impact of a model for turbulence modulation on the flow field predicted.

Each chapter in this thesis is structured so that they can be read independently from each other. Some readers might want to skip the extensive literature study in chapter 2 and go straight to the experimental study in chapter 3, whilst readers which are more into numerical modeling of physical phenomenon's might start with the background theory in chapter 2, move on to the formulation of the new source for turbulence modulation in chapter 4 and finish off with chapter 5 which deals with the practical implementation of non-spherical particles for engineering flows.

Much additional information can be found in the appendices. These contain a complete description of all sub-models parameters used in the CFD work as well as additional plots of the experimental data for both the clear and particle laden jets.

2. On Non-Spherical Particles and Turbulence

“Everything should be made as simple as possible, but not simpler.”
- Albert Einstein

In this chapter the progress on the motion of non-spherical particles and their interaction with the carrier phase is reviewed. Irregular non-spherical particles are found in most industrial particulate flows and in addition most engineering flows are turbulent. However, the vast majority of scientific investigations of particulate flows deals with perfectly spherical particles. The exact governing equations for turbulent flow have been known for over a century but the utilization of these is significantly impeded by the need to resolve the smallest flow structures and time scales. For most practical uses turbulence is modeled using an average equation which does not reflect the nature of turbulence. The modeling of industrial particulate flows depends on models for the averaged flow, the turbulence, the particles and the interaction between the particles and the carrier phase. The motion of spherical particles is considered to be well understood although only the motion of a single spherical particle travelling at almost the same velocity as the fluid is fully formulated. The current understanding on the modification of the carrier phase turbulence due to the presence of solid particles is limited. Different mechanisms have been suggested to explain experimental observations and different parameters have been identified as being important but no consensus exists in this field. It is known to be difficult to separate the direct modulation of the turbulence which can be attributed to various particle effects from the indirect effects due to the momentum exchange between the particles and the mean velocity field.

Classification of non-spherical particles

Particles come in all sort of shapes and sizes, in fact, due to the arbitrary nature of naturally occurring particles there are an indefinite number of possible shapes. This necessitates the need for a set of parameters to aid in the description of different particle shapes for the implementation in the numerical models and the dissemination of relevant information to other scientists. Numerous descriptions have been used in the particle shape terminology for particles which are not describable in mathematical terms.

Table 2: Commonly used particle shape terminology. [a](Black et al. 1996), [b](Clift, Grace and Weber 2005), [c](Christiansen and Barker 1965)

Acigular[a]	needle-shaped
Angular[a]	sharp-edged
Crystaline[a]	freely developed geometric shape
Dentritic[a]	a branched crystalline shape
Fibrous[a]	thread-like
Flake-like[a,c]	flat shape
Granular[a]	equidimensional irregular shape
Irregular[a]	lacking any symmetry
Modular[a]	rounded, irregular shape
Spherical[a]	of global shape
Axisymetric[b]	revolution bodies
Orthotropic[b]	plane of symmetry
Spherically isotropic[b]	regular polyhedral
Near-spherical[c]	equidimensional irregular shape
Cylinder-like[c]	one dominating dimension

Particles which are unambiguously described using mathematical terms, such as cubes, ellipsoids and tetrahedrals, are referred to as having a regular shape whilst particles with an arbitrary shape which is not possible to ascribe are referred to as irregular particles. Spherical particles can be placed in the group of regular particles, however, due to their unique status these are put in a group for themselves. Spherical particles are the only shape which projected area is the same no matter which angle it is viewed from. This implies that a complete description of the forces acting on a spherical particle is independent of the orientation except for the calculation of the Magnus force for spinning particles. Although most real flows contain irregular particles most investigations assume particles of spherical shape. For a lot of flows the particle used can be approximated with sphere within the acceptable levels of accuracy. For example the grinding of coal produce particles with small aspect ratios meaning that the shape has a small influence on the path of a particle and at the same time other effects, more important than the shape, are also neglected and only the most significant forces acting on the particle or the minimum effort needed to model the flight is used. Contrary to spherical particles no universal approach exists to deal with neither the motion nor the description of non-spherical particles. Of all the irregular shapes which exists it is possible to subcategorize them according to their origin: Some shapes have a well-defined geometry, although not defined in mathematically terms, but instead semantically. This could be agricultural products such as grain or it could be the leaf of the tree; the common denominator being some sort of generic shape. Some shapes have a more random like geometry but these are variations often formed by various production method. This could be the particles produced in a coal mill or the wood chips produced by the harvesting of forests; particles which when compared with one another are noticeable different in shape, but have common features inherent from the production method. Finally there are complex random shapes which could be agglomerates or snow flakes; composite clusters of particles of which no one is likely to be the same.

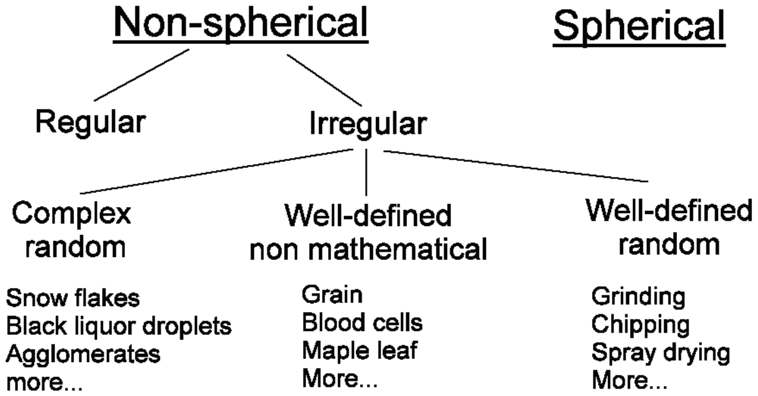

Figure 4: Categorization of particle shapes.

No matter how particle shapes are categorized this small analysis serves to show the many different aspects which must be considered when dealing with non-spherical particles and the great multiplicity of shapes. This is perhaps also the reason why, just as most investigations of particulate flows deal with spherical particles, most investigations of non-spherical particles deal with regular shapes. However, for practical use it is of less interest to categories particles because of the limitless variations and it is more interesting to find a unified way to describe all shapes of particles. Such methods contain one or more parameters of the particle shape which can be quantified in an unambiguous and uniform way for all particles. The simplest class of this type of categorization is the use of equivalent diameters. However, note that these definitions are only useful in the specification of the size of the particle and not the shape. The large number of different single parameter expressions has arisen due to the variety of scientific or industrial fields where size specification is used.

Table 3: Commonly used diameter definitions (Allen 1981).

Aerodynamic/drag diameter	d_d	Diameter of a sphere of unit density with the same terminal velocity as the particle
Stoke's diameter	d_{st}	Diameter of a sphere of same density and the same terminal velocity as the particle
Projected area	d_a	Diameter of a circle having the same area as the projection of the particle
Feret's diameter	d_F	The mean value of the distance between pairs of parallel tangents to the projected outline of the particle
Martin's diameter	d_M	The mean chord length of the projected outline of the particle
Mesh/sieve diameter	d_s	The width of the minimum square aperture through which the particle will pass
Volume equivalent diameter	d_{Veq}	Diameter of a sphere having the same volume as the particle
Area equivalent diameter	d_{Aeq}	Diameter of a sphere having the same surface area as the particle

For example, in investigations concerning the combustion of particles, the surface area and volume of the particle are the main parameters of interest since this determines the area over which reactions will occur and the residence time of the particle. Diameter definitions such as the projected area, Martin's diameter and Feret's diameter come from the analysis using microscopy where these diameters are easily measured while others, such as the aerodynamic diameter, come from sedimentation methods. Common for all these parameters, except perhaps the sieve diameter, are that they contain some relation to a particle with equivalent spherical diameter and they will hence collapse into the same diameter if the particle under consideration is a sphere. By using equivalent diameters all data about the shape of the particle is essentially lost and to be able to retain this information additional shape factors have been suggested to quantify the geometry of non-spherical particles.

Table 4: Commonly used shape factors. (Wadell 1934)

Corey shape factor	Ratio of the smallest principal length axis of the particle to the square root of the intermediate and longest principle length axis
Roundness	Ratio of the average radius of curvature of the corners to the radius of the largest inscribed circle
Sphericity	Ratio between the surface of a sphere with the same volume as the particle and the surface area of the actual particle

These shape factors can be used for both regular and irregular particles but is perhaps better suited for the latter since irregular particles are too complex to quantify in exact mathematical terms. (Kaspers 1982) Also shape factors which are based upon the projected area of a particle exist. These can more easily be measured using a microscope; however this procedure makes them inevitably prone to subjective operator error and is henceforth not mentioned further. Shape factors based on the physical extend of the particle in all 3 dimensions is inherently more difficult to measure and often less stringent definitions, based on microscopic measurements, are used. The roundness is quit cumbersome to measure and to quickly estimate the value a method of visual comparison of the particles in question with standard images of particles with known roundness must be used.

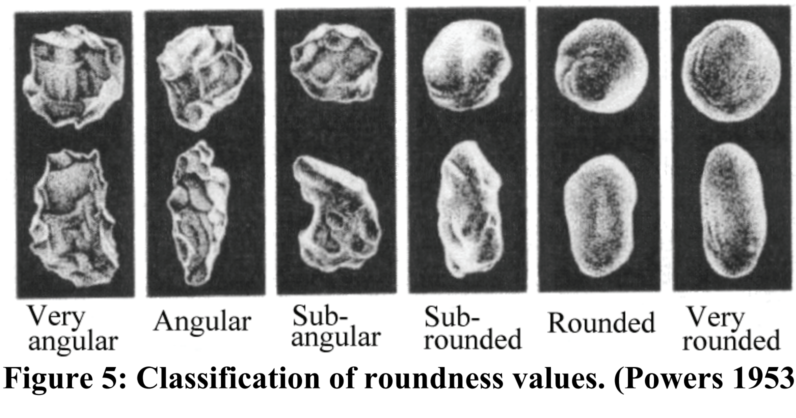

Figure 5: Classification of roundness values. (Powers 1953)

The Corey shape factor is next to the sphericity factor probably the most used shape factor. Both parameters have reported shortcomings, with respect to their ability to predict the particle dynamics, which are due to them being single parameter descriptions. But, the true reason for the greater popularity of the sphericity is its easy implementation in combustion problems. Several alternative shape factors (Thompson and Clark 1991; Elfasakhany 2005) have also been suggested in scientific papers over the years, but none has won greater acceptance or use despite claimed superiority. This is due to increasingly difficulties in measuring the particle parameters as the shape factor becomes more intricate; for a single parameter description the ease of measuring and implementing correlation based upon the shape factor is properly more important than the precision of the expression. The most commonly used shape factor is the sphericity, ψ, which similarly to other shape factors can be difficult to measure. Often the sphericity is approximated using limited information of the geometry of the particle:

$$\psi \approx \sqrt[3]{\frac{V_p}{V_s}} \approx \sqrt[3]{\frac{\text{longest} \times \text{intermidiate} \times \text{smallest dimension}}{\left(\text{longest dimension}\right)^3}} \tag{1}$$

Expressed using the formulation by Wadell (1934), the volume of the particle, V_p, can be found by immersion of the particle in a fluid and the volume of a circumscribing sphere, V_s, can be based on the long axis of the particle. Measurement of three dimensions of the particle: the longest dimension, the intermediate dimension, and the smallest dimension, another estimate of the sphericity can be made.

The most useful context in which shape factors are used, and hence their worth is to be evaluated, are their correlation with the drag coefficient for particles in free fall for a wide range of different shapes. The drag coefficient for arbitrary particles is typically found by measurement of the terminal velocity of the particle in free fall and relevant fluid parameter. However, as will be described later, the terminal falling velocity is not constant for all regimes of the Reynolds number and the resulting drag coefficient is very much an average. Most of these correlations employ the volume equivalent sphere diameter, d_{Veq}, as the characteristic size and the sphericity, ψ, to quantify the shape and is thus expressed as:

$$C_D = f\left(\text{Re}, \psi\right) \tag{2}$$

Different correlations of the drag coefficient of non-spherical particles have been compared against a large database of empirical date for non-spherical particles in the study of Chhabra et al. (1999). The average error reported from the different correlations varies between 16% and 43%; the lowest being the correlation suggested by Ganser (1993) which was then canonized to be the superior relation. The largest error encountered using this expression is 181% for empirical results of hollow cylinders and agglomerates of spherical particles; all shapes which are very far from the spherical ideal and which can hardly be characterized by equal volume spheres and sphericity. The farther away from the spherical ideal the shape of the particles, the poorer the correlations perform. This is not all that surprising since very different shapes which have the same surface area to volume ratio are assumed to have the same aerodynamic properties. The classical example to illustrate this is by considering particles shaped as cylinders of different length to diameter ratio; the so-called aspect ratio. The sphericity of a cylindrical particle can be expressed as a function

$$\psi = \frac{2\left(\frac{3}{2}\beta\right)^{2/3}}{1+2\beta}, \qquad \beta = \frac{L}{D} \tag{3}$$

where *β* is the aspect ratio expressed for a cylinder as the length, *L*, to the diameter, *D*, of the cylinder. From this expression it can be realized that both a cylinder with an aspect ratio less than one, commonly referred to as a disk, and a cylinder with an aspect ratio above one can have the same value of sphericity.

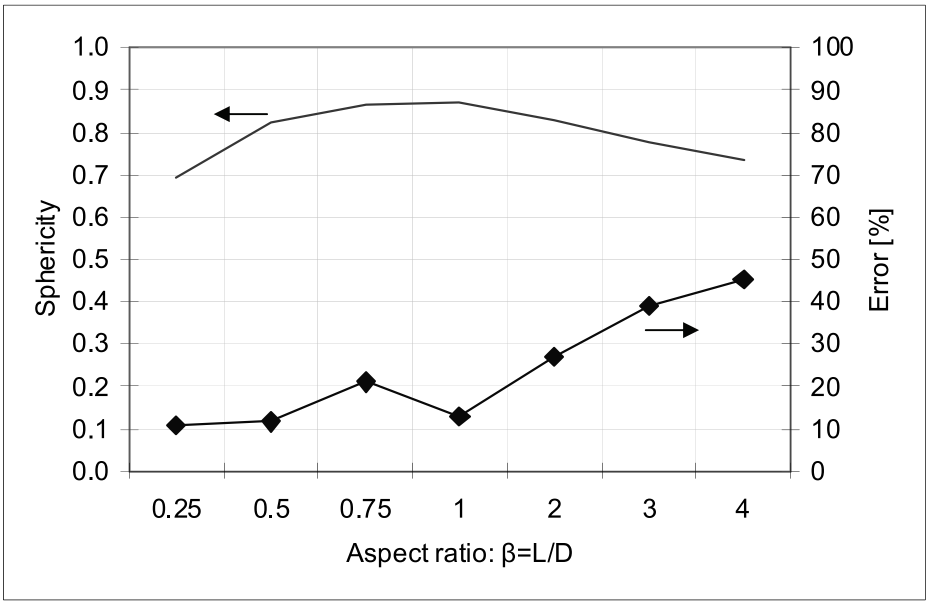

Figure 6: using the correlation from Ganser (1993) and the data from McKay et al. (1988)

Using the experimental data from McKay et al. (1988) for the drag coefficient of falling cylinders with small aspect ratios it can be seen that the drag coefficient is different from disks and cylinders and that even for small aspect ratios the correlation is poor for the case of cylinders. For disks the correlations are somewhat better but as the aspect ratio decreases further the error will similarly increase. It is somewhat contradictory that drag correlations for non-spherical based on the sphericity should be as popular as they are since it have been pointed out by several authors that the terminal velocity correlates poorly with sphericity (Clift et al. 2005). Generally it is suggested to only use correlations based on the sphericity on particle shapes with a sphericity approaching unity, which correspond to shapes with small aspect ratios and which only deviates slightly from the spherical ideal. In the work by Christensen and Baker (1965) it is suggested that if the maximum length to the minimum length is below 1.7 the particle should be treated as isotropic and correlations of the sphericity could be used. For values above 1.7 the shape is classified either as rod-like, which can be approximated with a cylinder, or flake-like, which can be approximated with a disk. However, it should be pointed out that if an investigation center about a specific shape, the best result is obtained by making an empirical fit of the drag coefficient as a function of the Reynolds number for that specific shape. As a final comment it is often requested by authors using shape factors that additional parameters is needed for further improvement (Chhabra et al. 1999) (Kankkunen et al. 2005). However, to the best of this author's knowledge, no such factors exist at present time.

Motion of a single spherical particle

The motion of a particle, whether spherical or non-spherical, is described in terms of translational and rotational motion.

Translational motion is described using a single equation which represents the conservation of translatory momentum for the particle, whereas rotational motion is most usually described by three equations representing the conservation of angular momentum in each of the three spatial directions. Combined, these equations represent six degrees of freedom for a particle in a three dimensional space.

$$m_p \frac{d\mathbf{v}_p}{dt} = \sum_i \mathbf{F}_i \tag{4}$$

$$I_{x'} \frac{d\omega_{x'}}{dt} = \sum T_{x',i} + \omega_{y'}\omega_{z'}\left(I_{y'} - I_{z'}\right) \tag{5}$$

$$I_{y'} \frac{d\omega_{y'}}{dt} = \sum T_{y',i} + \omega_{z'}\omega_{x'}\left(I_{z'} - I_{x'}\right) \tag{6}$$

$$I_{z'} \frac{d\omega_{z'}}{dt} = \sum T_{z',i} + \omega_{x'}\omega_{y'}\left(I_{x'} - I_{y'}\right) \tag{7}$$

For spherical particles only translatory motion are required for a complete description of the motion due to it being similar in appearance when viewed from different angles. Rotational motion of a sphere is usually taken in to account by the addition of an extra force term, expressing constant rotational velocity, instead of resorting to the full set of equations. The equation of motion for a single spherical particle can be derived from Newton's second law considering a force balance. The classical and most well known derivation is known as the Basset – Boussinesq – Oseen equation, the BBO equation, in honor of its developers. This derivation is made by assuming creeping flow[3] consequently meaning that the particle should be very small. Maxey and Riley (1983) re-derived the creeping equation of motion; clearly stating the pertinent assumptions and clarified several intricate theoretical parts, not dealt with previously (Michaelides 1997). The final equation they obtained, the MR equation, has been used ever since and is considered the final manifestation of the equation of motion for creeping flow:

$$\underbrace{\rho_p V_p \frac{d\mathbf{v}}{dt}}_{inertia} = \underbrace{6\pi a\mu(\mathbf{u}-\mathbf{v})}_{drag} + \underbrace{V_p(\rho_p-\rho_f)\mathbf{g}}_{gravity/buoyancy} + \underbrace{\rho_f V_p \frac{d\mathbf{u}}{dt}}_{\substack{pressure\\gradient}} + \underbrace{\tfrac{1}{2}\rho_f V_p \frac{d}{dt}(\mathbf{u}-\mathbf{v})}_{virtual\ mass} \underbrace{-6\pi a^2\mu\int_0^t\left(\frac{(d/d\tau)(\mathbf{u}-\mathbf{v})}{\left(\pi\mu(t-\tau)/\rho_f\right)^{1/2}}\right)d\tau}_{Basset\ history\ term} \tag{8}$$

The virtual mass, or added mass, is the force emanating from the acceleration of the fluid surrounding the particle and is similar in appearance as the inertia term. The Basset history force, or just history force, is the force emanating from the development of the boundary layer on the particle. Both forces are unsteady forces and the history term, due to the integral, is considered to be difficult to evaluate under practical circumstances. This equation can be supplemented by addition terms accounting for electrical or magnetic fields, thermophoretic forces and lift forces arising from velocity gradients (Saffman lift force) or rotation (Magnus force). Often an additional term, the Faxen correction term or Faxen force, accounting for the effect of a non-uniform flow field is used. The Stokes drag force is based on a uniform free stream velocity and the Faxen terms constitutes a second order expansion of the Stokes drag:

$$\mathbf{F}_D = 3\pi\mu d_p(\mathbf{u}-\mathbf{v}) + \mu\pi\frac{d_p^3}{8}\nabla^2\mathbf{u} \tag{9}$$

where ∇^2 is evaluated at the position of the particle. The very restrictive assumptions associated with the use of this equation make it beyond the reach for many practical engineering flows. However, the MR equation constitutes the foundation for expansions of the motion of particles at higher Reynolds numbers and the motion of non-spherical particles. Using order of magnitude expressions, as presented by Lazaro and Lasheras (1989), the full MR equation is reduced in complexity. For small heavy particles the drag and inertia terms dominate over

---

[3] Creeping flow assumption: The particle Reynolds number should be very small, $\mathrm{Re}_p \ll 1$, meaning that the viscous forces are dominant over the inertial forces. Furthermore, the particle is moving in a continuous medium, $Kn \gg 1$, there are no collisions with other particles (dilute flow), $\tau_p/\tau_C < 1$ or collisions with walls, $D_p/2L \ll 1$ (L is the characteristic length of the flow domain).

the pressure gradient term, the virtual mass term and the Basset history term. The relevant body forces, usually only the gravity term, are retained and the drag force is expressed as a function of the Reynolds number using empirical relations yielding a highly versatile expression:

$$\frac{d\mathbf{v}}{dt} = \frac{18\mu C_D \,\mathrm{Re}}{24\rho d_p^2}\left(\mathbf{u}-\mathbf{v}\right)+\mathbf{g} = \frac{1}{\tau_p}\left(\mathbf{u}-\mathbf{v}\right)+\mathbf{g} \tag{10}$$

This equation is used extensively in the simulation of coal combustion where the particles are assumed to be spherical. The factor $18\mu C_D Re/24\rho d^2_p$ has dimensions of reciprocal time and is referred to as the particles response time, τ_P. For the limits of low Reynolds number, Stokes flow, the factor $C_D Re/24$ approaches unity. Equation (10) is a first order differential equation and by solving, with an initial particle velocity of zero, it can be seen that the particle response time is the time required for a particle released from rest to achieve 63% of the free stream velocity.

Motion of non-spherical particles

From the simple expression derived in equation (10) it is easy to see the great interest of finding an expression for the drag coefficient as a function of shape of the particle. However, the drag on a non-spherical particle is dependent on its orientation. Primarily, the projected area, on which the drag is based on, may be several orders of magnitude different from one orientation to another but also the drag coefficient varies significantly depending on the orientation. Also, rotational effects are important when considering orientable particles and the equations for conservation of angular momentum must be taken into consideration as the translational motion depends directly on them. Non-spherical particles are associated with characteristic secondary motion depending on the Reynolds number regime and their shape. Moreover, in some Reynolds number regimes particles will take on a preferred direction. Most investigations of the motion of non-spherical particles deal with the generic shapes of ellipsoids, cylinders and disks since these can be made, by parameter variation, to resemble a great number of different shapes; most notoriously oblong particles and flat particles. Particles with an oblong shape, such as a prolate ellipsoid or a cylinder, are often used to resemble fibers, which particulate flow is a prime interests in the paper and pulp industry. Particles with a flat shape, such as an oblate ellipsoid or a disk, are mainly of academic interest unless the flow of skittles is considered.

For very low Reynolds numbers flow, $Re_p < 0.1$ (Stokes flow), both oblong and flat particles in a shear flow will move in slow orbits, known as Jefferys orbits, after G.B. Jeffery (1922) who was the first to describe the motion. One restriction in this analysis is that the particles have to obey certain symmetry conditions, but in this author's opinion also rough or irregular particles should exhibit this behavior providing that they have a large aspect ratio. Randomly irregular particles show no orbit-like motion and their flight is best described as tumbling. One interesting aspect of non-spherical particles in Stokes flow is that although they move in orbits the majority of the time they will be aligned or be at a small angle to the flow (Bernstein and Shapiro 1994). In practical terms it is much more useful to state that the particles tend to align themselves parallel to the flow since the effect is also visible in Poiseuille flow. Very much due to Jefferys pioneering work most investigations have since focused on particles moving in Stokes flow, however, we will not dwell on this topic and instead refer the reader to the work by Carlson (2007) and by Leal (1980) which contain exhaustive knowledge of particles in creeping flow.

At moderate Reynolds numbers flow, $0.1<Re_p<100$, inertial effects become important, and a steady recirculation zone start to build up on the rear of the particles. The pressure distribution on the particle, due to recirculation zone, forces the particle to align itself perpendicular to the flow. Most researchers states that all non-spherical particles tend to align themselves with their maximum cross-section normal to the flow. It is stated that this effect is more pronounced at the higher Reynolds numbers and for particles with a more pronounced non-spherical shape compared to near-spherical shapes. Most interesting is, that since the particles is steadily aligned perpendicular to the flow, empirical data for the generic shapes, such as an infinite long cylinder in cross-flow, may be used to model the motion. The drag coefficient of cylinders in cross-flow is well mapped and the experimental data is within 6% of the best correlations (White 1991). Also the influence of finite length or edge effects are very well understood and applying correlations of the drag coefficient for cylinder of finite length on an infinite cylinder agree within 3.5% of correlations of cylinders of infinite length (Clift et al. 2005).

High Reynolds number flow, $Re_p>100$, is characterized by significant secondary motion which is superimposed on the particles steady fall or rise. This starts with small oscillations, then periodic sidewards motion highly dependent on the shape, and finally evolves into chaotic tumbling motion as the Reynolds number increases further. The oscillations result from the distribution of pressure forces around it and the consequential change in the center of pressure due to the unsteadiness in the wake. Indeed, the oscillatory motion of symmetric non-spherical particles has a parallel to the well known shedding of vorticies behind a fixed cylinder, known as a von Karman vortex street, and photographic evidence by Willmarth et al. (1964) shows that the end of each period is indeed followed by the shedding of a vortex. The transition between these regimes; stable fall, periodic oscillatory motion and chaotic tumbling, is different for the three classes of particles mentioned here; ellipsoids cylinders and disks, and for each class the transition depends not only on the Reynolds number but also on another dimensional number; the dimensionless moment of inertia:

$$I^* = \frac{\pi\rho_p}{64\rho}\beta \tag{11}$$

It can be seen that the primary elements of this number is the density ratio and the aspect ratio. The density ratio is included to account for the difference in motion for different media and this is expected to be significant as also can be seen from the use of this ratio in the BBO equation. The aspect ratio expressed the influence of end effects: For cylinders, the effect of finite length causes it to oscillate in both the horizontal plane as well in the vertical plane there it causes sidestep motion. It is evident that the magnitude of these oscillations decrease as the aspect ratio increases and a very long cylinder may experience steady fall up to relative high Reynolds numbers. Disks are associated with two regimes of secondary motion besides the tumbling motion, although the distinctions between them are not sharp. Initial secondary motion is periodic oscillations where the stability of the motion can be related to the angle the disk departs from the horizontal axis. As the oscillations increases in amplitude the angle the disk makes passes a critical point and its flight becomes unsteady and is characterized by interchanging gliding periods, where the angle is almost 90 degree, and turning periods where the disk makes a 180 degree flip; this is referred to as glide-tumble motion.

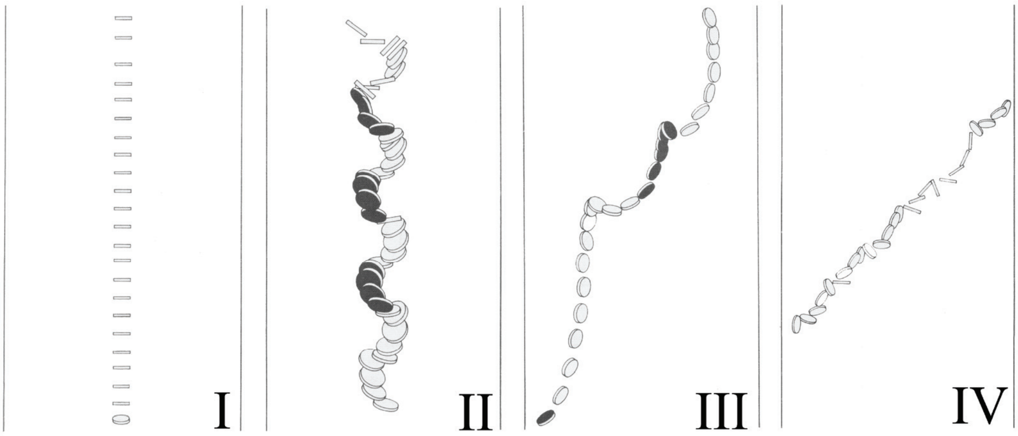

Figure 7: Regimes of motion for a disk. (I.) Steady fall. (II.) Periodic oscillations. (III.) Glide-tumble. (IV.) Tumbling. Modified from Stringham et al. (1969)

It is evident, from the turning motion, that disks, in the glide-tumbling regime, will not follow a vertical line but follow a path which is at an angle to the flow; this effect also applies for a disk in the tumbling region. Common for all shapes of particles are that there seems to be a correlation between the resistance to motion and the particles stability: As the frequency of oscillations increase, so does the drag coefficient based on the path velocity (Stringham et al. 1969). Similarly, when based on path velocity and the diameter of a circle with area equal to the maximum cross-sectional area of the particle, the drag coefficients for non-spherical particles are all located in a narrow band for intermediately Reynolds numbers, Re <2000, after that, the drag coefficient on disks diverge significantly due to a strong correlation between the drag coefficient and the dimensionless moment of inertia (Stringham et al. 1969).

Another aspect concerning the motion of non-spherical particles, which is of major importance for biomass, is the effect of a non-uniform mass distribution. This mean that the center of gravity is not located at the geometric center (for a symmetric particle) and will hence act to produce an additional torque on the particle, similar to the offset in the center of pressure caused by the wake effects. In practice, this means, since gravity is a steady force, that the particle will have a tendency to turn its heaviest side downwards. This may significantly alter its motion characteristics and possibly require an altogether different modeling approach. The best example of non-uniform mass distribution is the case of nodes on straw particles as investigated by Bilanski (1965). Straw of different length, which is this context can be viewed as circular cylinders, with respectively a node at the middle and a node at on end, was released in a vertical tunnel. It was shown that the particles which had a symmetric mass distribution, straw with no node or node at the middle, had the same resistance characteristics whereas particles with non-uniform mass distribution, straw with a node at no end, had a lower resistance to motion due to the particles being orientated in the vertical direction.

Orientation dependent forces and torques – Stokes flow

The method described in the section above can be used for any particle shape. However, the formulation of the forces and torques which act on the particle is almost exclusively formulated on the basis of an ellipsoidal shape. An ellipsoid has the advantage that it, by variation of its parameters, can be used to resemble a large array of different shapes; including that of a flake like particle (oblate ellipsoid) and a rod-like particle (prolate ellipsoid). Furthermore, this shape has no sharp edges which from a mathematical point of view would be treated as discontinuities. The groundbreaking work on the motion of ellipsoids was made by Jeffrey (1922) for suspension in a uniform shear flow under Stokes conditions where the formulation for the resistance force and torque is derived. This analysis has been expanded by Brenner[4] in the 1960's to arbitrary flow fields although still only under Stokes flow conditions. The translational resistance force is expressed in the form of infinite series of flow velocity and its spatial derivative with the inclusion of a translation matrix, ***K***. Unlike that of a spherical particle, spatial derivative higher than the second order also contribute to the translational resistance. However, according to Fan and Ahmadi (1995) higher order terms can be neglected for small particles since these corrections are proportional to higher order powers of the particles short axis. The first two terms in the series can be expressed as (Fan and Ahmadi 1995):

---

[4] The work of Jeffery was extended in the 1960's by Professor Howard Brenner in a series of publications: (Brenner 1964a,b,c,d), (Happel and Brenner 1965) and (Brenner and Condiff 1972).

$$\mathbf{F_R} = \mu \mathbf{K}'' \cdot (\mathbf{u} - \mathbf{v}) + \frac{\mu}{6} \mathbf{A}^{-1} \cdot \mathbf{K}' \cdot D^2 \mathbf{u}' \tag{12}$$

where μ is the dynamic viscosity, $\mathbf{u} = \left[u_x, u_y, u_z\right]$ is the fluid velocity vector with respect to the inertia frame and similarly $\mathbf{u}' = \left[u_{x'}, u_{y'}, u_{z'}\right]$ is that for the particle frame. It can easily be seen that equation (12) reduces to the Stokes drag and the Faxen force for the case of a sphere. Often, similar to the approach for the spherical parallel, the second term in equation (12) is neglected, resulting in an expression which is easier to evaluate. For an ellipsoid of revolution with semi-minor axis *a* and semi-major axis *b* the second derivative of ***u'*** is expressed as:

$$D^2 \mathbf{u}' = a^2 \frac{\partial^2 \mathbf{u}'}{\partial x'^2} + b^2 \frac{\partial^2 \mathbf{u}'}{\partial y'^2} + a^2 \frac{\partial^2 \mathbf{u}'}{\partial z'^2} \tag{13}$$

The translation matrix is expressed as:

$$\mathbf{K}'' = \mathbf{A}^{-1} \cdot \mathbf{K}' \cdot \mathbf{A} \tag{14}$$

where a mark and double mark again denote whether a quantity is expressed in the particle or co-moving frame. The particle frame translation matrix ***K'*** is a diagonal matrix with elements given by:

$$k_{x'x'} = k_{z'z'} = 16\pi a \left(\beta^2 - 1\right) \Big/ \left[\frac{2\beta^2 - 3}{\sqrt{\beta^2 - 1}} \ln\left(\beta + \sqrt{\beta^2 - 1}\right) + \beta \right] \tag{15}$$

$$k_{y'y'} = 8\pi a \left(\beta^2 - 1\right) \Big/ \left[\frac{2\beta^2 - 1}{\sqrt{\beta^2 - 1}} \ln\left(\beta + \sqrt{\beta^2 - 1}\right) - \beta \right] \tag{16}$$

where $\beta = a/b$ is the aspect ratio for a ellipsoid of revolution. This tensor depend only on the geometry of the body and thus only has to be solved once for any given shape. For axis-symmetric shapes the translation and rotation tensors are always symmetric while for non-symmetric bodies the rotation and translation are coupled and additional coupling tensors, which are not symmetric, have to be added (Gavze 1990). The components of torques from fluid resistance, which are used unchanged from Jeffery (1922) analysis, are given as:

$$T_{R,x'} = \frac{16\pi\mu a^3 \beta}{3\left(\beta^2 \beta_0 + \gamma_0\right)} \left[\left(\beta^2 - 1\right) \frac{1}{2} \left(\frac{\partial u_{z'}}{\partial y'} + \frac{\partial u_{y'}}{\partial z'} \right) + \left(\beta^2 + 1\right) \left(\frac{1}{2} \left(\frac{\partial u_{z'}}{\partial y'} - \frac{\partial u_{y'}}{\partial z'} \right) - w_{x'} \right) \right] \tag{17}$$

$$T_{R,y'} = \frac{32\pi\mu a^3\beta}{3(\gamma_0+\alpha_0)}\left(\frac{1}{2}\left(\frac{\partial u_{x'}}{\partial z'}-\frac{\partial u_{z'}}{\partial x'}\right)-w_{y'}\right) \tag{18}$$

$$T_{R,z'} = \frac{16\pi\mu a^3\beta}{3(\alpha_0+\beta^2\beta_0)}\left[\left(1-\beta^2\right)\frac{1}{2}\left(\frac{\partial u_{y'}}{\partial x'}+\frac{\partial u_{x'}}{\partial y'}\right)+\left(1+\beta^2\right)\left(\frac{1}{2}\left(\frac{\partial u_{y'}}{\partial x'}-\frac{\partial u_{x'}}{\partial y'}\right)-w_{z'}\right)\right] \tag{19}$$

where the parameters α_0, β_0 and γ_0 are given originally by Gallily and Cohen (1979) as

$$\alpha_0 = \gamma_0 = \frac{b^2}{b^2-a^2}+\frac{a^2b^2}{2\left(b^2-a^2\right)^{3/2}}\ln\left[\frac{b-\sqrt{b^2-a^2}}{b+\sqrt{b^2-a^2}}\right] \tag{20}$$

$$\beta_0 = -\frac{2a^2}{b^2-a^2}-\frac{a^2b}{\left(b^2-a^2\right)^{3/2}}\ln\left[\frac{b-\sqrt{b^2-a^2}}{b+\sqrt{b^2-a^2}}\right] \tag{21}$$

Substituting the expression for resistance force and torques, equations (12) and (17) – (19) into the equations of motion (4) – (7) yields the explicit equations of motion for an ellipsoid of revolution in an arbitrary flow field in the Stokes regime under steady motion. The mass and moments of inertia are simple relations of the geometry of an ellipsoid of revolution and are summarily given as: $m_p=(4/3)\pi a^3\beta\rho_p$, $I_{x'}= I_{z'}=(1+\beta^2)a^2m_p/5$ and $I_{y'}=2a^2m_p/5$. Interesting to note is that a particle in the Stokes regime in a shear field will have a final state which is described by the Jeffery's orbits, while a particle in a flow field which is characterized by zero vorticity will have a final state which is free of rotation. The resistance torque in the latter case arises from the initial rotation of the particle to account for the no slip boundary condition on the surface and thus acts to reduce the angular velocity of the particle.

A sphere in shear flow will experience a lift force due to the pressure distribution on the surface of the particle which arises from the velocity gradients. This force is known as the Saffman lift force after Saffman (1965) who formulated it for a sphere in the Stokes regime. The shear-induced lift force for an arbitrary-shaped particle was obtained by Harper and Chang (1968) by an extension of the original work by Saffman (1965) and has been formulated in the co-moving coordinate system by Fan and Ahmadi (2000). For an ellipsoid of revolution the shear-induced lift force is given by:

$$\mathbf{F}_\mathrm{L} = \frac{\mu}{\nu^{1/2}}\sqrt{\frac{\partial u_x}{\partial y}}\left(\mathbf{K}''\cdot\mathbf{L}\cdot\mathbf{K}''\right)\cdot\left(\mathbf{u}^\mathrm{L}-\mathbf{v}\right) \tag{22}$$

where **L**, the lift tensor, which is independent of the shape of the particle, is given as (Harper and Chang 1968):

$$\mathbf{L} = \begin{pmatrix} 0.0501 & 0 & 0.0329 \\ 0 & 0.0373 & 0 \\ 0.0182 & 0 & 0.0173 \end{pmatrix} \tag{23}$$

and $\mathbf{u^L}=[u_x,0,0]$ is the reference flow velocity. Lift forces play an important role at high shear flows, such as boundary layer flows, or for rotating particles to account for the lateral dispersion and migration which are experimentally observed. The interest on lift forces acting on non-spherical particles can be traced back to the time of Poiseuille (1841), who reported that blood cells keep away from the walls of capillaries. For spherical particles, the inclusion of additional terms to the BBO equation is done using the principle of superposition, however as several authors have noted that this is actually inconsistent with the creeping flow equations, which are for strictly rectilinear motion of a sphere (Michaelides 1997) (Leal 1980). For a spherical particle, in addition to the Saffman lift from shear flow, also the Magnus lift, caused by the rotation of the particle, contributes to the lift force. The Magnus effect (Magnus 1861) is notoriously difficult to measure or calculate accurately and is often neglected for simulations of spheres. For non-spherical particles the magnitude and importance of the Magnus force is difficult to estimate, but considering the increased resistance to rotation and the Magnus force dependency on the angular velocity and the associated Reynolds number it seems justified to neglect this effect for Stokes flow.

Body forces are independent of the shape of the particle which means that they can be included in the equation of motion using the standard methodology developed for spheres. For this investigation the most relevant body force is that emanating from the influence of gravity, known as the buoyancy force, which acts exclusively on the volume of the particle:

$$\mathbf{F_B} = V_p \rho_p \left(1 - \frac{\rho_c}{\rho_p} \right) \mathbf{g} \tag{24}$$

Of other possible body forces which are relevant to mention is the Coulomb force for charged particles, the thermophoretic force and the pressure gradient force. Unsteady forces include the virtual, or added, mass force which account for the acceleration of the surrounding fluid, and the Basset history force, which is seen to express the influence of the developing boundary layers[5]. Similarly to the above expression for the resistance force, the unsteady terms is dependent on the orientation of the particle and needs to be described using tensor notation. Following the notation by Gavze (1990) the equation of motion for a non-spherical particle can be formalized as:

---

[5] More correctly it represents the effect of the diffusion of vorticity around the particle.

$$\mathbb{F} = -\mathbb{R}\boldsymbol{u} - \mathbb{P}\cdot\dot{\boldsymbol{u}} - \int_0^t \mathbb{T}(t-\tau)\cdot\dot{\boldsymbol{u}}(\tau)d\tau, \qquad \mathbb{F} = \begin{bmatrix}\mathbf{F}\\ \mathbf{M}\end{bmatrix}, \quad \boldsymbol{u} = \begin{bmatrix}\mathbf{U}\\ \boldsymbol{\omega}\end{bmatrix} \qquad (25)$$

where $\mathbb{R}$, $\mathbb{P}$ and $\mathbb{T}$ are respectively the steady, potential and Basset tensor. However, the incorporation of the unsteady forces depends on finding the basic solutions for different shapes. This is quite a complicated problem due to the non-steadiness nature and no publications so far have taken up the challenge. The linearized Navier-Stokes equations, analytically solved for the oscillatory motion of a sphere and integrated for arbitrary time-dependent motion, yield the force acting on the particle: the BBO equation. Such an elaborate method is not suitable for orientation dependent shapes and it is suggested by Gavze (1990) that numerical methods should be used instead. Lawrence and Weinbaum (1986, 1988) conducted a study on a slightly eccentric ellipsoid of revolution with major semi-axis $b = a(1+\varepsilon)$, in oscillatory cross flow to extract the time-dependent terms. Note that only translational motion is considered for this analysis. In addition to relevant expansions of the steady state, virtual mass and Basset, expressed by the eccentricity, ε, an new term emerges which does not appear for spheres and is entirely accredited to the non-sphericity of the particle in question:

$$\begin{aligned}\mathbf{F}_{LW} = &-6\pi\mu a\left(1+\tfrac{1}{5}\varepsilon+\tfrac{37}{175}\varepsilon^2\right)\mathbf{u} \; - \; \frac{2\pi\mu a^3}{3\nu}\left(1+\tfrac{2}{5}\varepsilon+\tfrac{81}{175}\varepsilon^2\right)\frac{d\mathbf{u}}{dt} \\ &-\frac{6\pi^{\frac{1}{2}}\mu a^2}{\nu^{\frac{1}{2}}}\left(1+\tfrac{1}{5}\varepsilon+\tfrac{26}{175}\varepsilon^2\right)\int_0^t \frac{d\mathbf{u}}{d\tau}\frac{d\tau}{\left(t-\tau\right)^{\frac{1}{2}}} \; - \; \frac{6\pi^{\frac{1}{2}}\mu a^2}{\nu^{\frac{1}{2}}}\int_0^t \frac{d\mathbf{u}}{d\tau}G\left(t-\tau\right)d\tau\end{aligned} \qquad (26)$$

with the kernel function G(t) given as:

$$G(t) = \frac{8\varepsilon^2}{175}\operatorname{Im}\{(\pi\alpha)^{\frac{1}{2}}e^{\alpha t}erfc(\alpha t)^{\frac{1}{2}}\}, \qquad \alpha = 3e^{\frac{1}{3}i\pi} = \tfrac{3}{2}(1+\sqrt{3}i) \qquad (27)$$

The fourth term is similar to the Basset force being a memory integral but the behavior of *G(t)* is different from the Bassets terms $t^{1/2}$ dependency. *G(t)* is not infinite for small *t*, as $t^{1/2}$, and G(t) is consistently smaller than $t^{1/2}$. According to Lawrence and Weinbaum (1986) since the recent history is not emphasized as it is in the Basset term the contribution from the fourth term will be small. However, this analysis only applies for small eccentricities and for other body shapes it is likely that this term is more significant. In their later work, Lawrence and Weinbaum (1988) pointed out that the part in the different terms relating to the eccentricity should be replaced by tensors to be valid for different orientations and arbitrary shapes; however no general solution is presented. The terms are also evaluated at different aspect ratios and different frequencies. For bodies which are streamlined with respect to the flow, i.e. large aspect ratios, the added mass term is small, whereas the Stokes drag and the Basset term increase due to the increased surface area.

Orientation dependent forces and torques – Higher Reynolds number flow

The simpler formulation of the governing equations for fluid motion, which is achieved by neglecting the advection part of the full Navier-Stokes equations, allows for the analytical formulation of the time dependent equation of motion for spheres and the steady state equation of motion of axis-symmetric shapes. This limitation of Stokes flow is nonetheless severe, and the formulation of the forces and torques described above cannot be used for many engineering flows. To be exact Jeffery's (1922) solution is only strictly valid for zero Reynolds number and even at $Re \sim O(10^{-3})$ it has been proved that the inertial effect is sufficient to force non-spherical particle in a different orbit than that predicted by Jeffery (Karnis et al. 1963; 1966). For higher Reynolds numbers, $Re > 0.1$, the effect of flow separation will tend to slow down and stop any rotation caused by a velocity gradient (Ding and Aidun 2000). Empirical expansions of especially the steady state term have long been the backbone in investigations at higher Reynolds number flow for both spheres and non-spherical shapes alike. For non-spherical particle this is usually done by inclusion of equivalence factors, such as the sphericity. However, this is a highly questionable approach considering the known inability of equivalence factors not only to deal with the secondary motion, but also the fact, that it correlates poorly with the drag coefficient.

Recent advances into the modeling of non-spherical particles at Reynolds numbers above unity has sprung from the work of Ding and Aidun (2000), Qi and Luo (2003) and Qi (1997, 1999, 2000, 2001, 2005, 2006) who all used the lattice-Boltzmann formulation of the Navier-Stokes for different particle shapes. The lattice-Boltzmann method has been proven to be ably to reproduce experimental findings for Reynolds numbers above unity and is as such a valuable research tool. However, for application with an arbitrary geometry and multiple particles this method becomes far too computationally expensive for any practical use.

The reported secondary motion of non-spherical particles in a uniform flow field at higher Reynolds number flow, as outlined previously, was suggested to be caused by the wake of the particles. At higher Reynolds number the pressure distribution is unstable and the particle is forced away from its horizontal alignment which characterizes the motion at intermediate Reynolds numbers. Consider a particle which is released from an initial position inclined from the horizontal as illustrated in the figure below. The pressure distribution, as indicated with + and -, causes the resulting resistance force to work at the center of pressure rather than the center of geometry as was the case for Stokes flow. This non-coincidence of the center of pressure and center of gravity causes the sustained oscillations. Additionally, the pressure distribution also results in a lift force, known as profile lift, which moves the particle away from its otherwise vertical path.

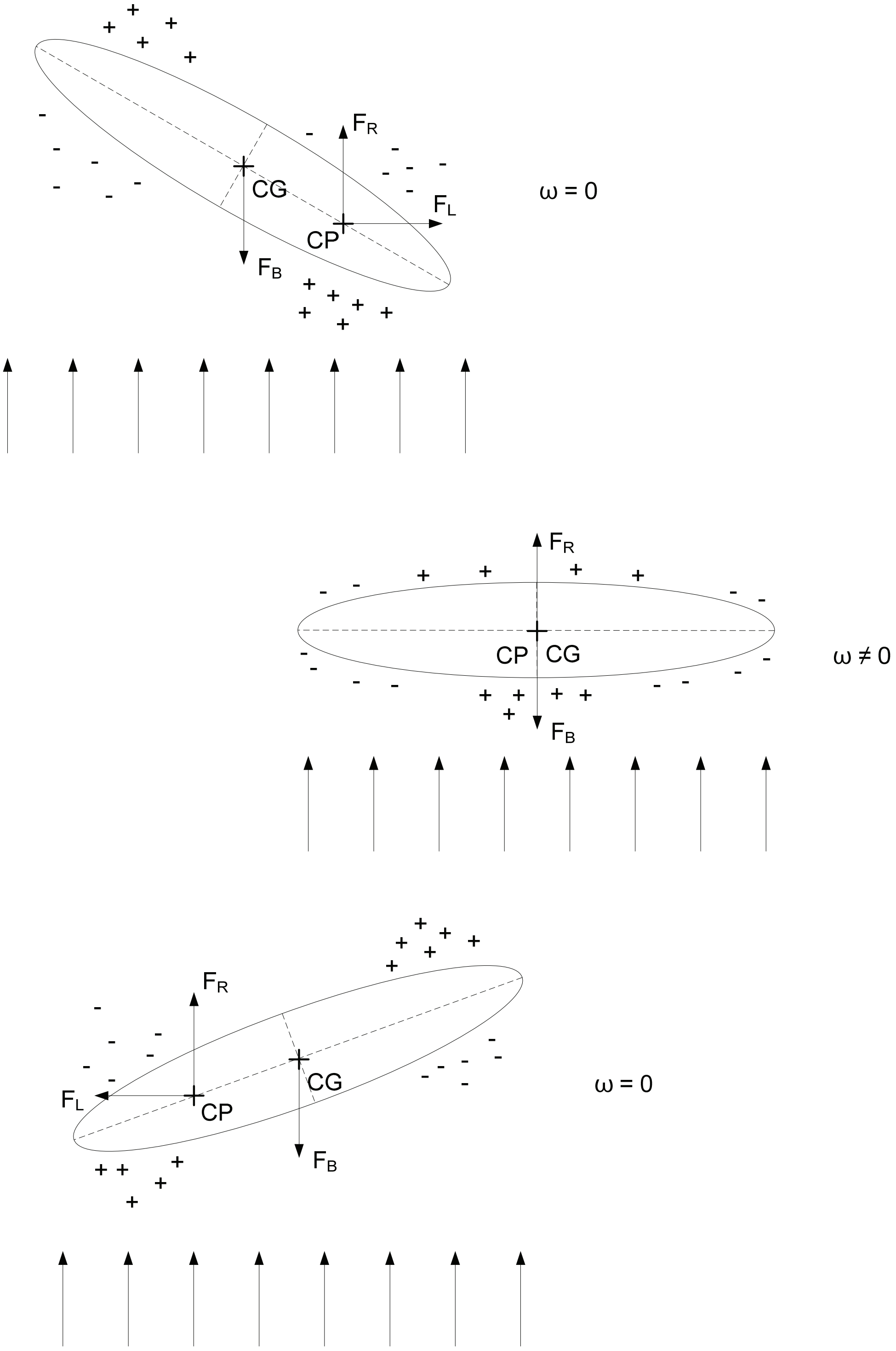

Figure 8: Location of forces and the pressure distribution of a particle at higher Reynolds numbers (Re>100) in uniform flow. CP is the Center of Pressure and CG is the Center of Gravity/Geometry. F_B is the buoyancy force, F_L is the lift force and F_R is the resistance force.

For modeling the motion at higher Reynolds number, the problem is reduced to finding appropriate expression for the total resistance force, the lift force and the location of the center of pressure. The traditional approach for spheres, to modify the equation of motion at higher Reynolds numbers, has been to incorporate a factor, *f*, dependent on the Reynolds number, which is determined experimentally. When transferred to the non-spherical shapes we get:

$$\mathbf{F_R} = \mu f \mathbf{K}'' \cdot (\mathbf{u} - \mathbf{v}) \tag{28}$$

The matrix ***K”*** already expresses the difference in the projected areas for different shapes and as the particle rotates and no additional measures have to be taken in that account. The factor *f* should in addition to be dependent on the Reynolds number also show dependence on both the shape and orientation. For a sphere the *f* is given as:

$$f = \frac{C_D \mathrm{Re}}{24} \tag{29}$$

which gives the correct limit of 1 for Stokes flow. However, due to the inherent complexity of such a parameter no such correlation has been developed. Available measurements and associated correlations come from investigation of different shapes with fixed axis in relation to the flow or from investigation of particles in free fall. The work by Stringham et al. (1969) summarizes the knowledge of the dependency of the drag coefficient of different shapes at Reynolds numbers in the range 10 – 100.000:

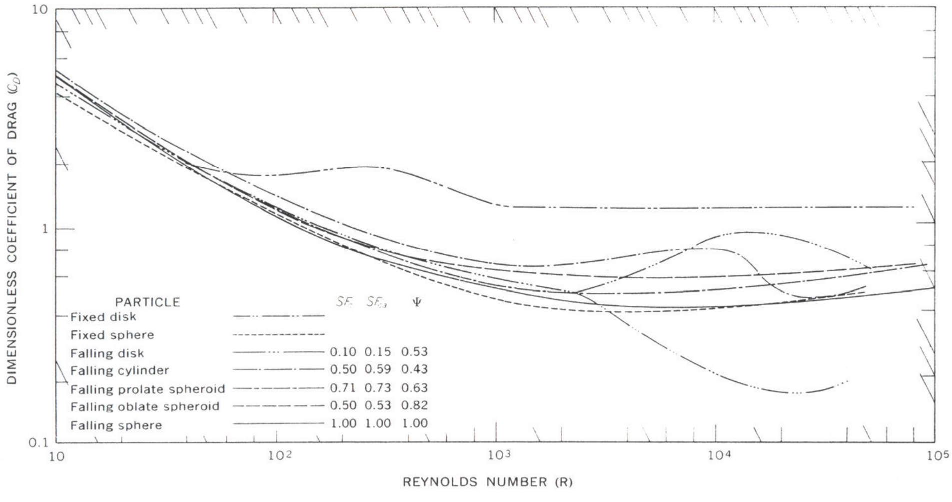

Figure 9: Composite graphs of coefficient of resistance as a function of Reynolds number for falling spheres, disks, oblate spheroids, cylinders and prolate spheroids based on path velocity and the diameter of a circle of area equal to the maximum cross-sectional area of the particle. Also shown are different equivalence factors expressing the shape of the particles used (Stringham et al. 1969).

It can be realized that the different shapes show a large degree of similarity and it seem prudent to formulate a general shape dependent correlation. The work of Militzer et al. (1989) introduces an empirical correlation for the drag coefficient valid for spheroids with aspect ratios between 0.2 and 5 over a Reynolds number range of 1 to 200. This is based on an expansion of the classical expression for spheres developed by Schiller and Naumann (1933) and the empirical data is obtained for freely falling particles:

$$C_D = \frac{24}{\mathrm{Re}}\left(1+0.15\,\mathrm{Re}^{0.687}\right)\frac{4+\beta}{5}\left(1+0.00096\frac{\mathrm{Re}}{\beta}-0.000754\,\mathrm{Re}\,\beta+\frac{0.0924}{\mathrm{Re}}+0.0027\beta^2\right) \quad (30)$$

The Reynolds number used is here based on the equatorial diameter and the β is the aspect ratio of the spheroid. However, the dependency of the orientation is not included in this expression and its applicability can as such be disputed. This approach is similar to that developed by Rosendahl (1998) and Yin et al. (2003) which is the only work known to the author to expand the modeling framework presented to higher Reynolds numbers. For calculation at Re > 200 it is suggested to base the drag coefficient on available expressions for sphericity (Yin et al. 2003). However, a look at figure 9 implies that expressions developed for spheres might as easily be applicable. For disks, relations incorporating the dimensionless moment of inertia would be the best approach.

The lift force seems to be related to the drag force for axisymmetric particles both for stokes flow and for the inertial regime. Applicable for higher Reynolds number flow can be mentioned the cross flow principle (Hoerner 1965) where the lift force on a inclined infinite long circular cylinder in the Newtons law regime can be estimated on basis of a relation of the base drag coefficient and the inclination angle:

$$C_L = C_D \sin^2\alpha_i \cos\alpha_i \quad (31)$$

This principle is used by Rosendahl (2000) and Yin et al. (2003) to calculate the lift coefficient for particles with limited aspect ratio and for the entire Reynolds number regime. It is doubtful if the cross-flow principle is applicable under such circumstances, however, this does yield a lift coefficient which is similar in magnitude to the drag coefficient and which displays the right asymptotic behavior for zero inclination angle. Also, using this method the lift force is calculated using the projected area normal to the direction of the lift force.

The resistance and lift force which act at the center of pressure, which is not coincident with the center of gravity, gives rise to torques. The location of the center of pressure on the particle is dependent on both the shape and the inclination angle. There exists no general accepted theory to predict the location of the center of pressure and no empirical correlations have been developed for the Reynolds number range in question, the specific shapes or as a function of the orientation. From airfoil theory the center of pressure is approximately located a distance of *0.25 x chord length* behind the leading edge for a multitude of profiles and valid for inclination angles in the range 0 - 15°. Modifying this expression for shapes with small aspect ratios, compare to airfoils, and for inclination angle larger then 15° the location of the center of pressure is suggested to expressed as (Yin et al. 2003):

$$x_{cp} = \frac{1}{2} a \left(1 - e^{3(1-\beta)}\right) \cos^3 \alpha_i \tag{32}$$

The torque can be calculated simply as the x_{cp} multiplied with the resulting force of the lift and resistance force in the appropriate reference frame. Again it is highly questionable if this rule of thumb for airfoils is actual applicable for particles where the aspect ratio and the Reynolds numbers are much smaller. Again it is prudent to note that this method is useful since it gives the right asymptotic behavior. Similar to the resistance of translation for higher Reynolds numbers, which is expressed by adding an additional factor *f*, dependent on both the Reynolds number and the shape, so can also the resistance to rotation be expressed. In the work by Rosendahl (2000) and Yin et al. (2003) the same correlations of the drag coefficient is used for the translation and rotational resistance, in the latter case based on the rotational Reynolds number Re_ω instead. This can be entered into equations (17) – (19).

The empirical model developed by Rosendahl (2000) show promising results when applied on a cylinder in free fall (Yin et al. 2003) and can as such be considered as a usable model for the steady motion of a single large non-spherical particle in a Newtonian fluid free from turbulence. Engineering flows generally introduce a number of interaction effects, between the particles and the fluid flow, which have to be addressed for a successful implementation into a modeling framework.

On multiphase models

The numerical methods used in the context of dispersed multi-phase flow can be divided into three categories:

- The Eulerian-Lagrangian method, where the trajectory of each individual particle is traced as they move through a continuous fluid phase under the influence of fluid dynamic forces.
- The Eulerian-Eulerian method, or two-fluid method, where both the carrier phase and particle phase are treated as a continuum. The particle phase is modeled using partial differential equations similar to those which are used for the continuous phase.
- The Probability Density Function (PDF) method, or the particle cloud method, where the trajectory of a group of particle is tracked while the

concentration of the cloud is represented by a Gaussian probability density function.

Eulerian-Lagrangian

In the Eulerian-Lagrangian method the trajectory of a number of particles is calculated by solving discretised equation of motion through a known velocity field. For a problem where only one-way coupling it considered the computation of the continuous phase precedes the calculation of the particle trajectories, while for a coupled simulation the algorithm alternates repeatedly between solving the continuous phase and the trajectories. The coupling is performed via source terms calculated at every discretized volume. The statistical result of the trajectories can be used to estimate the probability density function (PDF) at a given location. The Lagrangian reference frame is the natural reference frame for discrete entities, but to achieve statistical independence a large number of trajectories is required which makes the method computationally expensive. Often the Eulerian-Lagrangian methods implemented neglects the volume change in the continuous phase due to the presence of particles and the transport equations are solved assuming constant volume in each discretized volume. This assumption becomes less accurate at regions of high concentration or when large particles are modeled. Often each trajectory is seen to represent a group or stream of particles, in order to save computational resources, but this assumption produce poor numerical results due to poor statistics and may cause convergence problems for coupled simulations.

One of the earliest works describing the motion of non-spherical particles in a Lagrangian frame is that of Galilly and Cohen (1979) who demonstrated this method for small ellipsoidal particles with sizes down to 5 µm based on the largest axis. To simulate the influence of turbulence on the particles several approaches may be implemented for the Lagrangian reference frame. Overall we distinguish between models based on stochastic Markov-sequences, so called random walk models, and imitating the turbulence directly by means of a predefined turbulent like flow field. For work involving non-spherical particles the latter approach have been the most popular and the flight of non-spherical particles in isotropic turbulence have been studied using a Gaussian random field where the instantaneous velocity field is given as series of Fourier nodes with zero mean and specified standard deviation (Fan and Ahmadi 1995), (Olson 2001). The same idea has also been used to create vortex like structures which can be considered as a more qualitative description of turbulence. As such the turbulence boundary layer has been modeled using periodic vortical flow structures within various distances from the wall by Fan and Ahmadi (2000) and flow field consisting of four counter rotating 2D vortices by Shin and Maxey (1997).

The major limitation for investigations incorporating turbulence effects for non-spherical particles is that the flow around the particles is modeled as Stokes flow, using the fluid dynamics of Jeffery (1922), where the major axis length is smaller than the Kolmogorov length scale and the particle Reynolds number smaller than 0.1. For turbulent flow this typically results in rather small particles where also

Brownian motion becomes important. The study by Fan and Ahmadi (2000) introduces an additional Brownian force and Brownian torques in the equations of motion to supplement the fluid dynamic forces. At the same time the fluid dynamic forces are modified by introducing approximations of the translational and rotational slip factors. Keeping in line with the notion of the random nature of Brownian motion, this is again modeled as an independent Gaussian process. Clearly the similarities between Brownian and turbulent motion suggest that such a random walk model is could also be used for non-spherical particles in turbulent flow. Ideally models addressing non-spherical particles in turbulence should be put into the same context as the popular two-equation turbulence models to be applied on an arbitrary flow field and still be within the reach of present computational resources. This has still only been done using the sphericity approach (Sun et al. 2004), (Backreedy et al. 2005).

Eulerian-Eulerian

In the Eulerian-Eulerian method the particle phase is assumed to behave as a fluid and the behavior of both the dispersed phase and the carrier phase is modeled using the appropriate transport equations. For dense flow this assumption becomes more realistic and it is actually recommended to use this approach compared to the alternatives (Fluent 2006). Compared to the Eulerian-Lagrangian method the Eulerian-Eulerian method is less computationally expensive and the coupling between the phases, including turbulence and Brownian effects, is easier to implement. The drawback of the Eulerian-Eulerian method is its inability to capture the size distribution (also chemical composition, density, etc.) which is normally present. To accurately represent different sizes of particles each size would have to be modeled as a separate phase, with their own set of equations.

The classical work for non-spherical particles in the Eulerian reference frame is often referred as that of Hinze (1975). The basic idea is to use the Eulerian convection-dispersion equation to express the probability distribution, $\psi(r,p,t)$ of orientation, p, and position, r. In this manner dispersion coefficients can be formulated for both translational as well as rotational motion and the inclusion of turbulent or Brownian motion is done by expressing the appropriate dispersion coefficients. In the context of two-equation turbulence models the turbulent dispersion can be expressed simple by:

$$D_p = 0.7\left(\frac{4\varepsilon}{15\nu}\right)^{1/2} \tag{33}$$

where ε is the dissipation rate. Other estimates are given in the recent publications of Olson et al. (2004), Paschkewitz et al. (2004), Zhang et al. (2005) and Zhang et al. (2006). Usually the expressions given are complex relations of the orientation and interaction with the turbulence. Due to the nature of the Eulerian frame one would expect that the coefficients given need to be fine tuned in order to reproduce experimental results and can as such not be considered as universal models. The model by Zhang et al. (2005) has been compared with the experimental data by Bernstein and Shapiro (1994). The numerical result is able to reproduce the same tendencies as the experiments with respect to the orientation distribution but at some points the model may be off by as much as 100 %.

PDF method

In the PDF method the dispersed phase is modeled as a cloud of particles which is propagated along a path, determined by the equations of motion for a single particle. The behavior of the cloud is determined by a probability function which is dependent on the properties of the continuous phase including the turbulence characteristics. However, the formulation using statistical methods in combination with Lagrangian tracking means that performance of this model is poor for wall bounded flows. The motivation to use the PDF approach is that it is less computationally demanding and generally gives better statistics in low concentration regions of the flow compared to the Eulerian-Lagrangian method. At the same time it can easily treat different sizes without the severe additional cost of the Eulerian-Eulerian method. As far as the author is aware of no attempts have been made modeling the motion of non-spherical particles using the PDF approach.

Interaction effects

It should be stated that the characterization of different interactions regimes and the methods to deal with this has been formulated solely for the case of spherical particles. Usually these involve a characteristic lengths or measure for the size of the particles which for a spherical particle is obviously the diameter. For non-spherical particles, this usually best translate to the volume equivalent diameter and unless specifically mentioned otherwise this measure is used. The fluid, in which the particles are suspended, is restricted to Newtonian fluids. However, it should be mentioned that a particulate solution, as a whole, could display non-Newtonian behavior, which is dependent on the orientation of the particles (Carlsson 2007). The carrier phase is further treated as a continuum, meaning that the equations of motion described above are valid. This implies that the particles are significantly larger than the fluid molecules which are justified in the case of suspension of large biomass particles. The criteria for when the carrier phase can be treated as continuum is given by the Knudsen number which describes the ratio between the free mean path, λ, of a fluid molecule and the appropriate size of the particle:

$$Kn = \frac{2\lambda}{d_p}, \qquad \lambda = \frac{\mu}{\rho_c}\sqrt{\frac{\pi M_c}{2RT}} \tag{34}$$

where M_c is the molecular weight and R is the gas constant. The Knudsen number is named in honor of the Danish scientist Martin Knudsen (1871-1949) and determines whether statistical mechanics or fluid mechanics are suitable to model the motion of particles. Alternatively, the Knudsen number is also formulated to express the influence of rarefaction of the flow:

$$Kn = \frac{Ma}{\mathrm{Re}}\sqrt{\frac{\pi\gamma}{2}} \tag{35}$$

where γ is the ratio of the specific heats. In this manner also compressibility effects can be considered. For small particles, d_p<10 μm for air flow, the particles are said to slip and in this case the resistance force can be modified with a factor, the so-called Cunningham's correction factor, which depends upon the particle size. For elliptical particles appropriate slip factors have been developed by Fan and Ahmadi (2000) for both translational and rotational slip. The behavior of very small particles in a suspension is referred to as Brownian motion and can be characterized as chaotic or random like and is associated with increased diffusion. In the framework of Eulerian-Lagrangian modeling it has been suggested to include this effect as by introducing an additional fluctuating force in the equations of motion (Zhang et al. 2006). Both the components of Brownian force and torques in the particle frame are modeled by means of independent zero-mean Gausssian white-noise processes. In the framework of Eulerian-Eulerian modeling the effect of Brownian motion is easily included as additional diffusion in the same way as turbulence effects are included. For the orientation of non-spherical particles the relative influence of the fluid dynamic forces and the randomizing factors are described by the characteristic rotational Peclet number (Bernstein and Shapiro 1994):

$$Pe = W_0/D_0 \tag{36}$$

where W_0 is a characteristic velocity gradient and D_0 is the particle's rotational diffusion coefficient. D_0 comprises effects from both the Brownian and the turbulent diffusion and is simply calculated as $D_0=D_B+D_t$. Guidelines for the calculation of the diffusion coefficients are given in (Bernstein and Shapiro 1994). The rotational Peclet number can be seen as a measure for when randomizing factors should be taken into consideration. For high Peclet numbers the fluid dynamic forces tend to give the particles a preferred direction in a statistical sense[6] whereas for low Peclet numbers the turbulence or Brownian motion acts to give the particle an random orientation.

The interaction between particles and turbulence is, considering the title of this dissertation, of prime interest and a more thorough account of this subject will be presented in the following sections. Generally the influence of particles on the

---

[6] Although the motion is described by Jeffery's orbits, the particles spend most of their time with their long axis nearly aligned with the flow direction (Carlsson 2007)

carrier phase turbulence is known as turbulence modulation and the influence of turbulence on the particulate phase is known as turbulent dispersion. In a particulate suspension the particles continuously exchange momentum with the carrier phase as a consequence of the resistance forces which acts on the particles. The magnitude and the importance of these effects are determined by the amount of particles which is present. Although the amount of particles present can be quantified in many different ways, it is tradition to distinguish between different regimes of interaction by using the volume fraction. One very illustrative classification is given by Elgobashi (1994):

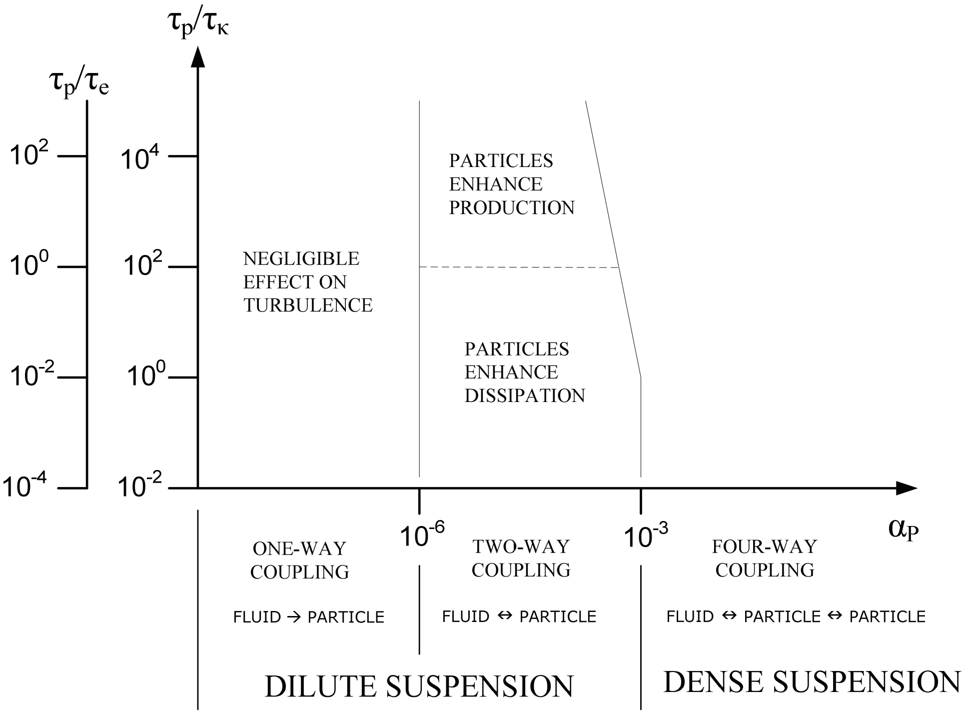

Figure 10: Map of regimes of interaction between particles and turbulence. Slightly modified from Elgobashi (1994).

For particle volume fractions less then 10^{-6}, particles are to few and far between to have a significant effect on the carrier phase and the interaction is known as one-way coupling. For particle volume fractions in the range from 10^{-6} to approximately 10^{-3}, there are enough particles to influence the carrier phase turbulence, the turbulent modulation or modification, but they are still to far apart so that particle collisions are not important. For higher particle volume fractions the time between particles collisions are at the same order as or smaller than the particle response time and the previously described equations of motion cease to be valid. The vertical axes on figure 10 represent the ratio between particle response time and relevant time scale of turbulence, but could also be seen as representing the ratio between the particle size and relevant turbulent length scale. The line separating the dilute and dense regimes is inclined indicating that larger particles, compared to the volume fraction, have a greater tendency to collide. The ratio between the particle response time and the time between collisions is the best measure for evaluating if the flow is dense or dilute, but the time between collisions can be difficult to quantify since it depends on the relative velocity between particles. For a turbulent particulate flow the relative velocity between particles should be related to the standard deviation of the particles fluctuating velocity, σ, and a criteria for when the flow is considered dilute can be expressed as (Sommerfeld 1994):

$$\frac{\tau_p}{\tau_C} \approx \frac{z\rho_c \sigma d_p}{1.33\mu_c} < 1 \tag{37}$$

where z is the mass loading. Furthermore, the standard deviation of the particles fluctuating velocity is the same order of the fluctuation velocity component of the carrier phase. For air at standard conditions the variations of the particle diameter with mass loading is shown in figure 11. For particles with diameters exceeding 1 mm the loading should be less the 0.1.

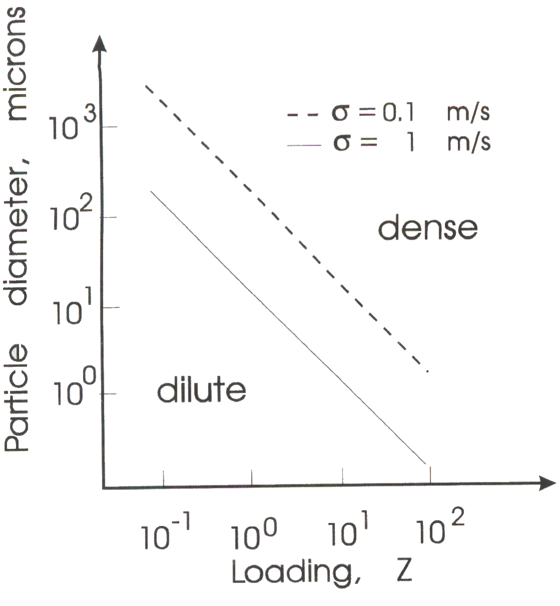

Figure 11: Dilute-dense flow regions for air at standard conditions. (Crowe, Sommerfeld and Tsuji 1998)

Simulation of dense flow requires the use of a more general Discrete Element Method where the individual particles, or parcels of multiple particles, are tracked with time. This is considered to be out of the scope of this work and the reader is instead referred to the recent work by Tsuji (2007) and Curtis and van Wachem (2004) for an update on this topic.

For dilute flow the carrier phase turbulence will always effect the particle phase. The appropriate non-dimensional number describing the particles reaction to the local turbulent fluctuations is known as the Stokes number:

$$St = \frac{\tau_p}{\tau_e} \tag{38}$$

The Stokes number is the ratio between the particles response time and an appropriate time scale of the flow, here expressed as the eddy turnover time. For Stokes numbers below unity the particles tend to follow the flow whilst for Stoke numbers above unity particles are less affected by the carrier phase turbulence. Tang et al. (1992) performed an experimental and numerical study of the particle laden wake behind a bluff body. For the studies, particles are introduced at the end of the body into the wake region. Figure 12 shows the dispersion patterns in the numerical study for Stokes numbers from 0.01 to 100. Note that the St = 0.01 particles mark the fluid elements while the St = 100 particles pass through the layer only slightly affected by the large vortices.

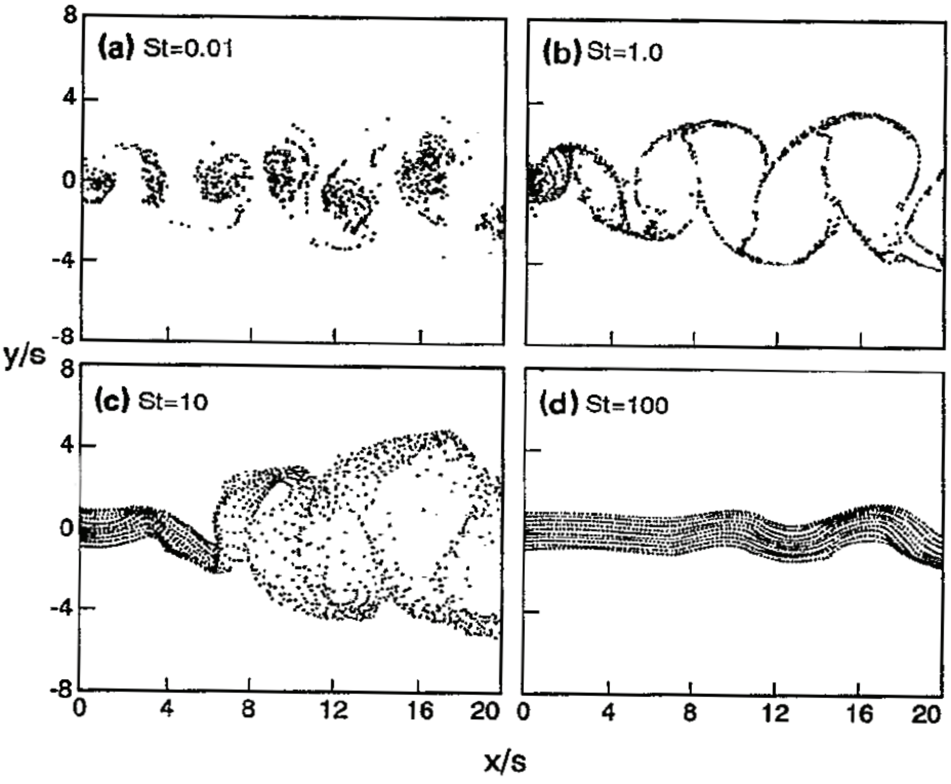

Figure 12: Instantaneous particle locations from two-dimensional discrete vortex simulation of plane wake. Particles introduced in the wake behind bluff body. Tang et al. (1992).

To evaluate the influence of the particles on the carrier phase an additional coupling parameter can be defined (Founti et al. 1999):

$$\Pi = \frac{C}{1+St} \tag{39}$$

Where the particle concentration, C, is the ratio of the mass of the dispersed phase to that of the carrier phase. If Π is smaller then unity the interaction between particles and the carrier phase can be considered as one-way coupling.

The distinction between augmentation and attenuation of turbulence is severely disputed, and the use of the Stokes number as in figure 10, might be questionable. The only criteria for which there is some consensus seems to be that small particles tend to attenuate turbulence and that large particle tend to augment turbulence. Sufficiently small particles are able to follow the turbulent fluctuations and extracts energy from the turbulent carrier phase through the drag force. The turbulent energy of the eddy is therefore transformed into the kinetic energy of the particle and the turbulence intensity will be reduced. Larger particles on the other hand do not follow the flow, and as such should extract even more energy, but the particles in question are so large that their wake generates additional turbulence and thereby globally augments the turbulence. Accordingly it has been suggested by Gore and Crowe (1989) that the ratio between the particle diameter and the turbulent length scale l_e could be used as a criterion for turbulence modulation. The appropriate parameter to evaluate the turbulent modulation by particles is by the change in the turbulence intensity compared with clear flow. In the figure below the data from a number of different experiments is compiled on basis of the suggested length scale ratio:

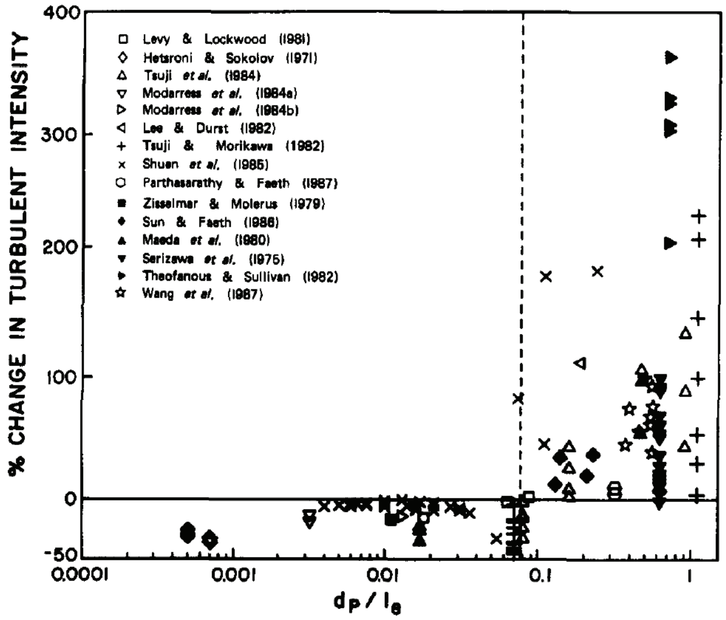

Figure 13: Change in turbulence intensity as function of length scale ratio (Gore and Crowe 1989)

From the figure it can be seen that a value of the length scale ratio d_p/l_e=0.1 offers a demarcation for distinction between when the addition of particles will cause an increase or decrease in the carrier phase turbulence. Although this is a purely empirical observation and a very simple expression, it has become widely accepted as the best criteria for evaluating the modulation effect. Yet a different criterion for turbulence modulation, formulated by Hetsroni (1989), is based on the particle Reynolds number. In this view, turbulence production is caused by the shedding of eddies in the wake of particles and the turbulence augmentation is expected for values of $\mathrm{Re}_p > 400$.

To evaluate turbulence modulation there are three competing criteria: The Stokes number, the particle Reynolds number and the ratio of length scales, which all claim to be important in particulate flows. Furthermore, to evaluate the magnitude of the turbulence modulation the appropriate parameter is either the mass loading or the volume fraction. The introduction of non-spherical particles brings in additional mechanisms for production and reduction of the carrier phase turbulence. This implies that additional parameters need to be formulated to evaluate the turbulence modulation encountered for non-spherical particles. Before the specific models developed to predict turbulence modulation are described it seems fitting first to have a more general description of turbulence and the methods used to simulate particulate flow.

Turbulence modulation by non-spherical particles

As previously stated there is no real consensus into the cause and effects of turbulence modulation. General observations seem to suggest that small particles attenuate the carrier phase turbulence whilst larger particles tend to augment it. From studies of power-spectral measurements of the fluctuating velocity it has been observed that the addition of particles results in a decrease of the turbulence energy in the high wave number region (Jou, Sheen and Lee 1993). This is interpreted as a result of the turbulence energy transfer from eddies to particles accelerated by the eddies (Tu and Fletcher 1994). This suggests that the characteristic length scale associated with dissipation is no longer the Kolmogorov scales but that also the inter-particle spacing and the particle diameter need to be considered. The production of turbulence is thought of as being due to the wake of the particles and as such should be a function of the velocity difference between the particles and carrier fluid.

In the case of turbulence modulation by non-spherical particles the type of interaction is more complicated than that of spherical particles due to the higher degree of freedom of motion for the particle. The secondary motion which is associated with all non-spherical particles while falling at higher Reynolds number, *i.e.* $Re_p>100$, in otherwise still environment, suggest that they are capable of transferring mechanical energy into turbulent kinetic energy in more modes that the case of spherical particles. Moreover this secondary motion generally occurs at lower particle Reynolds numbers depending on the non-dimensional moment of inertia. For moderate Reynolds numbers, *i.e.* $1<Re_p<100$, non-spherical particles in free fall tend to orient themselves with the maximum cross-section perpendicular to the flow direction. However, if exposed to turbulence the otherwise steady falling non-spherical particles will experience a wobbling or chaotic motion depending on their size and the magnitude of the turbulence (Klett 1995). This suggests that the secondary motion acts to attenuate the carrier phase turbulence by extracting turbulent kinetic energy into secondary motion. Most notable for freely falling non-spherical particles is that the drag coefficient is higher than that of the spherical ideal (Stringham, Simons and Guy 1969). This indicates that generic non-spherical particles are able to respond faster to the changes in the carrier phase velocity and that the response time is lower compared to volume equivalent spherical particles. The orientation dependent forces acting on the particles cause them to exhibit a more random behavior in their fluctuating velocities than the spherical counterparts (Black and McQuay 2001).

Only one study known by the author attempts to model the turbulence modification in the presence of non-spherical particles. Sun et al. (2004) derives a new particle-source term for the Navier-Stokes which includes the effect of non-spherical particles using a shape factor based on sphericity. Due to the increase in the drag coefficient, non-spherical particles are, not surprisingly, found to have a greater effect on the turbulence than volume equivalent spherical particles. Since the calculation of the secondary motion involves the solution of additional ordinary differential equation for the orientation and rotation most particle tracking computations rely on the assumption of spherical particles with modified average drag coefficients. However, as previously mentioned, a review and evaluation of available correlations done by Chhabra, Agarwal and Sinha (1999) shows that the error in calculation of the average drag coefficient compared to measurements can be in excess of 100%. Moreover the sphericity factor is often used as a basis to establish correlations of the drag coefficient, but this parameter is known to correlate poorly with the terminal velocity for shapes with large aspect ratios (Clift, Grace and Weber 2005; Mckay, Murphy and Hillis 1988). Using DNS in the near wall region Paschkewitz et al. (2004) showed how rigid slender fibers would align in between vortices, generating large stresses that oppose the vortex motion and thereby act to dissipate the eddies. Drag reductions of up 26% are calculated depending on the aspect ratio and the concentration, showing that the shape alone can significantly alter the turbulence characteristics.

Summary

The existing knowledge concerning the motion of non-spherical particles and their interaction with the carrier phase has been reviewed. The following conclusions can be drawn:

- Although mainly irregular shapes occurs in engineering flows most work has been done on spheres and most simulations are performed assuming non-spherical particles to be spheres.
- Theoretical derivations of the equation of motion for regular shapes exist for Stokes flow while only semi-empirical methods are available to predict the significant secondary motion at higher Reynolds number.
- For intermediate Reynolds numbers the motion of non-spherical particles are stable and drag correlations based on sphericity, although imprecise, can be used for a wide range of shapes to predict the trajectories of non-spherical particles.
- There is no consensus about the mechanisms for turbulence modulation in the presence of spherical particles and no model is able to predict the entire range of experimental observations. Observations suggest that large particles augment turbulence while small particles attenuate turbulence.
- Little knowledge exists about turbulence modulation in the presence of non-spherical particles but considerations regarding the motion suggest that additional effects may depend on the increase in the drag coefficient for non-spherical particles and the additional motion as well as alignment of non-spherical particles.

3. Measurement of Turbulence Modulation

“Statistics is like a miniskirt. It gives good ideas, but hides the most important.”

- *Ebbe Skovdahl*

This chapter deals with the measurement of turbulence modulation in an air carrier phase caused by the addition of spherical and non-spherical particles, respectively. The experimental technique Laser Doppler Anemometry[7], LDA, is used to measure the axial and radial velocity components in a particle laden axisymmetric vertical jet flow. For spherical particles three different sizes of particles are used and measurements are made for three different mass loadings. Two different shapes of non-spherical particles are considered: The disk and the prolate spheroid, and results are compared with those of volume equivalent spheres. Special attention has been directed to evaluating proposed turbulence modulation criteria such as the particle Reynolds number, the Stokes number and the length scale correlation d_p/l_e. Effort has also been directed towards the development of a correlation for turbulence modulation which is valid for the range of particle/flow parameters investigated. Measurements of a single phase jet and comparison with previous published results for the same can be found in Appendix A, while additional plots of the experimental data for particle laden jets can be found in Appendix B. Two previously suggested composite parameters for turbulence modulation have been evaluated on the basis of the present experimental data in Appendix C. Finally a brief description of the LDA technique is found in Appendix J.

Previous observations seem to suggest that small particles (d_p<200μm) attenuate the carrier phase turbulence while larger particles (d_p>200μm) tend to augment it. A number of effects are believed to influence the turbulence modulation observed. The most successful models, in the context of CFD, address this by incorporating mechanisms for both attenuation and augmentation of turbulence. Additional turbulence is often seen as a result of the unstable wake behind large particles and the reduction of turbulence is seen as depending on the particles ability to follow the turbulent eddies (Yuan and Michaelides 1992). A small particle caught in a turbulent eddy will thus be accelerated by the fluid motion, and momentum exchange through the drag force will act to dampen the fluid turbulent kinetic energy. This indicates that the Reynolds number and the Stokes number should be important parameters in the description of turbulence modulation (Hetsroni 1989; Elghobashi 1994). Furthermore, the magnitude of either effect is proportional to the presence of particles typically expressed either by the concentration or the loading (Kenning 1996).

Gore and Crowe (1989) sought to summarize the effects of particles on the fluid turbulence by compiling the experimental data available in literature from pipe and jet flow, shown in Figure 13. The critical parameter was proposed to be the

---

[7] The abbreviation Laser Doppler Velocimetry, LDV, is also often used instead of LDA.

ratio of the length scale of the particles to the length scale of the turbulence, d_p/l_e. This study suggested that for length scale ratios $d_p/l_e > 0.1$ particles will only augment the turbulence while for $d_p/l_e < 0.1$ particles will attenuate the turbulence. This is by many regarded as the parameter which best correlates the observed modulation of the carrier phase turbulence and consequently this parameter is in special focus for this investigation. Some sources have argued though, that turbulence modulation is too complex a phenomenon to be correlated by so simple a parameter and that it is a purely empirical parameter with no meticulous theoretical considerations to back it up. It is also noted that most previous measurements have been performed for a pipe with fully developed turbulent flow or for an axisymmetric jet in the self-similar region. For the case of pipes it is usual practice that the inlet length required for the fully developed condition is at least 75 pipe diameters. Considering the typical size of laboratories this entails maximum pipe diameters of around 30-40mm. Similarly, the physical space occupied by the various measurement probes lead to the use to the largest pipe possible to the best possible resolution. The integral length scale in the center of the pipe for a single phase fully developed turbulent pipe flow has been shown to be approximately proportional to the pipe diameter, $l_e/D=0.1$, for different Reynolds numbers (Hutchinson et al. 1971). The variation in the length scale ratio is thus achieved solely by varying the particle size. Following the above statement it cannot be unambiguously said that turbulence modulation correlates with the d_p/l_e ratio, it can only be proven strictly that for spheres traveling at terminal velocity that the observed effect on the carrier phase turbulence scales with the particle size. The same can be said for the case the axisymmetric jet. For this type of flow, measurements are most often reported for the self similar region which is located far downstream of the jet nozzle, say $x/D>30$. In this region the integral length scale for a single phase free jet is proportional to the distance from the nozzle, independent of the jet Reynolds number or nozzle diameter (Tennekes and Lumley 1972). Also, due to practical issues most investigations concerning jets deal with relatively small particles. Thus, this combination yields small length scale ratio d_p/l_e which fits well into the hypothesis of the supposed dependence on the d_p/l_e ratio since only attenuation has been observed for this type of flow. Thus it can be hypothesized that there is, at present, not sufficient grounds to suggest that the d_p/l_e ratio plays a significant role in turbulence modulation. Indeed, it can be put forward that little exact knowledge of the mechanics of turbulence modulation exists or on which non-dimension parameters should be used to properly correlate the observed effect of particles on the carrier phase turbulence.

Table 5: Properties of test particles.

	1	2	3	4	5
Shape	Sphere	Sphere	Sphere	Disk	Prolate spheroid
Aspect ratio	1:1	1:1	1:1	250:6480	6460:1860
Nominal diameter* (μm)	880	1350	1815	2444	2815
Size distribution* (μm)	590-1180	1030-1860	1350-2300	2250-2650	1650-3590
Standard deviation* (μm)	87	165	191	81	505
Density (kg/m^3)	2500	2500	2500	1100	750

*based on the volume equivalent diameter, d_{eq}.

The present experimental work intends to investigate the mechanics of turbulence modulation by conducting a parametric study where parameters, which are deemed important, are systematically varied. Especially it is attempted to vary the integral length scale, l_e, for a fixed particle diameter in order to possibly validate or invalidate the suggested d_p/l_e parameter. This is done by measuring the turbulence modulation at the centerline of an particle laden axisymmetric jet for which the integral length scale, l_e, varies linearly with respect to the distance from the nozzle. Considering the range of integral length scales in the flow, the particles have been chosen to cover a range above and below the $d_p/l_e=0.1$ criterion. As can be seen from Table 5 this means that the particles selected are rather large compared to previous studies. However, despite the large particle sizes, it is still necessary to perform the measurements in the developing region of the jet to provide the systematic variation of the length scale to meet the criteria. This necessitate that special attention is focused on the inlet conditions to ensure a smooth transition between the length scale present at the nozzle inlet and further downstream. The experiment suggested, using relatively large particle diameters, also entails that the Stokes number is much larger than unity thus allowing measurement at both high Stokes numbers and low d_p/l_e ratios. It was originally also intended to vary the inlet jet velocity, while maintaining constant particle velocity, to investigate different particle Reynolds numbers for the same particle size and d_p/l_e ratio, however, this was later dropped due to practical difficulties. Instead, the particle Reynolds number is varied by using different sizes of particles.

A commercial LDA system was used to measure the mean and RMS axial velocity along the centerline of the jet for both the gas and solids phase. Previously, LDA, with amplitude discrimination to separate the two phases, has been used extensively in the 1980's and early 1990's for turbulence modulation experiments. More recently, the technique Phase Doppler Anemometry, PDA, is used to accomplish the same. Generally, with respect to the accuracy, PDA is considered superior to LDA with amplitude discrimination. However, associated with both methods are significant bias and limitations which are discussed later in this text. The present investigation attempts to avoid these difficulties by exploiting the large size of the test particles compared to the seeding particles. Thus, due to the difference in the number density of the two phases only a statistically insignificant number of velocity samples can be accredited the test particles. Afterwards, the properties of the particulate phase can be detected by measuring without the addition of seeding.

Experimental Setup and Methods

The experimental setup is show schematically in Figure 14. A 70W ventilation fan re-circulates the airflow and maintains a constant nozzle velocity of 7m/s. The air flow rate is measured using an orifice meter placed on the return section of the pipe. Ventilation by-pass valves are used to quickly reduce the density of the tracer particles by taking fresh air in and rejecting the seeded air. Additionally, tracer particles are also added to the flow at the ventilation by-pass valves. Test particles are added to the flow via a gravimetric particle dispenser, which produces a repeatable steady flow of particles. Particle mass flow was measured by weighing particles after collection for a timed period. The test particles are allowed to mix with the air flow over a short distance, where the pipe is made of Plexiglas to allow for visual inspection. A wire-mesh combined with a flow contraction is placed at the entrance to a rectangular enclosure, with dimensions of 2000x500x500mm, to condition the flow further. Particles are separated from the airflow and collected for reuse at the settling chamber in bottom of the test rig. Mean and fluctuating gas velocities were measured using a commercial LDA system mounted on a 2-axis traversing system. The tracer particles were generated by means of a commercial liquid seeding generator, generating oil droplets in the range ~ 1μm. The jet nozzle has an inside diameter of 40 mm, and the ambient temperature and pressure was 296K and 97kPa respectively. Particle size distributions were measured using a microscope with a sample of more than 100 particles for each size group. Details of the test conditions are summarized in Table 6.

Table 6: Summary of test conditions.

	case 0	case 1	case 2	case 3	case 4	case 5
Particle shape	-	Sphere	Sphere	Sphere	Sphere	Sphere
Particle diameter [μm]	-	1820	1820	1820	1350	1350
Jet inlet velocity* [m/s]	7.23	7.35	7.30	7.34	7.32	7.25
Particle mass flow [g/s]	0	6.4	10.1	17.5	4.3	10.3
Loading [-]	0	0.6	0.95	1.7	0.4	0.95

	case 6	case 7	case 8	case 9	case 10
Particle shape	Sphere	Sphere	Sphere	Disk	Prolate spheroid
Particle diameter [μm]	1350	880	880	2444	2815
Jet inlet velocity* [m/s]	7.19	7.23	7.23	9.13	7.23
Particle mass flow [g/s]	17.3	11.1	15.4	18.5	21.9
Loading [-]	1.6	1.05	1.45	1.34	2.0

*measured at x/D =0.5

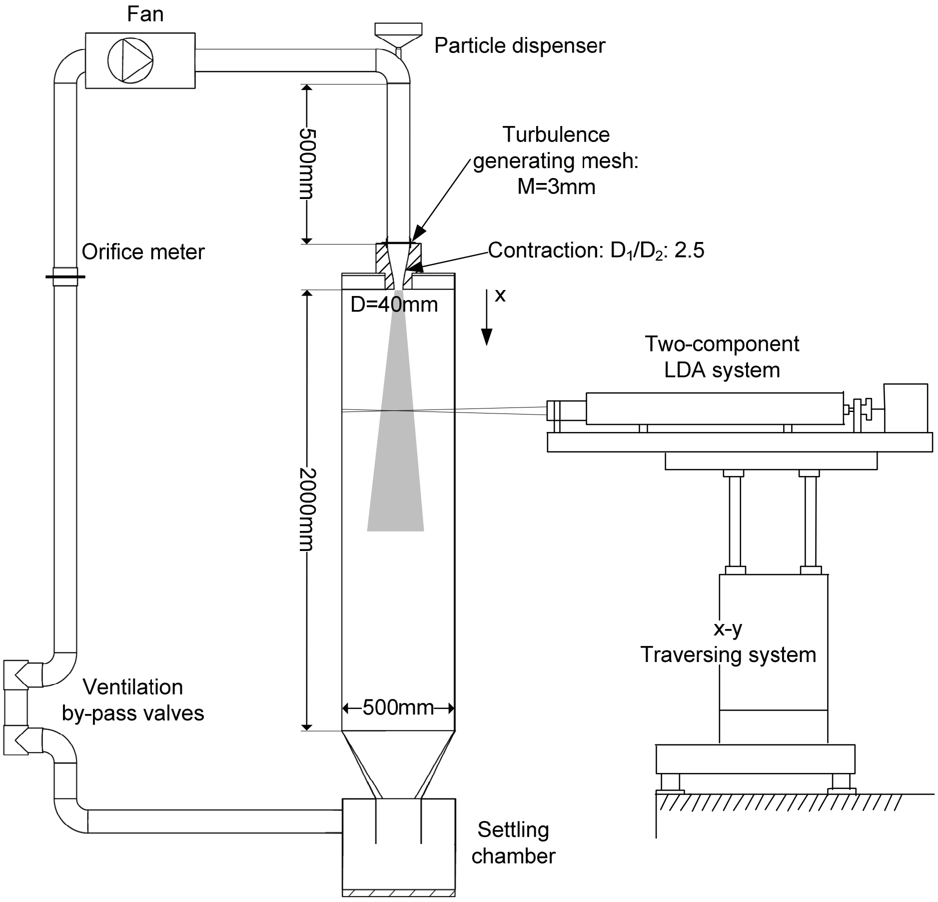

Figure 14: Sketch of the experimental setup.

A quick survey of previously published results concerning turbulence modulation reveals a large spread in data which lead to the conflicting conclusions mentioned in the previous section. A few remaining issues concerning the present and previously used test rigs and the experimental techniques for particle laden-flows are therefore relevant for further elaboration. The key to understanding this experiment is that the particles used are substantially larger than previous studies, which both creates new problems and diminish issues often associated with the use of smaller particles.

Test particle conditions

To allow comparison with numerical models it is important to ensure that particles are spherical with a narrow size distribution. Furthermore, the particles should be solid, non-evaporating, non-agglomerating, non-static etc. To meet these criteria it is common to use either glass or polymer beads. However, in literature, it is also possible to find experimentalists using sand particles (Shuen et al. 1985) or even cylindrical particles (Tsuji et al. 1984) to approximate the spherical ideal. Furthermore, particle size sorting techniques does not discriminate between ideally spherical particles and particles with imperfections and some techniques produce size distributions with a large spread. When particles are pneumatically transported, electrostatic charging of the particles, especially for small particles, increases the change of clustering or adhesion to walls (Tsuji et al. 1984). Also any residual humidity might cause particle to cluster together and thus introduce the need for drying. All of these factors can lead to an increase in the drag coefficient compared to that of an ideal sphere, which cause a modification to the coupling with the carrier phase and thus makes it difficult to evaluate turbulence modification. All of these issues are diminished using larger particles whose size also allow for a continuous visual monitoring of any possible deterioration of particle conditions.

For the present experiment glass beads have been used in the case of spheres. The particles have been studied using microscopy and subsequent picture analysis. Due to problems with the glare point and other reflections from the transparent glass particles meant it was not possible to use any automated algorithm to check for circularity. Instead circles were manually fitted to each particle, thus providing both an accurately determination of the diameter and a means of visually checking for consistency. An image of the spherical particles is shown in Figure 15. For all tested particles the majority appeared to be spherical, although the largest particles in each group had a tendency to be slightly ellipsoidal in nature which is consistent with the sieve separation technique. Test particles were collected at the bottom of the settling chamber and recycled by manually replenishing the particle dispenser. This procedure unavoidably caused some degradation of the particles which was dependent on the particle material. For the spheres, which were made of glass no degradation could be detected after the experiments were concluded. For the disks, which were made of polystyrene, both deformation and fragmentation could be detected, however, only a small fraction was affected. For the prolate spheroids only fragmentation was detected which similarly only affected a smaller portion.

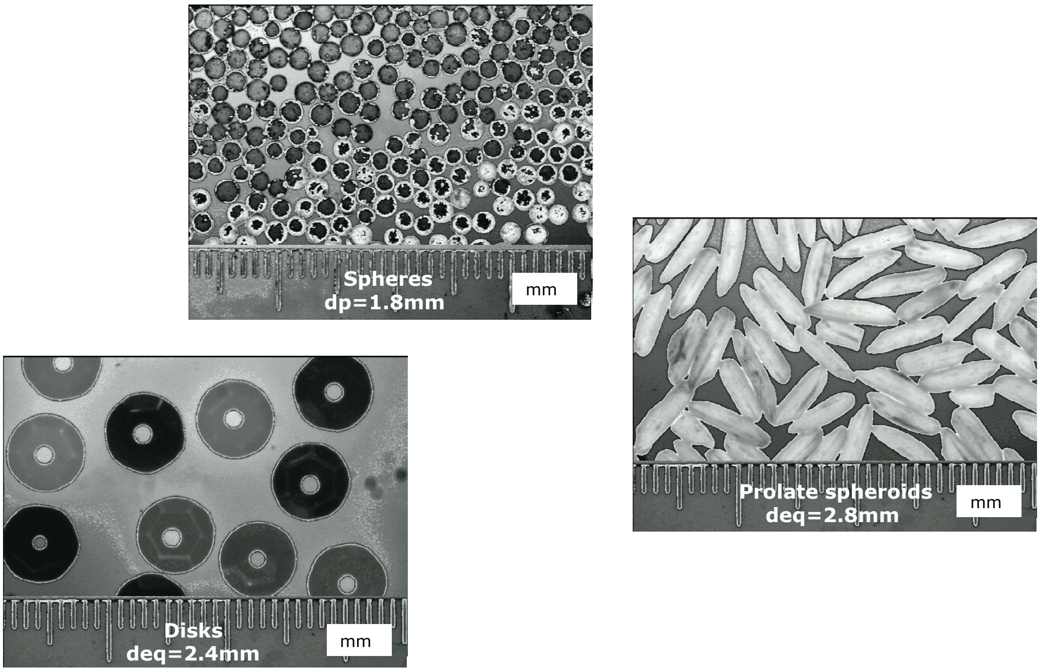

Figure 15: Test particles.

Inlet conditions

The inlet condition of a jet should be easily reproducible and allow for an inlet boundary profile to be applied for Computational Fluid Dynamics. For a single phase jet these conditions are met either by using a nozzle, which produces an approximate top-hat profile, or by a fully developed pipe flow velocity profile. For particle laden flow fully developed turbulent two-phase flow is most often used as the inlet condition. The usual practice is to choose the development length of the pipe between 75D and 135D which is three to four times more that what would is required for the similar single phase flow case. However, a criterion only based on the length of the pipe is not sufficient to unambiguously state whether the particle-laden flow is fully developed. For a single particle released from rest in a uniform flow field it is possible to determine the time it takes the particle to reach its steady state velocity. Similarly, it is possible to determine the residence time of the accelerating particle given the length of the pipe. Thus it is possible to determine if the particle reaches its steady state velocity, a criteria for fully developed flow, before the start of the measurement section. A survey of previous experiments is shown in Figure 16 where the particle response time is based on the particle having reached 95% of their steady state value. The solid line indicates when the particle residence time equals their response time.

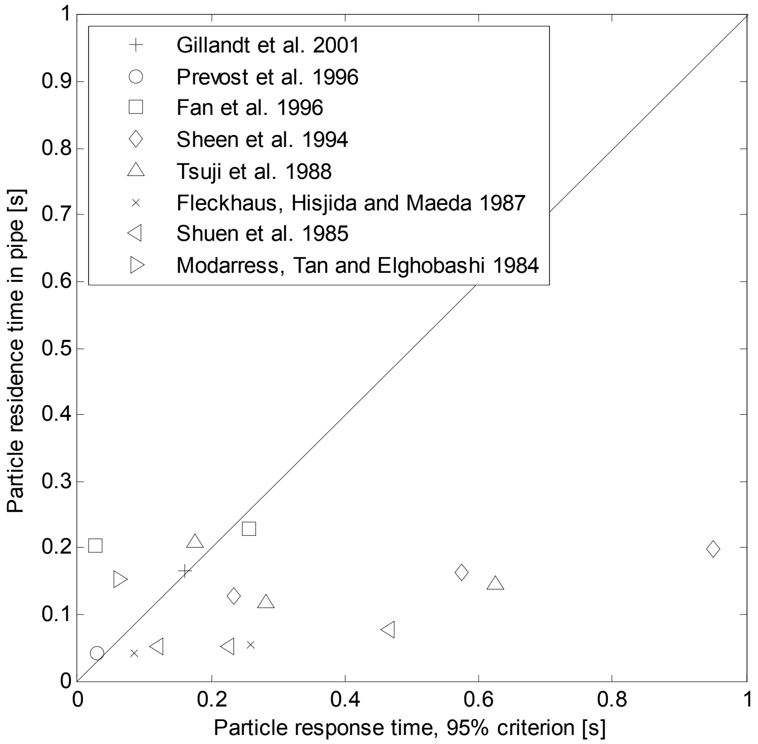

Figure 16: Evaluation of previous experiments ability to be fully developed.

It is evident that only a few investigations can claim to have a fully developed two-phase flow base on this criterion. Furthermore, this criterion only considers the development of the mean translatory velocity of the particles and not the fluctuating velocity of the particles which is often influential for the two-way coupling between the phases (Elghobashi 1994). For pipe flows the development of the fluctuating component of the particle velocity is very dependent on the initial conditions together with the roughness of the internal surface. The experiments by Govan et al. (1990) which focused on measuring the Lagrangian statistics of 500μm particles in a 20m vertical pipe, 620D, indicated that the fully-developed behavior was not achieved after 19m. Thus, to achieve a truly fully developed two-phase flow it is necessary to use a pipe length which is difficult to implement in typical laboratory settings.

For the measurement of turbulence modulation often a systematic variation of a single parameter, which is hypothesized to influence the properties of the flow, is desired while other parameters are held constant. This has previously been achieved by varying the mass loading or the size of the particles. However, for the fully developed condition this variation also gives rises to differences in the concentration profile in the radial direction of the pipe (Vreman 2007). Thus for a variation of the particle diameter, with constant loading, a fully developed condition influences the local particle concentration profile.

To counter the above issues a design using a combination of a wire-mesh grid and a nozzle to create a flow to approximate a uniform profile for both carrier phase velocity and particle concentration are proposed. This design is similar to that used by Barlow and Morrison (1990) for dense jets. The interaction between the particles, the wire-mesh and the walls of the nozzle creates an inlet condition for the particle velocity which is best described as a spray with an angle of 27 degrees. The acceleration of the air as it passes through the contraction entails that the mean air velocity is greater than the mean axial particle velocity at the nozzle exit. Since the mean particle velocity increases and surpasses that of the mean velocity downstream of the nozzle this special inlet condition allows for measurements at similar particle Reynolds number but at different values of the d_p/l_e ratio. Furthermore, it will also give an indication whether the acceleration of the particles close to the nozzle acts to decrease or increase the carrier phase turbulence. Figure 17 shows the evolution of the mean velocity of both phases together with the investigated range of Reynolds numbers.

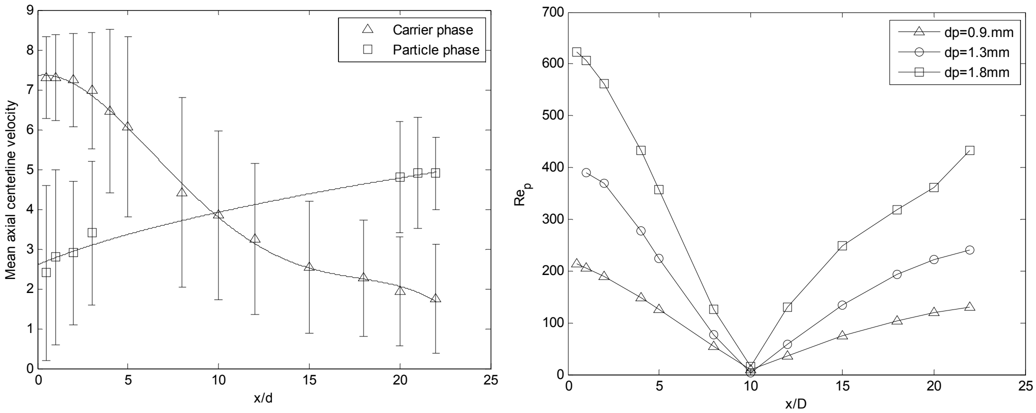

Figure 17: Left: Mean velocity and spread of the carrier phase and the particle phase for 1.8 mm particles. The standard deviation times 2 is shown as error bars. Right: Investigated range of particle Reynolds number.

Measurement technique

Many previous investigations of two phase flow have been made by seeding the continuous phase with small seeding particles and use the method of amplitude discrimination to distinguish between LDA signals originating from the large test particle and signals from the much smaller seeding particles. Amplitude discrimination techniques have been associated with bias resulting from the non-uniform light intensity distribution in the measurement volume (Modarress, Tan and Elghobashi 1984). Furthermore, low amplitude signals resulting from large particles intersecting the edge can be interpreted as coming from seeding particles. For dilute flow the data rate for the seeding particles far exceeds that of the test particles and the resulting error can be assumed to be statistically insignificant (Modarress 1982). Recent investigations have also relied on the PDA technique to distinguish between the two phases. However, for the present experiment the size difference between the seeding and test particles exceeds the range for simultaneous measurement of both phases. Moreover, the PDA technique assumes all particles to be ideal spheres and cannot be applied on the generic non-spherical particles used in the present investigation.

The present investigation basically measures each phase separately, thus it is not necessary to apply any of the previous mentioned techniques to distinguish between large test particle and small seeding particles. This technique is based on the following assumptions for particle-laden flow:

- When the carrier phase is impregnated with seeding particles only a statistically insignificant number of detected signals originates from the large test particles.
- Measurement of the particle phase can be made independently of the measurement of the carrier phase by removing the seeding.

The bias resulting from the test particles, in the presence of seeding, can be found by considering the difference in number density of the two phases. First, consider that size difference between the two phases is in the order of 1/1000 or 3 orders of magnitude. This means that the difference in number density, for the same concentration, will be around 9 orders of magnitude. The concentration of the seeding phase can be estimated to be around 10^{-9} kg/m^3 whereas the concentration of the test particle varies between 10^{-3} and 10^{-7} kg/m^3 indicating a worst case of detection probability of around 1 test per 1000 seeding particles. Still, for large difference in velocity this would result in a significant bias for the measurement of the RMS velocity. This is particularly important since there is a high concentration of test particles and a significant slip velocity close to the jet nozzle. To counter this, signals which originates from the test particles have been manually removed from the dataset to further improve the accuracy of the measurements as shown in Figure 18. Note that for most cases only very few samples have been removed by this account.

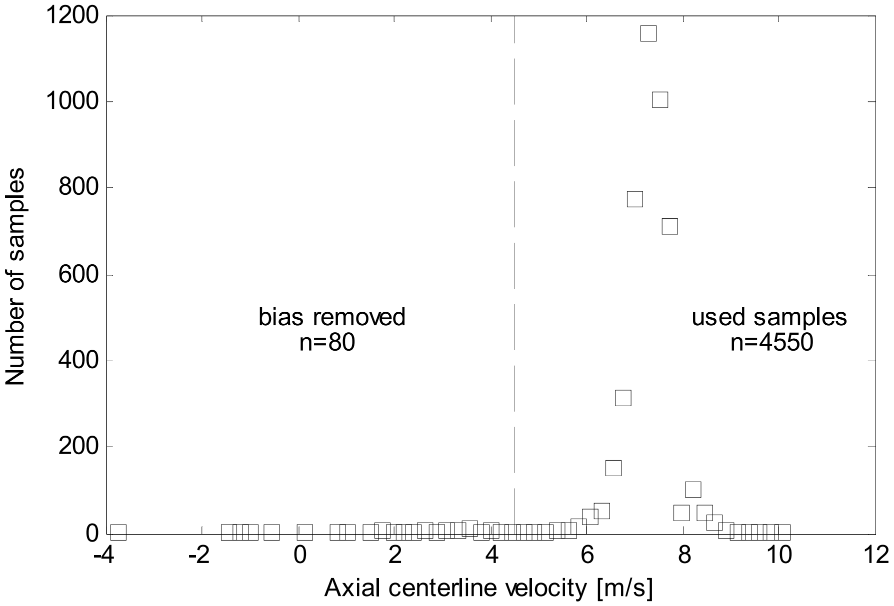

Figure 18: Measurement of carrier phase velocities. Velocity distribution at x/D=0.5, d_p=880µm, z=1. Note that this is a worst case scenario.

Measurement of the particle phase were subsequently performed in the absence of seeding. However, the resulting velocity Probability Density Function, PDF, unexpectedly revealed a bimodal distribution as shown in Figure 19. This is interpreted as being due to residual seeding particles being released from the surface of the reused test particles. Thus it was not unambiguously possible to measure the velocity of the particle phase. However, at positions where the slip velocity between the phases was large, it was possible to apply a velocity filtering approach based on the axial velocity probability density function to distinguish between the two phases and thereby derive the requested information regarding the particle phase. This technique has previously been applied by Lee and Durst (1982) for vertical particle-laden pipe flow and by Barlow and Morrison (1990) for a dense two-phase jet flow. Note that it is only possible to measure the particle velocity close to the inlet and far downstream. The particle velocity in the intermediate region is approximated using the particle equation of motion.

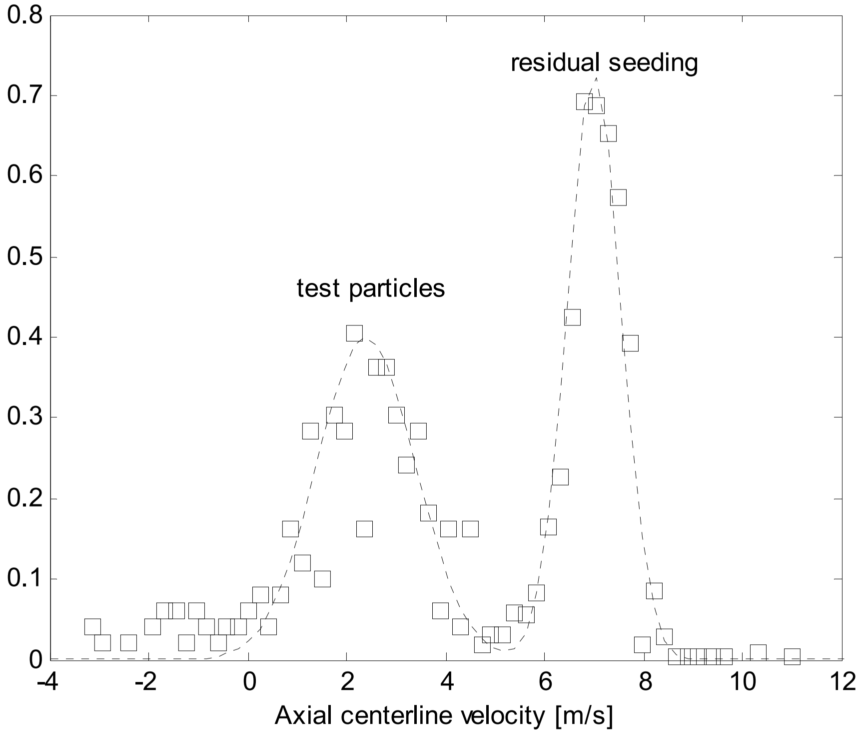

Figure 19: Measurement of particle phase velocities. Note that no seeding was added. Normalized velocity distribution at x/D=0.5, d_p=880µm, z=1.

In order to contain and re-circulate the seeding a closed loop design has been opted for. Using this design the concentration bias which otherwise would exist when measuring in the outskirts of the jet is also avoided. However, this design generally also impedes the development of the jet due to the no slip condition at the walls. In order to achieve comparability with other investigations, measurements have only been conducted in the range where the jet can be considered as a free jet *i.e.* where the influence of the walls and exit are minimal. This has been verified by comparing the measurements of the single phase jet to available literature. Thus only the top half of the test section, $x/D=0\text{-}25$, was used for measurements to avoid the influence from the outlet as well as the walls. It is desired to categorize any measured turbulence modifications according to the length scale correlation, d_p/l_e, suggested by Gore and Crowe (1989). For this, a correlation of the integral length scale at the centerline of a clear jet, $l_e=0.039x$, originally submitted by Wygnanski and Fiedler (1969) has been used. This is the same correlation as used by Gore and Crowe (1989). They also suggested to obtain an estimate of the integral length scale immediately after the nozzle exit by using the criteria of $l_e=0.1D$ (Hutchinson, Hewitt and Dukler 1971). The length scale in the overlap region is very dependent on the particular case. For this case a linear dependence is assumed between the near nozzle region and the point where the correlations for the clear jet can be used. For this particular case this assumption works well since the predicted length scales are of similar magnitude and because the jet flow itself is turbulent. Thus a peak or drop in the integral length scale is not to be expected. For the self preserving free jet both the spreading rate and the turbulence length scale depend on the distance from the inlet (Tennekes and Lumley 1972). These can be considered to be proportional to each other. Figure 20 shows a graphical representation of the expressions used for the integral length scale along with measurements of the jet width. It can be seen that the measured jet width is consistent with previous investigations. Some criticism has been raised about the measurements by Wygnanski and Fiedler (1969). As can be seen the spreading rate is somewhat lower than what was measured by Panchapakesan and Lumley (1993) and Hussein et al. (1994). This is widely accepted as being due to the flow containment used by Wygnanski and Fiedler (1969) meaning that the jet was not completely free but instead affected by far field backflow which in turn make the jet more narrow and thereby lowers the spreading rate. The present experiments involve a similar confined jet and consequently it is valid to use the fit proposed by Wygnanski and Fiedler (1969) only it is noted that this is for a confined jet and not a free jet. It should be noted that direct measurement of the integral length scale would encompass two-point correlations which is out of the scope for the present investigation.

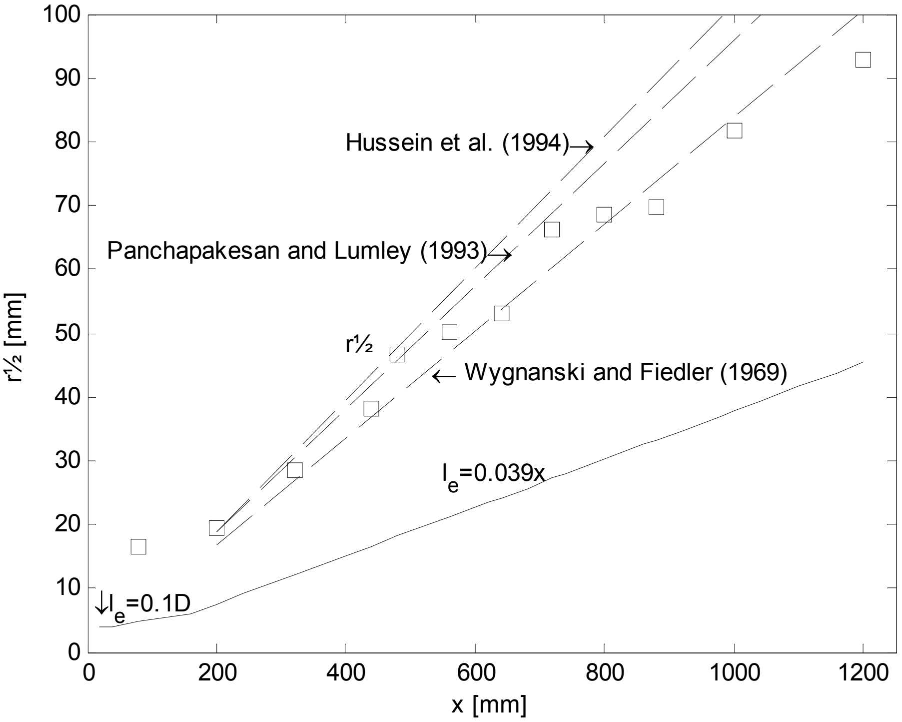

Figure 20: The dependence of length scales on axial distance downstream of the nozzle from present clear flow measurements. r½ is the radius of the jet where the mean velocity is half of the centerline velocity, i.e. the jet radius.

To quantify the modification of turbulence due to the addition of particles the percentage change in the turbulence intensity is used:

$$\frac{\sigma-\sigma_0}{\sigma_0}\cdot 100\%, \quad \sigma = u'/\bar{u}, \quad \bar{u}=\frac{1}{n}\sum_{i=1}^{n}u_i, \quad u'=\sqrt{\frac{1}{n}\sum_{i=1}^{n}(u_i-\bar{u})^2} \tag{40}$$

Here σ denotes the turbulence intensity of the particle laden flow and σ_0 the turbulence intensity of the clear flow. All values are local values and only the axial velocity is considered. This can be categorized as a parameter which is easy to measure, since it only involves one velocity component, but also a parameter with limited accuracy. The division between two values, each associated with a limited accuracy, results in a value with even poorer accuracy. As it can be deduced from equation (40) two such divisions are performed for the evaluation. Other parameters to evaluate turbulence modulation can be based on the turbulent kinetic energy or even on the Reynolds stresses. However, these expressions are more difficult to measure and evaluate since they require measurement of three velocity component and/or cross-correlation of fluctuating velocity components. Furthermore, the inclusion of several measurements does not necessarily make the final evaluation more precise. The fluctuating velocity in the axial direction is the most prominent of the fluctuating velocity components and it thus makes sense to base the evaluation of turbulence modulation on this parameter solely. Often it is also chosen to normalize parameters using quantities which exist at a base point such as a jet inlet or at the centerline of a fully developed pipe flow. However, this again makes the direct comparison with other studies more difficult. Finally, it should be stated that no matter which parameter is chosen for the evaluation of the turbulence modulation, the accuracy will always be less than that which is associated with the measurement of the mean and fluctuation velocities. This turbulence modulation parameter has frequently been used in existing literature and is used in the present investigation to allow for easy comparison with previously published results. It should be mentioned that the radial velocity component often is more affected by the presence of particle than the axial velocity.

Uncertainties

The precision of the x-y system for position adjustment was 12.5μm for all axes. The error associated with the mass loading was for the worst case calculated to 4% using a 95% confidence interval. For the Laser Doppler Anemometry measurements a minimum of 1500 samples were collected for each data point. Based on the number of samples, *N*, the error, *e*, associated with the velocity measurements, e_u, the turbulence intensity, e_σ, and the turbulence modulation, e_M, can be estimated by:

$$e_u \approx \frac{2}{\sqrt{N}} \tag{41}$$

$$e_\sigma \approx 2 \times e_u, \quad \left(\sigma = \frac{u' \pm e_u}{\bar{u} \pm e_u} \right) \tag{42}$$

$$e_M \approx 2 \times e_\sigma \approx 4 \times e_u, \quad \left(M = \frac{\sigma \pm e_\sigma - \sigma_0 \pm e_\sigma}{\sigma_0 \pm e_\sigma} \right) \tag{43}$$

This yields a maximum error of 5% for the velocity measurements while this figure doubles to 10% for the intensity measurements which again doubles to 20% for the turbulence modulation since this involves the multiplication of values and their associated errors.

Results and discussion

In this section the results obtained are shown for different non-dimensional parameters in order to evaluate these. An example of the results normalized using the non-dimensional distance from the nozzle is shown in Figure 21. This figure represents 10 % of the total measurements performed. In the following it is attempted to display this databank using different normalizations in order to determine which parameters best correlates the data and thus get an indication of which mechanisms is important for turbulence modulation.

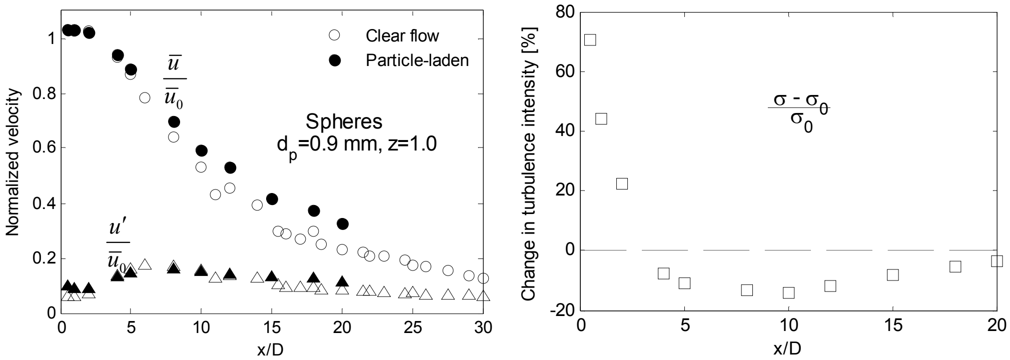

Figure 21: Left: Normalized mean and RMS velocity for spheres with d_p=0.9mm, z=1.0. Right: Percentage change in turbulence intensity.

Particle Reynolds number

From the study of large fixed spheres it is known that flow instabilities in the free surface layer causes the wake of the sphere to oscillate and detach discrete pockets of vorticity. The onset of wake instability is reported to occur at particle Reynolds numbers, $Re_p \approx 130$, while $Re_p \approx 270$ is the lower critical Reynolds number for which vortex shedding occurs (Clift, Grace and Weber 2005). Considering vortex shedding to be responsible for the observed turbulence augmentation Hetsroni (1989) suggested that the lower critical Reynolds number could be used as a criterion for the enhancement or the suppression of the carrier phase turbulence. Figure 22 shows the turbulence modulation for all measurements versus their particle Reynolds number. Also, please refer to Figure 17 for the variation of the mean velocity and particle Reynolds number with the distance downstream of the nozzle. Close to the nozzle the slip velocity is large with the carrier phase velocity being larger than the particle velocity. This results in equally large particle Reynolds numbers close to the inlet, which decreases as the velocity of the two phases approaches each other as they evolve downstream of the jet. The region close to the inlet is associated with augmentation of the carrier phase turbulence for all the investigated particles while the region far downstream is associated with attenuation. Figure 22 reveals that both attenuation and augmentation is encountered for large particle Reynolds number. Thus there does not seem to be a definitive strong correlation between the particle Reynolds number and the turbulence modulation. However, for spheres especially there seems to be some indication that attenuation is more prominent at low particle Reynolds numbers and that augmentation is only occurring at values above $Re_p=110$ and is exclusive at Reynolds numbers higher than $Re_p=400$. However, it also seems that the shift between attenuation and augmentation is dependent on either the particle size or the d_p/l_e ratio in addition to the particle Reynolds number. According to countless previous wind tunnel experiments using large spheres vortex shedding only occurs at values above $Re_p=270$. Thus it seems that the phenomenon of vortex shedding cannot solely explain the significant increase in the intensity change observed for the smallest particles. It is interesting to note that augmentation is prominent close to the jet inlet where the mean particle velocity is lower than the mean carrier phase velocity so this increase in the turbulence intensity cannot be explained by energy transfer resulting from interfacial forces. For the disks and prolate spheroids there seem to be no correlation with the Reynolds number as attenuation is encountered at high Reynolds numbers. If the particle Reynolds number was evaluated on the basis of the largest dimensions of the non-spherical particles it would generally result in larger particle Reynolds numbers making the Reynolds number correlation further unlikely.

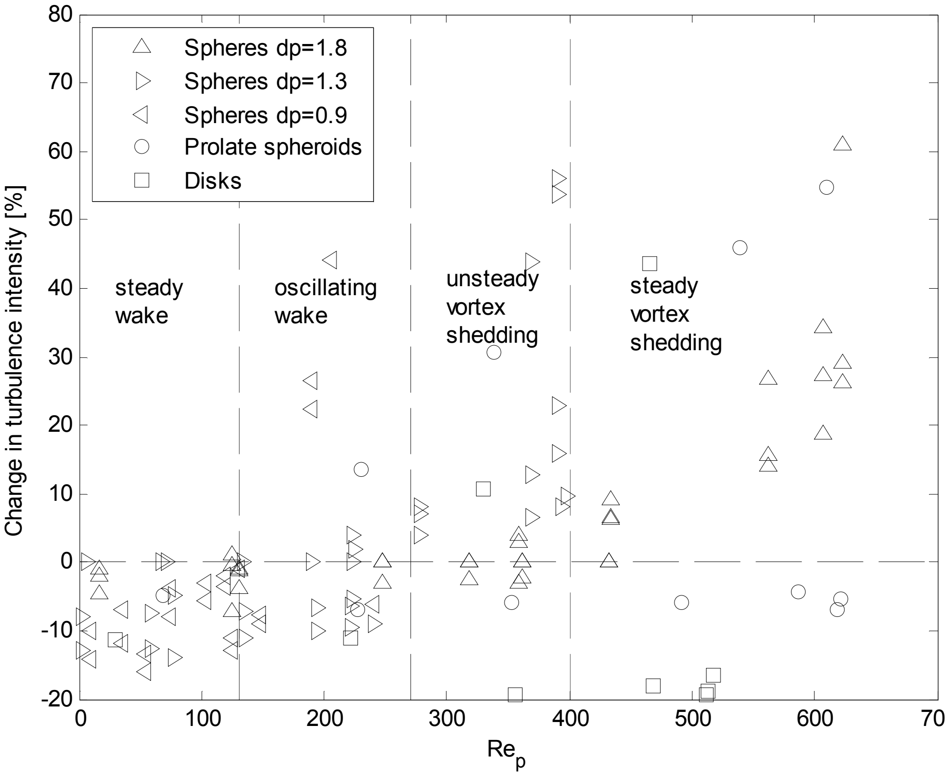

Figure 22: Percentage change in the turbulence intensity versus the particle Reynolds number. For disks and prolate spheroids the particle Reynolds number is evaluated on basis of the volume equivalent diameter. Note that existing wake regimes have been superimposed over the experimental data.

Time scale ratio

From studies of power-spectral measurements of the fluctuating velocity it has been observed that the addition of particles results in a decrease of the turbulence energy in the high wave number region (Jou, Sheen and Lee 1993). This is interpreted as a result of the turbulence energy transfer from eddies to particles following the eddies (Tu and Fletcher 1994). The ability for particles to follow the flow is best described by the Stokes number, the ratio of the particle response time, τ_p, to the eddy turnover time, τ_e. The criterion for turbulence augmentation based on timescales is a Stokes number above unity (Elghobashi 1994). The

Stokes number is formed by the ratio of the response time of the particles, τ_p, to the timescale of the large eddies, τ_e:

$$St = \frac{\tau_p}{\tau_e} = \frac{\tau_V / f}{l_e / u'} \tag{44}$$

where τ_V is the Stokesian response time, $\rho_p d_p^2/18\mu$, and f is the Schiller and Naumann (1933) correction for spheres at higher Reynolds numbers. Figure 23 shows the intensity change for all measurement points against the Stokes number, *St*. For all particles the Stokes number is greater than unity which indicates that the motion of the particles is only little affected by the motion of the large eddies; a perception which is also confirmed by visual observation of the particle phase. It is clear that turbulence modulation effects do not correlate well with the Stokes number. Large particles which do not follow the characteristic eddies are still able to attenuate the carrier phase turbulence and measurements at large Stokes numbers do not necessarily augment the turbulence intensity. Thus the Stokes number alone cannot explain the attenuation observed at locations far downstream of the nozzle.

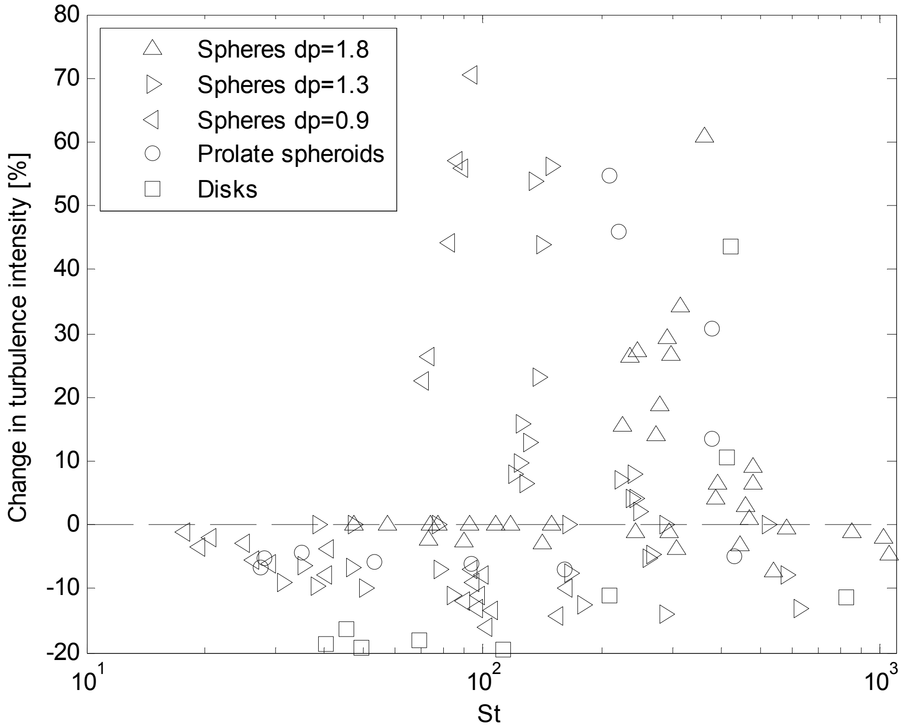

Figure 23: Percentage change in the turbulence intensity versus the Stokes number. For disks and prolate spheroids the particles response time is evaluated on the basis of the volume equivalent diameter.

Length scale ratio

Gore and Crowe (1989) sought to summarize the effects of particles on the fluid turbulence by compiling the data available in literature. The critical parameter was proposed to be the ratio of the length scale of the particles to the length scale of the turbulence, d_p/l_e. This was in line with the observation that particles which were sufficiently smaller than the turbulence length scale would follow the motion of the most energetic eddies while larger particles would create their own turbulence in their wake. From experimental data available in literature at that time a threshold value of $d_p/l_e=0.1$ between attenuation and augmentation was suggested. Figure 24 shows data for the modulation of the carrier phase turbulence at the centerline of the jet. The suggested criteria for turbulence modulation, $d_p/l_e =0.1$, by Gore and Crowe (1989) is indicated with a slashed line. It can be seen that attenuation is possible at length scale ratios above the suggested criterion. This is possible due to a combination of very large particles combined with high mass loading and the development of the relative velocity. However, there is a clear trend that for large ratios there is only enhancement of the carrier phase and for low ratios there is only attenuation. For low length scale ratios the measured modulation seems to approach the clear flow instead of attenuating the flow even more. This is due to the decrease in the particle concentration as the jet is developing and the particles are both increasing in speed and are further apart.

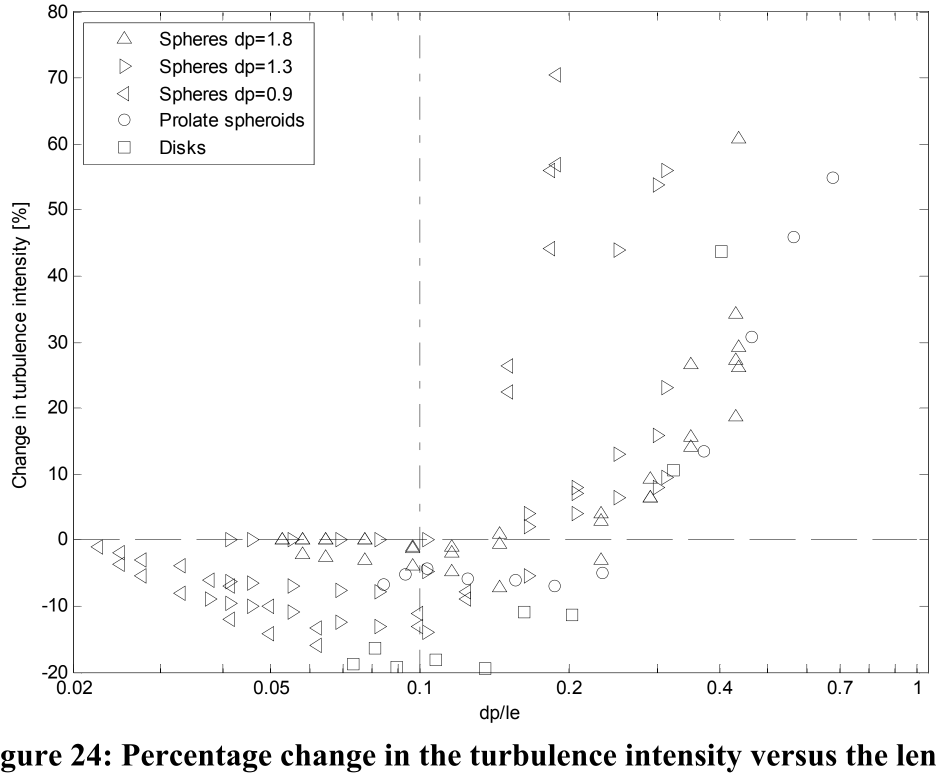

Figure 24: Percentage change in the turbulence intensity versus the length scale ratio d_p/l_e. For disks and prolate spheroids the particles size is evaluated on basis of the volume equivalent diameter. The criteria by Gore and Crowe (1989), $d_p/l_e = 0.1$, is shown as a vertical line.

Particle concentration

Another often used measure associated with the magnitude of the coupling is the mass loading, the ratio of particle mass flux to the carrier phase mass flux. Generally, when using the mass loading as a measure of the coupling between the phases it is also necessary to consider the density ratio and the particle size as this determines the number of particles available for interaction. These parameters can inherently be combined to yield the number density as a third measure of the magnitude of interaction. Geiss et al. (2004) reports that turbulence modulation is only observed above a threshold value of number density of 30-40 particles/cc, corresponding to a volume fraction of around $\alpha=3\cdot 10^{-5}$. Fan, Zhao and Jin (1996) reports that turbulence modulation effects were strongly correlated with both the mass loading and the particle diameter. Other related parameters are the mass fraction, used by Geiss et al. (2004), and the volume loading, the ratio of volume fluxes. By studying dense jets Barlow and Morrison (1990) found that high volume loading reduces the mean slip velocity between the phases, whereas in the dilute regime the mean slip velocity was equal to the terminal velocity of the particles. By arguing that particles represent surfaces which are able to support stresses, Kenning and Crowe (1997) suggested that the characteristic length scale, associated with dissipation, is no longer the Kolmogorov scales but that also the inter-particle spacing and the particle diameter need to be considered. For the use of computational fluid dynamics the appropriate parameter to express the presence of particles in the Eulerian reference frame is the concentration of particles represented in units of kg per cubic meters. The volume fraction are closely related to both the inter particle spacing, l_{int}, and the particle mass concentration, C. For dilute two-phase flow applies that:

$$\pi d_p^3 \big/ 6 l_{int}^3 = \alpha = C\,\rho_c \big/ \rho_p \tag{45}$$

which suggest that these parameters can be used as substitutes for one another. Turbulence modulation effects are present for all particulate flows. However, for very dilute flow this effect is not measureable, while for dense flows inter-particle collisions have a dominating effect on the flow. The ratio between the particle response time and the time between collisions are the best measure for evaluating if the flow is dense or dilute, but the time between collisions is difficult to quantify since it depends on the relative velocity between particles. Most often the volume fraction of particles is used a rough criterion to distinguish between the different regimes. For volume fractions less than $\alpha=10^{-6}$, one-way coupling, particles have negligible effect on turbulence while for volume fractions larger then $\alpha=10^{-3}$, four-way-coupling, particle collisions significantly influence the interaction between the particle and carrier phase which is present between $10^{-6}<\alpha<10^{-3}$, two-way coupling (Elghobashi 1994). It is evident that the coupling between the phases is stronger as more particles are added to the flow. The particle concentration can be found by counting particles and registering their velocity as they pass a control volume during a time period. For the current setup this was not possible. Alternatively, the volume fraction of the particles, α, can be approximated by considering the particle velocity, u_p, and the particle mass flux, $\dot{m}_p$, at the centerline. The following expression is used to approximate the volume fraction at the centerline:

$$\alpha = \frac{\dot{m}_p}{\rho_p u_p A_s} \tag{46}$$

where A_s is the cross-sectional area of the particle stream. This expression assumes that the particle concentration is evenly distributed across the cross-sectional area of the particle stream which contradicts previous experimental findings which suggest that the particle concentration is greatest in the center of the jet. However, this estimate should provide the correct order of magnitude of the volume fraction. For the present investigation the greatest particle concentrations are found near the inlet, where α is in the order of 10^{-3}. The volume fraction decreases downstream due to the spreading of the jet and the increase in mean velocity of the particles. As a consequence, the volume fraction is correlated with the length scale of the large eddies and the influence of these two parameters cannot be separated using the current setup. For locations far downstream of the jet the volume fraction is in the order of 10^{-6} and the flow can be considered as one-way coupled and the particle phase is not able to affect the turbulence of the carrier phase.

Figure 25 shows the intensity change for the investigated range of particle volume fraction, α. For a large range of volume fractions it is possible to have both attenuation and augmentation. However, it is clear that at low volume fractions only attenuation is encountered whereas at high volume fractions only augmentation is encountered. However, the volume fraction for the present experiment is very closely correlated with the turbulence length scale and it is not possible to separate the effects of these two parameters. As the volume fraction approaches the one-way coupling regime the turbulence modulation effect diminishes. The lowest value for which a change in the turbulence intensity has been measured is $\alpha=4\cdot10^{-6}$. In fact it seems that the modulation effects are being impeded by the lower volume fraction at values below $\alpha=10^{-5}$. Furthermore, the volume fraction of the tracer particles is estimated to be in the order of $\alpha=10^{-10}$ which is significantly below the limit for two-way coupling and it is assumed that they have only a negligible effect on the carrier phase.

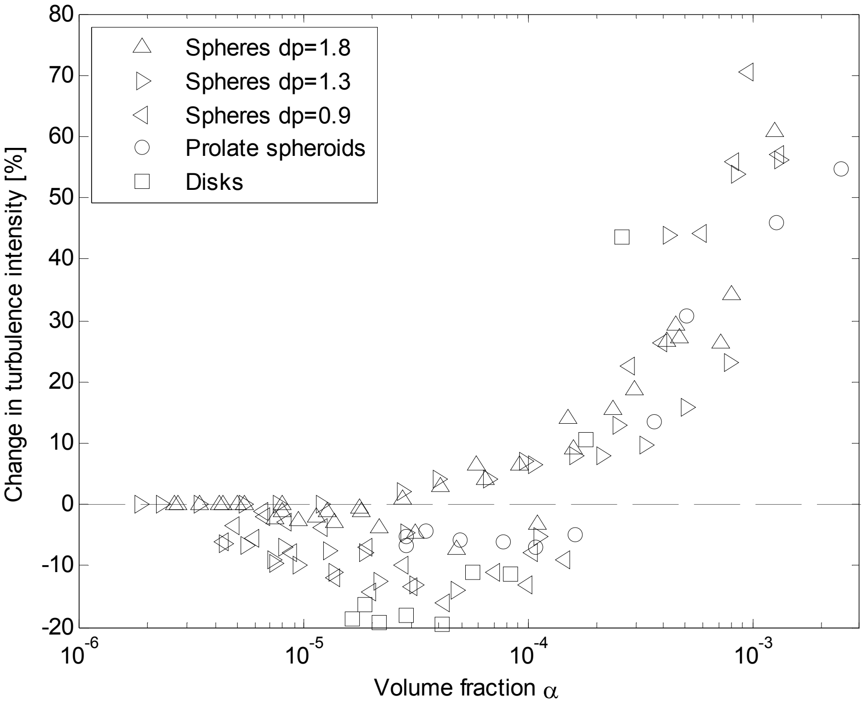

Figure 25: Percentage change in the turbulence intensity versus the volume fraction *α*.

Empirical correlation for spheres

It can be acknowledged that any single universal parameter, able to predict the turbulence modulation which has been observed at the spectrum of experimental investigations of particle-laden flows, does not exist. In view of the failure of existing criteria and models it is thus desired to develop an expression which can correlate the existing data using the databank of the present investigation where information of many different quantities is stored. The methods which have been used to derive the aforementioned criteria have been based either on a mechanistic approach like the particle Reynolds number and the Stokes number. If these had turned out to correlate well with the observed turbulence modulation it would have resulted in a new insight into particle-fluid interaction which explains the efforts. However, in lieu of these methods it is possible to develop criteria and correlations which are based purely on experimental observations. A prime example of this is the length scale criteria by Gore and Crowe (1989) which is based on observations with only little theoretical support. It should be noted that such a model may be of little value for the development of numerical models, but has the potential to serve as a base model for which to evaluate the performance of non-spherical particles. Especially in the view, that it has not been able to acquire non-spherical and spherical particles with exactly the same diameter and density. To develop such an expression it is prudent to examine the dependence of each parameter individually.

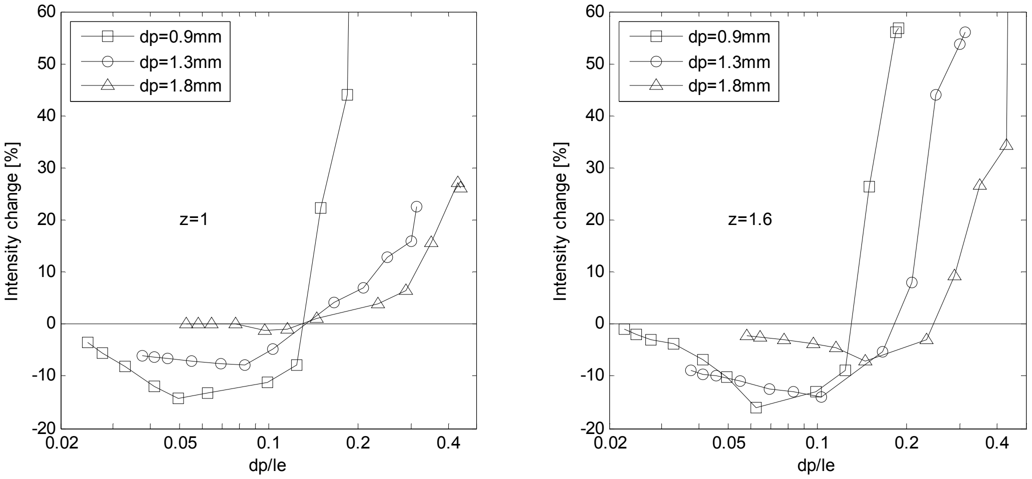

Figure 26: Dependency on particle size. The percentage change in turbulence intensity as function of the length scale ratio for different particle sizes and constant global mass loading.

It has already been stated that the particle volume fraction is important and there seem also to be some justification that the length scale ratio plays a significant role. Other key parameters are the mass loading, which does not necessarily scale with the concentration, the slip velocity and the particle size itself. Figure 26 shows the dependence of the percentage change in turbulence intensity for constant mass loading as a series of the length scale ratio, d_p/l_e, for each particle size used in the present investigation. It appears that the influence of the particle phase on the carrier phase turbulence increases with decreasing particle size. However, for constant mass loading the volume fraction increases as the particle size decreases and it is clear that the volume fraction also has an effect of the coupling between the phases. More notably, it can be seen that for the same particle size and mass loading that this can both have an attenuating or augmenting effect, depending on the length scale of the turbulence. In the lower range of length scale ratios the volume fraction approaches the one-way coupling regime and the results approach the single phase values. Especially the results for *z=1.0* seem to exhibit a pivot point for which the results for all three series collapse into one point. This is a little less clear for z=1.6 and the eligible pivot point do not coincide with the zero intensity change line but is located slightly below. Interesting to note is that both pivot points are located roughly at the same value on the d_p/l_e axis.

Figure 27 shows, in a similar way, the dependence of the intensity change on the loading for constant particle size. The results show that an increase in the mass loading also corresponds to an increase in the magnitude of turbulence modulation experienced by the carrier phase velocity. Similar to the effect of the particle size, the mass loading both promotes the attenuation or augmentation depending on the value of d_p/l_e. Similar to the case of particle size, an increase in mass loading also increases the volume fraction. Considering both Figure 26 and Figure 27 it is evident that for some configurations there is a very large increase in the intensity change.

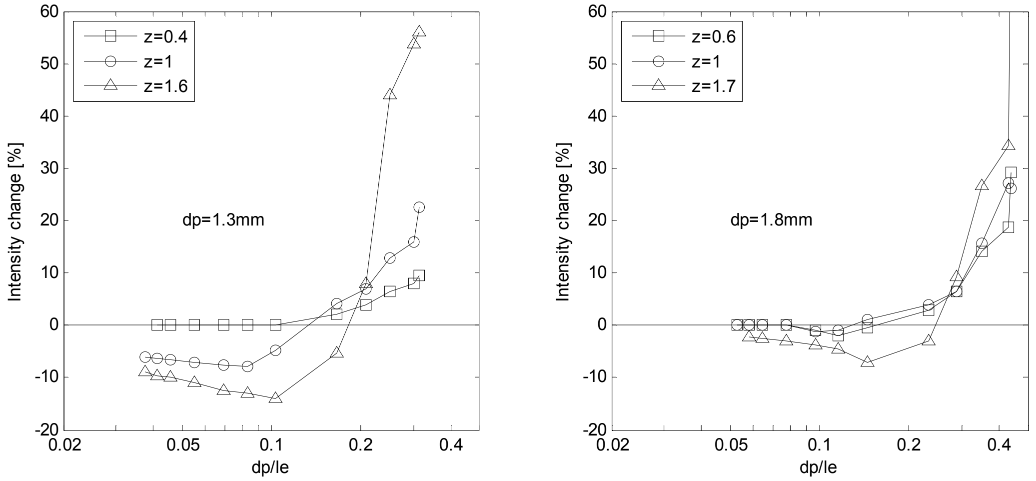

Figure 27: Dependency on mass loading. The percentage change in turbulence intensity as function of the length scale ratio for different global mass loadings and constant particle size.

Combining the observed effects of the mass loading and the particle diameter and realizing that the mass flow rate of the carrier phase is constant, for the present investigation it is possible to define a non-dimensional number as:

$$N_M = \frac{\dot{m}_p}{\mu d_p} \tag{47}$$

where the viscosity of the carrier phase is the only additional parameter. It is clear that this factor cannot stand alone when predicting turbulence modulation and it is necessary to incorporate a functional dependency of both the length scale ratio and the concentration of particles. Figure 28 emerges as the fractional change in turbulence intensity is divided by the non-dimension number from equation (47). All measurements with a volume fraction lower then $\alpha=2\cdot10^{-5}$ has been disregarded since these fall in the transition zone between the one- and two-way coupling regime and the modulation effects are consequently weakened. Similarly, measurements with a volume fraction higher then $\alpha=10^{-3}$ are not shown since these border the dense regime. Given the accuracy of the experiment a rough correlation can be identified. The following empirical expression is suggested to predict the turbulence modulation experience by the carrier phase in the presence of particles:

$$\frac{\sigma-\sigma_0}{\sigma_0}\cdot 100\% = \frac{\dot{m}_p}{\mu d_p}\left(0.34\frac{d_p}{l_e}-0.05\right) \tag{48}$$

The scatter of the results justifies the use of a simple linear fit considering the error associated with the experiment. The validity of the proposed expression is restricted by the extent of the data for which it is based on. Thus it can only claim to be valid for volume fractions between $\alpha=2\cdot10^{-5}$ and $\alpha=10^{-3}$, mass loadings between 0.5 to 1.7, particle diameters between 0.9 to 1.8 mm and d_p/l_e ratios between 0.1 and 0.5. However, it should be noted that this expression produces the expected trends in the limits of both high and low values of the length scale ratio. Note also that the suggested correlation does not identify any fundamental mechanisms for production or dissipation of turbulence due to the presence of particles. This correlation merely addresses the observed trends in the measurements.

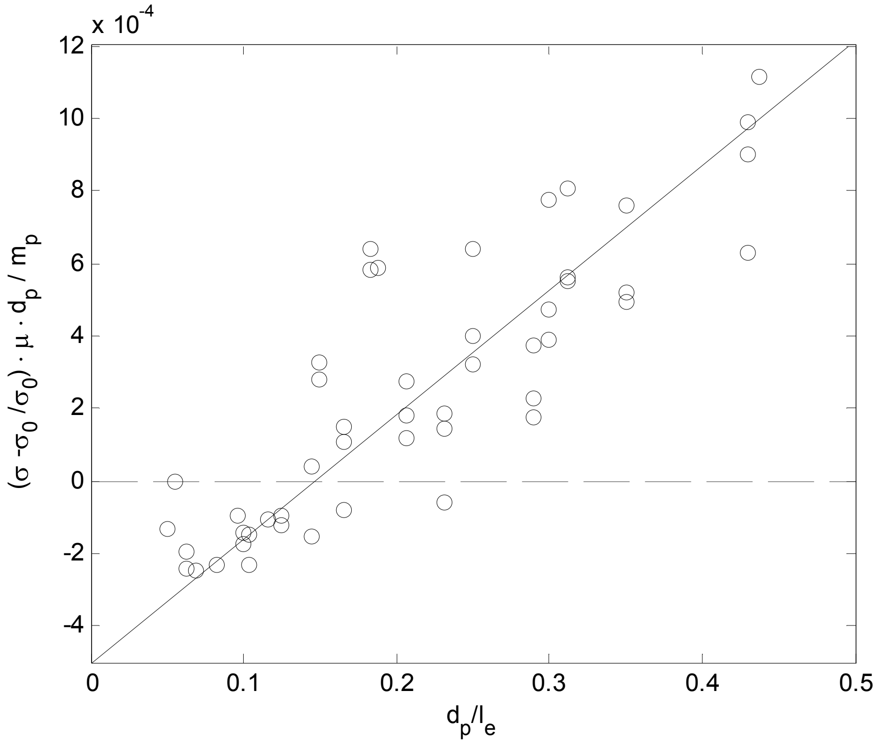

Figure 28: Fractional change in turbulence intensity versus d_p/l_e. Only measurement points with a volume fraction between $\alpha=2\cdot10^{-5}$ and $\alpha=10^{-3}$ are shown.

Comparison between spheres and non-spherical particles

Figure 29 shows the results for the length scale ratio suggested by Gore and Crowe (1989). In the upper left figure it can be seen that the overall tendencies for the change in the turbulence intensity is similar for the investigated particles However, for low ranges of d_{eq}/l_e the disk shape cause significantly more attenuation than other shapes and the prolate spheroid attenuates the turbulence slightly more than the spherical particles. Using the empirical fit presented above for the prediction of the turbulence modulation by spherical particles it is possible to examine the derivation of the results obtained for non-spherical shapes compared to the expected results. First, for good order, it can be seen that there is excellent agreement between the empirical fit and the result for spheres. Here the case of $d_p=1.8$ *mm*, $z=1$ has been chosen to be representative for the experiments conducted for spheres and this particular case closely match that of the non-spherical cases. For the results in the lower range of d_{eq}/l_e the measurements are made for settings with a low volume fraction where the flow can be considered as one-way coupled, where the model is not valid. For the disks and the prolate spheroids the correlation between the measurements and the empirical model is poor. Since the empirical fit is developed for spheres the discrepancy can be considered as the additional effect attributed to the shape of the particles.

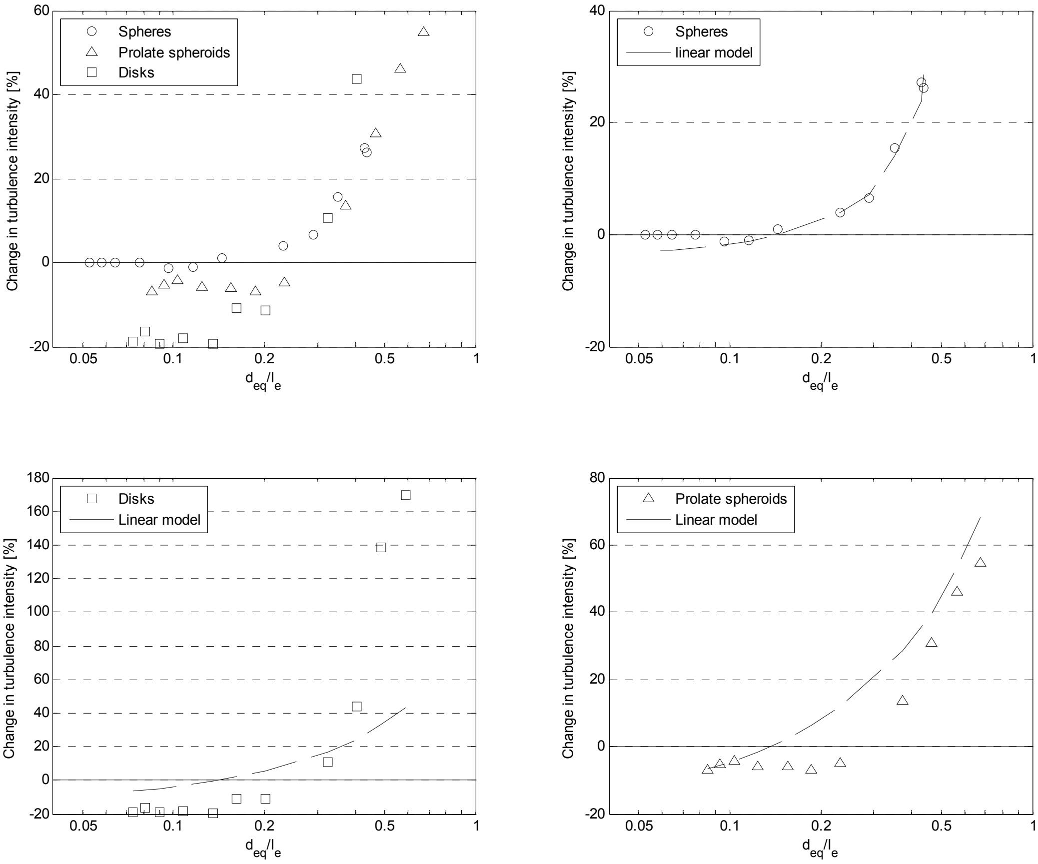

Figure 29: The percentage change in turbulence intensity versus the ratio of the volume equivalent particle diameter to the integral length scale of the clear flow for different particle types. Experimental results have been compared with an empirical model to predict the turbulence modulation inflicted by spherical particles. Notice that the y-axes are not the same for the figures.

For both the disks and the prolate spheroids the results indicate that they cause more attenuation than that predicted by the empirical model, indicating that both shapes cause additional attenuation. For the disks the turbulence modulation in the high d_{eq}/l_e range are significantly above that predicted by the model. Considering the high volume fraction at these settings and that the longest dimension of the disks is almost three times longer than the volume equivalent diameter, this additional effect may be due to particle collisions or other phenomenon's related to dense flows. It is clear that the disk shaped particles have the greatest effect on the turbulence for the range of shapes encountered, both with regards to attenuation and augmentation. This result can be explained to a part by the difference in drag coefficients. There is significant differences in results for large values of the particle Reynolds number when there is significant difference in the drag coefficient while the results seems to converge for results with low values of the particle Reynolds number. The effect of the secondary motion is difficult to estimate considering the present measurements and requires more detailed information of the turbulence as well as the flight of the non-spherical particles.

Summary

The influence of different parameters for turbulence modulation on a particle laden jet was studied by Laser Doppler Anemometry. The following conclusions can be made:

- In the investigated range of the Stokes number $St=10^1 - 10^3$ both augmentation and attenuation of the carrier phase turbulence are detected. The turbulence modulation does not correlate well with the Stokes number and the perception that it is the particles following the turbulent eddies which are solely responsible for the attenuation of the carrier phase turbulence cannot be verified.
- For spheres turbulence attenuation is only measured for values below $Re_p=400$ while significant augmentation is observed at $Re_p=200$. Since vortex shedding in the wake of particles is restricted to particle Reynolds numbers above $Re_p=270$ the perception that vortex shedding is solely responsible for the augmentation of the carrier phase cannot be confirmed.
- For volume fractions above $\alpha=2\cdot10^{-4}$ only augmentation is observed while for values below $\alpha=2\cdot10^{-5}$ only attenuation is detected. This indicates that turbulence modulation and the volume fraction are correlated. However, the effect of the volume fraction cannot be separated from the influence of the length scale ratios for the present experiment since these are both proportional to the distance from the jet nozzle. No turbulence modulation have been detected below $\alpha=4\cdot10^{-6}$. which indicate that the suggested criteria of $\alpha=10^{-6}$ is sufficient for the distinction between the one- and two-way coupling regimes.
- For low values of the length scale ratio of the particle size to the turbulence eddy size, d_p/l_e, particles tend to attenuate the turbulence while for high values they tend to augment the turbulence. For the combination of large particles with high mass loading, attenuation of the carrier phase turbulence have observed beyond the criterion, $d_p/l_e=0.1$.

- An empirical expression to predict the turbulence modulation has been proposed. This correlates the fractional change in turbulence intensity with the mass loading, particle diameter and the integral length scale. This is able to predict the turbulence modulation for spherical particles within the range of the present investigation.
- The turbulence modulation expression developed for spherical particles perform exceedingly poorer when applied on non-spherical particles with increasing extremity in shape. For the range of shapes investigated the empirical model for turbulence modulation under-predicted the attenuation effect of the non-spherical particles. This indicate that the departure from the spherical ideal act to decrease the turbulence intensity.

4. Numerical Model and Validation

"This is a definite relation of the exact kind for which I was in search. Of course without integration the equations only gave the relation without showing at all in what way the motion might depend upon it. It seemed, however, to be certain, if the eddies were due to one particular cause, that integration would show the birth of eddies to depend on some definite value of [that group of variables]."

- *Osborne Reynolds*

This chapter deals with the numerical modeling of particle laden flow in the presence of particles. A new model for turbulence modulation is derived from the governing equations of fluid flow considering the additional presence of particles. This is evaluated first using a simple closure strategy for fully developed pipe flow at the centerline and compared with available experimental measurements. Next, the model is implemented into a CFD basis using the standard k-ε model and applied on particle-laden pipe flow and jet flow. For pipe flow, the predictions are evaluated using available experimental measurements by respectively Tsuji et al. (1984) and Kulick et al. (1994) while the present results for a particle-laden jet, presented in the previous chapter, are used to evaluate the predictions for jet flow.

The aim for practical use in large scale simulations of industrial biomass boilers forms the basis of most choices made with regards to models and schemes. As such the standard k-ε turbulence model has been selected rather than resorting to more intricate turbulence models knowing the deficiency for this model but also considering its widespread use and known stability for rough meshes. However, it is important to point out that in the evaluation of the new model on basis of pipe and jet flow is made on fully grid independent meshes and that every step has been taken to ensure a correct solution of the flow field. The commercial code Fluent® 6.3 is used for all simulations. The Fluent user guide, (Fluent 2006), is generally regarded as an exhaustive source of information and since individual schemes and the solver routines have been become standard procedures the reader is referred to the Fluent manual for more information. Procedures for dealing with the modification of the turbulence equations are not standard and have to be implemented in the code using so-called User Defined Functions (UDF) which can access and modify the variables stored by the solver. The source code for the UDF together with a brief explanation can be found in appendix J while a derivation of the new model for the Reynolds Stress Model can be found in appendix F. An evaluation of the relative magnitudes of the correlations, which is part of the source terms for the standard, consistent and new model can be found in appendix G. Finally, the 6 degree-of-freedom model by Yin et al. (2003) is explained in appendix E and an outline of particle dispersion modeling can be found in appendix D.

Governing equations for the fluid phase

The governing equations of fluid flow can be derived from fundamental conservative principles. If the principle of conservation of mass is applied on a control volume the continuity equation is obtained:

$$\frac{\partial \rho}{\partial t} + \frac{\partial \rho u_i}{\partial x_i} = 0 \tag{49}$$

Note that for incompressible flows the density is constant and the time derivative is thus zero. For dilute particle concentrations the influence of the particle phase on the continuity equation is negligible and particles are simulated as having zero volume.

When the principle of conservation of momentum is applied on a control volume the stresses acting on the surface exchange momentum with the surrounding control volumes / boundaries.

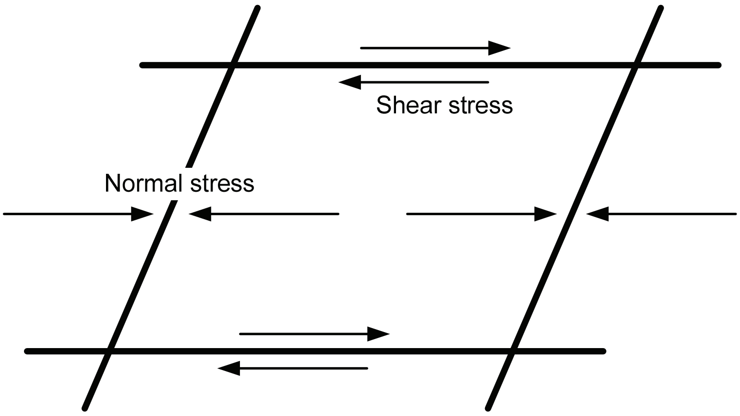

Figure 30: Stresses on a 2D control volume in a single direction.

The final form of the momentum equation for the three spatial directions is known as the Navier-Stokes equation, which is valid for Newtonian fluids, for both compressible and incompressible and for laminar and turbulent flows:

$$\frac{\partial \rho u_i}{\partial t} + u_j \frac{\partial \rho u_i}{\partial x_j} = -\frac{\partial P}{\partial x_i} + \frac{\partial \tau_{ij}}{\partial x_j} + \rho g_i + S_{upi} \tag{50}$$

where the stress tensor by:

$$\tau_{ij} = \mu \left(\frac{\partial u_i}{\partial x_j} + \frac{\partial u_j}{\partial x_i} - \delta_{ij} \frac{\partial u_k}{\partial x_k} \right) \tag{51}$$

where δ_{ij} is the Kronecker delta function. For the case of incompressible flow equation (50) can be simplified to the following:

$$\rho \frac{\partial u_i}{\partial t} + u_j \rho \frac{\partial u_i}{\partial x_j} = -\frac{\partial P}{\partial x_i} + \mu \frac{\partial^2 u_i}{\partial x_i x_j} + \rho g_i + S_{upi} \tag{52}$$

which is an often used representation for the Navier-Stokes equation. The influence of particles is included in the NS-equation through the source term S_{up} which represents the exchange of momentum between the two phases. In the absence of mass exchange, from evaporating or combusting particles, S_{up} summarizes the interfacial forces acting on all the particles inside the control volume. Usually only the drag force is considered and the momentum source term can be expressed as:

$$S_{upi} = \frac{\alpha \rho_p}{\tau_p}\left(u_{pi} - u_i\right) \tag{53}$$

Where α is the volume fraction of particles and τ_p is the particle response time given by:

$$\tau_p = \frac{\tau_V}{f} \qquad \tau_V = \frac{\rho_p d_p^2}{18\mu} \qquad f = 1 + 0.15\,\mathrm{Re}^{0.687} \qquad \mathrm{Re} = \frac{\rho \left|u_{pi} - u_i\right| d_p}{\mu} \tag{54}$$

For Eulerian/Lagrangian simulations the volume fraction is not readily available and S_{up} is instead found using the PSI-Cell method devised by Crowe (1977) which is standard in Fluent. If the particles trajectories are known the averaged source term for each cell can be determined as:

$$\overline{S_{upi}} = n\left\langle m_p\left(\frac{du_{pi}}{dt} - g_i\right)\right\rangle \tag{55}$$

where n is the mean number of particle in the per unit volume, m_p is the particle mass and < … > indicate mean values over all particle trajectory realizations. Further details can be found in the comprehensive review of the Lagrangian approaches for the behavior of discrete particles in turbulent flow by Gouesbet and Berlemount (1999).

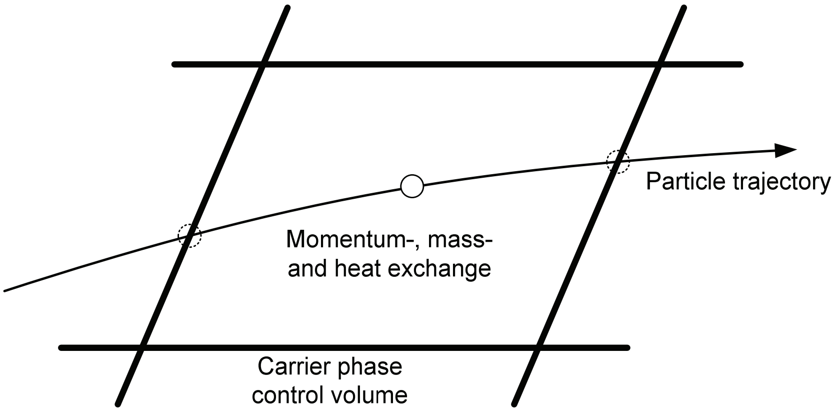

Figure 31: The momentum exchange can be found by considering the acceleration /deceleration of the particle as it traverses the control volume.

The NS-equation provides an exact description of turbulent flows. However, the direct use of the NS-equation to simulate turbulent flows requires that the spatial and temporal discretization is sufficient to resolve the finest turbulence scales. The lower size of turbulent eddies are limited only by the viscosity of the fluid. The smaller an eddy, the greater the velocity gradient and the greater the viscous stress that counteracts the eddy motion. At this limit the kinetic energy of the eddy is dissipated into internal energy and the scales of these eddies are hence characterized by the dissipation rate. From dimensional analysis the smallest scales, respectively the length, time and velocity scale, can be obtained as:

$$\eta_K = \left(\frac{\nu^3}{\varepsilon}\right)^{1/4}, \qquad \tau_K = \left(\frac{\nu}{\varepsilon}\right)^{1/2}, \qquad \upsilon_K = \left(\nu\varepsilon\right)^{1/4} \tag{56}$$

These scales are known as the Kolmogorov scales and a Reynolds number buildt on these scales equals unity. To perform a CFD simulation with full resolution of the Kolmogorov scales is know as Direct Numerical Simulation and is still out of reach for practical engineering purposes. The classical approach to overcome this problem is to only resolve the main flow field and merely model the effect of the turbulence on the mean flow. If the instantaneous velocity in equation (50) is substituted with the mean and the fluctuating velocity:

$$u_i = \overline{u}_i + u_i' \tag{57}$$

and ensample averaging is performed on the resulting equation the Navier-Stokes equation is reduced to the so-called Reynolds Averaged Navier Stokes (RANS) equation:

$$\frac{\partial \overline{\rho u_i}}{\partial t} + \overline{u}_j \frac{\partial \overline{\rho u_i}}{\partial x_j} = -\frac{\partial \overline{P}}{\partial x_i} + \frac{\partial}{\partial x_j}\left(\overline{\tau}_{ij} - \overline{\rho u_i' u_j'}\right) + \overline{\rho g}_i + \overline{S}_{upi} \tag{58}$$

where the additional term which has appeared is the Reynolds stresses which can be interpreted as the influence of the turbulent eddies on the mean flow. These terms are unknown and additional efforts have to be done to accurately predict this term. The classical approach is to assume that the Reynolds stresses have a similar effect as the viscous stresses. Based on this observation the following approximation to the Reynolds stresses was proposed by Boussinesq in 1877:

$$\overline{\rho u_i' u_j'} = \mu_t \left(\frac{\partial u_i}{\partial x_j} + \frac{\partial u_j}{\partial x_i} \right) \tag{59}$$

One significant implication using the Boussinesq approximation is that the turbulence is modeled as being isotropic, whereas practical engineering flows often is highly anisotropic. Furthermore, the turbulent viscosity is only constant for homogeneous flow and has to be estimated a priori. According to Prandtl's (1925) and Taylor's (1915) analysis the turbulent viscosity is proportional to a length scale and a velocity scale of the turbulence. In the context of the *k*-*ε* turbulence model the turbulent viscosity is found from the following equation:

$$\mu_t = \rho C_\mu \frac{k^2}{\varepsilon} \tag{60}$$

where C_μ is a constant. The turbulent kinetic energy, *k*, and the dissipation rate, *ε*, can related to the length, l_e, and velocity scale of the characteristic eddy by:

$$k = \frac{3}{2} u'^2 \quad , \quad \varepsilon = C_\mu^{3/4} \frac{k}{l_e} \tag{61}$$

To obtain an equation for the turbulent kinetic energy of the gas phase including the effect of the particles equation (52) is first multiplied with the instantaneous velocity u_i to give the total kinetic energy. By applying Reynolds decomposition, performing ensample averaging and subtracting the mean kinetic energy we end up with and expression of the turbulent kinetic energy per unit mass, $k = \frac{1}{2} u_i'^2$:

$$\underbrace{\rho \frac{\partial k}{\partial t} + \rho \bar{u}_j \frac{\partial k}{\partial x_i}}_{I} = \underbrace{-\rho \overline{u_i' u_j'} \frac{\partial \bar{u}_i}{\partial x_j}}_{II} + \underbrace{\frac{\partial}{\partial x_i} \left(\mu \frac{\partial k}{\partial x_i} \right)}_{III} - \underbrace{\frac{\partial}{\partial x_i} \left(\overline{\rho u_i' u_i' u_j'} + \overline{u_i' P'} \right)}_{IV} + \underbrace{\overline{\frac{\partial u_i' \partial u_j'}{\partial x_i \partial x_j}}}_{V} + \underbrace{\overline{u_i' S_{upi}}}_{VI} \tag{62}$$

where:

I. Represent the total change of the of the carrier phase turbulent kinetic energy
II. Represent the production of turbulence due to main flow gradients
III. Represent the work done by viscous shear stresses

IV. Represent the diffusion or mean convective transport with turbulent movement
V. Represent the dissipation of turbulent kinetic energy which is always positive
VI. Represent the work done by the carrier phase fluctuating velocities on the particle phase

The exact *k*-equation contains terms which are unknown and have to be modeled. Following the standard procedure in the formulation of the *k-e* model (Launder and Spalding 1972) the *k*-equation is simplified to the following general form:

$$\rho \frac{\partial k}{\partial t} + \rho \bar{u}_j \frac{\partial k}{\partial x_i} = \frac{\partial}{\partial x_i}\left(\left(\mu + \frac{\mu_t}{\sigma_k} \right) \frac{\partial k}{\partial x_j} \right) + \rho P_k - \rho \varepsilon + S_{kp} \tag{63}$$

where σ_k is a constant S_{kp} is the particle source term and the production term P_k is modeled as being proportional to the mean rate stress tensor:

$$P_k = \mu_t \left(\frac{\partial \bar{u}_i}{\partial x_j} + \frac{\partial \bar{u}_j}{\partial x_i} \right) \frac{\partial \bar{u}_i}{\partial x_j} \tag{64}$$

Similar to the *k*-equation, the exact *ε*-equation can be derived from the Navier-Stokes equation. However, this equation contains several new unknown correlations of the fluctuating velocity, pressure and velocity gradients. According to Wilcox (2002) these correlations are hopelessly difficult to measure so there is little hope to find guidance from experiments regarding suitable approximations. Again following the standard procedure the *ε*-equation modeled using the same general form as for the *k*-equation:

$$\rho \frac{\partial \varepsilon}{\partial t} + \rho \bar{u}_j \frac{\partial \varepsilon}{\partial x_i} = \frac{\partial}{\partial x_i}\left(\left(\mu + \frac{\mu_t}{\sigma_\varepsilon} \right) \frac{\partial \varepsilon}{\partial x_j} \right) + \rho P_\varepsilon - \rho Q_\varepsilon + S_{\varepsilon p} \tag{65}$$

The production, P_ε, and disintegration, Q_ε, of *ε* together with the addition dissipation due to particles $S_{\varepsilon p}$ is assumed to be proportional to the similar terms in the *k*-equation. To get the right units each term are multiplied with *ε/k*:

$$P_\varepsilon = C_\varepsilon \frac{\varepsilon}{k} P_k \qquad Q_\varepsilon = C_{\varepsilon 2} \frac{\varepsilon}{k} \varepsilon \qquad S_{\varepsilon p} = C_{\varepsilon 3} \frac{\varepsilon}{k} S_{kp} \tag{66}$$

The standard *k-e* model for particle laden flow thus contains 6 universal constants which are found from wind tunnel experiments, theory of boundary layer flow and computer optimization:

$$\sigma_k = 1.0 \qquad \sigma_\varepsilon = 1.3 \qquad C_\mu = 0.09 \qquad C_{\varepsilon 1} = 1.44 \qquad C_{\varepsilon 2} = 1.92 \qquad C_{\varepsilon 3} = 1.0 \tag{67}$$

Existing models for turbulence modulation

Several approaches have been proposed to model the source term S_{kp} and thereby account for the influence of particles on the carrier phase turbulence. These can be divided into three distinct categories. The largest group of models derived the source term due to particles using the standard approach of Reynolds averaging used to derive the turbulence equations. This results in a source term which always acts as sink for the turbulent kinetic energy and thus is only able to predict attenuation. This method has been labeled the standard approach (Lain and Sommerfeld 2003). The turbulence equations for particle laden flow can also be derived by considering that the instantaneous carrier phase velocity at the surface the particle must be equal to the particle velocity. This results in a term which for dilute flows is always positive and thus only acts to enhance the turbulent kinetic energy. This method is commonly referred to as the consistent approach (Lain and Sommerfeld 2003). The last type of models can be referred to as semi-empirical or semi-heuristic. These are based on a mechanistic approach where additional source terms are defined as functional relationships of the wake size or other particle related parameters. In contrast to the standard and the consistent approach, models based on this approach are capable of predicting both attenuation and augmentation of turbulence. However, such an approach has been criticized for lacking rigor since the models are not derived from the balance equations of mass, momentum and energy, and thus cannot be introduced into conventional closure models without violating fundamental physical principles. The present work introduces a new derivation of the source term for particle-turbulence interaction consistent with the governing equations of fluid flow. The resulting source term represents a hybrid between the standard and consistent approaches and is capable of predicting both attenuation and augmentation.

Standard approach

The source term for the standard approach is derived by multiplying the momentum equation by u_i and applying a Reynolds averaging procedure (Chen and Wood 1985; Gouesbet and Berlemont 1999; Lightstone and Hodgson 2004). After subtracting the mean kinetic energy, an expression for the turbulent kinetic energy due to the presence of particles results as:

$$S_{kp} = \overline{u_i' S_{upi}'} \tag{68}$$

If only the drag force is considered this term can be expressed as:

$$S_{kp} = \frac{\alpha\rho_p}{\tau_p}\left(\overline{u'_i u'_{pi}} - \overline{u'_i u'_i}\right), \qquad \overline{u'_i u'_i} = 2k \tag{69}$$

Equation (69) is often referred to as being dissipative considering that the particles are accelerated by the motion of the fluid and thus the particle velocity u'_{pi} is smaller than the fluid velocity u'_i (Elghobashi 1994). Usually, models based on this approach are only capable of predicting attenuation. Several authors have presented models for the unknown first term. Here we only present the most recent development of the standard approach. Thus by considering the crossing trajectory effect, the unknown correlation can be derived analytically as (Lightstone and Hodgson 2004):

$$\overline{u'_i u'_{pi}} = 2k\frac{\tau^*}{\tau^* + \tau_p}, \qquad \frac{1}{\tau^*} = \frac{|u_i - u_{pi}|}{L_I} + \frac{1}{\tau_{L_I}} \qquad L_I = 2\tau_{L_I}\sqrt{2k/3} \qquad \tau_{L_I} = 0.135\frac{k}{\varepsilon} \tag{70}$$

where τ_{LI} and L_I is the Lagrangian time and length scale. The additional dissipation due to the particles, $S_{\varepsilon p}$, is assumed to be proportional to the similar terms in the k-equation. To get the right units each term is multiplied by ε/k:

$$S_{\varepsilon p} = C_{\varepsilon 3}\frac{\varepsilon}{k}S_{kp} \tag{71}$$

where the value of the constant $C_{\varepsilon 3}$ is suggested to be 1.1.

Consistent approach

Another approach, which provides what is commonly known as the consistent terms, starts with the mechanical energy equation for the fluid phase and subtracts the product of the mean velocity and the momentum equation to obtain an expression for the turbulent kinetic energy (Crowe 2000). The source term due to the presence of the particles is then given as:

$$S_{kp} = \overline{u_{pi}S_{upi}} - \overline{u}_i\overline{S}_{upi} \tag{72}$$

If the drag force is again used as the momentum source term, as in equation (58), the following expression for the kinetic energy source term due to the presence of particles can be obtained after Reynolds averaging:

$$S_{kp} = \frac{\alpha\rho_p}{\tau_p}\left(\left|\overline{u}_i - \overline{u}_{pi}\right|^2 + \left(\overline{u'_{pi}u'_{pi}} - \overline{u'_i u'_{pi}}\right)\right) \tag{73}$$

The first term can be identified as the transfer of energy by the drag force while the last two terms are seen to represent the transfer of kinetic energy of the particle motion to the kinetic energy of the of the fluid. The first term is always positive and increases in magnitude with particle size for particles traveling at terminal velocity. According to Crowe (2000) the last two terms can be neglected for dilute flow but become important for dense flow where particle collisions tend to increase the particle kinetic energy. Thus models based on this consistent approach are only able to predict an augmentation of the carrier phase turbulence; the opposite of the standard approach. The source term to the dissipation rate is found similarly as for the standard approach, however, the value of the constant $C_{\varepsilon 3}$ should be changed to 1.8 (Lain and Sommerfeld 2003). This value is often discussed and several observations suggest that this value is not universal (Squires and Eaton 1992; Boulet and Moissette 2002).

Semi-empirical or semi-heuristic approach

The third approach to formulate appropriate source terms to the turbulence equations deals with additional semi-empirical production and dissipation terms based on energy transfer mechanisms associated with the particles. The production of turbulence is most often attributed to the wake of the particle where the velocity defect and vortex shedding are well known phenomena which influence the carrier phase. Yuan and Michaelides (1992) and Yarin and Hetsroni (1994) have both presented models in which production terms rely on descriptions of the wake, while Kenning and Crowe (1997) introduces a hybrid length scale, in replacement of the traditional dissipation length scale to account for the additional dissipation. These models have succeeded in predicting some changes in the turbulence intensity but have been criticized for not providing a theoretical base consistent with the closures presented above (Boulet and Moussette 2002).

New model for turbulence modulation

The standard and the consistent approach are theoretically correct in that they are both derived considering the conservation of energy, but neither are fully capable of predicting both attenuation and augmentation of the fluid phase. Semi-empirical models use a mechanistic approach to formulate terms which with some success, can account for both attenuation and augmentation, but these models are criticized for not being based on a solid theoretical basis. Thus, what is desired is a model which is derived on a theoretical basis but which contains both production and dissipation terms which can be related to fundamental mechanisms.

Referring to the comprehensive DNS study by Vreman (2007) for inspiration, two basic mechanisms can be identified as causes for turbulence modulation in pipe flows: One is due to the particles mean velocity profile generally being more uniform than the carrier phase mean velocity profile, and the other resulting from the particle-eddy interaction which leads to additional dissipation. The present derivation uses this observation to identify two different forcing terms due to the presence of the particles. One which acts globally, in a Reynolds averaged sense, and one which act locally due to the ability of the surface of the particles to support stresses. The momentum source term is extended to yield two simple forcing terms reflecting the basic mechanisms:

$$S_{upi} = S_{upi,1} + S_{upi,2} = \frac{\alpha\rho_p}{\tau_p}\left(u_{pi} - \overline{u}_i\right) + \frac{\alpha\rho_p}{\tau_p}\left(\overline{u}_i - u_i\right) \tag{74}$$

If the consistent approach is applied on the first term and the standard approach on the second, the source term due to particles can be expressed as:

$$S_{kp} = \frac{\alpha\rho_p}{\tau_p}\left(u_{pi} - \overline{u}_i\right)\left(u_{pi} - \overline{u}_i\right) + \frac{\alpha\rho_p}{\tau_p}u_i'\left(\overline{u}_i - u_i\right) \tag{75}$$

By applying different methods to derive the source term for the turbulent kinetic energy equation, one recognizes the different origin of the forcing terms. Performing Reynolds decomposition along with Reynolds averaging the final expression emerges as:

$$S_{kp} = \frac{\alpha\rho_p}{\tau_p}\left(\left|\overline{u}_i - \overline{u}_{pi}\right|^2 + \overline{u'_{pi}u'_{pi}} - 2k\right) \tag{76}$$

This term can also be achieved by adding the source terms of the standard and consistent method and thus represent a combination of both approaches. It should be noted that a similar expression is also suggested in Geiss et al. (2004), where it emerges from the exploitation of the entropy inequality, in which the energy balance equation as well as the motion and continuity equation have been included as constraint conditions. The terms in equation (76) can be related to the two mechanisms for the transfer of mechanical energy of the particle phase to the turbulent kinetic energy of the fluid phase. These mechanisms are illustrated in Figure 32.

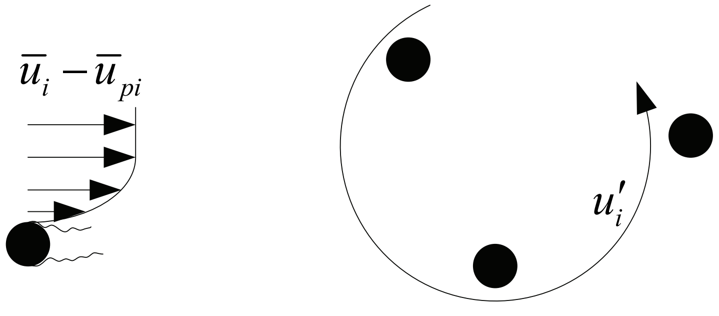

Figure 32: Mechanisms for turbulence modulation.

Particles represent surfaces which are capable of supporting stresses and thus generate addition turbulence due to the flow gradient. This additional turbulence manifests itself in the wake of the particles and is often referred to as wake induced turbulence. This is also addressed by the consistent approach and is dependent on concentration, the relative velocity between the particle and the fluid phase which, for particles traveling at terminal velocity, is highly dependent on the particle size. This term reflects the conversion of mechanical work by the drag force and is thus related to the first mechanism.

The correlated motion between particles and turbulent eddies tend to attenuate the turbulence as the particles are accelerated by the fluid motion. This mechanism should be dependent on concentration, relevant turbulence quantities and the particle response time. This mechanism is also addressed by the standard approach but not the consistent approach and reflects the second mechanism.

The source term for the dissipation equation can again be found using equation (71) where the constant $C_{\varepsilon 3}$ is set initially to 1.0. Several different values of the proportionality constant between values of 1 and 2 have been tried, however, the effect on the final outcome is very limited and the initial value of 1.0 has been maintained. It can be realized that this derivation yields the desired effects relating to experimental observations. For small particles the first term will be small compared the third term and thus the overall effect of the source term is to attenuate turbulence. For large particles falling at terminal velocity the first term will be dominant and source term will thus be able to reproduce the large augmentation which has been observed.

Simple closures to test the new source term

The suggested equation for the turbulence kinetic energy budget for particle laden flows now appear:

$$\rho\frac{\partial k}{\partial t}+\rho\bar{u}_j\frac{\partial k}{\partial x_i}=\frac{\partial}{\partial x_i}\left(\mu+\frac{\mu_t}{\sigma_k}\frac{\partial k}{\partial x_i}\right)-\rho\overline{u_i'u_j'}\frac{\partial\bar{u}_i}{\partial x_j}+\frac{\alpha\rho_p}{\tau_p}\left(\left|\bar{u}_i-\bar{u}_{pi}\right|^2+\overline{u_{pi}'u_{pi}'}-2k\right)-\rho\varepsilon \quad (77)$$

When this equation is applied to the thought experiment by Crowe (2000), where particles are artificially fixed in position in an otherwise steady and uniform flow[8], equation (77) is reduced to the following:

$$\frac{\alpha\rho_p}{\tau_p}\left(\left|\bar{u}_i\right|^2-2k\right)-\rho\varepsilon=0 \quad (78)$$

---

[8] A flow with no spatial or temporal gradients in the averaged properties. This represents an ideal case which can be used to compare models.

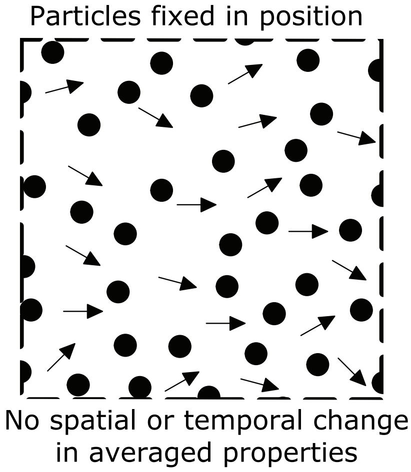

Figure 33: Schematic of the artificial flow where particles are fixed in position developed by Crowe (2000) for test of turbulence modulation models.

which states that the turbulence produced by the particles is dissipated by the combined dissipative effect of the particles and viscosity. Thus the source term modeled is consistent in the way that it provides a plausible closure for this idealized flow.

Another simple closure for the turbulence modulation at the centerline of a pipe also presented by Crowe (2000) may also serve to evaluate this new term. When applied to the case of a fully developed dilute particle laden flow in a vertical pipe, for which experimental data is available, equation (77) for the flow near the pipe centerline is reduced to:

$$-\rho\overline{u_i'u_j'}\frac{\partial \overline{u}_i}{\partial x_j} + \frac{\alpha\rho_p}{\tau_p}\left(\left|\overline{u}_i - \overline{u}_{pi}\right|^2 - 2k\right) - \rho\varepsilon = 0 \tag{79}$$

Using the closure scheme provided by Crowe (2000) where the terminal velocity $g\tau_V/f$ is used for the velocity difference, equation (79) reduces to:

$$\rho\frac{k_0^{3/2}}{l_e} + \frac{\alpha\rho_p f}{\tau_V}\left(\left(\frac{g\tau_V}{f}\right)^2 - 2k\right) - \rho\frac{k^{3/2}}{l_e} = 0 \tag{80}$$

where respectively k and k_0 are the turbulent kinetic energy of the clear flow and particle-laden flow and l_e is the integral length scale. Notice that unlike the work by Crowe (2000) it is not necessary to resort to a hybrid length scale. Without using the hybrid length scale in the closure scheme the model suggested by Crowe (2000) is only able to predict augmentation. However, the use of the hybrid length scale produces obviously erroneous results for low particle volume fractions. Here, the following supporting equations are used:

$$f^{5/2} = 0.058\frac{g\tau_V d_p \rho}{\mu} \qquad \tau_V = \frac{\rho_p d_p^2}{18\mu} \qquad \alpha = \left(\frac{\rho}{\rho_p}\right)C \qquad k_0 = \frac{3}{2}\left(\bar{u}\sigma_0\right)^2 \qquad k = \frac{3}{2}\left(\bar{u}\sigma\right)^2 \quad (81)$$

where respectively *σ* and *σ₀* is the turbulence intensity of the clear and particle laden flow. The correlation for *f* is an approximation which is valid for particles traveling at terminal velocity (Crowe 2000). The fractional change of the turbulence intensity for a pipe flow with mean velocity of 10 m/s laden with glass particles in a 40 mm pipe and a particle free turbulence intensity of 0.06, have been solved using an iterative procedure. The turbulence length scale at the center of the pipe is set at l_e=4 mm (Hutchinson et al. 1971). The particle size has been varied for particle mass concentrations of 0.1, 1 and 5 producing the curves seen in Figure 34.

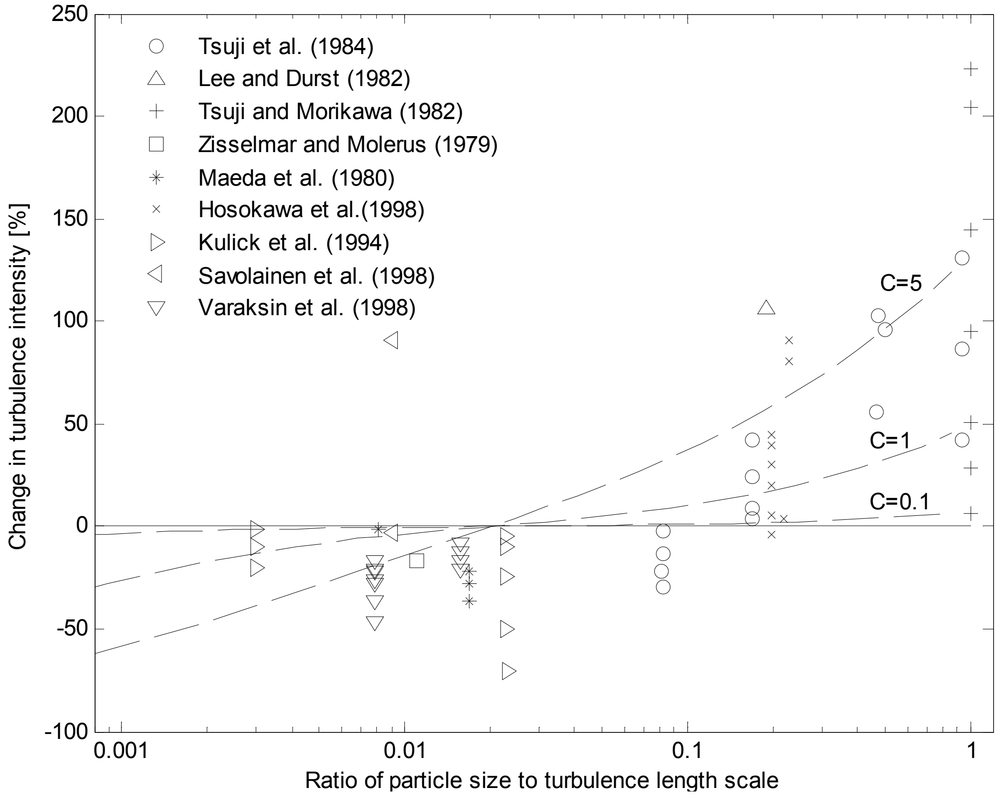

Figure 34: Comparison of model prediction and data for the turbulence modulation at the centerline of a vertical pipe.

Similar to the model by Crowe (2000) the curves show the same trends as the experimental measurements. Furthermore, this model also predicts the correct behavior when approaching the one-way coupling regime. Making the pipe in the model smaller will generally move the curves towards the right on the x-axis while using a larger pipe will move them to the left. Using relative velocities other than the terminal velocity can similarly dramatically change the prediction due to the sensitivity of the source term. In this closure scheme only the effect on the *k*-equation is considered whereas it is known that the effect of the momentum coupling tends to decrease the turbulence intensity further. Finally, the double correlation of the particles fluctuating velocity, which is neglected here, becomes important for dense flows in particular but also for wall bounded flows (Vreman 2007).

Table 7: Source terms evaluated in present investigation.

Standard:	$S_{kp} = \dfrac{\alpha\rho_p}{\tau_p}\left(2k\dfrac{\tau^*}{\tau^* + \tau_p} - 2k\right)$
Consistent:	$S_{kp} = \dfrac{\alpha\rho_p}{\tau_p}\left\lvert\overline{u}_i - \overline{u}_{pi}\right\rvert^2$
New:	$S_{kp} = \dfrac{\alpha\rho_p}{\tau_p}\left(\left\lvert\overline{u}_i - \overline{u}_{pi}\right\rvert^2 - 2k\right)$

The three models evaluated in this paper have been applied on the same simple closure scheme as presented above. Table 7 summarizes the source terms used in the evaluation of the different approaches. Note that some terms have been neglected for simplicity. Terms containing the fluctuating particle velocity are assumed only to become significant, compared to other terms, at locations close to the wall or in the case of dense flows and can thus be neglected safely at centerline of a pipe. Figure 35 shows the result for the same 40 mm pipe where the particle size is varied between 10 and 4000 µm with unity loading. It can be seen that the consistent model is only able to predict augmentation whereas the standard model, here represented by the model by Lightstone and Hodgson (2004) is only able to predict attenuation.

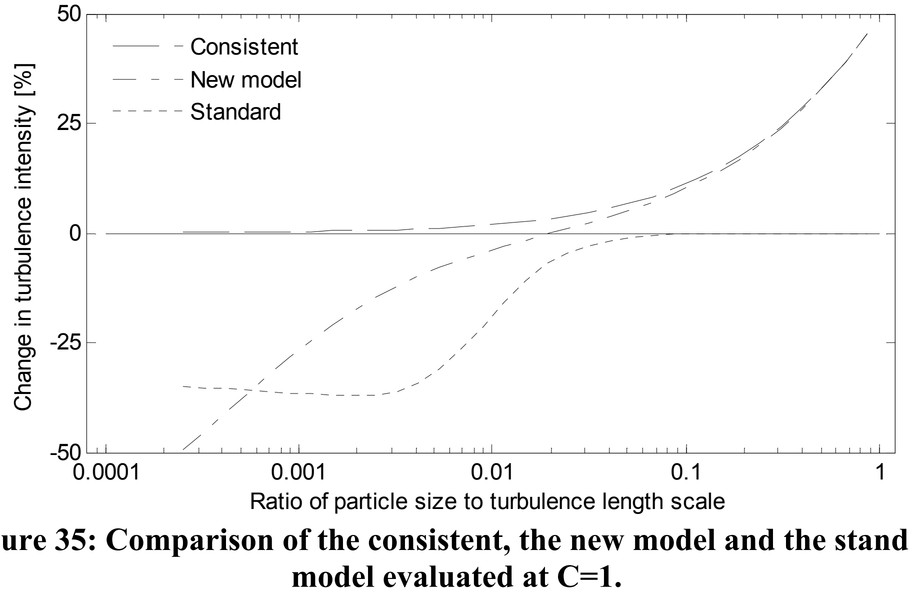

Figure 35: Comparison of the consistent, the new model and the standard model evaluated at C=1.

The new model, which is essentially a hybrid between the standard and consistent approach, is able to predict both augmentation and attenuation. For very large particle sizes the particle-eddy interaction mechanism diminishes and the evaluation of the consistent and the new model become the same while the standard model predicts zero turbulence modulation. For small particles the consistent approach predicts zero modulation whereas both the standard and new model predicts significant attenuation.

Fully developed pipe flow laden with spheres

On the basis of the preliminary evaluation of the new source term based on simple closure schemes, three cases have been chosen to evaluate the performance of the new source term in the k-ε framework. Case 1 consists of the largest particles where significant augmentation is expected while Case 3 comprises small particles where attenuation is expected. Case 2 encompass medium sized particles which have a d_p/l_e ratio close to the criterion defined by Gore and Crowe (1989) which marks the boundary between attenuation and augmentation and thus very little modification of the carrier phase is to be expected. Cases 1 and 2 is taken from the experimental study by Tsuji et al. (1984) while case 3 is taken from Kulick et al. (1994). Both studies deals with the air-particle flow in a vertical pipe, where Laser Doppler Velocimetry has been used to measure the carrier phase velocity in the axial direction. Experimental results are available for a range of different pipe Reynolds numbers, particle mass loadings and particle diameters. The details of the experimental settings are shown in Table 8.

Table 8: Test cases.

	Case 1	Case 2	Case 3
d_p (μm)	1420	243	70
ρ (kg/m^3)	1030	1020	8800
Loading	0.6	0.5	0.4
D (mm)	30.5	30.5	40.0
$u_{c,centerline}$ (m/s)	13.4	13.4	10.5
u_{mean} (m/s)	11.26	11.26	8.85
$\dot{m}_p$ (kg/s)	0.00605	0.00504	0.00545
d_p/l_e *	0.47	0.08	0.02

* evaluated at centerline: $l_e = 0.1D$

Besides the differences in flow rate, pipe diameter and particle materials it should be noted that the study Tsuji et al. (1984) is an upward flow whereas the study by Kulick et al. (1994) is a downward flow. Results for all cases are given at 5 m, which corresponds to 164D and 125D, from the inlet where the flow can be considered to be fully developed. Polystyrene (cases 1 and 2) and copper (case 3) particles are used which yields a density ratio of around or above 1/1000. According to the guidelines provided in (Sommerfeld, van Wachem and

Oliemans 2007) the influence of added mass, Basset history force and pressure gradient is negligible for the motion of the particles. Only loadings for which the flow can be considered as dilute (Elghobashi 1994) are used and particle collisions can thus be neglected. The pipe used in the experiments were made of glass; thus the pipe wall can be considered as being smooth and particle-wall collisions are assumed to be perfectly elastic for the no slip wall boundary. The calculations have been performed on a 2 dimensional axisymmetric mesh discretised with 20x800 (case 1 and 2) and 30x800 (case 3) control volumes in the radial and axial directions respectively. This mesh has been proven to produce grid independent results. At the inlet a top hat velocity profile has been specified and the initial velocities for the particles are set equal to the gas phase. A total of 25,000 particle trajectories have been simulated to provide statistically independent results. At the pipe exit zero gauge pressure has been specified across the entire boundary and the particles are allowed to escape.

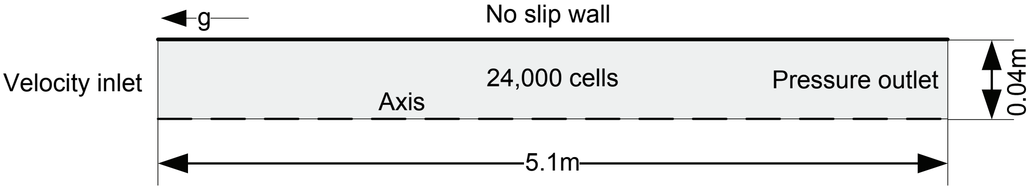

Figure 36: Pipe flow geometry. Note figure not to scale.

Figure 37 shows the concentration profiles for the three cases and the different models considered. It can be seen that the largest particles are concentrated towards the center of the pipe whereas the concentration profile for the smallest particles is mostly evenly distributed except close to the wall where particles have accumulated. Since the source terms for all models considered are proportional to the particle concentration it can be concluded that for large particles the numerical values of the source terms are several magnitudes larger at the pipe center than in the near wall region. For case 1 and 2 there is a clear coupling between the source term formulation and the particle concentration whereas for the smallest particles a flat particle concentration profile can be assumed for all source terms.

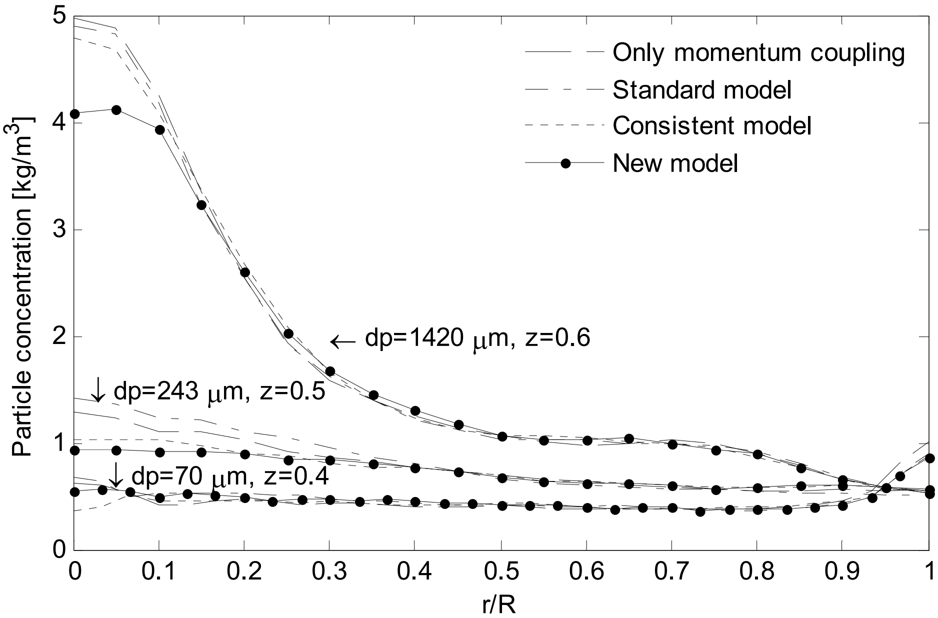

Figure 37: Concentration profiles of the three different cases for the three models and simulations with only momentum coupling. Note that for the present cases no experimental data exists for the particles concentration.

Figure 38 comprises the results from the different models for case 1 and also shows the measurements by Tsuji et al. (1984) for this case. For the mean velocity all models tend to flatten the velocity profile slightly. This effect is most pronounced for the new model and for the model by Lightstone and Hodgson (2004). This effect is however difficult to perceive in the experimental data where the difference between the clear flow and particle laden profiles is minimal. Furthermore it can be noticed that it is not possible to reproduce the clear flow velocity profile exactly, a problem which also can be found in other investigations dealing with the numerical simulation of this case (Lain and Sommerfeld 2003; Yan, Lightstone and Wood 2007). For the fluctuating velocity component the model by Lightstone and Hodgson (2004) and the simulation using momentum coupling only predicts an attenuation of the flow while both the new model and the model by Lain and Sommerfeld (2003) predict augmentation of the turbulence. It can be noted that the new model performs slightly better than the model by Lain and Sommerfeld (2003). Again it should be noted that it is not possible to predict the exact same clear flow profile as measured by Tsuji et al. (1984). This is, in part, due to the Boussinesq approximation, fundamental to the k-ε model, which treats the turbulence as being isotropic. Thus the fluctuating velocity u' is calculated as $\sqrt{\frac{2}{3}k}$.

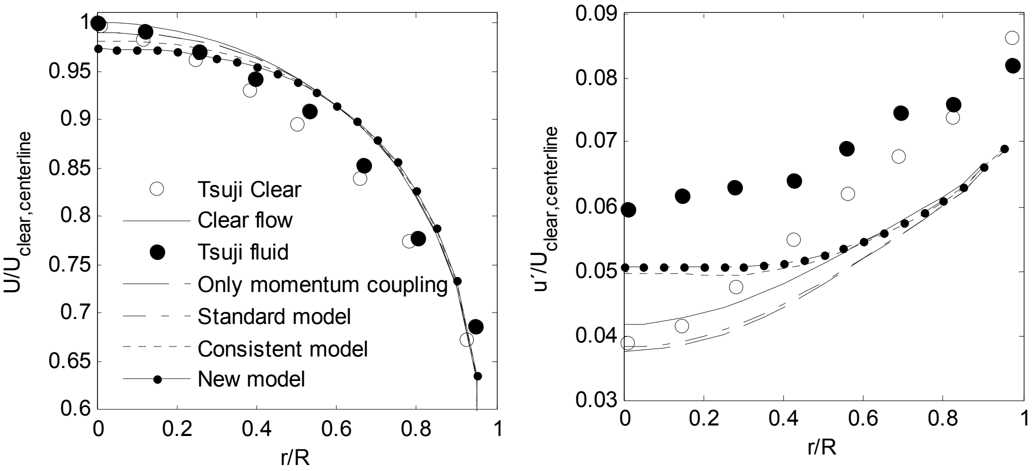

Figure 38: Non-dimensional radial profiles of the axial mean and fluctuating velocity components for case 1: dp=1420µm, z=0.6, $U_{clear,centerline}$=13.4m/s.

Figure 39 comprises the results of the numerical simulations and the measurements by Tsuji et al. (1984) for case 2. For all the models tested the mean velocity profiles for this case is almost indistinguishable from the clear flow profile, whereas for the measurements the particle-laden profile is somewhat flatter than the clear flow profile and similarly the measurements of the fluctuating velocity component is dampened compared to the clear flow profile. The prediction for the standard approach as well as the prediction with the momentum source term only display the same trend as the measurements, whereas the new model and the consistent approach predicts an augmentation of the carrier phase. For this case the standard approach provides the best approximation to the experimental data at the centerline. It can be noticed that the new model performs better then the consistent approach and the model predicts only a relatively small change at the centerline which can be expected on basis of the d_p/l_e ratio.

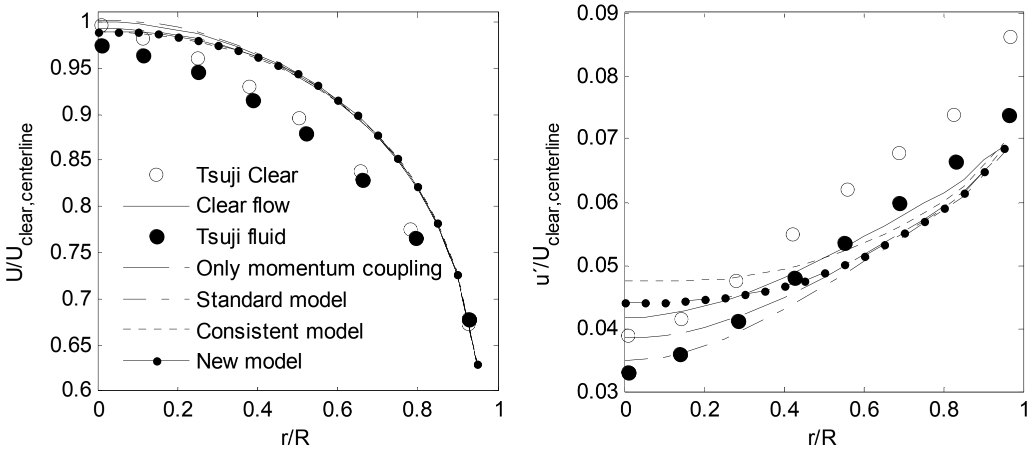

Figure 39: Non-dimensional radial profiles of the axial mean and fluctuating velocity components for case 2: d_p=243µm, z=0.5, $U_{clear,centerline}$=13.4m/s.

Figure 40 comprises the results of the numerical simulation for case 3 which is compared to the experimental results by Kulick et al. (1994). The measurement of the mean velocity profile for the clear flow is indistinguishable from that of the particle-laden flow. For the prediction of the mean velocity profile there is similarly hardly any difference between the clear flow and the prediction by the different models. For the fluctuating flow all models now predicts attenuation of the carrier phase at the centerline. For this case the relative velocity which play an essential role in predicting the augmentation caused by larger particles is relatively small and thus for the consistent model only the effect by the momentum coupling is causing the attenuation. For the new model and the standard model additional terms exist which caused the prediction to become less than that caused by the momentum coupling alone.

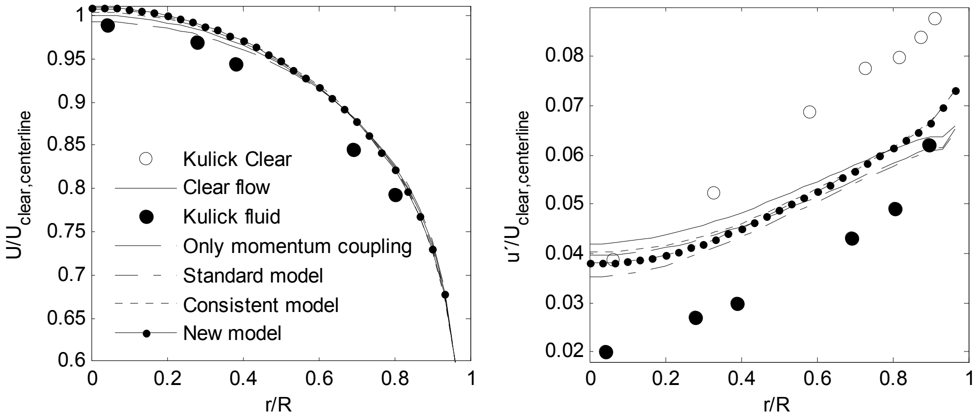

Figure 40: Non-dimensional radial profiles of the axial mean and fluctuating velocity components for case 3: d_p=70μm, z=0.4, $U_{clear,centerline}$=10.5m/s. For the mean velocity profile the experimental results by Kulick et al. (1994) for the clear flow is indistinguishable from the particle laden flow.

Figure 41 shows an evaluation of the different terms in the new model for case 2. It can be seen that both attenuation and augmentation is present at different regions of the flow. The relative velocity approaches zero in a region of the flow since the mean particle velocity is more uniform than the mean fluid velocity. In the region, where the relative velocity is small, there is significant attenuation of the fluid turbulence. Close to the wall the relative velocity increases rapidly and thus there is significant augmentation in the near wall also for small and heavy particles. At the center of the pipe the square of the relative velocity is larger then the twice the turbulent kinetic energy and the resultant evaluation of the entire source term is thus positive. At the centerline $\overline{u'_{pi}u'_{pi}}$ is an order of magnitude smaller than the other terms and can be neglected. However, this term increases in magnitude closer to the wall due to the particle-wall collisions and always acts as a source. Furthermore, it can be realized the often used assumption where the relative velocity is approximated by the terminal velocity is only valid in the center of the pipe.

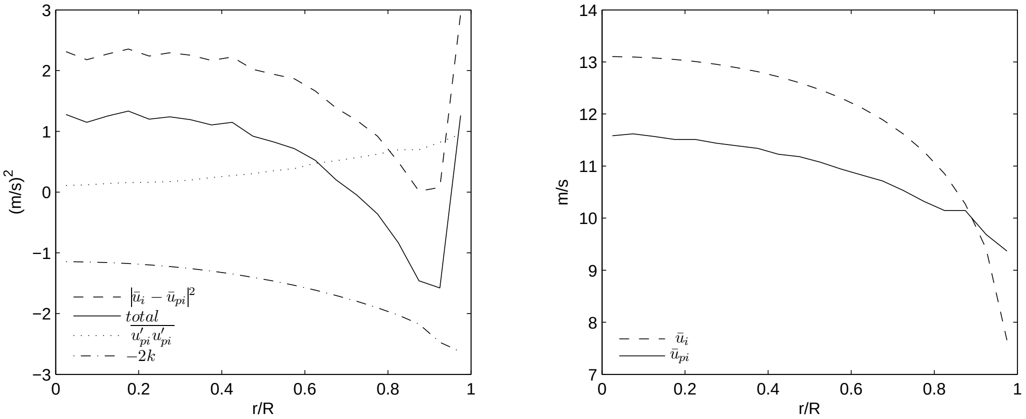

Figure 41: Evaluation of the different terms in the new model and mean flow velocity profiles for case 2.

Particle-laden jet flow

Finally it is also desired to see the performance of the developed model extension on the particle-laden jet flow treated in the previous chapter. For this two cases have been selected as representative for the range of experiments performed. Case A involves spherical glass beads at unity loading, while case B deals with the non-spherical shape of prolate spheroids which is characterized by an aspect ratio of 3.5. The test cases have been summarized in Table 9 and addition information about the experimental conditions can be found in chapter 3.

Table 9: Test cases.

	Case A	Case B
Shape	Sphere	Prolate spheroid
d_p *(μm)*	880	2815
ρ (kg/m^3)	2500	750
Loading	1.05	2.0
D_{nozzle} *(mm)*	40	40
u_0 *(m/s)**	7	7
$\dot{m}_p$ *(kg/s)*	0.0111	0.0219
d_p/l_e	0.19-0.02	0.70-0.08

*nominal inlet velocity

These simulations are also performed to evaluate the performance of a simplified model compared to the full model. This simplified model is based on the terminal velocity of the particles and drastically reduces the computational time and memory requirements compared to the full model. The different strategies for implementing the new source term are further discussed in appendix I. However, note that this particular flow involves a significant departure from the assumption that particles have reached terminal velocity. Furthermore, for the case involving non-spherical particles, these simulations act to evaluate the performance of the new source term in conjunction with different models for particle motion. As such the both the 6 degree-of-freedom model developed by Yin et al. (2003) and a model based on the modification of the drag coefficient using the sphericity have been tested. The model by Yin et al. (2004) is further explained in appendix E. Results are given at the centerline of the jet where experimental measurements are available. Similar to the previous case of pipe flow a number of forces acting on the particles have been neglected. However, it should be noted that near the nozzle the particle concentration is so large that the flow may be considered as dense. The calculations have been performed on a 2 dimensional axisymmetric mesh discretised with 100x250 control volumes in the radial and axial directions respectively. This mesh has been proven to produce grid independent results. At the inlet a top hat velocity profile has been specified and the velocity magnitude has been adjusted to yield the same velocity as measured at x/D=0.5. A total of 30,000 particle trajectories have been simulated to provide statistically independent results. At the pipe exit zero gauge pressure has been specified across the entire boundary and the particles are allowed to escape. The particle inlet condition has been specified using a so-called group injection with 40 particle streams to form a cone like injection where the angle is adjusted to what is observed experimentally. The flow geometry is illustrated in Figure 42.

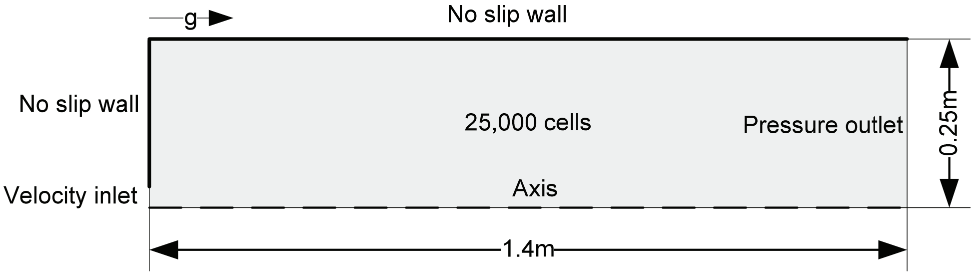

Figure 42: Jet flow geometry. Note figure not to scale.

Note that the use of an axisymmetric boundary condition results in a geometry which is cylindrical compared to the rectangular geometry used in the experimental setup. The effect of the differences in geometry on the flow is noticeable close to the wall. However, at the centerline the differences in the enclosure geometry have a small influence, justifying the use an axisymmetric boundary condition which greatly reduces the computational requirements. In Figure 43 the numerical solution of the clear flow is shown at different cross-sections of the jet and compared to the experimental result.

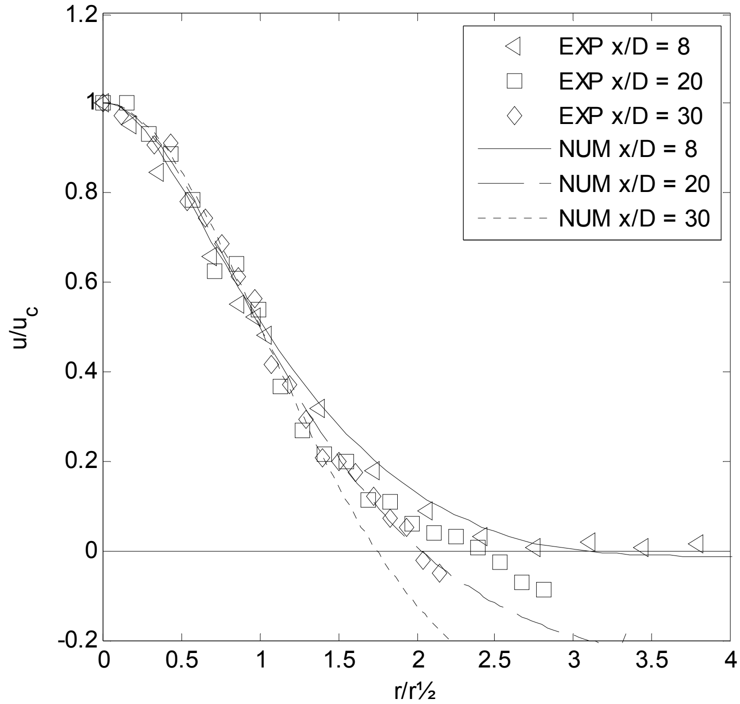

Figure 43: Radial velocity profiles for clear flow.

It can be seen that the numerical prediction is a close match to the experimental prediction near the centerline whereas a higher level of backflow is predicted compared to the measurements close to the wall. This is expected since the geometry simulated encompass a smaller volume compared the experimental setup. The standard *k-ε* model is known to not to predict the correct spreading rate for a free jet. To combat this, the constant $C_{\varepsilon 1}$ in the *k-ε* model has been modified according to the experimental measurement of the spreading of the clear jet. A value of $C_{\varepsilon 1}$= 1.5 has been used instead of the default value of 1.44. This is the same correction which is suggested in Yan et al. (2007).

Figure 44 shows the normalized mean centerline velocity for the jet laden with spheres. It can be seen that the prediction for a clear jet does not match exactly with that which is measured. This is believed to be due to the inability of the *k-ε* model to predict the highly anisotropic flow which is a jet. The particle laden jet has been evaluated by using the default momentum coupling and by applying the new source term. It can be seen that the addition of particles acts to retard the mean axial centerline velocity. Furthermore, it is clear that this effect is greater for the simulation using the new model compared to that which only uses the default momentum coupling. This effect is coupled to the turbulent kinetic energy which acts to increase the mixing and thus reduces the mean axial velocity.

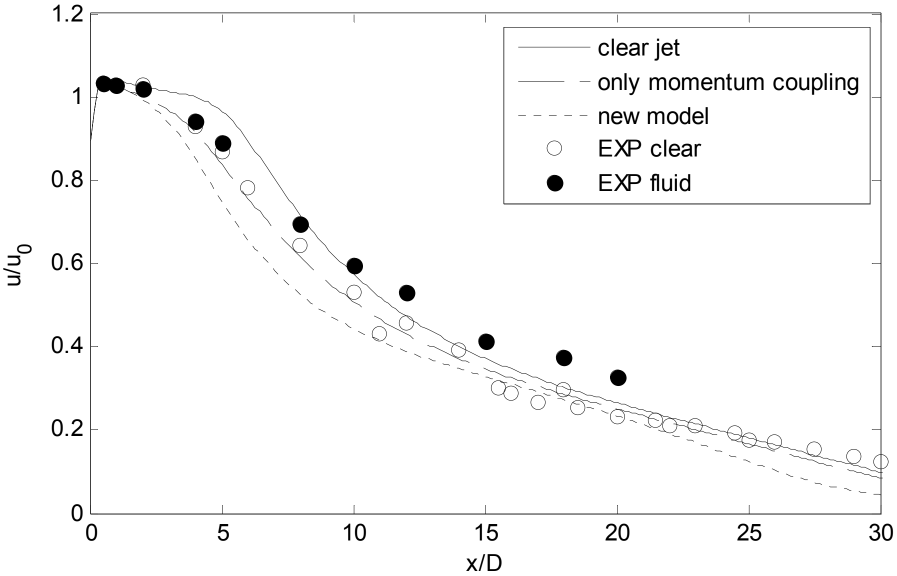

Figure 44: Mean centerline velocity for case A, spheres.

Figure 45 show the normalized fluctuating centerline velocity for the jet laden with spheres. It can be seen that the prediction for the clear jet is significantly below that which is measured. For the addition of particles the initial turbulence intensity has been adjusted according to what is measured. When evaluated on this basis both simulations of the particle laden jet act to increase the turbulence intensity in the first part of the jet. Clearly, the initial large slip velocity causes the source term for the turbulent kinetic energy to produce additional turbulence compared to the simulation using only momentum coupling. At a location downstream both simulations predict a reduction in the fluctuating velocity compared to that of the clear jet. It can be seen that the new model predicts a lower fluctuating velocity compared to both the clear flow and the particle laden flow simulation using only momentum coupling at around x/D=15. At this point the evaluation of the new model results in an overall reduction in turbulence kinetic energy and thus a reduction of the fluctuating velocity. The simulation using the new model seems to predict an abrupt change around x/D=9. This is believed to be caused by the velocity of the particles increasing beyond that of the fluid phase.

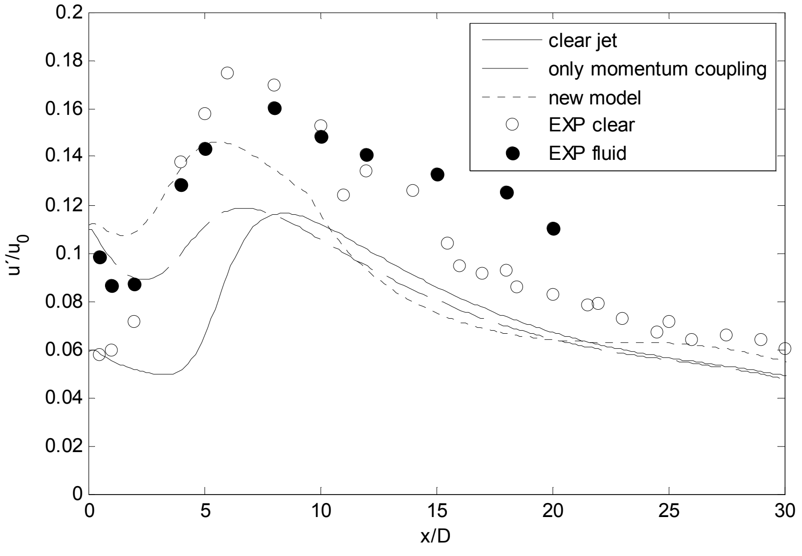

Figure 45: Fluctuating centerline velocity for case A, spheres.

Figure 46 shows the particle concentration at the centerline and at a line parallel to the centerline offset with 5mm. It can be seen that the overall trend of the predicted particle concentration corresponds with that of the experimental investigation. However, it can be seen that the lines in Figure 46 follow somewhat a stairway pattern and that the difference between the two lines is somewhat more than what can be expected at two locations which are very close to each other. This is due to the particles parcels traveling almost parallel with the grid and by the fact that the relative large particles are only little affected by the particle dispersion model. This combination leads to these jumps in concentration as the individual parcels passes from one cell to another.

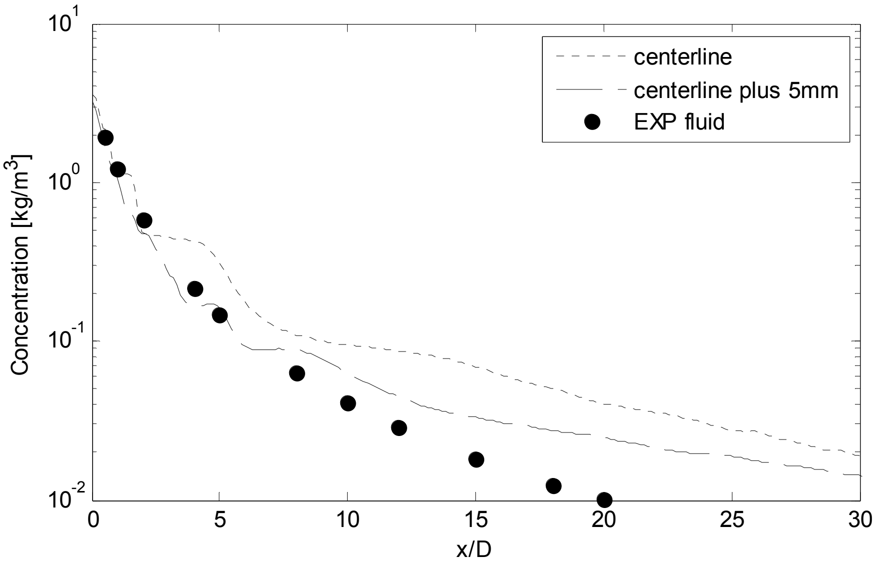

Figure 46: Particle concentration at centerline and offset 5mm for case A, spheres.

Figure 47 shows the normalized mean centerline velocity for the jet laden with prolate spheroids. The similar trends as reported for the spheres also manifest themselves for the case with non-spherical particles. However, the magnitude of the effect is not as great as that of the spheres. This is believed to be due to the greater drag coefficient and lower density associated with the non-spherical particles which act to reduce the slip velocity and thus the magnitude of the turbulence modulation. The particle laden jet has been evaluated using respectively the full model and the simplified model for turbulence modulation which uses the terminal velocity instead of the slip velocity. For the simplified model two different methods for the particle motion have been considered. It can be seen that the result for the two different methods for the particle motion are almost identical whereas the result for the full model predict a significant greater velocity at high x/D. Although, the experimental measurement only extends to x/D=22 it is evident that the full model predicts a similar trend to that observed experimentally. For both, the curves for the clear and particle laden flow crosses approximately at x/D=15.

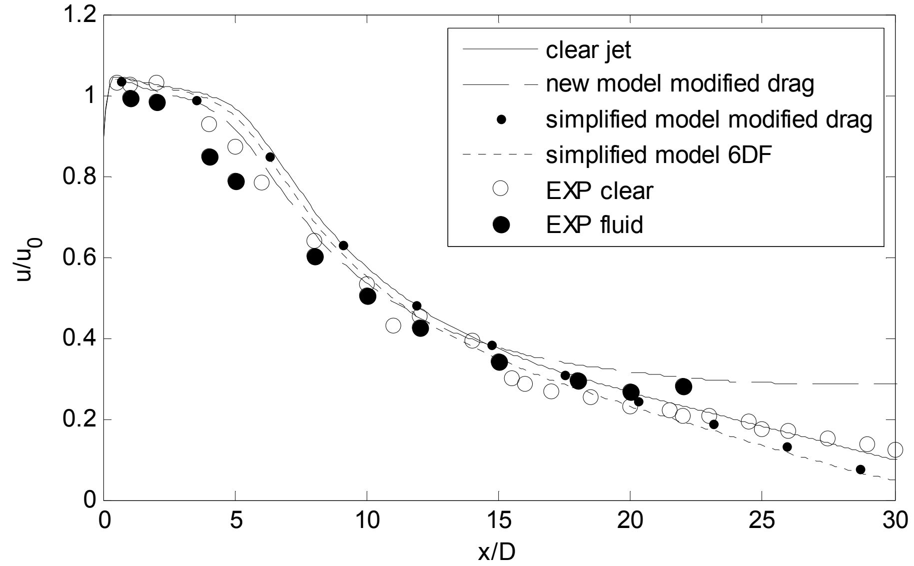

Figure 47: Mean centerline velocity for case B, prolate spheroids.

Figure 48 shows the normalized fluctuating centerline velocity for the jet laden with prolate spheroids. Again it can be seen that the prediction for both the clear and particle laden jet is below that which is measured. Compared to the prediction of the clear jet all simulations of the particle laden jet seem to increase the fluctuating velocity. Again the effect of the full model is greater than that of the simplified model and the prediction using different methods for particle motion are almost identical.

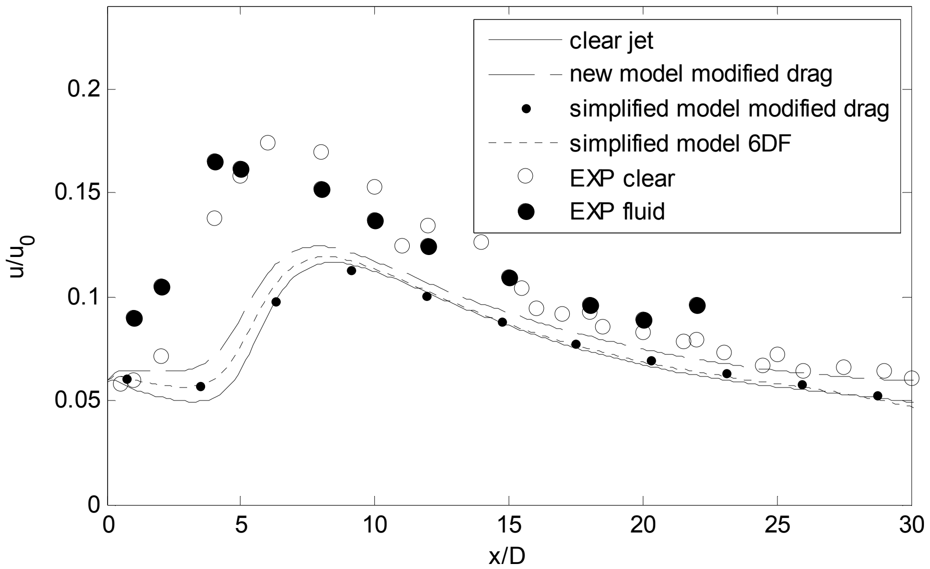

Figure 48: Fluctuating centerline velocity for case B, prolate spheroids.

Summary

A new source term for turbulence modulation has been derived from the conservative equations of fluid flow and compared with existing models as well as existing experimental results. The following conclusions can be drawn:

- Existing models are not able to predict the entire of experimental observations as such the standard approach is only able to predict attenuation whereas the consistent approach only contains mechanisms which enhance the turbulence.
- The new model contains mechanisms for both the suppression and enhancement of turbulence and is able to predict the observed trends.
- The suggested simplification is only able to predict the turbulence modulation in the case when particles are traveling at terminal velocity and the performance for developing flows is poor compared to the full model.
- For the shape investigated the outcome of the different methods for the motion of non-spherical particles was almost identical.

5. Pulverized Straw Combustion

“If history is any guide, oil will eventually be overtaken by less-costly alternatives well before conventional oil reserves run out. Indeed, oil displaced coal despite still vast untapped reserves of coal, and coal displaced wood without denuding our forest lands”

- *Alan Greenspan*

This chapter deals with the simulation of a commercial multifuel low NOx burner which has been installed in the CHP plant Amager unit 1. This burner is designed for firing with pulverized coal but can be used for firing with pulverized solid biomass by changing the burner operational settings. The combustion characteristic of coal and straw is compared by performing a CFD analysis of the combusting flow resulting from a single burner using the burner operational settings specified by the manufacturer for each fuel. The simulation strategies for coal combustion used extensively by the power plant industry have been tested and subsequently modified to deal with the case of straw combustion. Special attention has been focused on the influence of the larger particle size and the non-spherical shape of pulverized straw on different sub-models. The effect of turbulence modulation by non-spherical particles is also included herein. Investigated modeling choices encompass the particle size and shape distribution, the modification of particle motion and heating due to the departure from the spherical ideal, the devolatilization rate of straw, the influence of inlet boundary conditions as well as the effect of particles on the carrier phase turbulence. The commercial code Fluent® 6.3 has been used for all simulations. Procedures for dealing with turbulence modulation have been implemented using User Defined Functions (UDF) as described in the previous chapter. The full set of equations involved in the combustion modeling presented in this chapter is given in appendix H and a brief description of the operating principles of low NOx burners is given in appendix I.

The recent years have seen a development towards finding alternatives to firing with fossil fuels, such as coal, to supply society with energy. Arguments such as global warming, rising sea levels and climate changes have been flashed into the mind of the common citizen from politicians and scientists alike. A more current effect is the rise of international tensions that resort from the concentration of fossil fuel resources in only a few locations. Biomass is the only energy source that can replace fossil fuels directly and is thus regarded as the most important of the so-called renewable energy sources (IEA 2006). However, many additional concerns need to be addressed to complete the transition from coal to solid biomass products. Issues range from availability of biomass fuels, collection and transport to power plants, preparation of fuels, injection of fuels into furnace, proper combustion, corrosion and slagging issues, quality of residual ash, flue gas cleaning and emission control. One major ethical issue which also must be addressed is the utilization of agricultural lands or indigenous forest reserves for production of biomass fuels. At present, focus is on using municipal waste, residual wood and straw and not dedicated energy crops for the electricity generation in Denmark. The energy potential of these biomass resources has been evaluated to constitute approximately 1/3 of the current Danish energy consumption and thus there is still a need for other energy sources. For suspension firing, pulverized straw and wood are used in co-firing with coal to compensate for combustion issues which results from the difference in fuel composition and condition. Suspension firing is general regarded as the most efficient method to convert the chemical energy bound in the fuel into heat and electricity compared to competing technologies such as fluidized bed or vibrating grate firing. Thus, there is an incitement to upgrading existing coal fired CHP plants to co-fire as much solid biomass as possible and to ensure that the combustion is as efficient as possible. This chapter deals very specifically with the development of the modeling technique which is used in evolution of more efficient plants.

In Denmark the suspension fired CHP plant Amager unit 1, scheduled for re-commissioning in 2009, has been refitted for co-firing of estimated 50% on mass basis with pulverized straw and wood. This estimate has later been modified to as much biomass as possible promising even greater use of biomass. The original coal/oil boiler from 1971 has been completely replaced by a new 500 ton/h Benson boiler placed and suspended in the existing boiler house. Biomass is to arrive to the plant in the form of straw and wood pellets. Three roller mills, traditionally used for coal, supply a total of twelve multifuel low NOx burners capable of operating on oil, coal, wood and straw. Maximum load can be achieved using only two mills, when operating on coal, so that one mill can be closed for maintenance. Each mill is only to be operated using a single type of fuel at a time, each of the three fuel supply lines operates with one fuel at a time and each burner is operated on a single type of fuel at a time. Thus, it is ensured that the whole feeding system is optimized depending on the type of fuel used and that different settings can be applied to both mills and burners for each fuel. When operating on a feedstock of biomass fuel air preheating to the mills is significantly lower than that applied when operating on coal, due to the risk of ignition. Similarly, the air supply to the mills, and hence the primary air supply to the burners, are also greater due to risk of backfire. As can be seen in Table 10 the air mass flow distribution for straw is significantly different from that for coal. The greater demand for primary air mass flow for straw combined with the lower oxygen requirements entrails that the ratio between auxiliary and the primary air mass flows are almost unity whereas the same number for coal combustion is five times greater. As we will see later on this greatly alters the near-burner flow pattern and affects the combustion properties.

Table 10: Air mass flow distribution.

	Coal	Straw
A/F - PA	1.9	2.2
A/F - total	9.47	5.24
excess air ratio	1.14	1.10
(SA+TA)/PA	5.0	1.3

The yearly consumption of wood pellets is expected to be 40.000 tons whereas the same number for straw pellets is 110.000 tons (Gjernes 2006). This will substitute around 95.000 tons of coal out of the 250.000 tons of coal which is needed annually for 100% coal firing. To put these numbers into perspective it can be stated that an estimated annual 3.7 mio. ton of surplus straw is available for energy generation in Denmark and of this, about 1/3 is currently used for power generation (Energistyrelsen 2009).

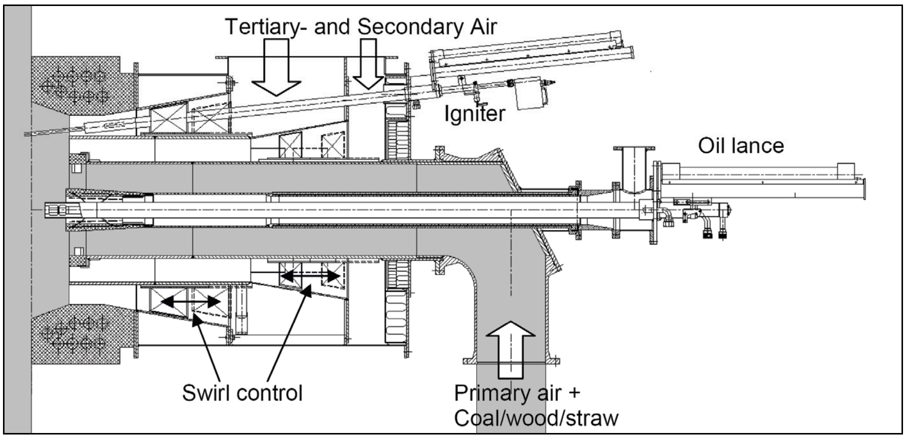

Figure 49: Burner layout, modeled flow domains are shaded, modified from (Gjernes 2006).

The multifuel low NOx burner is shown in Figure 49. The switch between different fuels is achieved by specifying different burner setting for the internal distribution and swirl control. For straw secondary and tertiary air represent around 60% of the air needed for combustion where the same number from coal combustion is 90%. The result is a flame where air is gradually mixed with fuel to allow for both fuel rich zones and oxygen lean zones to limit NOx formation. This is also known as staged combustion and is the primary mean to limit NOx formation in a low NOx burner.

A number of issues arise in the transition from firing with coal to firing with straw. Traditional low NOx burner design are designed and optimized for coal combustion, thus the introduction of straw is foreseen to require addition design considerations for optimal firing. As a first iteration in this process the introduction of the multifuel burner, where the shift from coal to straw is handled solely by changing burner settings for the internal air distribution and the level of swirl (Gjernes 2006). The present work investigates different model choices influence on the combustion characteristics of an industrial multifuel low NOx burner as is to be installed in Amager unit 1. A base case simulation for both coal and straw is shown using the design airflow conditions provided by the burner manufacturer Burmeister & Wain Energy (BWE). Modeling challenges dealt with in the present work, in the context of CFD, can be summarized as follows:

- Particle size and shape distribution
- Devolatilization kinetics
- Inlet boundary conditions
- Particle-turbulence interaction

Fuel characterization

The difference in chemical composition and particle size/shape distribution results in different combustion characteristics for coal and straw. Table 11 shows the composition of straw and coal and highlights some of the critical differences between these fuels. The heating value of straw is significantly lower compared to coal requiring a larger fuel throughput compared to coal firing. This also suggests that less excess air is needed for straw combustion which is reflected in the ratios given in Table 10.

Table 11: Coal and straw composition supplied by the burner manufacturer, BWE

	Coal	Straw
Volatiles	40.0w%	72.0w%
Ash	13.1w%	4.5w%
Moisture	9.0w%	10.0w%
Char	37. 9w%	13.5w%
LHV	24.7MJ/kg	15MJ/kg

Note that ultimate analysis for straw along with properties of reactions and burner settings is given in appendix H. Straw has significantly higher volatile matter content than coal and the fixed carbon-to-volatile matter ratio is much below unity. Additionally, straw also begins to release volatiles at a lower temperature and more rapidly than coal, thus reducing the ignition temperature compared to coal. This also indicates that special care should be given to the design of the air supply to provide sufficient oxygen for the faster release of volatile matter in order not to delay combustion (Yin et al. 2004). However, it should be noted that the larger particle size associated with biomass particles counteracts this tendency due to temperature gradients. The gaseous species formation shows the same complexities as that of coal (Baxter 2005). SOx emissions generally decrease proportional to the sulfur present in the fuel whereas NOx depend on both fuel and firing conditions. However, the NOx precursor formation investigation for straw and coal co-firing by Wu et al. (2007) suggest that biomass predominately forms NH_3 whereas coal predominately forms HCN as gas-phase compounds. In addition, biofuels often have less fuel bound nitrogen which act to reduce NOx emissions, as demonstrated on co-firing tests at Seward station (Battista et al. 2000). However, it should be emphasized that the fuel N contents varies greatly from one type of biomass to another. The composition of solid fuels is often illustrated using a van Krevelen diagram which plots fuels according to their atomic ratios H/C and O/C. Figure 50 shows a van Krevelen diagram for various solid fuels. It can be seen that biomass fuels are associated with significant larger H/C and O/C ratios compared to coal.

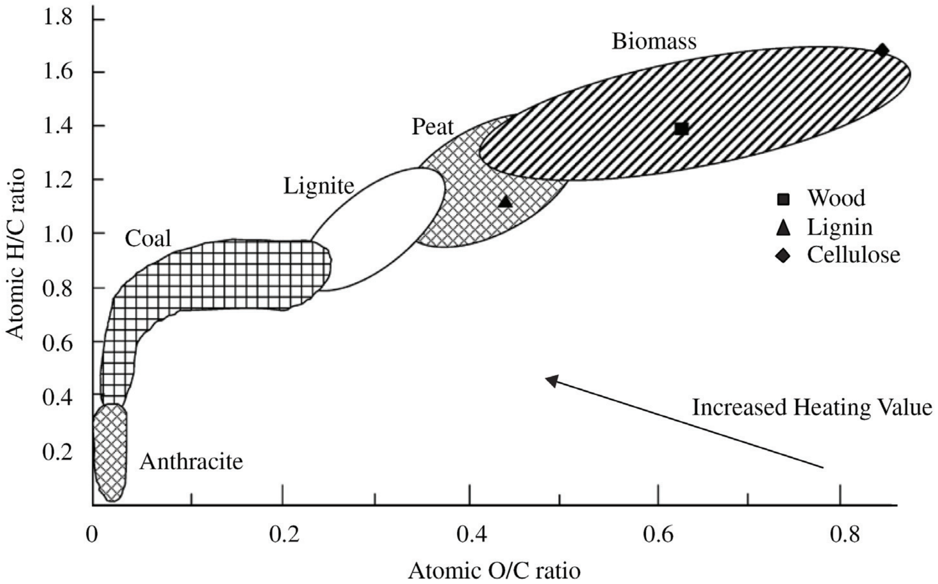

Figure 50: Van Krevelen diagram for various solid fuels (Prins et al. 2007).

The difference between pulverized coal and biomass flames has been shown previously from firing in laboratory scale test furnaces. Ballester et al. (2005) compared the flames of bituminous coal, lignite and wood, for similar operating conditions and found that wood flames display two distinct combustion zone: An intense combustion of volatiles released from small particles close to the burner and a second further downstream which is attributed to devolatilization of larger particles and char burnout. Furthermore, the wood flame is significantly longer and is associated with more unburnt hydrocarbons due to the lower temperatures downstream in the furnace. The study by Damstedt et al. (2007) dealt with 50w% straw and coal co-firing and showed that large particles penetrate the internal recirculation zones and elongates the flame structure by forming a secondary combustion zone downstream of the burner. Lokare et al. (2005) measured the ash deposition rates from different solid biomass fuels and showed that this varies greatly depending on the type of biomass. Bharadwaj et al. (2004) and Lu et al. (2008) looked at the devolatilization of large non-spherical biomass particles and demonstrated the insufficiency of modeling such particles as spheres. Similarly, a number of numerical investigations have also been undertaken. Abbas et al. (1994) undertook a parametric study of the co-firing of sawdust and coal and found an optimum of 30% wood co-firing for minimum NOx emissions and maximum particle burnout. Apparently, the faster devolatilization of wood creates an intense near burner combustion zone which enhanced the coal combustion in the internal recirculation zones. Unfortunately, it seems that a poor choice of model constants for the devolatilization of wood might have corrupted the results. For all circumstances any optimum would be greatly dependent on the size distribution, moisture content and fuel bound nitrogen. Elfasakhany and Bai (2006) looked at the influence of several sub-models for wood combustion. It is found that the flame temperature and major species are less sensitive to the devolatilisation mechanisms while the predictions of unburned hydrocarbons and CO are very dependent of the devolatilisation sub-model. Many additional biomass combustion and co-firing issues are thoroughly covered in the reviews articles by Williams, Pourkashanian and Jones (2001), Nussbaumer (2003), Demirbas (2003) and Cui and Grace (2006).

Particle size and shape distribution

Lignocellulosic biomass has a fibrous structure and is difficult to fracture by applying compression forces unlike coal which is a brittle material. This results in an increase in the energy used for the milling process together with biomass particles which is inherently non-spherical in shape. The shape distribution of resulting biomass particles consists of near-spherical particles, similar to coal, but in addition pulverized biomass also contains particles which can be described as flake-like or rod-like, both with aspect ratios exceeding 10. It is also clear that the energy consumed in the milling process also increases proportionally as the final size of biomass particles decreases. Thus an increased effort to reduce the size of the biomass particles will result in a decrease of the total efficiency of the plant and cannot justify the use of dust firing compared to other combustion technologies. Using a size limit where 95% by weight of the dry matter has to pass through a 1000μm mesh and at least 12% has to pass through a 125μm mesh the electric power requirements is estimated to 150kW/t for dry pine chips or 3% of the heating value of the fuel (Esteban and Carrasco 2006). Similar results were obtained by Mani et al. (2004) which further reveals that comminution power demands to reach a given size increases with moisture content and with fiber strength. Undoubtedly, the specified particle size and shape have a significant influence upon the combustion process. However, existing data is scarce and generally unreliable. Qualitative observations of pulverized wood and straw suggest that particles are highly non-spherical, mainly flake-like and rod-like. The size and shape distribution observed is similarly highly dependent on the combined comminution process of mill and pre-pelleting processes as well as dependent of the type of biomass. As such it is observed that wood particles tend to be more rod-like whereas straw particles tend to be flattened. However, sieve analyses, on which most reported size distributions are based, tend to either over or under predict the size of the particles based on their equivalent volume diameter depending on their shape. Moreover, sieve analysis does not say anything of the enhancement of the surface area of a non-spherical particle compared to a sphere of equivalent volume. No quantitative data regarding the shape of pulverized straw particles exists, whereas, several authors have published data regarding the size distribution of biomass particles. This data has been summarized in Figure 51 and appropriate Rosin-Rammler is specified in Table 12.

Table 12: Rosin-Rammler distribution parameters of biomass particles

	Source	$d_{p,ave}$	Spread
Wood, hammer mill	Esteban and Carrasco (2006)	360μm	1.5
Wood, traditional coal mill	Holm et al. (2006)	900μm	1.5
Wood, laboratory cutter	Holm et al. (2006)	370μm	2.3
Fine straw, laboratory cutter	Damstedt (2007)	160μm	2.0
Medium straw, laboratory cutter	Damstedt (2007)	450μm	2.3
Large straw, laboratory cutter	Damstedt (2007)	590μm	1.9
Straw, shredder	Rosendahl et al. (2007)	l_{ave}≈16000μm	1.4

It can be seen that the size distribution resulting from a laboratory cutter tends to be more narrow compared to that which results from a milling process. Similarly, the size distribution from a traditional coal mill for biomass particles is more narrow compared to that of coal (Spread≈1.2) when evaluated on basis of the Rosin-Rammler spread parameter. There is no doubt that any application of mechanical and aerodynamic filters for biomass particles will act to reduce the spread of the resulting distribution. For the present investigation we also wish to rectify the size distribution for the effect of non-sphericity. This is done by specifying a single sphericity factor to be applied for all particles in a distribution. To approximate a suitable value for the sphericity, in the absence of actual measurements, it is postulated that the Stokes number, for a biomass particle should match that of an equivalent coal particle in order to pass the aerodynamic filter/trap which is endemic in the design of a traditional coal mill.

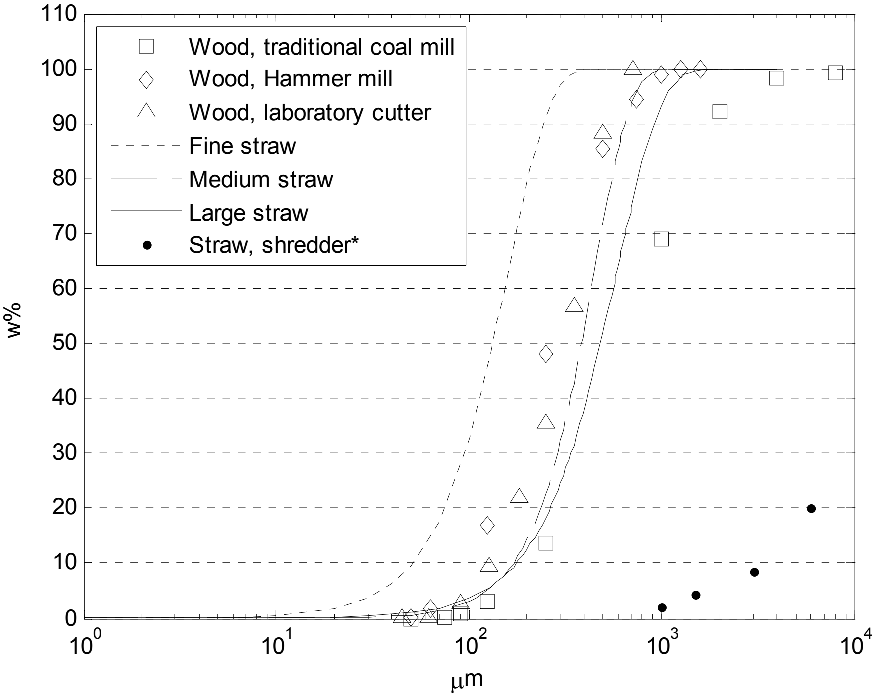

Figure 51: Cumulative size distribution of biomass particles. *size based on length of straws.

Since the Stokes number for non-spherical particle is dependent of both the Reynolds number as well as the sphericity it is possible for a large biomass particle, evaluated on basis of the equivalent diameter, to have similar aerodynamic properties as that of a much smaller coal particle provided that the sphericity is sufficiently low.

Table 13 show the calculated sphericity for three sizes of biomass particles where the air flow is assumed to be the same for the two cases and the particles are assumed to travel at terminal velocity.

Table 13: Calculated sphericity factor and burning enhancement factor if the aerodynamic properties are to be similar to a 60 μm coal particle.

d_p	ψ	Θ
200μm	0.34	2.4
300μm	0.12	5.7
600μm	0.03	23

Based on the sphericity factor, ψ, the burning enhancement factor compared to a sphere with the same diameter, Θ, can be calculated as (Yin et al. 2004):

$$\Theta = \frac{0.3\psi + 0.7}{\psi} \tag{82}$$

The burning enhancement factor was developed by Gera et al. (2002) who found that the increase in surface area of a cylindrical switchgrass particle was larger then the increase in the overall burning rate. Thus, the burning enhancement factor can be seen as an estimate on the efficiency of the increase in surface area to promote combustion for an arbitrary shaped particle. To get a better feeling of these numbers a sphericity factor of 0.34 corresponds to a disk with an aspect ratio of 1/20, i.e. a bulky disk, whereas a sphericity factor of 0.03 corresponds to disk with an aspect ratio of 1/800, i.e. a very flat disk. It should be noted that the expression by Yin (2004) is a fit of the more complex expression found in Gera et al. (2002).

For the present investigation, three different biomass particle distributions are considered; all based on a modification of "Large straw, laboratory cutter" from Table 12. It is assumed that this distribution consists of disks with a specific aspect ratio and where the diameter of the disk is what is reflected by the sieve analysis. Depending on the aspect ratio assumed, a measure of the average volume equivalent diameter is found. The spread is similarly set to 1.5 to reflect the wider particle distribution resulting from the milling process. Table 14 gives an overview of the particle distribution parameters used in this work.

Table 14: Particle parameters

	Assumed aspect ratio	**$d_{p,ave}$**	**Sphericity**
Large	1/5	500μm	0.64
Medium	1/25	300μm	0.28
Small	1/75	200μm	0.14
Coal	-	60μm	1

Devolatilization kinetics

A sensible prediction of the rate of the release of volatile matter is necessary for the success of any simulation. Where the size and shape of a particle for a given set of physical properties is determining for the rate of heating of the particle, the devolatilisation rate determines the release of volatile matter for a specific particle temperature. Determination of the devolatilization rate is typically carried out by means of thermo-gravimetric analysis. Small samples of biomass are ground so fine that that size dependence is not a factor which is to be considered and heated up with different temperature slopes. Extensive work has been done previously by several authors towards determining the devolatilization kinetics of biomass. The present investigation is limited to selected works all using single rate expressions. The kinetic rate, *k*, is defined by an Arrhenius type expression:

$$k = Ae^{-E/RT} \tag{83}$$

where A is the pre-exponential factor, E is the activation energy, R is the universal gas constant and T is the temperature. Model constants found in different investigations are shown in Table 15.

Table 15: Single rate devolatilization constants

	A [1/s]	E [J/kmol]
Zhou et al. 2005 (Danish straw)	1.56E+10	13.8E-07
Lanzetta and Di Blasi 1998 (corn stalks)	6.30 E+06	9.15E-07
Lanzetta and Di Blasi 1998 (Straw)	2.43 E+04	6.46E-07
Yang et al. 2005 (Biomass)	7.00 E+04	8.30E-07
Fluent default (wood)	3.82 E+05	7.40E-07

Figure 52 outlines the devolatilization rate dependence on temperature for the different investigation given in Table 15.

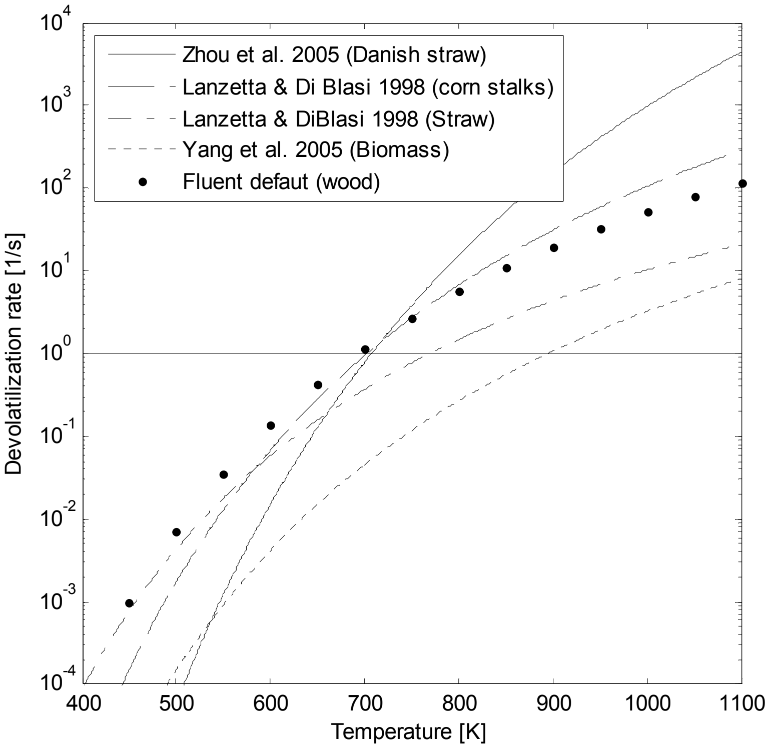

Figure 52: Biomass devolatilization rates.

It is clear from Table 15 and Figure 52 that there is an apparent difference in the rate expressions. This result can both represent a difference in the kinetics of the different samples but also be due to measurement accuracy and difference in methodology. Clearly, the composition and the devolatilization rate of straw and other biomass fuels are dependent regional and seasonal differences. Thus, it is prudent to include an evaluation of devolatilization kinetics in the sensitivity analysis of a given simulation. For the present work the rate expressions for straw by Zhou et al. (2005) and Lanzetta and Di Blasi (1998) are evaluated. For additional information on biomass kinetics the reader is referred to the recent review paper by Di Blasi (2008).

Model implementation

Current models used to predict the motion of pulverized coal particles rely on a spherical assumption, which may deviate significantly from reality for the case of bio-dust. Qualitative observations suggest that pulverized straw particles are highly non-spherical (flake-like, rod-like), greatly enhancing the surface area, compared to a sphere, which represents the minimum in terms of surface-to-volume ratio. Clearly this affects the motion, heating and surface reactions of a biomass particle and appropriate modeling choices have to be taken to improve the design for co-firing of biomass in utility boilers. Some attempts to model pulverized biomass particles have been demonstrated previously. Gera et al. (2002) compared spherical particles with no internal conduction with that of cylindrical particles with internal gradients of same equivalent diameter and found that there is a significant difference in the burnout statistics for particles larger than 1 mm. Similarly, Rosendahl (2000) and later Yin et al. (2004) developed a 6 degree-of-freedom model for cylindrical particle motion and found that the trajectories differ significantly from those of perfect spheres of the same equivalent diameter. This model involves the formulation of orientation dependant lift forces, due to the non-sphericity of the particle. Additionally, Elfasakhany et al. (2008) developed an expression for the force acting on combusting particles due to the anisotropic release of volatiles. Thus these forces act to describe the trans-lateral motion of biomass particles. Backreedy et al. (2005) and Ma et al. (2007) used a modified expression for the drag coefficient as a function of the sphericity but did not incorporate the modified surface area into the combustion model. This demonstrates the proficiency of a simplified model for particle motion to simulate combustion processes where non-spherical particles are involved. For the present work straw particles, traveling at terminal velocity, have a Reynolds number around unity based on the equivalent diameter. The flow around particles in this range is influenced by inertial forces which stabilizes the motion of the non-spherical particles, and makes them orientate themselves with maximum cross-section normal to the flow (Clift, Grace and Webber 1978; Field et al. 1997; Sørensen 2005). Thus, there is no secondary particle motion induced by the flow field and only for wall bounded flows is it justified to resolve the rotational motion of the particles. The influence of turbulence tends to cause particles to wobble (Klett 1995). In the terms of a traditional random walk model turbulence is modeled by adding an additional random velocity component to the mean velocity to emulate the effect of turbulence. If it is assumed, that the particle rotational response time is sufficiently low compared to the characteristic time of turbulence, it would sufficient to assume that the particle is always aligned with the flow and the motion of the particle can be solved using only a modified drag coefficient along with a traditional random walk model for turbulent dispersion to model any additional effect of secondary motion due to the non-sphericity of straw particles. If the rotational response time is large compared for the characteristic time of turbulence a more advance particle model, possible a 6 degree of freedom model, would be required to model the turbulence particle interaction correctly. The present investigation imagines straw particle as being a disk in the lack of more precise information regarding the multiphase flow. At present time no model exists to model the motion of a disk or a random flat shape. Similarly, it is not given that a 6 degree of freedom model for a disk would give a satisfying representation of a random shaped particle. Possibly for such a model to function satisfactory it would most likely be necessary to calibrate the model constants to take the shape effects into account. This is considered to be out of the range of the present work. Thus, for the simulations presented in this section a traditional random walk model, as described in appendix D, is used to model the particle dispersion. Similar, arguments can be stated concerning the internal heat transfer. For the large straw particle with d_p= 500μm traveling at terminal velocity the Biot number can be calculated to around 0.1 which would justify the assumption of lumped particles. In this calculation the shape of the particle is only considered indirectly by considering the increase in the surface area compared to a sphere. Indeed, the enhanced surface area of a non-spherical particle compared to a sphere seems to be a key factor to model the additional heat transfer. A revisit to Newton's law of cooling and the Stefan-Boltzmann's law reveals that the surface area is the only parameter it is necessary to modify. The convective heat transfer coefficient can be calculated with sufficient accuracy using correlations of the Nusselt number developed for equivalent volume spheres if based on the characteristic dimension of the non-spherical particle (Clift, Grace and Weber 1978). However, since the exact dimensions of an individual arbitrary shaped particle are unknown it is clear that the rate of heat transfer can only be predicted with a low accuracy.

The philosophy behind the model selection of this paper is that they are relevant in for the prediction of the flow in industrial boilers. Key factors are to limit the computational intensity, focus on stability of model and tweak existing standard models rather than implement advanced sub-models. Similarly, it can be argued that the total accuracy of a given simulation is not greater then the accuracy of the worst submodel or assumption. Thus model choices implemented should be of the same general accuracy.

General numerical procedure

The applied standard modeling approaches are only discussed very briefly here. For additional information of general CFD methodology and submodels the reader is referred to dedicated literature on this subject such as Versteeg and Malalasekera (2007). The CFD simulations presented in the present paper have been accomplished using the commercial CFD code Fluent 6.3. Details about this code can be found in the Fluent User Guide (Fluent 2006). The grid, with highlighted details, used in this work is shown in Figure 53. It consists of 680.000 cells; a mixture of hexagonal and polygonal cells. This represents a single burner attached to a cylindrical furnace. Additionally a funnel shaped outlet volume is attached to the furnace volume to avoid backflow in the simulations and move the influence of the outlet boundary condition away from the furnace. 10 diameters of the fuel pipe leading up to the burner are simulated to get fully developed conditions at the entrance to the burner. The dimensions of the furnace are 8m in diameter and 11m in length. The funnel shaped outlet volume adds an addition 13m. The length of just the burner is approximately 2.5m.

Boundary conditions

The secondary and tertiary air inlets are located at the entrance to the burner and the flow in the SA and TA sections of the burner is thus not modeled. Figure 49 shows an outline of the burner modeling methodology. The swirl blades are adjustable and the exact location of these, for straw operation, is not known beforehand. Instead swirl angle of respectively 50 and 60 degrees for the SA and TA inlets are specified. Clearly the combustion in the near burner zone of the burner is very dependent upon the level of swirl and further measurements or simulations are necessary to determine the exact level of swirl. This would be the object of a future investigation but is out of scope of the present work. Instead, attention has been focused on determining the flow field and particle concentration at the inlet plane of the burner.

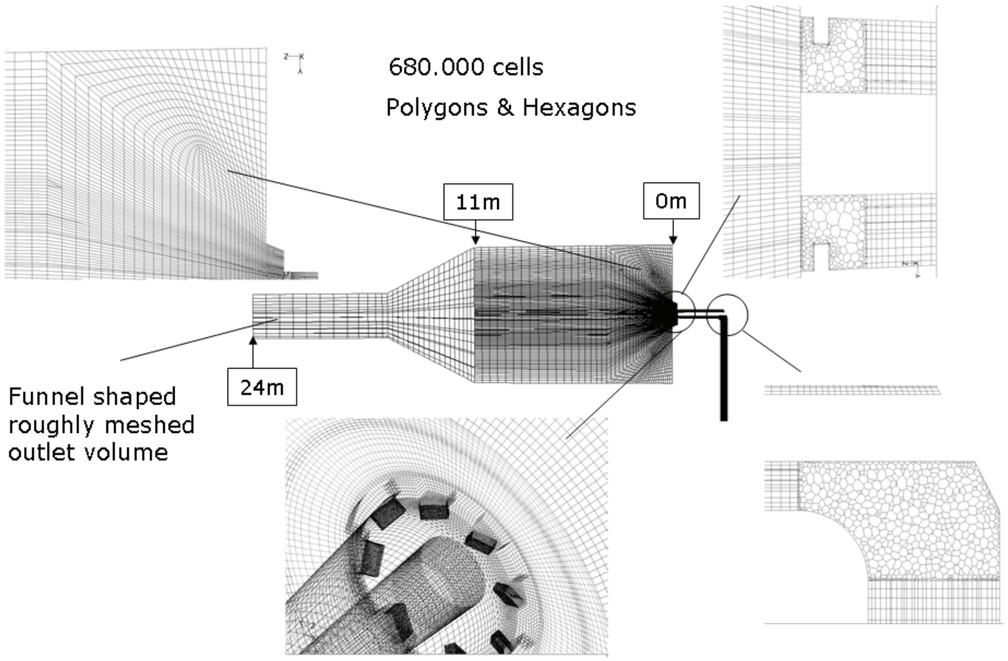

Figure 53: Mesh for the CFD simulations

Current simulation methodology most often specifies uniform velocity and concentration distribution at the inlet plane, however, the burner geometry includes a 90 degree bend upstream, which is known to induce a maldistributed concentration profile known as roping. Consequently, it is not possible to utilize a 2D axisymmetric geometry and it is necessary to resort to full 3D simulation in order to capture the influence of the upstream geometry. PA, SA and TA flow inlets are specified as mass flow inlets using the specification supplied by the manufactor and all outer flow constraints are specified as no slip walls. Particles are injected at the PA inlet by specifying the same velocity as the air.

Turbulence modeling

Turbulence has been simulated using the standard k-ε model with standard wall functions for a first node located at y^{+}~30 to 60. The standard k-ε model is generally considered inaccurate and especially for swirling flows a number of 2-equation models have been suggested for improved results. However, the standard k-ε model remains an industrial workhorse and its well documented ability, or lack of, to simulate turbulence has been preferred over more recent closures such as the SST k-ω model. A more realistic description of turbulence can only be achieved using more sophisticated closure strategies such as LES or DNS but the computational demands for the present geometry clearly excludes this possibility. The standard particle dispersion model provided by Fluent has been used to model the influence of turbulence on the particle-trajectories. This is referred to as a random walk model where the fluctuating velocity, due to turbulence, is based on the continuous phase turbulent kinetic energy and a Gaussian random function. The influence of particles on the gas-phase momentum is simulated using the PSI-Cell model (Crowe et al. 1977) which has been implemented into Fluent as standard.

Turbulence modulation

The effect of particles on the carrier phase momentum equation is well known whereas the effect of particles on the turbulence equations is often neglected due to the inability of so-called turbulence modulation models to accurately predict the values observed from experimental investigations. However, it is widely accepted that large particles tend to augment turbulence whereas smaller particles tend to attenuate turbulence. Biomass particles are significantly greater than coal particles, thus it is of prime interest to determine if the modification of turbulence acts to increase or decrease the efficiency of combustion, which is coupled to the level of turbulence. Firing with coal particles, which are considered small, leads to the conclusion that they only act to decrease the carrier phase turbulence. For the present work the model described in Mandø et al. (2009) is used to evaluate the effect of particles on the carrier phase turbulence. This expression is based on a theoretical derivation and is able, at least qualitatively, to predict the observed effects of turbulence modulation. Note that this modification is only implemented for a single case and not for all tested cases. The source term for the k-equation is stated as:

$$S_{kp} = \frac{\alpha\rho_p}{\tau_p}\left(\left|\bar{u}_i - \bar{u}_{pi}\right|^2 + \overline{u'_{pi}u'_{pi}} - 2k\right) \tag{84}$$

where α is the volume fraction, ρ_p is the particle density and τ_p is the particle response time. Mean velocities are indicated with a bar and fluctuating components with a prime. The combination $\alpha\rho_p$ is the particle mass concentration, which is calculated default by the solver. In order to speed up the calculation procedure and stability of the solver, the terminal particle velocity is used in place of the slip velocity and the term involving the particle fluctuating velocity is neglected. For most parts of the flow the assumption of terminal velocity is valid. However, it is well known that this assumption is not valid close to walls and in zones with large acceleration or deceleration of the fluid/ particles. The source term is incorporated into Fluent and coupled to the gas phase equations via user-defined functions (UDF).

Particle motion

The particle equation of motion is solved for each trajectory. A total of 100.000 particle trajectories are simulated for good statistics and the particle size distribution has been resolved by specifying a total of 180 particle diameters for the Rosin-Rammler specification method. The particle equation of motion is specified as:

$$\rho_p \frac{du_p}{dt} = \frac{18\mu}{d_p^2}\frac{C_D \operatorname{Re}_p}{24}\left(u_i - u_{pi}\right) + g_i\left(\rho - \rho_p\right) + F_{Saffman} \tag{85}$$

where g_i is the gravitational acceleration and $F_{Saffman}$ is the Saffman lift force. This formulation neglects some terms compared to the BBO/MR-equation and only the steady state drag, the buoyancy and the Saffman lift force is considered. Using the usual order-of-magnitude considerations, as those that can be found in Lazaro and Lasheras (1989), it is acceptable to neglect additional terms for a small and heavy particle such as a typical coal particle. Computation of order-of-magnitude estimates for a spherical straw particles show an increase of importance for the additional terms due to the lower density and larger size. However, the effect of non-sphericity has not been considered. As shown previously this acts to increase the drag coefficient compared to an equivalent volume sphere. Furthermore, it is not possible to derive the Basset history force for an arbitrary shape as this depends on the development of the boundary layer which is coupled to the shape of the particle. To include the effect of non-sphericity the steady state drag coefficient is modified using the expression by Haider and Levenspiel (1989):

$$\begin{aligned}
C_D &= \frac{24}{\operatorname{Re}_p}\left(1 + b_1 \operatorname{Re}_p^{b_2}\right) + \frac{b_3 \operatorname{Re}_p}{b_4 + \operatorname{Re}_p} \\
b_1 &= \exp\left(2.3288 - 6.4581\psi + 2.4486\psi^2\right) \\
b_2 &= 0.0964 + 0.5565\psi \\
b_3 &= \exp\left(4.905 - 13.8944\psi + 18.4222\psi^2 - 10.2599\psi^3\right) \\
b_4 &= \exp\left(1.4681 - 12.2584\psi + 20.7322\psi^2 - 15.8855\psi^3\right)
\end{aligned} \tag{86}$$

where the Reynolds number Re_p is based on the diameter of a volume equivalent sphere. This is the default expression which is implemented into Fluent to correct for non-sphericity. Several other correction methods exists and the accuracy of these have been compared by Chhabra et al. (1999) against a large databank of different shapes. This investigation shows that expressions developed to deal with a multitude of shapes using only a single shape parameter are associated with average errors between 16-43% and maximum errors up to 276%. The expression in equation (86) is found to perform among the best of the evaluated methods with an average and maximum error of respectively 22% and 276% and is thus retained. In view of the large errors in the used expression for the steady state drag, the uncertainty in the actual shape of particles as well as the known issued of the methodology to model the turbulence, it seems acceptable to neglect addition terms in the equation of motion.

The Saffman lift force becomes important in presence of the strong shear fields in the combustion zones of a low NOx burner to model the additional translateral motion. The applicability of the known analytical expressions of the lift force is still restricted to laminar flow, concurrent motion of particle and fluid, linear shear and very small Reynolds numbers (Li and Ahmadi 1992; Michaelides 1997). Furthermore, the effects of non-sphericity and rotational motion, Magnus force, may impose additional lift forces much larger then that inflicted by shear. Clearly, the use of large arbitrary shaped particles does not make the used assumptions more valid compared to the case of a small near-spherical coal particle. For the present investigation these additional effects are not modeled. It should be mentioned that an inclusion of such effects would possible require the use of a 6 degree of freedom model together with knowledge of the geometry and the dependence of forces for different angles of attack. Truly the challenges are stacking up for the quest of a complete description of the motion of a large arbitrarily shaped particle! Additional forces resulting for the rotation and orientation of the non-spherical particle may be included by a modification/calibration of the dispersion model due to the seemingly random nature of these forces. However, this is out of the scope of the present investigation.

Wall collisions

Two different approaches towards the modeling of wall collisions have been investigated in the present work. Firstly the default approach by Fluent, assuming perfect elastic collisions, is tested. Secondly, a modified expression is used to test the influence of inelastic collisions, rough walls and eccentric collisions.

The Fluent GUI allows the possibility to modify the normal and tangential coefficient of restitution as a function of the impact angle. By default both coefficients are set to unity and the particle retains all normal and tangential momentum. The physics behind wall collisions under ideal conditions have been explored by Kharaz et al. (2001). For the collision between a smooth surface and a hard sphere the normal coefficient of restitution is constant at a value of 0.98 for all impact angles whereas the tangential coefficient of restitution reaches a minimum value 0.6 at a impact angle of 70 degrees where an impact angle of zero imply a glancing collision. The initial kinetic energy of the particle loss in the collision is converted to rotational energy, to heat via frictional sliding and dissipative wave propagation.

Collisions involving rough surfaces have been thoroughly investigated by Prof. Sommerfeld and associates during the past couple of decades (Sommerfeld 1992; Sommerfeld and Huber 1999; Sommerfeld 2003; Sommerfeld and Kussin 2003; Sommerfeld and Kussin 2004; Lain and Sommerfeld 2008). Observations show, that the impact on rough surfaces tends to randomize the rebound depending on the relative size of the roughness and particle involved. Especially, it is possible to gain a large increase in the normal coefficient of restitution for small impact angles. As an alternative to fully resolve the wall roughness, as demonstrated by Frank (1993), intricate collisions models, involving randomizing factors, have been proposed to model the impact of spheres. Similar to the effect of rough walls, it seems prudent to assume that the collision of an arbitrary shaped particle with a surface, smooth or rough, will exhibit random rebound and the possibility of large normal coefficients of restitution. For the present work we have focused on implementing a simple model which merely indicates the influence of wall collisions on combustion properties rather then using an advanced model which applicability will be limited since there is no information available about the influence of arbitrary particle shape on the collision characteristics. The idea behind the modification is to use the adjustment possibilities given by the Fluent GUI to model a worst case scenario for the fate of each collision between an arbitrary shape particle and rough wall thus circumventing implementing a complex particle collision model. The normal and tangential restitution coefficient is modified so that the rebound angle is a constant 80 degrees, mimicking an adverse rebound for every collision. The overall coefficient of restitution is set to 0.9 to illustrate the kinetic energy loss to friction, rotation and dissipation by wave propagation. Figure 54 shows the calculated coefficients of restitution for this scenario. It can be seen that the normal coefficient of restitution is very large at small angles according to the restrictions posed. Both coefficients of restitution approach the limit of 0.9 for an impact angle of 80 degrees. This value has been retained for collisions with an impact angle between 80 and 90 degrees.

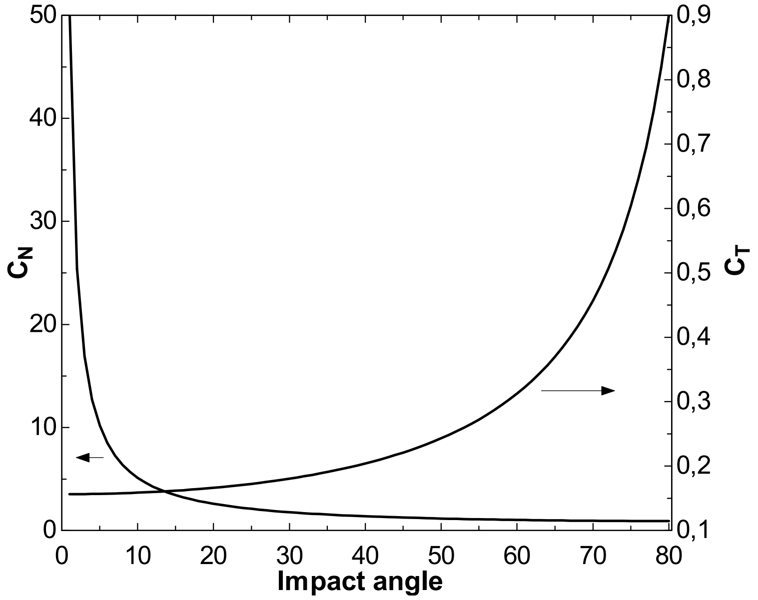

Figure 54: Coefficients of restitution.

Heating of non-spherical particles

The heat balance, without mass transfer, for a particle can be stated as:

$$m_p C_p \frac{dT_p}{dt} = hA_p\left(T_\infty - T_p\right) + \varepsilon_p A_p \sigma\left(\theta_R^4 - T_p^4\right) \tag{87}$$

where m_p is the particle mass, C_p the particle heat capacity coefficient, T_p particle temperature, h convective heat transfer, A_p particle surface area, T_∞ local fluid temperature at particle position, ε particle emissivity, σ Stefan–Boltzmann constant and θ_R is the radiation temperature. The effect of non-sphericity has only been implemented by enhancement of the particle surface area compared to that of a volume equivalent sphere with same diameter. Thus the convective heat transfer coefficient is based on correlations developed for spheres. Similarly it may be stated that the Stefan-Boltzmann's law is only strictly valid for a sphere. Ideally efficiency factors, similar to the previously mentioned burning enhancement factor, Θ, should be develop to relate the efficiency of convective and radiate heat transfer to the sphericity factor.

For the devolatilization and char combustion the standard models in Fluent have been used. The single-rate kinetic devolatilization model is used to predict the volatile yield rate and the diffusion-limited surface reaction rate model is used to predict the char burnout of the particle.

Gas-phase reactions

For the description of the gas composition inside the furnace the species transport approach in Fluent has been used. For this purpose 6 species have been defined: H_2O, CO, CO_2, CH_xO_y, O_2, N_2. All regions inside the furnace can be described by a mixture of these species with varying composition. These species participate in 2 homogeneous gas reactions that are assumed to describe the combustion process sufficiently:

$$\begin{aligned} &CHxOy + 0.54O_2 \rightarrow CO + 1.12H_2O \\ &CO + 0.5O_2 \rightarrow CO_2 \end{aligned} \qquad (88)$$

where the coefficients x and y are 2.25 and 1.05 respectively. The default reactions and the associated Arrhenius parameters for the description of the reaction kinetics provided by Fluent have been used. The reaction scheme has been kept as simple as possible to enhance the numerical stability and the convergence behavior. For the description of the interaction of turbulence and chemistry the Finite rate/Eddy dissipation model has been used. For the description of the radiative heat transfer in the homogeneous gas phase the so-called Discrete Ordinates model with 4 theta and phi divisions is used. The absorption characteristics of the different species in the gas phase have been implemented using the Weighted Sum of Gray Gases Model (WSGGM). For more on the numerical approach, the specific schemes and models the reader is referred to the Fluent documentation (Fluent 2006).

Results and discussion

The purpose of the present work is twofold: Firstly it is intended to give a comparison between coal and straw combustion using actual firing parameters as intended for the CHP plant Amager unit 1. Secondly it is intended to give an analysis of different modeling choices influence on the simulated parameters of the straw combustion case. To do this a single simulation for straw is selected as base case to evaluate the difference between straw and coal. The different model choices for straw combustion are evaluate by changing one parameter at a time compared to the base case. The base case for straw combustion are based on the single rate devolatilization kinetics suggested by Zhou et al. (2005), the medium size and shape distribution described in Table 14, the Fluent default wall collision model for perfect elastic collisions and no additional turbulence modulation model. The sensitivity analysis for straw simulation encompasses the following cases:

- Large particle size distribution
- Small particles size distribution
- Lanzetta and Di Blasi (1998) devolatilization kinetics
- Modified wall collision model
- Uniform particle mass flux at inlet plane
- With turbulence modulation model

Coal versus straw combustion

Figure 55 through Figure 58 show the result of the CFD simulation of a multifuel low NOx burner using coal and straw as fuel respectively. First of all it is necessary to remark that the simulation is not performed on an axis-symmetric grid which for the straw combustion case especially has resulted in a slightly misalignment of the flame compared to the center axis of the furnace. Furthermore, the effect of gravity tends to defect the flame slightly towards the bottom of the furnace. Moreover, the inclusion of the entire inlet pipe entails that the velocity and particle distribution in the inlet plane to the furnace is not uniform which again greatly influences the characteristics of the flame. This maldistribution is mainly up-down and only to a smaller degree left-right. This maldistribution is greatly influenced by the wall-collision model which is treated later in this dissertation. Considering the restrictions mentioned above the results are shown on the horizontal half plane which is assumed to be representative for the entire flame. Figure 55 shows the temperature distribution inside the furnace. It can be seen that the straw flame is significantly longer than the coal flame. Similarly, the coal flame is wider near the burner and it is attached to the flame holder whereas the straw flame seems to first ignite a bit downstream of the flame holder. Figure 57 show a plot of the axial velocity. It can be seen that the straw flame is associated with a significantly smaller recirculation zone compared to the coal flame. Similarly for the straw combustion case, the jet like structure resulting from the primary air flow has a larger penetration than the coal case. These features are a direct consequence of the airflow distribution between the PA, SA and TA which again is a consequence of considerations regarding flammability, fuel entrainment, oxygen requirements etc. For the present case this gives rise to an air mass flow rate which is twice that used for the coal case for the PA. Similarly the TA air mass flow rate for the coal case is two times larger than the straw case. The larger penetration here experienced for biomass fuels is also consistent with that observed at laboratory flow reactors (Ballester et al. 2005; Damstedt et al. 2007).

Figure 56 shows the volume fraction of the volatile matter. It can be seen that the coal devolatilization process is complete after about 4.5m whereas for straw combustion the devolatilization process continue up to 9m; twice that of the coal case. Figure 58 shows the contours of O_2 volume fraction. It can be seen that the low oxygen zone extends far downstream.

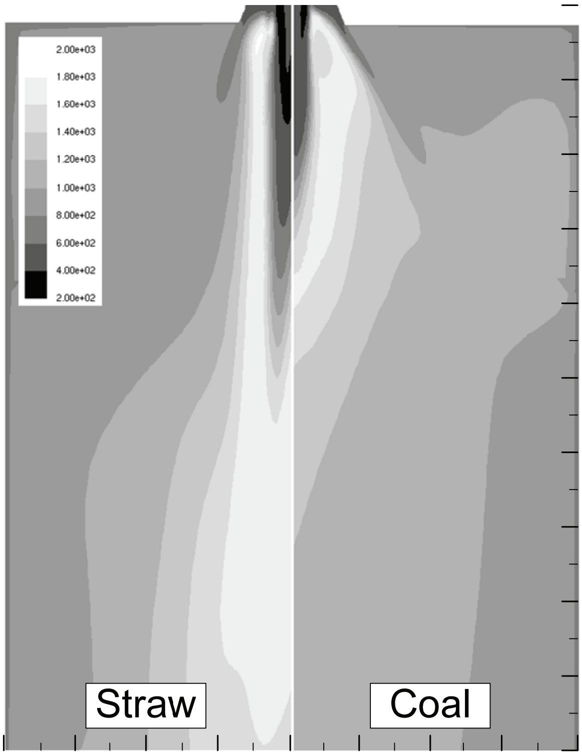

Figure 55: Contours of temperature [K] on horizontal half plane. Grid: 4x10m

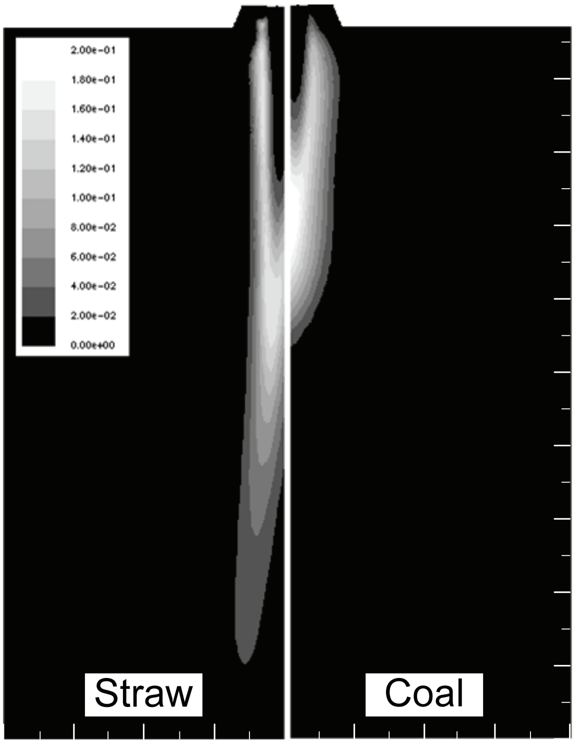

Figure 56: Contours of CH_xO_y volume fraction on horizontal half plane. Grid: 4x10m

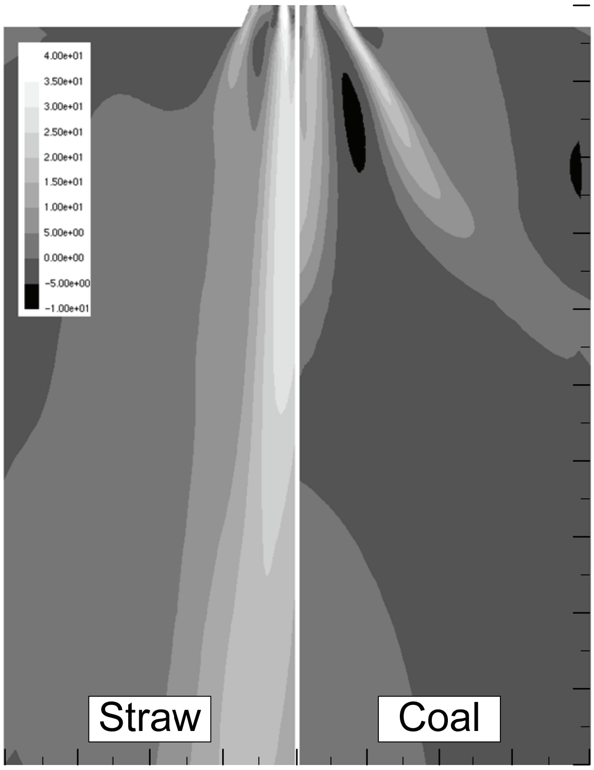

Figure 57: Contours of axial velocity [m/s] on horizontal half plane. Grid: 4x10m

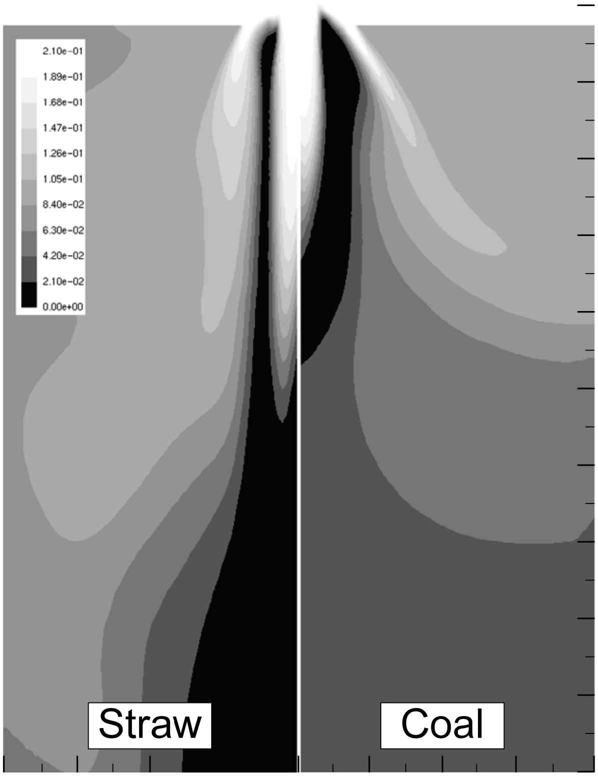

Figure 58: Contours of O_2 volume fraction on horizontal half plane. Grid: 4x10m.

Influence of particle size

Three different particle size and shape distributions were considered for the present investigation where the medium case ($d_{p,ave}$=300μm, ψ=0.28), used for the base case, was considered as the most realistic. The medium distribution was thus in accordance with the criteria by Esteban and Carrasco (2006) for acceptable power demand in the comminution processes to obtain a specific size distribution. The large ($d_{p,ave}$=500μm, ψ=0.64) and small ($d_{p,ave}$ =200μm, ψ=0.14) size distributions cases have been chosen to clearly show the impact of the particle size and shape. The simulation involving the small case shows only little or no difference compared to the medium case, whereas the large case only ignites far downstream in the boiler and the flame is blown off the burner. The unburnt char fraction present in the particles at the outlet decreases slightly for the small case and significantly increases for the large case. The main characteristic seems to be that the fraction of particles entrained by the recirculation zone for the large distribution is too small to allow for a sustained flame near the burner. The larger Stokes numbers associated with the large distribution entail that most particles are carried downstream in the cold central jet like structure and are only slowly heated. Considering the power demands for the comminution process and the combustion efficiency there seems to be an optimum when the particle size distribution is just small enough to allow for a sustained flame attached to the flame holder. Additional grinding to obtain smaller particle sizes will be unnecessary since the combustion properties does not change significant for a smaller size distribution. This result consequently also underlines the importance to maintain a constant size and shape distribution from the mill.

Influence of wall collision model

The often used assumption of a uniform particle and velocity distribution at the inlet to the burner is evaluated by considering the entire course of the internal burner geometry. However, this flow involves particle walls collisions which mechanisms are highly dependent on the wall roughness and particle parameters. Two wall collisions models have been considered and the result is compared with a simulation where particles are released 0.2 m before the inlet to the burner. This corresponds to a traditional simulation where the influence of the burner geometry is not considered *i.e.* the case of uniform particle distribution at the inlet plane. Figure 59 and Figure 60 show some sample particle trajectories inside the burner using the two different wall collision models tested in the present investigation. Particles of different diameters have been released from a common point on the inlet plane to the simulated flow field close to the pipe wall. It can be seen that there is a significant difference between the two approaches. For the default approach in Fluent, which assumes perfect elastic collision and a smooth wall, particle trajectories are reflected in their encounter with the wall while the modified wall collision model imposes a strong enhancement of the particle velocity component normal to the wall.

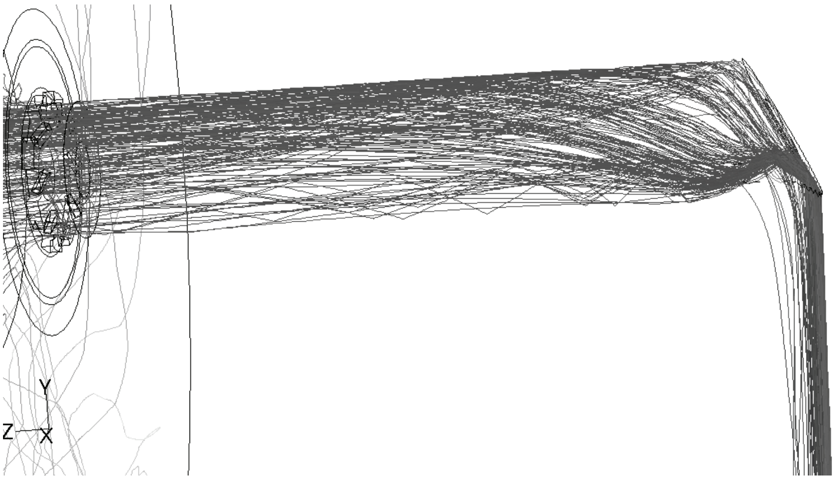

Figure 59: Sample trajectories for standard wall collisions.

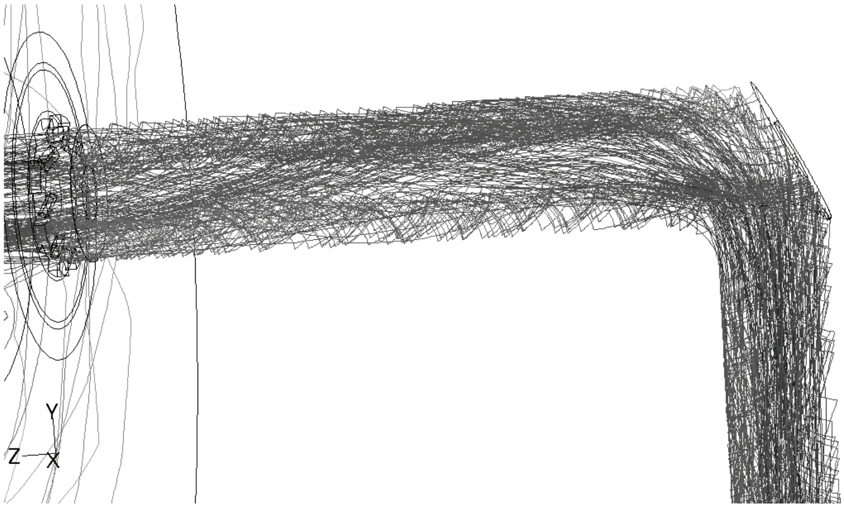

Figure 60: Sample trajectories for modified wall collisions.

In addition to turbulence dispersion and shear induced lift forces the modified wall collision model act as a mechanism to redistribute particles in the vicinity of the wall. This thus alters not only the particle concentration in a cross section of the pipe but also greatly increases the radial and the tangential velocity component and thus introduces a mechanism to transfer momentum from the main flow to the kinetic energy of the particle phase.

Figure 61 shows the normalized particle mass flux in the burner cross-section 0.2m upstream of the furnace inlet for standard and modified wall collision model. It can be seen that the Fluent standard wall collision model predicts larger particle concentration close to the wall compared to the simulation using modified wall collisions. Both approaches predict a maldistribution in the particle concentration in the up-down direction.

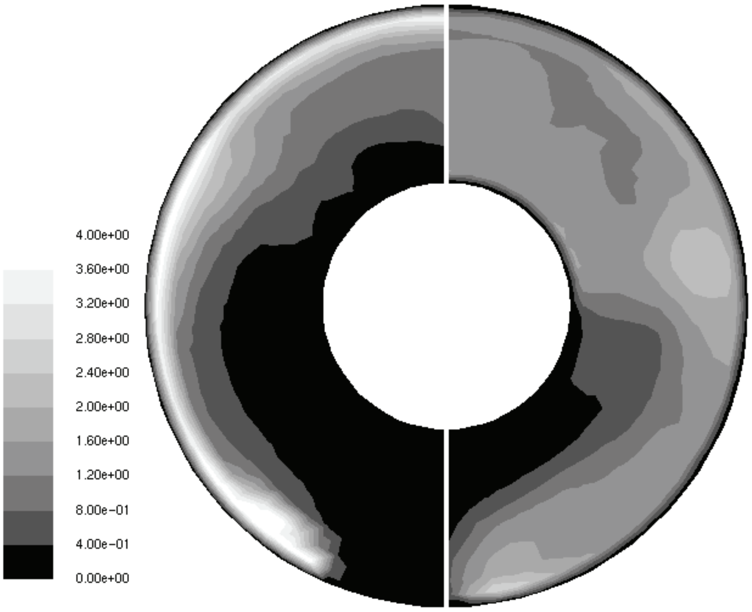

Figure 61: Contours of normalized particle mass flux, $f_p/f_{p,ave}$ for inlet pipe cross-section 0.2m upstream of boiler inlet. Left: Fluent default wall collisions; Right: Modified wall collisions

The concentration distribution of Figure 61 is a result of the complex flow pattern inside the burner; as the particles flow around the bend in the pipe they are moved towards the upper side of the burner annulus due to a Stokes number in the order of unity when based on the bending radius. The flow around the bend induces secondary vortices which transports particles downward. The flow around the central pipe, containing the oil-lance, seems to provoke a left right asymmetry in secondary vortices. Unsteady simulations without particles seem to suggest that this is a steady asymmetry and not vortex shedding phenomenon as is associated with a cylinder in cross-flow. The main difference between the results displayed in Figure 61 is the additional mechanism to redistribute particles contained in the modified wall collisions. If the result for modified wall collisions is compared to a simulation where the particles are assumed uniformly distributed in the plane 0.2m upstream of the inlet to the furnace the main difference is the up-down maldistribution. When the unburnt char fraction of particles at the furnace outlet is evaluated for the three cases the case of standard wall function show less unburnt char compared to both the case of modified wall functions and the case where the particle concentration is uniformly distributed at the inlet plane to the furnace. This is believed to be caused by the larger fraction of particles being entrained in the recirculation zone due to the particle concentration in the inlet plane.

The author believes that this behavior of the particles for the modified wall collisions are in qualitative agreement with the results published by Sommerfeld and Kussins (2003) for 195 μm glass spheres on a rough wall. Ideally any wall collision model should be dependent on the relative size between the roughness and the particle size. However, independently of the wall roughness it seems prudent to assume that arbitrary shaped particles will have a less than ideal rebound compared to perfect spheres on a smooth surface. Since the two tested models for wall collisions represent the best and worst possible scenario for each hit it is believed that the actual situation will lie somewhere between these two extremes. To assume uniform particle distribution at inlet plane is a poor choice since this scenario does not capture the maldistribution between the upper and lower part of the annular cross-section.

Influence of turbulence modulation model

It can be assumed that coal particles, which for this discussion are considered small, will act to reduce the intensity of turbulence. Biomass particles, which for this discussion are often considered large, may on the other hand act to increase the intensity of turbulence. The actual mechanisms and models to deal with turbulence modulation are still being developed and the applicability of such models must also be compared to the ability of the primary turbulence model to accurately model turbulence. When this is said, with the present work we wish to demonstrate the influence of turbulence modulation on the combustion properties.

Figure 62 shows the turbulent kinetic energy in the horizontal half plane inside the furnace close to the burner when evaluated with and without a model for turbulence modulation. It can be seen that the presence of straw particles tends to attenuate the turbulence.

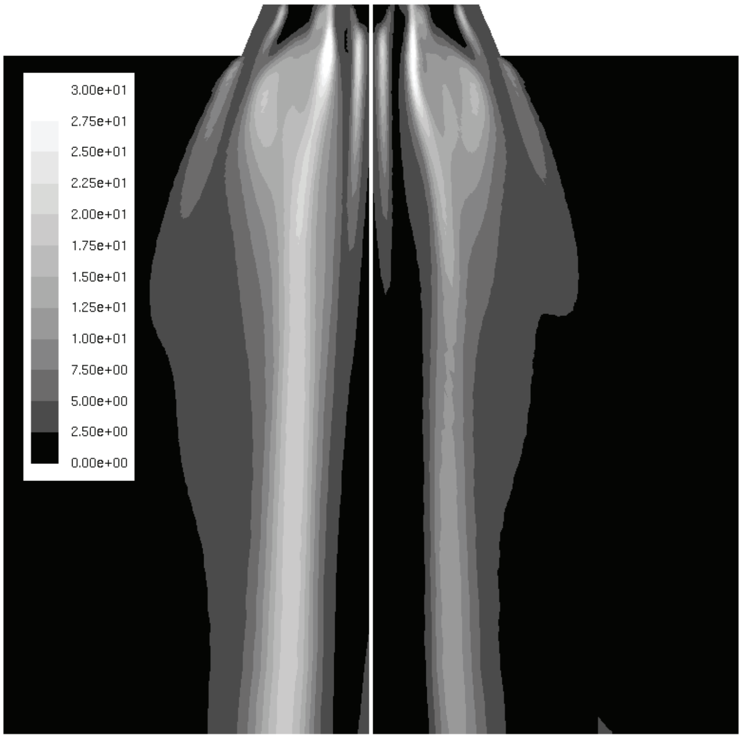

Figure 62: Contours of turbulent kinetic energy [m^2/s^2] Left: No modification; Right: With turbulence modulation model, dimensions: 2x4m

Even though straw particles are considered large the shape of the particles tends to increase their drag coefficient and thereby decrease the slip/terminal velocity which is the essential to produce additional turbulent kinetic energy according to equation (84). When evaluated on the basis of the unburnt char present in the particles at the outlet of the furnace the decrease in turbulence acts to increase the amount of char left in the particles. This is viewed as a consequence of the eddy dissipation model which determines the rate of combustion reactions. Thus a reduction in turbulent kinetic energy yields a reduction in reaction rate for the case using the turbulence modulation model.

Relative importance of modeling choices

To evaluate the relative influence of each modeling choice, using a single parameter, the fraction of unburnt char present in the particles at the outlet plane is used. Clearly, it is desired to have as low as possible level of unburnt char for optimal operation of any boiler. The difference for each of the modeling choices compared to the base case gives an indication on the importance of the particular modeling choice. Table 16 outlines the amount of unburnt char at the outlet plane for each of the straw simulations.

Table 16: Unburnt char fraction at outlet for different cases and change compared to the base case.

	Unburnt char	Change
Base case	10.2 %	0 %
Small particle size	8.6 %	-16 %
Large particle size	23.4 %	129 %
Devolatilization kinetics	9.8 %	-4 %
Modified wall collisions	16.2 %	59 %
Uniform particle mass flux	13.4 %	31 %
Turbulence modulation	15.3 %	50 %

It can be seen that using a smaller particle distribution or different devolatilization kinetics have minimal influence. Whereas specifying a larger particle distribution has a great deteriorating effect due to the flame blowoff. The concentration distribution at the inlet plane, whether specified or modeled, does also have a great influence on the unburnt char fraction. When evaluated using the unburned char as parameter, the uniform particle mass flux at the inlet plane to the burner seems like good compromise despite its inability to capture the particle concentration maldistribution. The application of a turbulence modulation model ranks high on the list of relative importance for different modeling choices. However, the user should carefully consider the accuracy and interaction of applied submodels before implementing such initiatives. Here we merely wished to show the qualitative effect of turbulence modulation of larger biomass particles.

Summary

CFD simulations of pulverized coal and straw combustion using a commercial multifuel low NOx burner have been undertaken with specific attention of the impact of modeling choices for straw combustion. The following conclusions can be drawn:

- It is possible to use the same modeling approach and sub-models used for coal combustion to model straw combustion.
- Straw combustion is associated with a significantly longer flame and smaller recirculation zones compared to coal combustion.
- The particle size and shape distribution are critical for the correct prediction of the combustion.
- The particle mass flux at the inlet plane is not uniformly distributed. Depending on the particle-wall collision model applied, when the entire burner geometry is simulated, the particle mass flux specified at the inlet plane is shown to either improve or deteriorate the combustion efficiency.
- The choice of straw devolatilization model is less significant compared to other modeling choices.
- Straw particles tend to decrease the carrier phase turbulence. However, the application of a turbulence modulation model must be carefully considered

6. Summary, Discussion and Future Development

The motion of spherical and non-spherical particles and their effect on the carrier phase turbulence have been investigated by means of a study of previously published work, an experimental study of a particle laden jet and by deriving a model consistent with the conservative equations of fluid motion. This new model has been implemented into a CFD basis and used to predict the complex flow which emerges from a multifuel low NOx burner.

At the start of this project there was no consensus towards the influence of particles on the carrier phase turbulence and no model has so far been able to reproduce the entire spectrum of experimental measurements. Although several mechanisms for turbulence modulation had been suggested in the past, the only general consensus in the scientific community was that small particles tend to attenuate the carrier phase turbulence while large particles tend to augment the turbulence. To gain insight into the general mechanisms concerning particle turbulence interaction a test rig was constructed and the turbulence modulation resulting from different particle sizes, concentration and shapes were measured using laser-optical methods. Using this parametric study it was possible to evaluate some of the suggested criteria for turbulence modulation based on proposed mechanisms. The results showed a strong correlation with particle concentration as expected and the measureable lower boundary for two-way coupling was found to be around 10^{-5} which matches that of previous investigations. An often mentioned mechanism for turbulence production is the unsteady wake of large particles and from the study of large spheres it is known that this is best described by the particle Reynolds number, Re_p. The present study reveals that this mechanism alone is not sufficient to explain the observed trends. However, there does seem to be a tendency towards an enhancement of turbulence for large values of Re_p and a decrease for low values. Another mechanism suggested is the correlated motion between particles and the fluid motion. As a small particle enters an eddy it will be accelerated by fluid motion and momentum exchange via the drag force act to decrease the velocity of the eddy and thereby reduce the turbulence intensity. This phenomenon is best described by the Stokes number. The present investigation involves particle Stokes numbers which are much greater unity, implying that particles are only little affected by the eddies and thus that only augmentation of the carrier phase turbulence is to be expected. However, the present results show that the presence of particles is able to dampen the turbulence intensity at some locations downstream of the jet. Clearly, at those location the largest, most energetic eddies are still larger than the particles and thus there should still be a basis for this mechanism to proceed. Thus, to evaluate the attenuation caused by the particles the length scale ratio suggested by Gore and Crowe (1989) might be the appropriate non-dimensional parameter to use. Indeed, the entire experimental setup was tuned in order to test the suggested parameter d_p/l_e effect on the measured turbulence modulation. Previous measurements, for which the justification for this parameter is shown, have all been performed on experimental setups which involves similar sized pipe flow, and thus the variation with regards to the ratio d_p/l_e have only been done be varying the particle size. The present experiment contrary involves the variation of the turbulent length scale l_e for a fixed d_p where the particle size is chosen such that measurements is performed on both sides of the criterion $d_p/l_e = 0.1$. Similar to the particle Reynolds number, the result shows a clear correlation for this parameter but the length scale ratio alone is not sufficient alone to explain the observed trends. These observations is an indicator for that the mechanisms involved in the modulation of turbulence is the result of two or more distinct mechanisms and that a single non-dimensional number is not sufficient to explain/predict the observed trends. This is factored into the derivation of the theoretical model where the forcing term, resulting from the presence of particle, to the momentum equation is split in two. Subsequently, the two different approaches to derive the source term to the turbulence equations are applied on each part of the momentum forcing term resulting in the new model. This novel model consists of three contributions to the turbulent kinetic energy:

$$S_{kp} = \frac{\alpha \rho_p}{\tau_p}\left(\underbrace{\left|\overline{u}_i - \overline{u}_{pi}\right|^2}_{I} + \underbrace{\overline{u'_{pi}u'_{pi}}}_{II} \underbrace{-2k}_{III} \right) \tag{89}$$

Contribution *I*, the slip velocity squared, is interpreted as the production of turbulence resulting from the velocity gradients which again is due to the no slip condition imposed on the particle surface. Contribution II and III, respectively the particle and the fluids turbulent kinetic energy times two, is interpreted as the average effect of particle – eddy interaction. The mechanisms as explained from equation (89) are illustrated in Figure 63. It can be imagined that contribution I is the steady forcing term which can be related to the local flow field around an individual particle whereas term II and III is related to the average flow field energy balance or more vividly to the interaction between particles and eddies in an average formulation.

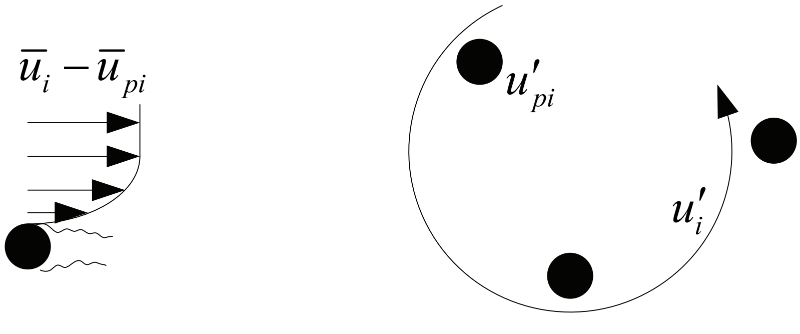

Figure 63: Illustration of mechanisms involved in particle – turbulence interaction.

The eddies/turbulence, represented by term III, are dampened by the presence of particles while simultaneously the fluctuating kinetic energy of the particles, represented by term III, act to transfer there energy to the turbulent eddies. The relative magnitude of these terms has been evaluated for the pipe flow case study in chapter 2 and an additional analysis are given in appendix G. For most practical cases contribution III are larger than contribution II which fit with the notion that the particles are accelerated by motion of the eddies. Figure 41 shows the evaluation of the different terms for pipe flow. It can be seen that contribution II decreases proportional to the distance of the wall indicating the particle wall collision influence on the fluctuating particle kinetic energy.

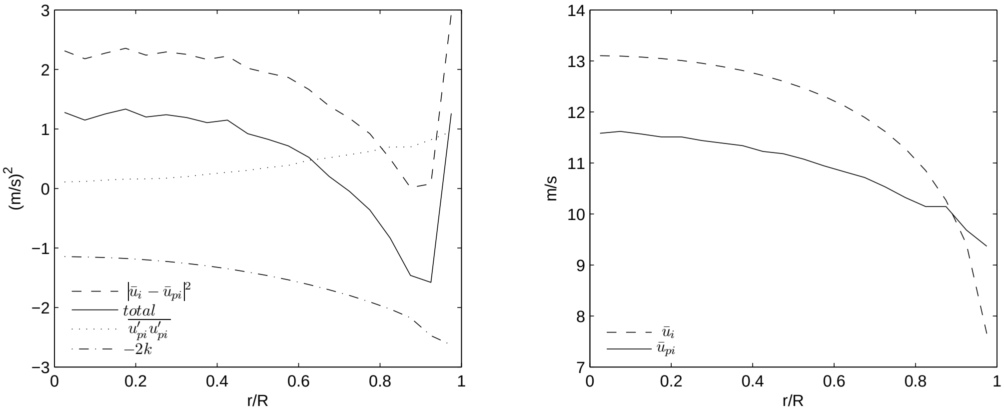

Figure 64: Evaluation of the different terms in the new model and mean flow velocity profiles for case 2.

Contribution I can be significantly greater than both contributions II and III for larger particles accelerated by gravity and totally negligible for very small particles or other cases where the drag force is much greater than the body forces. A better idea of what it happening can be achieved by picturing the turbulence and particle unsteady motion in the frequency domain. For a fully developed flow the magnitude of the spectrum of turbulence is limited by the geometry of the flow, which is responsible for the turbulence production, while the magnitude of the spectrum of particle kinetic energy is limited by the magnitude of turbulence. However, for developing/unsteady flow additional turbulence may be generated due to flow shear, and similarly, the initial condition of particles may give rise to much larger particle oscillations compared to fully developed flow. The influence of the particle wake on the turbulence spectrum is well known. A von Karman vortex street will create a peak at a single frequency while for an unsteady wake the contribution will be scattered over a range of frequencies. The study by Losenno (2004) involves the effect of particles on the spectrum of turbulence and it is possible to interpret the different effects herein discussed. It is clear, that there is a connection between the mechanisms discussed in chapter 3 and chapter 4. The experiments revealed that the magnitude of intensity change scaled with the particle volume fraction, the particle Reynolds number and the d_p/l_e ratio, but that none of these non-dimensional numbers alone could explain the observed trends. Each of these numbers can be interpreted as characterizing the mechanisms revealed by the rigorous theoretical derivation of the source term to the turbulent kinetic energy balance resulting from the presence of particles. As such the particle Reynolds number scales with the slip velocity which is found in contribution I and similarly the d_p/l_e ratio is inherently connected to the particle – eddy interaction which is reflected in contribution II and III. Evidently, if the experimental trends are interpreted using the theoretical model a clear resemblance is revealed as shown in Figure 65.

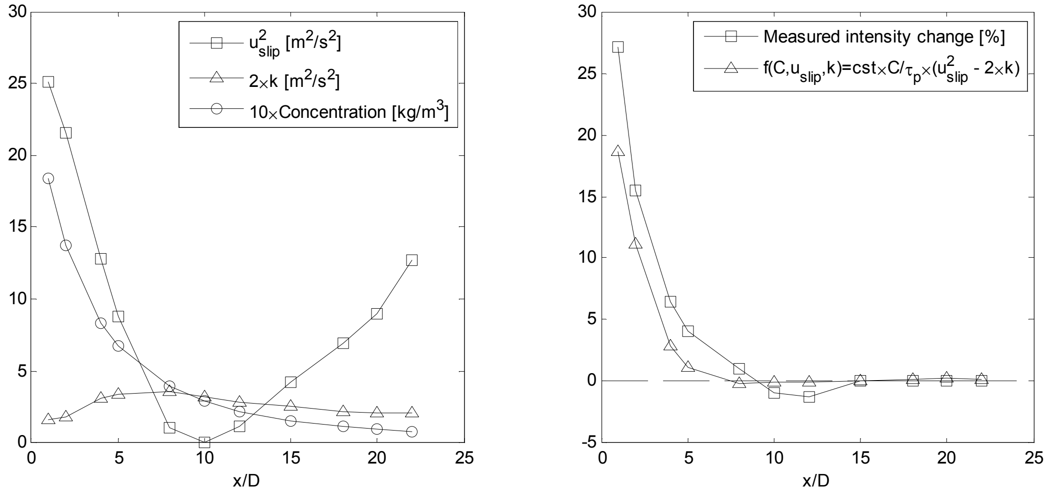

Figure 65: Simple evaluation of theoretical model using the experimental data, d_p=1.8mm, z=1.0

The great augmentation of turbulence close to the inlet is thus interpreted as being due to the large slip velocity and the attenuation further downstream is caused by the drop in slip velocity decreases the additional generation of turbulence below that which is dissipated due to the particle eddy interaction. Further downstream the concentration decreases so that the increase in slip velocity is not reflected in an increase in the measured turbulence intensity. It is also interesting to note that existing theoretically derived models for turbulence modulation cannot explain the observed trends at the centerline of the jet. It is quite possible that mechanistic/semi-empirical/semi-heuristic models have a chance to predict the observed trends but as stated previously they are not rigorously derived from a momentum balance, but rely on the combination of contributions arising from different concepts and are thus inherently biased. One tendency revealed by the experiments which is not reflected in the model is the result for different particle diameter at same loading as shown in Figure 26.

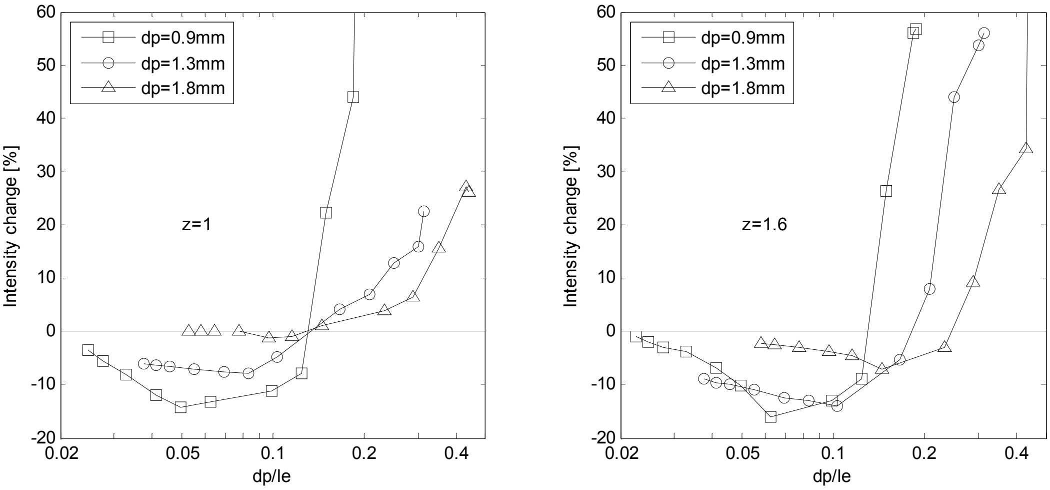

Figure 66: Dependency on particle size. The percentage change in turbulence intensity as function of the length scale ratio for different particle sizes and constant global mass loading.

The slip velocity associated with the smallest particles is lower than that associated with the larger particles and thus from evaluation of the theoretical model one should expect that the result for the smallest particles was below the result for the larger particles at all locations. One explanation for this discrepancy may be that the theoretical model is derived for dilute flow where the additional effect of particle-particle collisions is neglected. Similar to particle-wall collisions, particle-particle collisions act to increase the particle kinetic energy and via the $u'_{pi}u'_{pi}$ term feed to the turbulence kinetic energy. Evaluation of whether the flow is dilute or dense is best performed by the ratio of the particle response time and the time between collisions. Proper evaluation of the ratio reveals that the flow is less dense for decreasing particle sizes. Another explanation for this could be to consider the particle number density in place of the particle concentration. The number density scale with the particle concentration but increases for decreasing particle sizes. The number density is important since this increases the surface area which is available to host shear stress. Thus for a fixed particle loading the use of a smaller particle size would increase the surface area available to host shear stress and theoretically increase the total amount of turbulent kinetic energy compared to the similar flow with same loading but larger particle size.

The large amount of data generated from the parametric study also allowed the formulation of a pure empirical model which was able to predict the turbulence modulation for spherical particles in the range of experimental parameters:

$$\frac{\sigma - \sigma_0}{\sigma_0} \cdot 100\% = \frac{\dot{m}_p}{\mu d_p}\left(0.34\frac{d_p}{l_e} - 0.05\right) \tag{90}$$

This is used to compare the turbulence modulation resulting from spherical particle with that experienced by non-spherical particles to determine the additional effect of shape. Note that this expression is only valid in the given range of values on which the expression is based. This can be emphasized by applying the expression to predict the intensity change at the centerline of a pipe. In Figure 67 it can be seen that the empirical expression predicts unrealistic values for low values of the d_p/l_e ratio suggesting that a higher order correlation is required.

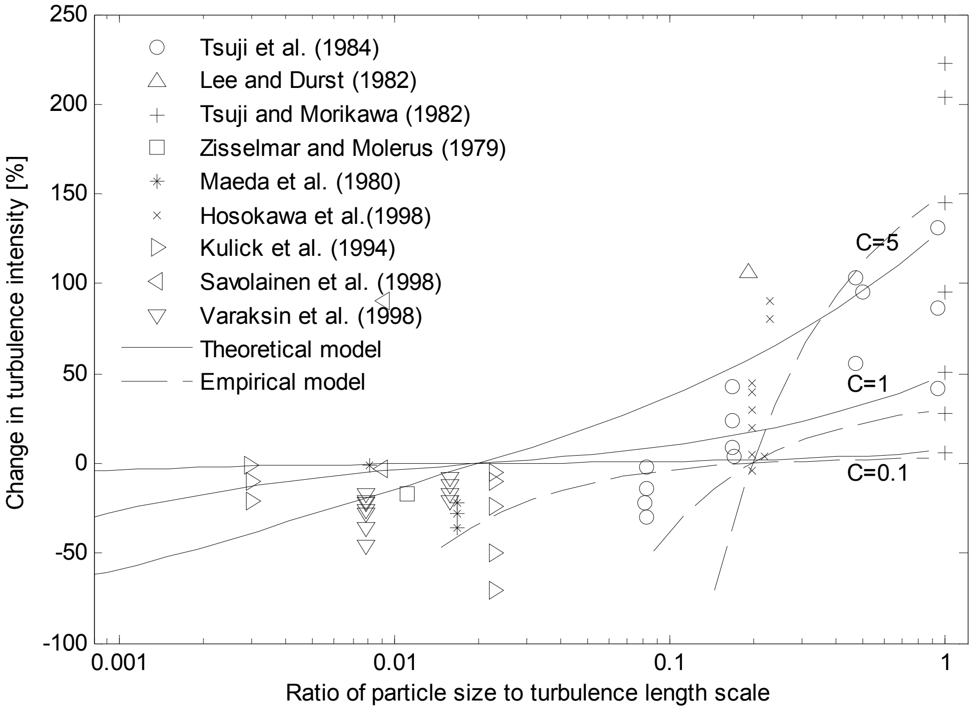

Figure 67: Comparison of model prediction and data for the turbulence modulation at the centerline of a vertical pipe.

However, as can be seen in Figure 68 top right it was found that this correlation was sufficient to predict the result for spheres for using different loading and size in the performed range of parameters. Performing additional experiments, using non-spherical particles with similar size and for similar loading, it is possible to show the additional effect of shape. For this two well-defined shapes were selected, disk and prolate spheroids. Firstly, it can be seen that the result for the non-spherical particles follows the same trend as that observed for spherical particles when the characteristic dimension used is the diameter of a volume equivalent sphere. Secondly, when compared with the expected values from the empirical model it is clear that there is some additional effect due to shape and that this effect is different for the two shapes considered.

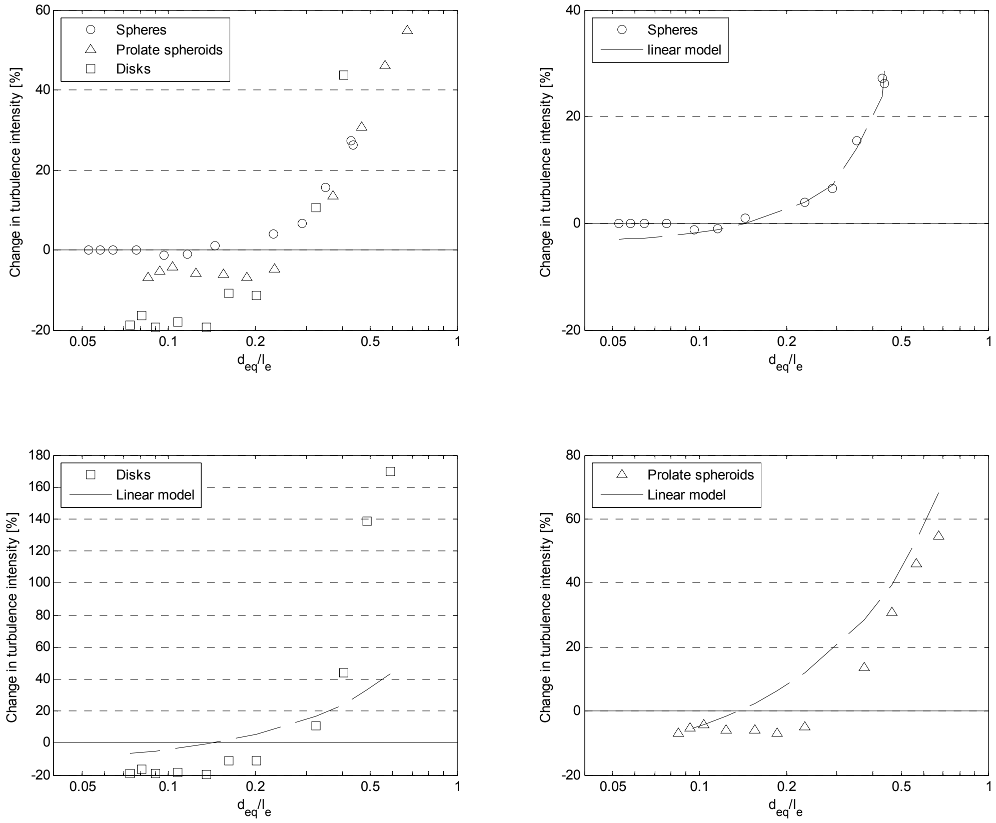

Figure 68: The percentage change in turbulence intensity versus the ratio of the volume equivalent particle diameter to the integral length scale of the clear flow for different particle types. Experimental results have been compared with an empirical model to predict the turbulence modulation inflicted by spherical particles. Notice that the y-axes are not the same for the figures.

The disks seem to have both a greater augmenting effect at high d_p/l_e ratios and greater attenuating effect at low ratios compared to spheres whereas prolate spheroids tended to attenuate the turbulence at all d_p/l_e ratios compared to spheres. The actual mechanisms involved for non-spherical particles are difficult to conclude from this experiment and any statement made must be considered as speculation. However, it can be argued that the additional turbulence modification is a result of partly the mean motion and partly the interaction of the non-spherical particles with the turbulent eddies. The mean motion of non-spherical particles can be modeled using models of different levels of sophistication. For high particle Reynolds number flow the motion of non-spherical particles are associated with significant secondary motion which have been suggested to be modeled using semi-empirical models by formulation of translateral lift forces. For low Reynolds number flow theoretical derivation of the equations of motion for a non-spherical particle in linear shear shows that particles will initiate rotational motion and that additional terms appear in the BBO-equation. For medium ranged particle Reynolds number flow particles are stabilized by the formation of a stable recirculation in the wake of the particle, which therefore tend to orient themselves with maximum cross-section normal to the flow. Particles in this range can thus be modeled by only considering the translational motion using appropriate modification of the drag coefficient depending on the shape of the particles. Considering the theoretical model derived for turbulence modulation the effect of shape is implicitly modeled since the modification of particle motion affects the particle mean slip velocity and the particle response time. However, the interaction with turbulent eddies must be assumed to depend on the alignment of the particle with the eddy.

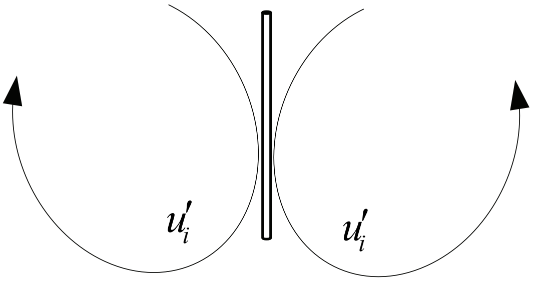

Figure 69: Alignment of a slender fiber between two vortices.

Maybe the formulation and use of a rotational response time may prove to be useful to consider for modeling purposes. Clearly, the turbulent kinetic energy exchange between the particle and the turbulent eddy must be affected by the alignment and the shape of the particle. For example the study by Paschekewitz et al. (2004) showed additional drag reduction by the weakening of the near wall turbulent structures due to the alignment of slender fibers in inter-vortex region. At least this result is in qualitative agreement with the present experimental result for a prolate spheroid, which is similarly oblong in shape and which showed an additional reduction of turbulence. Another, explanation can be that the turbulence generated in the wake of the particles are dependent of the characteristic dimension of the particle. If the diameter for a sphere, a disk and a prolate spheroid is used as the characteristic dimension the diameter of the disk will be larger than the diameter of an equivalent sphere but this will again be larger than the diameter of a prolate spheroid.

The theoretical model has been implemented into the framework of Computational Fluid Dynamics and coupled to the commercial code Fluent using User Defined Functions. The derived model is applied as a source term for the standard k-ε model. The choice of a commercial code and the standard k-ε model is made such that the model can be applied for a wide range of engineering flows since additional sub-models can be added by selection using the Fluent GUI. However, to do this it is important to be aware of the interaction and impact of the propose model for turbulence modulation and other sub-models. Furthermore, the memory requirements of the particle loop used to evaluate the source term proved to be too much for the available resources for the boiler geometry and a simplified version, which bypassed the particle loop, was used instead. It can be stated that the available options in Fluent involving user defined coupling between the Eulerian and Lagrangian formulation was very computationally intensive. However, there is great potential for improvement if the Fluent source code is made a bit more accessible. This simplified version used the terminal velocity in place of the slip velocity and neglected contribution II. Thus it is also important to realize the limitation of this simplification. Chapter 4 investigated the flow field emerging from a multi-fuel burner and results showed that the turbulence was dampened since the particle used was associated with a low slip velocity. The results revealed that the combustion rate was significantly affected due to the direct coupling with the eddy-dissipated model while the effect on the mean flow field was hardly noticeable. Of special interest was the formulation of the particle wall collision sub-model which was showed to have a great effect on the particle trajectories and the concentration profile. Although no simulation was made, using the modified wall collision model simultaneously with the model for turbulence modulation, it can be imagined that the application of a rough wall will act to increase the carrier phase turbulence due to the significant enhancement of fluctuating particle kinetic energy resulting from irregular bouncing. Although, it should be mention that this enhancement also depends on the applied coefficient of restitution which act to reduce the particles momentum. However, these effects will only be captured if the full model is applied since the simplified model assumes that the particles travel at terminal velocity and the $u'_{pi}u'_{pi}$ term is neglected. Thus only the modification of the particle concentration would be noticed by the turbulence modulation model. Indeed, the proper modeling of the wall collision may be of major significance. For example, Boulet and Moissette (2002) noticed especially poor results for turbulence modulation terms near the wall for three different formulations of the turbulence modulation source terms. With the current formulation involving an additional term which is especially important close to the wall, there is some optimism that this will be able to improve modeling of wall bounded flows. The Lagrangian particle model in Fluent is developed for dilute flow and assumes that particle-particle collisions are negligible. Thus, the additional particle kinetic energy resulting from particle-particle collisions is not passed on the turbulence via contribution II. The turbulence modulation also interacts with the particle-dispersion models. In the case of the eddy-dispersion model an increase of the turbulence kinetic energy results in an increase in particle dispersion and similar a decrease in the turbulence kinetic energy results in a decrease in the dispersion of particles. Thus, the modification of the fluid phase by the particles in coupled back to the motion of the particle phase. Most of the models mentioned in the context of CFD involve some empirical constants which are adjusted for optimal performance of the sub-model. It could be argued that some of these constants should be modified in the case of particle-laden flow where the turbulence modulation is also considered. Indeed, it can be argued that our limited understanding of turbulence lead to limited models, biased experiments lead to erroneous conclusions especially when numerical models is adjusted to fit the experimental results. Future improvement of our understanding of particle-laden flow depends on the development of more accurate simulation methodology. This study have shown the failure of the RANS modeling technique to accurately predict the turbulent kinetic energy compared to experimental results even for clear flow. We can thus not expect any model for turbulence modulation to be any more accurate. Simulations involving more advance turbulence prediction methodology such as LES or DNS should also be accompanied with improvement in the particle handling ability. This could involve the coupling of DEM models with CFD or/and the resolution of the particle boundary layer to predict the shear stress and the resulting production of turbulence. Similarly this would involve the resolution of the particle eddy interaction and the possible alignment of non-spherical particle with turbulent vortices. However, this is dreams and wishful thinking, at present and in the near future we are stuck with RANS for practical modeling.

Appendix A: Measurement of a single phase axisymmetric jet

An illustration of a jet providing the concepts used in the illustrations in this appendix are shown in Figure 70. A jet can be divided into three distinct regions: The potential core region, the transition region and the self similar region. The self similar region is name as it is since normalized velocity profiles at different distance downstream of the jet inlet collapse into a single line. Dependent on the inlet conditions the potential core and transition regions can have different extent downstream. For an initial laminar flow at the nozzle inlet the extent of the potential core is between 5-10 D and the extent of the transition region is between 10-20 D. Thus profiles of the self similar jet are typically reported beyond 30 D. For a flow with turbulent conditions at the nozzle entrance, such as the present setup, the extent of the potential core and the transition regions can be considerable decreased. Since the jet entrains fluid it is important that any surrounding walls are placed sufficiently far away from the jet centerline to avoid backflow and recirculation zones which can affect the development of the jet. For the present setup other factors such as the as containment of the seeding particles, smoke, and the recycling of test particle for the multiphase purposes have limited the clearance space. Furthermore, the effect of the outlet of the test section also extends upstream and influences the development of the jet.

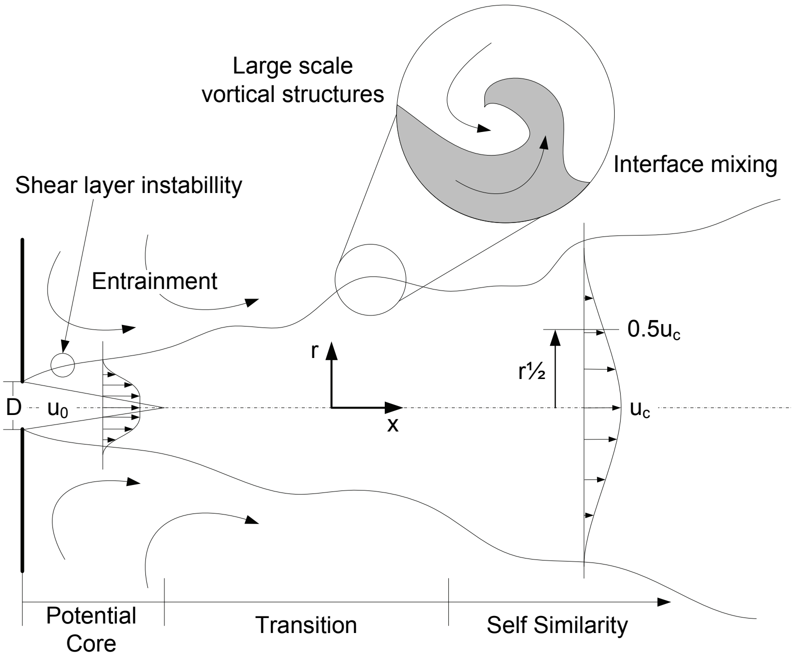

Figure 70: Schematics of jet flow.

Axial velocity

For a single phase axisymmetric jet in the self similarity region the axial velocity profile can be approximated with a Gaussian distribution function given as (Beer and Chigier 1972):

$$\frac{\overline{u}}{\overline{u}_c} = \exp\left(k_u \frac{D}{r}\right) \qquad k_u = 82...92 \tag{91}$$

k_u is a constant which can be chosen between 82-92; here a value of 87 is used. Overall the present data seem to match the Gaussian profiles, seen in Figure 71, nicely given the accuracy of the measurements. Close to the inlet at x/D=2 the profile is significant steeper which agrees with this position being located in the potential region. Given the accuracy of the measurements it is not possible to determine when the jet is truly self similar, here we only notice that the jet appears to be self similar already at x/D=8. It is also possible to see the backflow which is present close to the walls farthest away from the centerline. Although this phenomenon affects the outskirts of the velocity profiles it seems that profiles close to the centerline is largely unaffected.

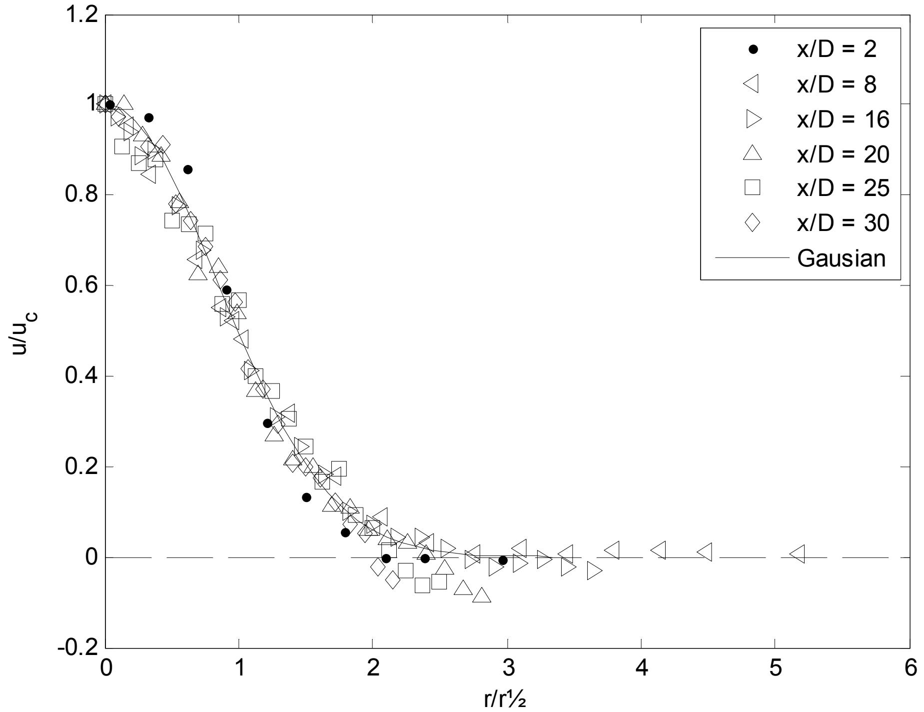

Figure 71: Normalized mean axial velocity profiles of a single phase jet compared with a Gaussian distribution profile.

Normal and shear stresses

In Figure 72 is shown profiles of the axial and radial normal stresses together with the shear stress normalized by twice the mean axial velocity. The experimental measurements by Hussein et al. (1994) are given for comparison. Data at x/D= 8 has been chosen to be representative for the trends of the radial profiles at different positions downstream of the jet inlet. However, the data at different values of x/D does not collapse into a single line. Generally the profiles measured close to the inlet have a smaller magnitude compared to profiles at locations further downstream. Thus the value for <uu> at the centerline for x/D = 30 is 0.24 which is considerable above that given by Hussein et al. (1994). However, it is clear that the same trends as that presented by Hussein et al. (1994) are present in the current dataset. One thing to notice is that there is still significant normal stress present far from the jet centerline which indicates that there is still significant turbulence in what otherwise would be considered as still air.

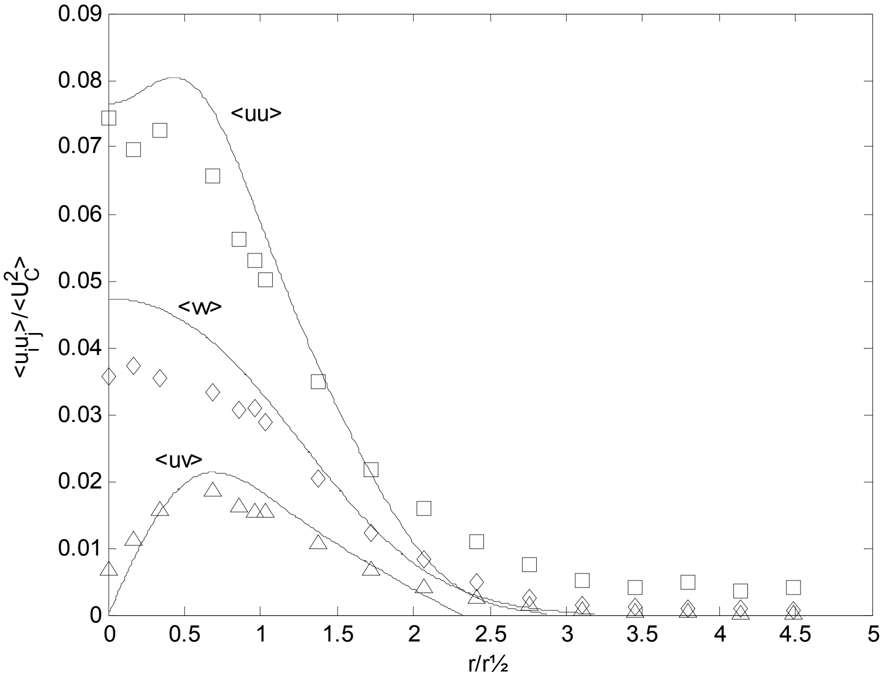

Figure 72: Radial profiles of normal and shear stress measure at x/D=8. Fully drawn lines represent experimental data for the self similar region by Hussein et al. (1994)

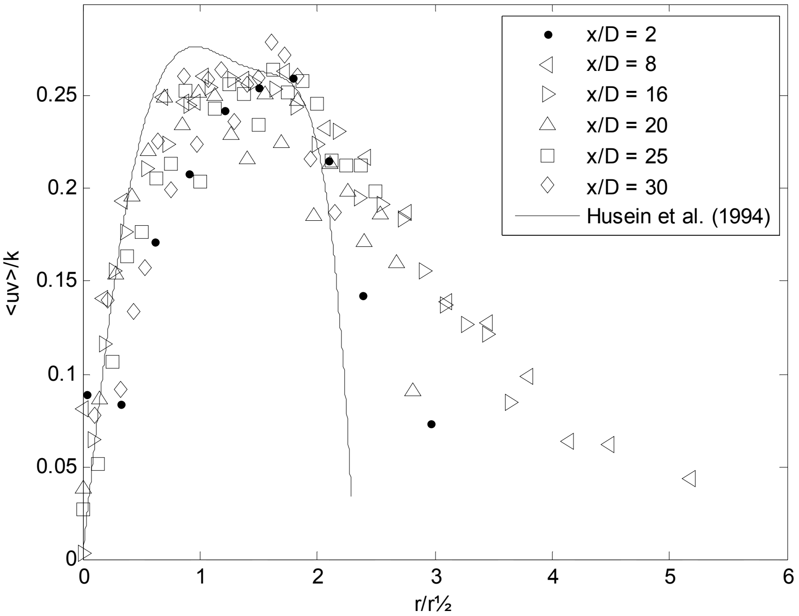

Figure 73: Radial profiles of shear stress at different locations downstream of the jet inlet normalized with the turbulent kinetic energy.

One way to view this residual turbulence is to view it as background noise in the measurements.

Figure 73 shows the shear stress at different positions downstream of the jet inlet normalized by the turbulent kinetic energy. For this normalization the profiles can be said to collapse into a single line again considering in inherent accuracy of the measurements. It can be seen that the magnitude closely resemble that measured by Hussein et al. (1994). Furthermore, also the trends up to r/r½ = 2 are also closely matched whereas beyond that the measurement seem to diverge somewhat. It is unclear if this presence of shear stress far from the jet centerline is an expression of measurement error or reflects a tendency in the measurement.

Spreading rate

The self similar jet is also characterized by having a constant spreading rate which is non-dependent of the jet Reynolds number. Investigation by Panchapakesan and Lumley (1993) and Hussein et al. (1994) report spreading rates around 0.1 while Wygnanski and Fiedler (1969) measured the spreading rate at 0.084 which is consistent with the present investigation. The discrepancy between these measurements is suggested to be due to the flow containment present in the experiment by Wygnanski and Fiedler (1969). This gives rise to a weak but large recirculation zone which acts to retard the jet centerline velocity at high x/D ratios. For the present experiment the measured spreading rate is in accordance to previous investigations. It should be noted that the centerline velocity, see Figure 75, at around x/D=25, x=1000mm begins to deviate significantly from that expected of a free self similar jet.

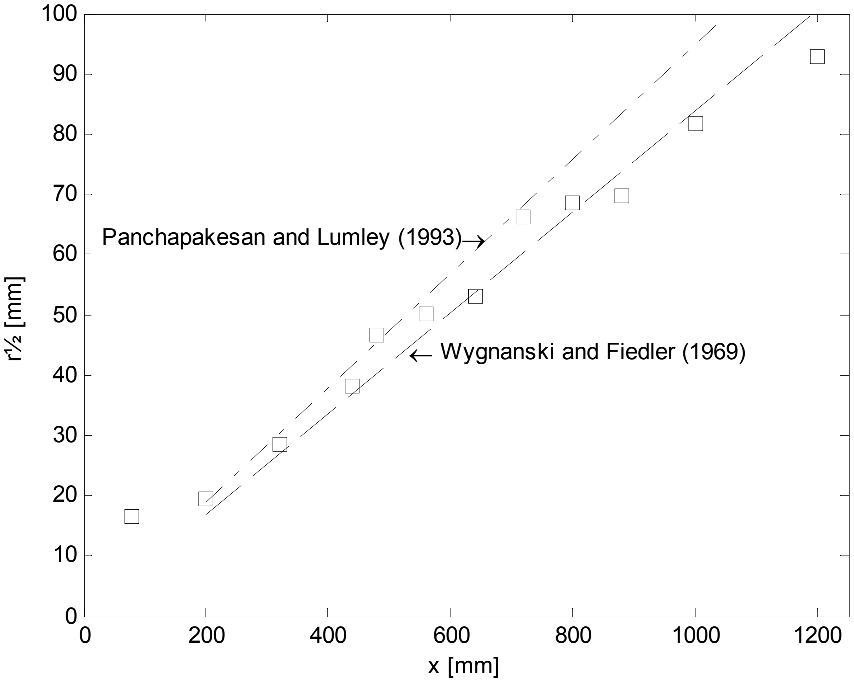

Figure 74: Spreading rate of the single phase axisymmetric jet. r½ is the radial position where the axial velocity is half of that at the centerline. x is the axial distance down stream of the jet inlet.

Another explanation to explain the discrepancy is the accuracy of the measurements. Figure 74 shows that a constant spreading rate can be assumed already at x/D = 5 (x = 200mm) and is sustained until x/D = 25 (x=1000mm).

Centerline velocity

Similar to the spreading rate the axial velocity at the centerline decreases at a constant rate in the self similar region. Figure 75 shows the development of the axial velocity at the centerline compared with the measurements by Panchapakesan and Lumley (1994). Both investigations shown that at x/D = 5 the axial velocity decreases with a constant rate. For at present investigation this trend is maintained up to x/D =25 whereafter the effect of the outlet, located at x/D = 50, significantly affects the centerline velocity compared to the ideal free jet. Compared to Panchapakesan and Lumley (1994) the centerline velocity of the present investigation decreases slightly faster.

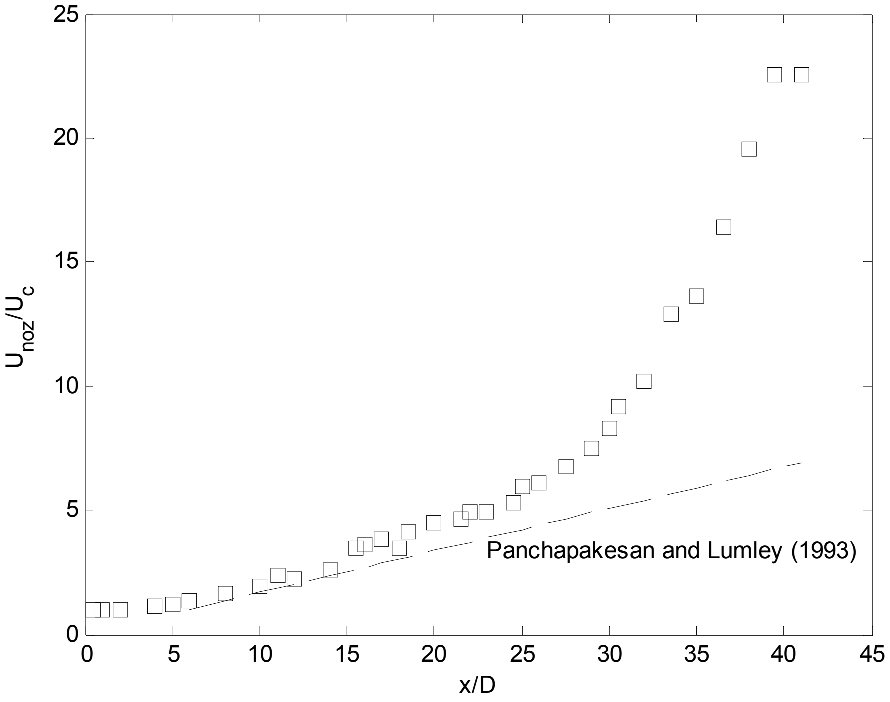

Figure 75: Axial velocity at the centerline of the jet normalized by the inlet velocity.

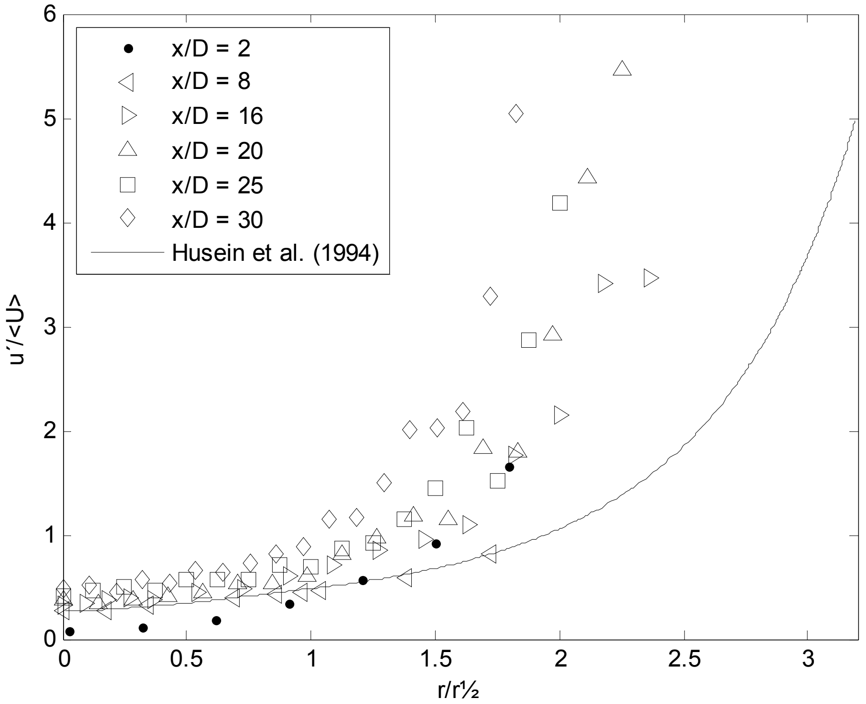

Figure 76: Axial RMS velocity normalized with the mean axial velocity.

Turbulence intensity

Figure 76 shows the turbulence intensity at different locations. The present measurements follow the general trend. However, the measured turbulence intensity increases significant faster as we are moving away from the centerline compared to the measurements of Hussein et al. (1994). At the centerline the turbulence intensity is similarly increasing at increasing distances downstream. At x/D=2 the turbulence intensity is significantly smaller than at other locations, since this is measured inside the potential core.

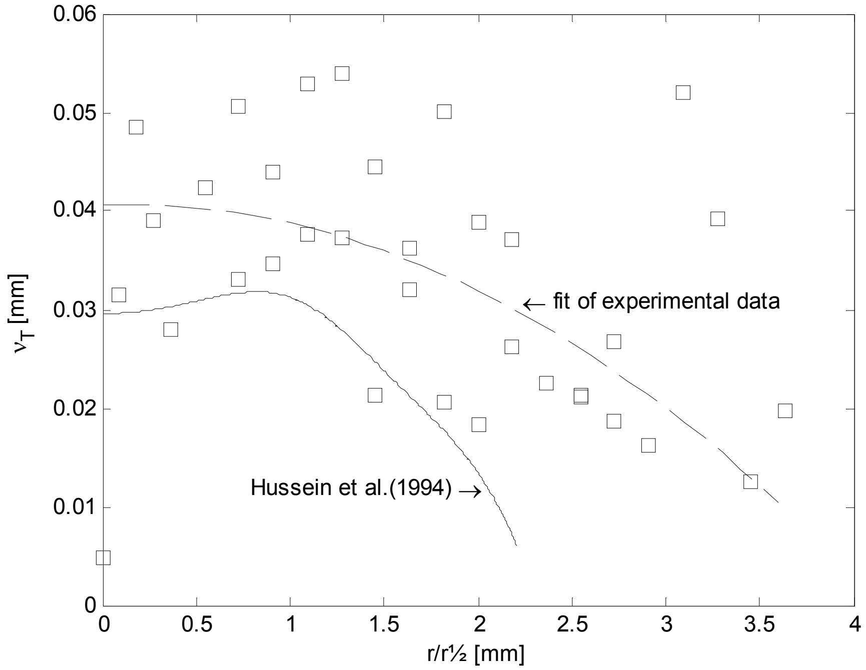

Figure 77: Radial profile of the turbulent viscosity at x/D=16.

Turbulent viscosity

The turbulent viscosity can be calculated from the following expression:

$$\langle uv \rangle = -\nu_T \frac{\partial \langle U \rangle}{\partial r} \tag{92}$$

In Figure 77 is shown experimental data measured at x/D = 16 compared with that of Hussein et al. (1994). The present measurements display a large spread due to the increased accuracy required with the calculation of the gradient in expression (92) and which is difficult to achieve with the present setup. Due to the spread in the data a simple second order polynomial fit of the data points is given, which does not necessarily expresses the true nature of the development of the turbulent viscosity in the radial direction. It can be seen that the turbulent viscosity of the present data is larger than that of Hussein et al. (1994). This is in agreement with the previous shown trends of the development of the axial velocity.

Turbulence spectra

Figure 78 shows the longitudinal spectrum measured at x/D =16 at the centerline. This has been compared with the measurement by Champagne (1970) and a line with constant inclination of -5/3 corresponding to the theoretical inclination of inertial sub-range. It is clear, that the present spectrum is consistent with previous measurements for lower wave numbers whereas the highest wave numbers are not resolved by the present setup where the Kolmogorov scales have been calculated to be smaller than the measurement volume.

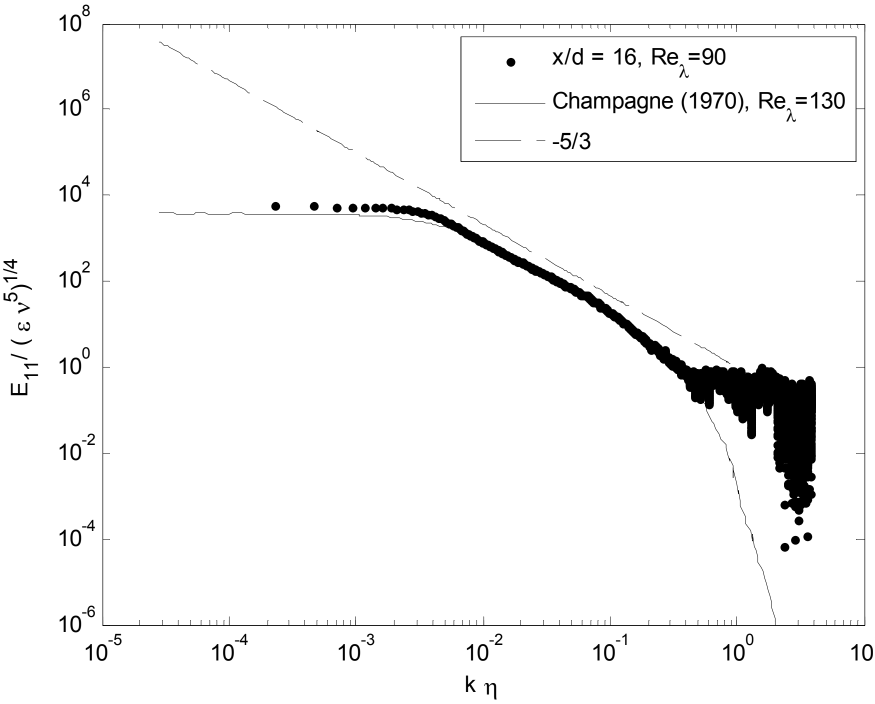

Figure 78: Sample longitudinal spectrum for the single phase jet with inlet velocity of 7 m/s compared with the data by Champagne (1970) and a line with a -5/3 inclination.

Appendix B: Measurements of particle laden jets

This appendix contains all data acquired for the measurement at the centerline of a particle-laden jet. The measured data is presented as plots of the mean and RMS velocity normalized with the velocity at the inlet as a function of the distance downstream from the inlet normalized by the inlet diameter. Each plot represents a unique combination of particle size and mass loading.

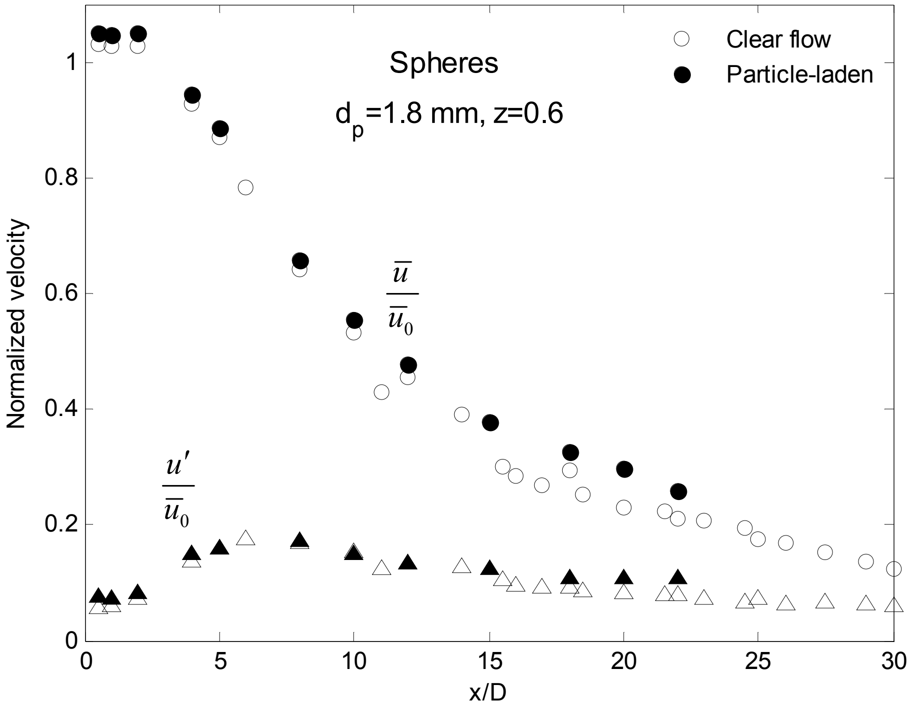

Figure 79: Normalized mean and RMS velocity for spheres with d_p=1.8mm, z=0.6.

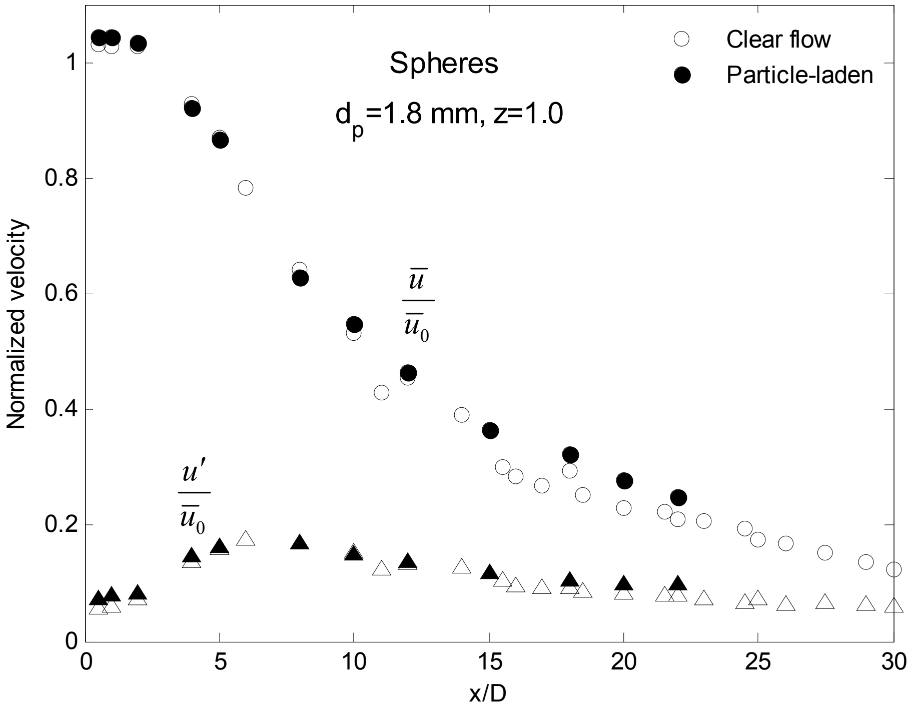

Figure 80: Normalized mean and RMS velocity for spheres with d_p=1.8mm, z=1.0.

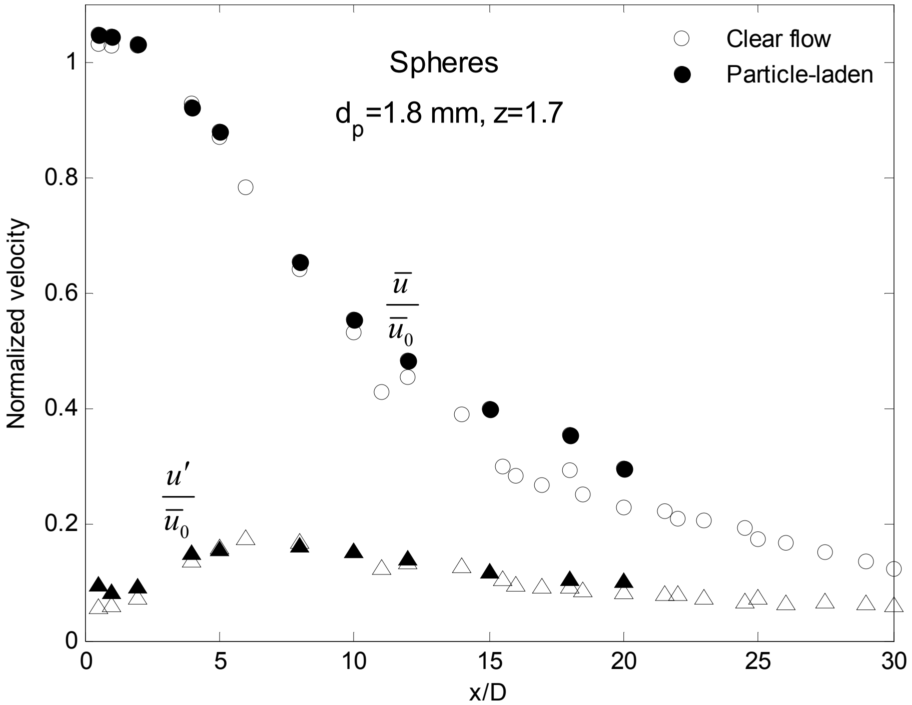

Figure 81: Normalized mean and RMS velocity for spheres with d_p=1.8mm, z=1.7.

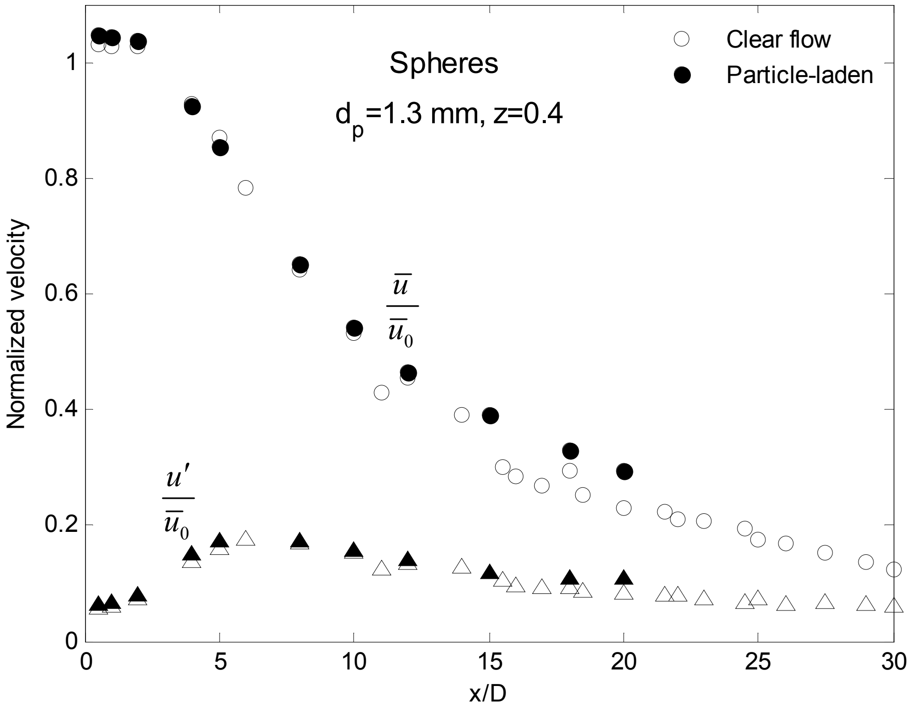

Figure 82: Normalized mean and RMS velocity for spheres with d_p=1.3mm, z=0.4.

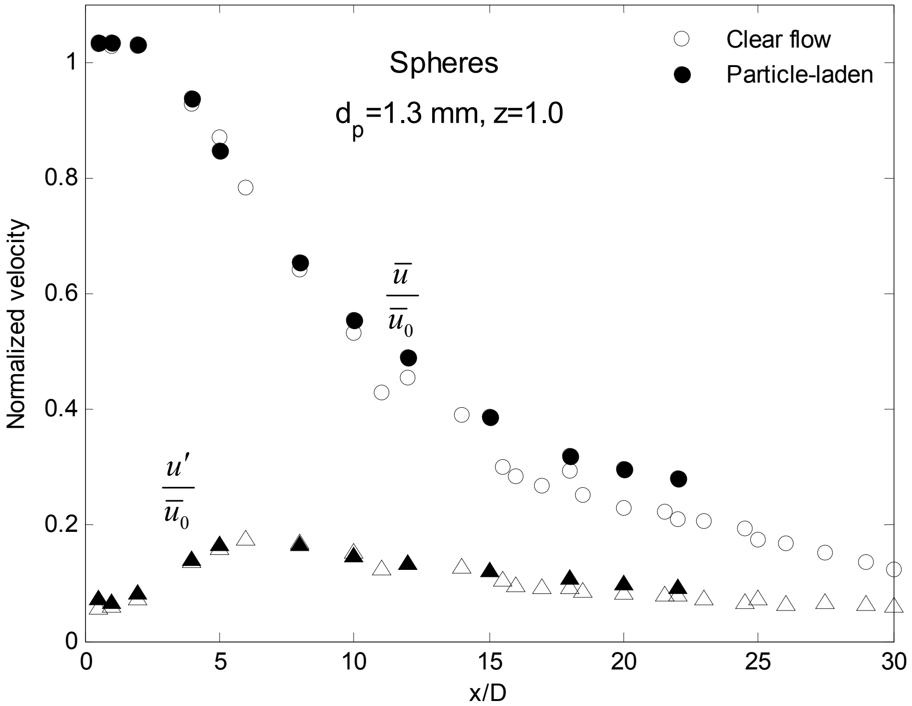

Figure 83: Normalized mean and RMS velocity for spheres with d_p=1.3mm, z=1.0.

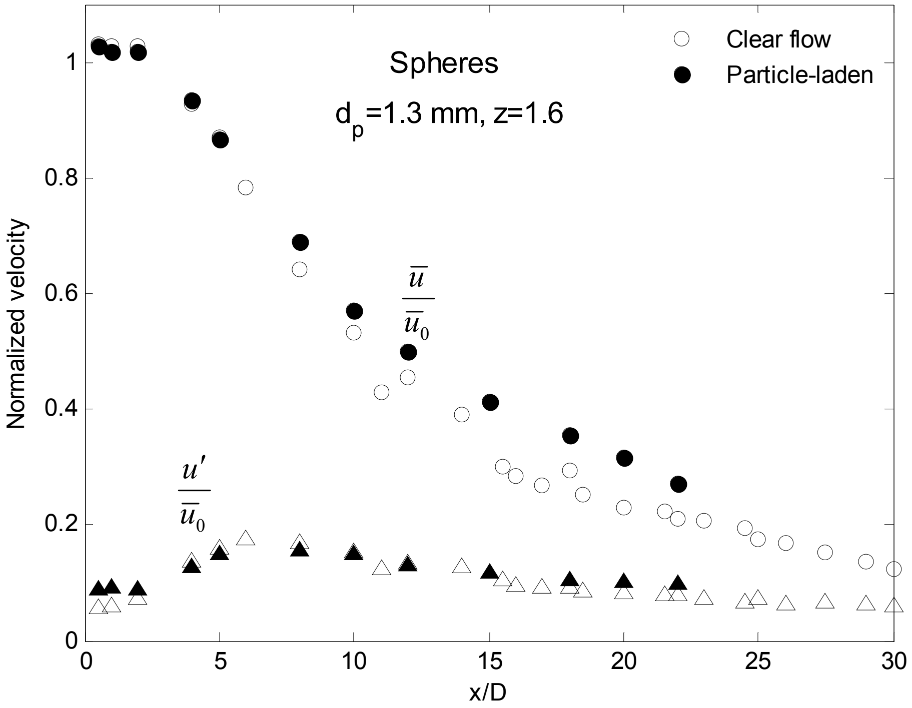

Figure 84: Normalized mean and RMS velocity for spheres with d_p=1.3mm, z=1.6.

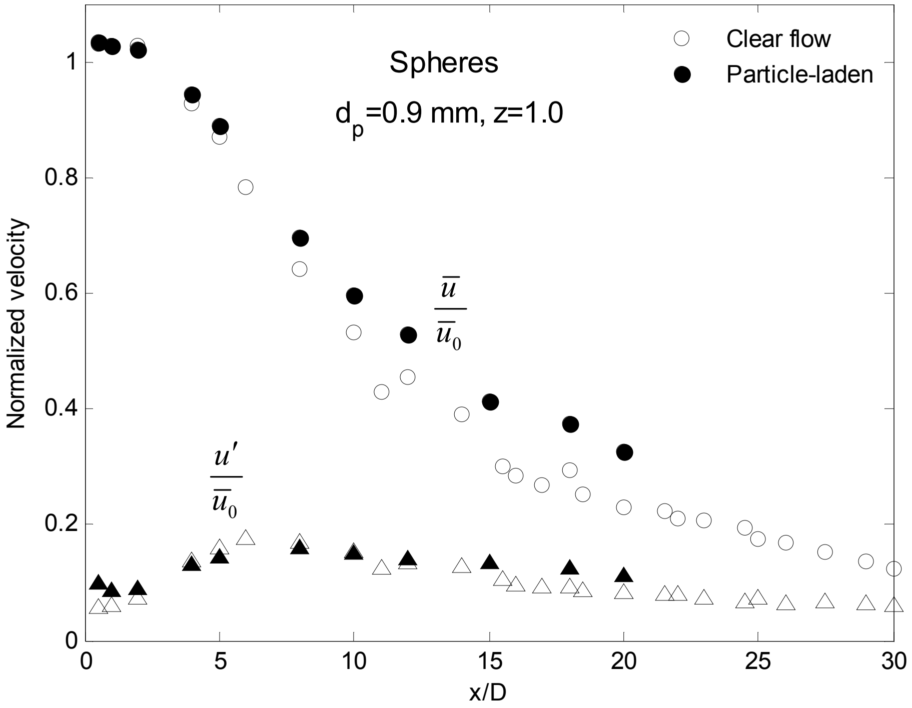

Figure 85: Normalized mean and RMS velocity for spheres with d_p=0.9mm, z=1.0.

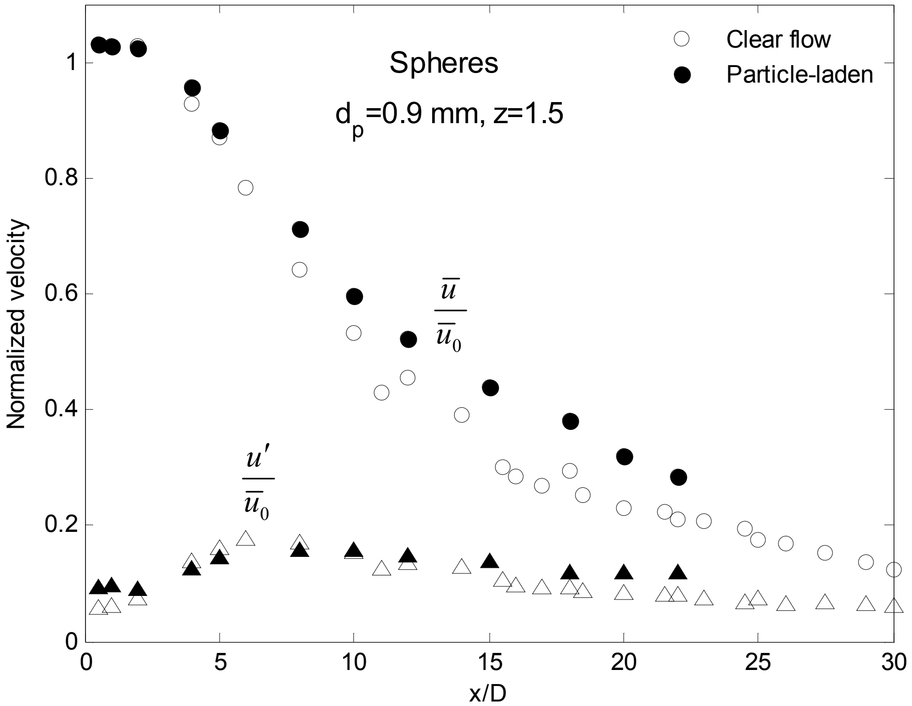

Figure 86: Normalized mean and RMS velocity for spheres with d_p=0.9mm, z=1.5.

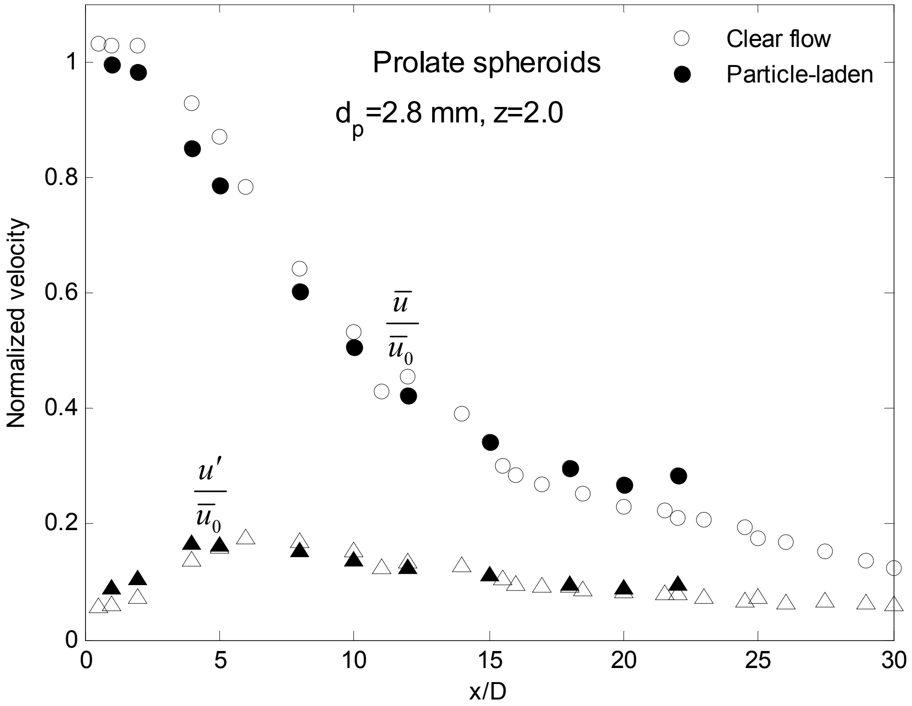

Figure 87: Normalized mean and RMS velocity for prolate spheroids with d_p=2.8mm, z=2.0.

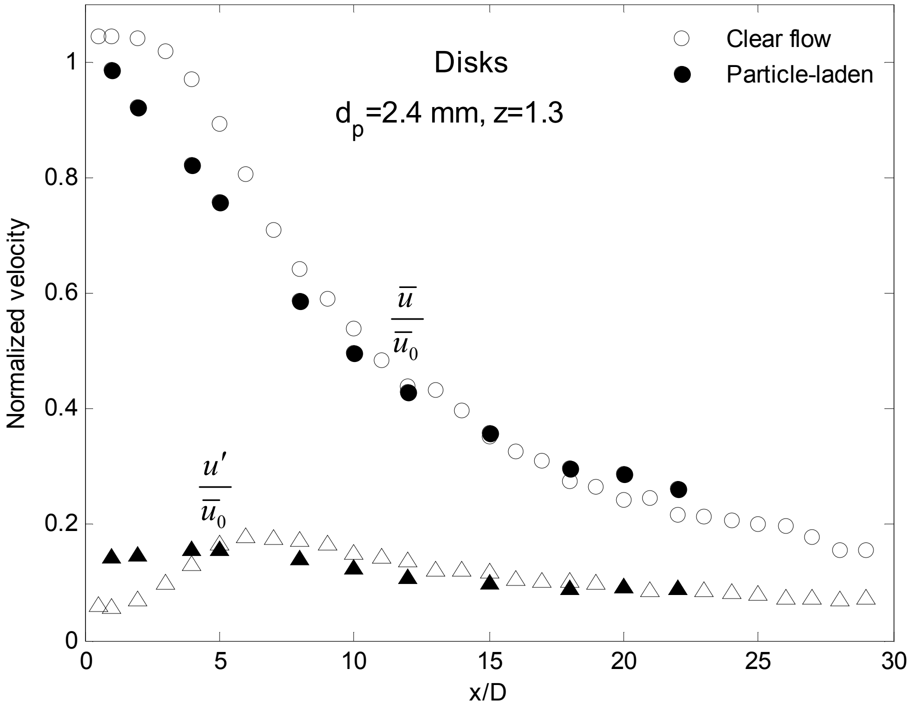

Figure 88: Normalized mean and RMS velocity for disks with d_p=2.4mm, z=1.3.

Appendix C: Evaluation of composite modulation parameters

In addition to the Stokes number, the particle Reynolds number and the length scale ratio which have been suggested to be determining for turbulence modulation also two composite modulation parameters have been suggested by Kenning and Crowe (1997) and by Crowe (2000). Both of these parameters are derived form the transport equation of turbulent kinetic energy where the contribution from the particle phase is considered. From observations that the turbulence generated by freefalling particles was correlated with the volume fraction and the inter-particle spacing, $l_{int,}$ Kenning and Crowe (1997) suggested a hybrid length scale:

$$l_h = \frac{2l_e l_{\text{int}}}{l_e + l_{\text{int}}} \tag{93}$$

to determine the viscous dissipation caused by the particles. Also considering the production by particles and the inherent dissipation they arrive at the following modulation parameter, M_{KC}:

$$M_{KC} = \left(\frac{l_h}{l_e} + \frac{l_h}{k_0^{3/2}} \frac{f\left(u-v\right)^2}{\tau_V} \frac{\tilde{\rho}_p}{\tilde{\rho}_c} \right)^{1/3} - 1 \qquad (94)$$

where k_0 is single phase turbulent kinetic energy, $\tilde{\rho}_p$ and $\tilde{\rho}_c$ is respectively the particle and carrier phase bulk density. The modulation parameter is to be evaluated on the basis of the change in turbulence intensity, $(\sigma - \sigma_0)/\sigma_0$, which has been adopted as the basis of evaluating the turbulence modulation. Using similar approach and approximating the slip velocity with the terminal velocity Crowe (2000) derives the expression:

$$M_C = \left(\frac{1 + C l_e^3 \dfrac{g^2}{u^4} \dfrac{\rho_p u}{\mu_c} \dfrac{1.5^{-3/2}}{18 \sigma_0 f} \dfrac{d_p^2}{l_e^2}}{1 + \left(C \dfrac{\rho_c}{\rho_p} \dfrac{6}{\pi} \right)^{1/3} \dfrac{l_e}{d_p}} \right)^{1/3} - 1 \qquad (95)$$

where f, for the terminal velocity, is approximated as:

$$f^{5/2} = \frac{0.058 g \tau_V d_p \rho_c}{\mu_c} \qquad (96)$$

Both parameters are composite expressions which reflect the influence of the particle size, turbulence length scale and the volume fraction but not the mass loading. In the derivation of the modulation parameter by Crowe (2000) a hybrid length scale which is equal to half of that used by Kenning and Crowe (1997). The investigation by Crowe (2000) wanted to show that turbulence modulation is dependent of the d_p/l_e length scale ratio and in extension of this notion it is chosen to present the result using this parameter as x-axis. Furthermore, since the approximation of f and indeed the entire expression is valid solely for spherical particles only the results for the spherical particles are shown. Figure 89 shows an overview of the results of the present investigation and compares the results with the suggested modulation parameters. The 8 graphs are placed in order with increasing mass loading from left to right and decreasing particle sizes from up to down. It is clear that the parameter suggested by Kenning and Crowe (1997) does not provide a particularly good fit to the present experimental results. This is most likely due to the failure to provide a strong coupling with the particle concentration which varies greatly for the present flow. The parameter by Crowe (2000) seems to capture some of the trends in some cases, but in some cases it provides but a poor fit to the experimental results. By only regarding the later parameter it is clear that this divergence occurs in the lower range of the d_p/l_e scale. For the present investigation this coincides with the transition from the two-way to the one-way coupling regimes. By reviewing the paper by Crowe (2000) it is clear that this model in the low range of d_p/l_e ratios, where the attenuation is dominant, it not sensitive towards the volume fraction and predicts significant attenuation well into the one-way coupling regime, $\alpha<10^{-6}$. To make the model by Crowe (2000) express the right asymptotic behavior towards the one-way coupling regime an exponential decay is assumed and a modified model emerges as:

$$M_{C,\mathrm{mod}} = M_C \cdot \exp\left(-7 \cdot 10^{-6} / \alpha\right) \tag{97}$$

This expression is entered as the slashed line in Figure 89. It can be seen that this simple modification provides a significantly better fit to some of the present experimental data. However, this modification is somewhat unsatisfying in that it does not address the fundamental mechanisms from which this model is derived. Furthermore, there is nothing that indicates that an exponential decay is superior to any other correction, but accuracy of the measured data does not justify a more sophisticated expression. If the ratio between the mass loading and the particle diameter is computed for each of the graphs in Figure 89 it can be observed that the modified model represents a reasonable fit to the present results if this ratio is close to or above unity. If this ratio is below unity there is increasingly disagreement between the model and the experimental data. This suggests that this ratio have some additional influence on the turbulence modulation in view of the suggested model. Considering that the mass flow rate of the carrier phase is constant for the present investigation this ratio can be non-dimensionalised as:

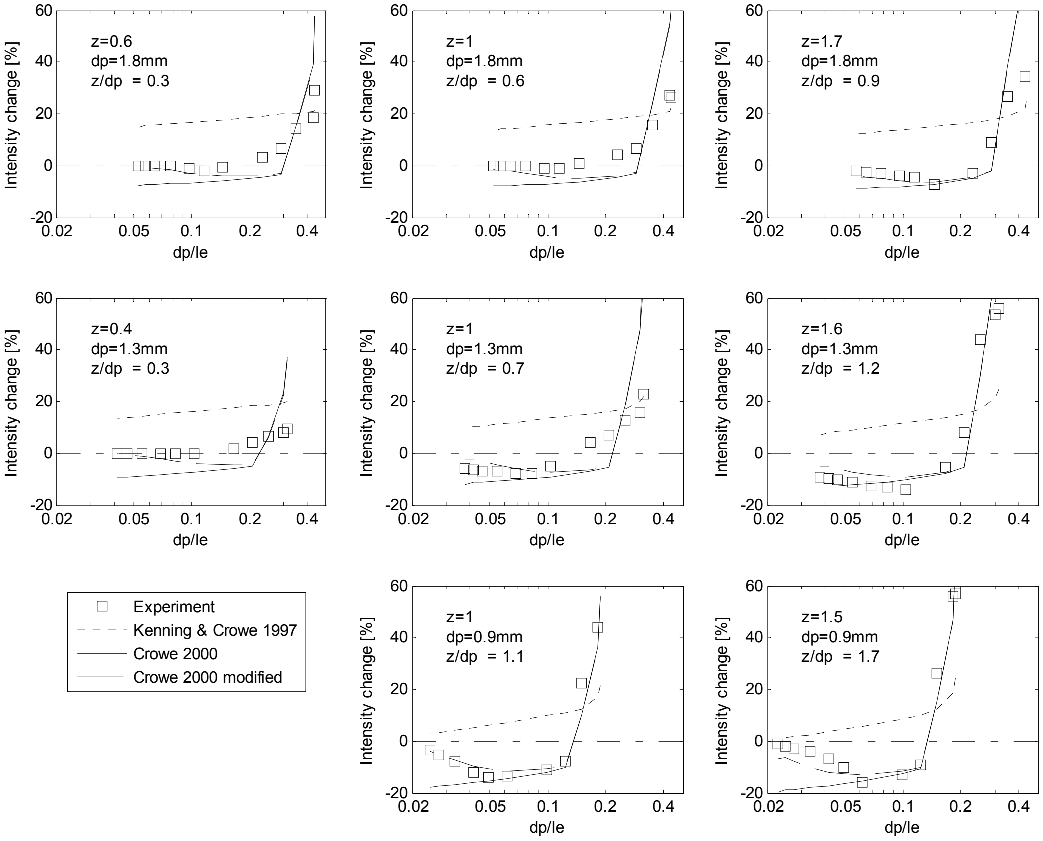

Figure 89: The percentage change in turbulence intensity as function of the length scale ratio for different global mass loadings and particle sizes. Comparison with the modulation parameters suggested by Kenning and Crowe (1997) and Crowe (2000) together with a modified version of Crowe (2000) to give the correct behavior for the low volume fractions.

$$N_M = \frac{\dot{m}_p}{\mu d_p} \tag{98}$$

where the viscosity of the carrier phase is the only additional parameter. It is clear that this factor cannot stand alone when predicting turbulence modulation and it is necessary to incorporate a functional dependency of both the length scale ratio and the concentration of particles.

Appendix D: Turbulent dispersion

Turbulent dispersion of particles is a term used to describe the transport phenomena of discrete particles in a turbulent carrier phase. In the context of dispersion models an often imposed restriction is that the flow can be described as being dilute and that particle-particle collisions is negligible. Turbulent dispersion is a macroscopic process where the motion of the turbulent eddies is acting on the particles as opposed to molecular diffusion or Brownian motion where collision with individual fluid particles is responsible for the particle motion. In this work the term turbulent dispersion is restricted to the effect of the turbulent carrier phase on the discrete particles, where the opposite, the effect of particles on the turbulent carrier phase, is referred to as turbulence modulation.

In the context of turbulent dispersion the particle size relative to the turbulent length scales is important parameter to determine the nature of the interaction. If the particle is smaller than the Kolmogorov scales the particle can be conceptual viewed to be trapped inside one eddy for a given interaction time, τ_{int}, where after it passes on to another eddy. For a particle larger than the Kolmogorov scales the interaction with an eddy larger than the particle is similar to the case of the smaller particle. If the particle encounters an eddy which is smaller than itself it can completely dissipate the eddy or change is structure (Calabrese and Middleman 1979). Commonly turbulent dissipation models assumes that the particle is always significantly smaller than the eddies which it is interacting with inline with the assumption of one way coupling between the turbulent carrier phase and the discrete particle phase.

Another important parameter for turbulent dispersion is the mass or the inertia of the particle. Generally a particle with low inertia is said to be able to follow the motion of the eddies while particles with higher inertia is less affected by the motion of the eddies. This phenomenon is commonly known as the inertia effect and it is characterized by the Stokes number; the ratio of the particle response time, τ_p, to the time scale of the eddy, τ_e. Particles at St<<1 will exhibit a motion which corresponds to a fluid particle while particles at St>>1 will pass though the eddy with minimal alteration of the particle velocity due to the turbulent fluctuations. At intermediate Stokes numbers the turbulent dispersion of the discrete particle has been observed to exceed that of fluid particles due to a slingshot like effect (Tang et al. 1992).

Depending on the terminal velocity of the particle it may remain trapped inside the eddy for the entire eddy life time or it may pass on to another eddy before the decay of the original eddy. This is commonly known as the Crossing Trajectory Effect (CTE). Thus the eddy-particle interaction time, τ_{int}, is taken as the minimum of the eddy life time, τ_e, and the time it takes the particle to cross the eddy, τ_{cr}:

$$\tau_{int} = \min\left(\tau_e, \tau_{cr}\right) \tag{99}$$

To compute the particle trajectories the equation of motion for a single particle is to be solved. It can analytically be solved over small time steps, *Δt*, where the carrier phase velocity, u_c, and the particle response time are assumed to be constant. Considering the acceleration, *a*, of the particle by all other forces than the drag force the new particle velocity and position are determined by:

$$u_p^{n+1} = u_p^n + e^{-\Delta t/\tau_p}\left(u_p^n - u_c^n\right) - a\tau_p\left(e^{-\Delta t/\tau_p} - 1\right) \tag{100}$$

$$x_p^{n+1} = x_p^n + \Delta t\left(u^n + a\tau_p\right) + \tau_p\left(1 - e^{-\Delta t/\tau_p}\right)\left(u_p^n - u^n - a\tau_p\right) \tag{101}$$

Generally the analytic solution is considered to be an efficient algorithm to compute particle trajectories. However, for large time steps or in situations where the particles are not in hydrodynamic equilibrium with the carrier phase velocity it becomes inaccurate and other numerical schemes may be advantageously applied. The main problem is to determine the instantaneous fluid velocity that appears in equation (100) and the time step over which it can be assumed to be constant. In the context of RANS models the fluctuating velocity component is not resolved but only modeled. To include the effect of the carrier phase fluctuating velocity component on the particle trajectories a so-called Stochastic Separated Flow (SSF) modeling approach is utilized where the fluctuating velocity components are discrete piecewise constant functions of time. Their random value is kept constant over an interval of time given by the interaction time. Knowing the interaction time and the random sampled fluctuating velocity the particle trajectory can be found by solving equation (100) and (101) using the interaction time as time step. Obviously, both the interaction time and the fluctuation velocity component need to be sampled from local turbulence properties. The interaction time is determined considering the eddy life time and the particle crossing time. The crossing time is determined from the linearized particle equation of motion:

$$t_{cr} = -\tau_p \ln\left(1 - \frac{l_e}{\tau_p\left|u_c - u_p\right|}\right) \tag{102}$$

where l_e is the characteristic size of the eddy. Obviously equation (102) has no solution when $l_e > \tau_p|u_c - u_p|$. In such a case, the stopping distance is smaller than the size of the eddy and the particle can be assumed to be trapped inside of the eddy. The appropriate interaction time is then the eddy life time. For isotropic flow the two required turbulent scales l_e and τ_e can be determined by the general expressions:

$$\tau_e = A\frac{k}{\varepsilon}\ ,\ \ l_e = B\frac{k^{3/2}}{\varepsilon} \tag{103}$$

where *A* and *B* are two dependent constants. Using the relationship:

$$\tau_e = \frac{l_e}{u'} \ , \ \ k = \frac{3}{2}u'^2 \tag{104}$$

it can be proven that the ratio *A/B* should be equal to $\sqrt{1.5}$. In literature a range of different values for *A* and *B* is used and thus the value of *A* ranges from 0.135 to 0.56 (Shirolkar et al. 1996). For the commercial code used in this study the default values of *A* and *B* is respectively 0.15 and 0.164. However, it is possible to select a random eddy life time where A is defined as a variable:

$$A = -\log(r) \tag{105}$$

where *r* is a uniform random number between 0 and 1. The option of random eddy life generally yields a more realistic description of the carrier phase turbulence seen by the particles. The fluctuating velocity component that prevail during the interaction time are sampled from a Gaussian Probability Distribution Function (PDF) so that:

$$u' = \varsigma\sqrt{\overline{u'^2}} = \varsigma\sqrt{2k/3} \tag{106}$$

where ζ is a normally distributed random number.

The model described above is also often referred to as a Discrete Random Walk model or as the eddy life time model. General limitations for these models are that they are restricted to high Reynolds number flows, where the molecular diffusion can be neglected. In diffusion dominated flows, where small particles should be uniformly distributed, they will instead tend to concentrate in low turbulence regions. Also the particles should be considered to be passive, meaning that no agglomeration is taking place. Furthermore, the described model is not able to rigorously account for the time correlations in the fluctuating carrier phase velocities. Conceptually the eddy velocity is not constant during its life time and instead the particle should be exposed to a range of time correlated velocities while inside the eddy. This is done in time correlated models by using an autocorrelation function. These models are more computational intensive but have the potential to more accurately account for the turbulent dispersion encountered in real flows (Hennick and Lightstone 2000). Dispersion models have only been developed to predict the behavior of spherical particles. Generally non-spherical particles are associated with larger dispersion (Lozano 2004). Due to the larger surface area of a non-spherical compared to a volume equivalent spherical particle the drag force can significantly larger which enables the particles to have a faster response time to the turbulent fluctuations. However, also the secondary motion contributes to the observed dispersion.

Appendix E: Equations of motion for a cylinder at high Re

This appendix contains an account of the model described in Rosendahl (2000) and Yin et al. (2003) and which is used in the current work to predict the motion of cylindrical particles.
For cylindrical particles at higher Reynolds numbers the general equation of translatory particle motion can be expressed as (Yin et al. 2003):

$$\rho_p V_p \frac{du_{pi}}{dt} = F_D + F_L + F_{PG} + F_{VM} + V_p\left(\rho_p - \rho\right) g_i \tag{107}$$

where F_D, F_L, F_{PG} and F_{VM} represent drag force, lift force, pressure gradient force and virtual mass force respectively. The last term represent the buoyancy. F_{PG} and F_{VM} can be approximated using the same calculation method as for spherical particle:

$$F_{PG} = \rho V_p \left(\frac{\partial u_i}{\partial t} + u_j \frac{\partial u_i}{\partial x_j} \right) \qquad F_{VM} = \frac{1}{2} \rho V \frac{d}{dt}\left(u_i - u_{pi}\right) \tag{108}$$

whereas $\mathrm{F_D}$ and F_L is orientation dependent. The general expression for the drag force valid for all shapes can be expressed as the following:

$$F_D = \frac{1}{2} \rho C_D A_{eff1} \left| u_i - u_{pi} \right| \left(u_i - u_{pi} \right) \tag{109}$$

where the effective area A_{eff1} is determined in the direction normal to the direction of motion. Using ideas from the aerodynamic theory of wing sections it is possible to define the incidence angle, α_i, the angle between the main axis and the direction of motion, and the center of pressure, x_{cp}, the distance from the leading edge to the location where the resulting forces of lift and drag act.

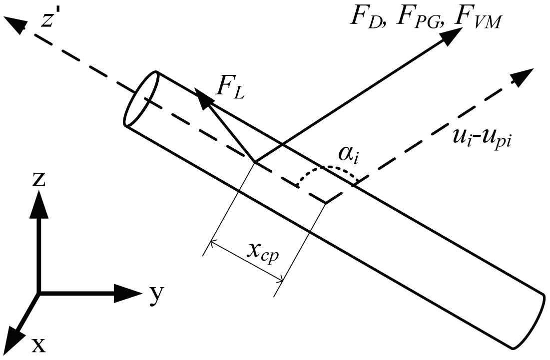

Figure 90: Incidence angle, center of pressure and contact forces.

The effective area A_{effl} can be expressed by a functional relationship of the incidence angle and the particles dimensions, here the particle semi-short axis *a* and semi-long axis *b* is used[9]:

$$A_{effl} = \pi a^2 \left(\cos^2 \alpha_i + \left(\frac{4b}{a\pi} \right)^2 \sin^2 \alpha_i \right)^{1/2} \tag{110}$$

The drag coefficient C_D has been measured for a wide range of shapes but is not commonly available as functional relationship of both Reynolds number, orientation and geometric parameters of the particle for which it ideally should be. One way to deal with this problem is by the using the sphericity factor, ψ, and the volume equivalent diameter, d_{eq}, as geometric parameters and ignore the orientation dependency. Here the following expression for the drag coefficient is used (Chhabra, Agarwal and Sinha 1999; Ganser 1993):

$$C_D = \frac{24}{\mathrm{Re}_p K_1} \left(1 + 0.1118 \left(\mathrm{Re}_p K_1 K_2 \right)^{0.6567} \right) + \frac{0.4305}{1 + 3305 / \left(\mathrm{Re}_p K_1 K_2 \right)} \tag{111}$$

where

$$K_1 = \left(\frac{\sqrt{\frac{4}{\pi} A_{effl}}}{3 d_{eq}} + \frac{2}{3 \psi^{1/2}} \right)^{-1} \qquad K_2 = 10^{1.8148 (-\log \psi)^{0.5743}} \tag{112}$$

The lift force is in general very dependent on the shape and inclination angle of the particle and is thus difficult to estimate. For an infinitely long infinite cylinder in the Newtons law regime the lift force can be determined using the cross flow principle where the lift force is related to the drag force and inclination angle (Hoerner 1965). If this principle is assumed to be valid for

---

[9] For a cylinder *a* is equal to the radius and *b* would be the half-length

finite length cylinder at lower Reynolds numbers the lift coefficient can be determined by the following expression:

$$C_L = C_D \sin^2 \alpha_i \cos \alpha_i \tag{113}$$

Furthermore, the lift force for an axis-symmetric should also by invariant under a 180° rotation of the particle major axis and vanish for α_i=0. Thus the lift force related to the particle major axis, z', is expressed as follows:

$$F_L = \frac{1}{2} \rho C_D A_{eff2} \frac{z' \cdot \left(u_i - u_{pi}\right)}{\left|u_i - u_{pi}\right|} \left(z' \times \left(u_i - u_{pi}\right)\right) \times \left(u_i - u_{pi}\right) \tag{114}$$

where the area normal to the lift force is defined as:

$$A_{eff1} = \pi a^2 \left(\sin^2 \alpha_i + \left(\frac{4b}{a\pi} \right)^2 \cos^2 \alpha_i \right)^{1/2} \tag{115}$$

Torques acting on the particle can be divided into two contributions: one caused by that the center of pressure and the center of gravity is not coincident and one resulting from resistance forces due to rotation. The contact forces act in the center of pressure which is located a distance, x_{cp}, from the center of gravity. Using the major axis, z', the torque can be expresses as:

$$T_1 = \left(x_{cp} z'\right) \times \left(F_D + F_L + F_{PG} + F_{VM}\right) \tag{116}$$

The location of the center of pressure depends upon the incidence angle and the particles aspect ratio. The following semi-empirical expression has been proposed to correlate x_{cp} (Rosendahl 2000):

$$x_{cp} = 0.25b\left(1 - e^{3(1-b/a)}\right)\left|\cos^3 \alpha_i\right| \tag{117}$$

To calculate the torque in the particle reference frame the following transformation is used:

$$T_{I,x'} = \mathbf{A} T_I \tag{118}$$

where A is a the transformation matrix between the particle frame and the co-moving inertial reference frame. The torque due to resistance to rotation always acts to decrease the angular velocity and can be obtained by integration over the surface area of the particle. For a simple uniform flow field this torque can be expressed in the particle reference frame directly as:

$$T_{2,x'} = \tfrac{1}{64} C_D \rho \times 2a \times \omega_{x'}^2 \times (2b)^4 \tag{119}$$

When both rotational and translational motion are included it is customary to use different coordinate systems and account for the relation between them by transformation of coordinates. The particle position is trivially determined from the relation:

$$\frac{dx_i}{dt} = u_{pi} \tag{120}$$

where x_i is the position vector expressed in the inertial frame. The rotational motion uses the particle frame $\mathbf{x}' = [x', y', z']$ with origin at the particles mass center and its axes aligned with the primary axes of the particle while the co-moving coordinate $\mathbf{x}'' = [x'', y'', z'']$ has its axes aligned with that of the inertial frame.

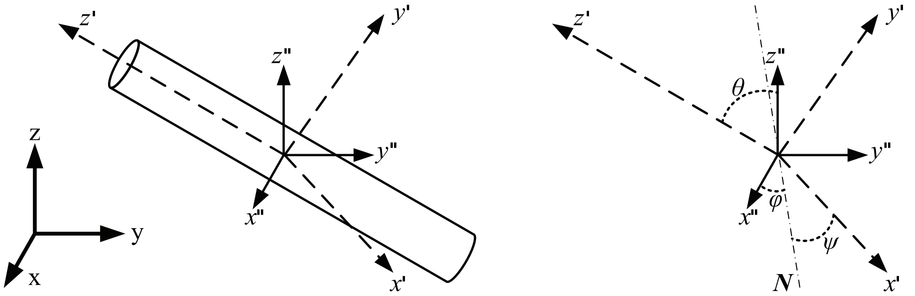

Figure 91: Coordinate system and Euler angles.
$N = \boldsymbol{plane}(\boldsymbol{x}', \boldsymbol{y}') \cap \boldsymbol{plane}(\boldsymbol{x}'', \boldsymbol{y}'')$.

The transformation between the co-moving and the particle frame coordinates can be found in the classical mechanics book by Goldstein (1980):

$$\mathbf{x}' = \mathbf{A} \cdot \mathbf{x}'' \tag{121}$$

where **A** is the transformation matrix whose elements represent the directional cosines of the angles $[\theta, \phi, \psi]$ between the axes. These angles, named Euler angles in honor of Leonard Euler who was the first to define them, are however not suitable for particles which undergo full rotation due to a singularity which occurs when they are used in relation to the angular velocities of the particle. Instead Euler's four parameters $[\varepsilon_1, \varepsilon_2, \varepsilon_3, \eta]$, which are also known as quaternions, can be used. The four Euler parameters represent an expansion of the three Euler angles to eliminate the singularity. The transformation matrix using the Euler parameters are given by Hughes (1986):

$$\mathbf{A} = \begin{bmatrix} 1-2\left(\varepsilon_2^2+\varepsilon_3^2\right) & 2\left(\varepsilon_2\varepsilon_1+\varepsilon_3\eta\right) & 2\left(\varepsilon_1\varepsilon_3-\varepsilon_2\eta\right) \\ 2\left(\varepsilon_2\varepsilon_1-\varepsilon_3\eta\right) & 1-2\left(\varepsilon_3^2+\varepsilon_1^2\right) & 2\left(\varepsilon_3\varepsilon_2+\varepsilon_1\eta\right) \\ 2\left(\varepsilon_1\varepsilon_3+\varepsilon_2\eta\right) & 2\left(\varepsilon_3\varepsilon_2-\varepsilon_1\eta\right) & 1-2\left(\varepsilon_1^2+\varepsilon_2^2\right) \end{bmatrix} \tag{122}$$

The Euler parameters are related to the Euler parameters by:

$$\varepsilon_1 = \cos\frac{\phi-\psi}{2}\sin\frac{\theta}{2},\quad \varepsilon_2 = \sin\frac{\phi-\psi}{2}\sin\frac{\theta}{2},\quad \varepsilon_3 = \sin\frac{\phi-\psi}{2}\cos\frac{\theta}{2},\quad \eta = \cos\frac{\phi-\psi}{2}\cos\frac{\theta}{2} \tag{123}$$

The time rate of change of the Euler parameters, which are related to the angular velocity of the particle, are calculated by:

$$\begin{bmatrix} \dfrac{d\varepsilon_1}{dt} \\ \dfrac{d\varepsilon_2}{dt} \\ \dfrac{d\varepsilon_3}{dt} \\ \dfrac{d\eta}{dt} \end{bmatrix} = \frac{1}{2}\begin{bmatrix} \eta\omega_{x'} - \varepsilon_1\omega_{y'} + \varepsilon_2\omega_{z'} \\ \varepsilon_3\omega_{x'} + \eta\omega_{y'} - \varepsilon_1\omega_{z'} \\ -\varepsilon_2\omega_{x'} + \varepsilon_1\omega_{y'} + \eta\omega_{z'} \\ -\varepsilon_1\omega_{x'} - \varepsilon_2\omega_{y'} - \varepsilon_3\omega_{z'} \end{bmatrix} \tag{124}$$

When the forces and torques that act on the particle are known, the translational and rotational motions of a non-spherical particle may easily be evaluated by using equations (4) – (7) found in chapter 2.

This method represents the only procedure which deals with coupled equation for particle motion at higher Reynolds number. If should be emphasized that this is a semi-empirical model where some effects have been approximated while other effects have been neglected altogether. From the motion of spherical particle forces such as the Basset History force, Saffman lift force and Faxen Force are known to have and influence on particle motion but becomes hopelessly difficult to express for non-spherical particles at higher Reynolds numbers. This model has been verified against measurement of a PVC cylinder falling in a tank of still water, where it performed excellently (Yin et al. 2003).

Appendix F: Particle source term for the Reynolds Stress Model

The Reynolds Stress Model (RSM) similarly to the k-ε model achieves closure to the RANS equation by using transport equations to describe the Reynolds stresses. However, the RSM does not use Boussinesq approximation but instead uses a transport equation for each of the six Reynolds stresses plus an additional transport equation for the dissipation rate. Although, many of the terms which results from the derivation of the exact Reynolds stress equations are unknown and have to be modeled, the RSM tries to reproduce the dynamics of each stress component which in turn enables better modeling of the stresses. The exact transport equation for the Reynolds stresses, derived from the Navier-Stokes equation in a similar way as the *k*-equation, can be stated as:

$$\begin{aligned} &\frac{\partial}{\partial t}\left(\overline{\rho u_i' u_j'}\right)+\frac{\partial}{\partial x_k}\left(\overline{\rho u_i' u_j' \bar{u}_k}\right)=-\left(\overline{\rho u_i' u_k'}\frac{\partial \bar{u}_j}{\partial x_k}+\overline{\rho u_j' u_k'}\frac{\partial \bar{u}_i}{\partial x_k}\right)+\frac{\partial}{\partial x_k}\left(\mu\frac{\partial \overline{u_i' u_j'}}{\partial x_k}\right) \\ &+\frac{\partial}{\partial x_k}\left(-\overline{\rho u_i' u_j' u_k'}-\overline{P' u_i'}\delta_{jk}-\overline{P' u_j'}\delta_{ik}\right)+\overline{P'\left(\frac{\partial u_j'}{\partial x_j}+\frac{\partial u_j'}{\partial x_i}\right)}-2\mu\overline{\frac{\partial u_i'}{\partial x_k}\frac{\partial u_j'}{\partial x_k}}+S_{R_{ijp}} \end{aligned} \tag{125}$$

The starting point for the derivation of the particle source terms in the framework of the Reynolds Stress Model is the following general expression for the source term due to particles:

$$S_{R_{ijp}}=\overline{u_j S_{upi}}+\overline{u_i S_{upj}}-\left(\bar{u}_j\overline{S_{upi}}+\bar{u}_i\overline{S_{upj}}\right) \tag{126}$$

If only the drag force for spherical particles is considered the momentum source due to the presence of particles, S_{upi} can be expressed as:

$$S_{upi}=\frac{\alpha\rho_p}{\tau_p}\left(u_{pi}-u_i\right) \tag{127}$$

If a Reynolds averaging procedure is applied on equation (126) the standard terms appears as:

$$S_{R_{ijp}}=\frac{\alpha\rho_p}{\tau_p}\left(\overline{u_i' u_{pj}'}+\overline{u_j' u_{pi}'}-2\overline{u_i' u_j'}\right) \tag{128}$$

This expression is similar as that which can be derived for the *k*-equation using the standard approach. Again it can be deduced that this term always will act to dampen the stresses. For the consistent approach the instantaneous velocities are to be evaluated at the local position of the particles where the following applies (Lain and Sommerfeld 2003):

$$u_i\big|_s = u_{pi}\big|_s \tag{129}$$

If this expression is substituted into equation (126) the basic source term for the consistent approach emerges:

$$S_{R_{ijp}} = \overline{u_{pj}S_{upi}} + \overline{u_{pi}S_{upj}} - \left(\overline{u}_j\,\overline{S_{upi}} + \overline{u}_i\,\overline{S_{upj}}\right) \tag{130}$$

If equation (127) is substituted into equation (130) the following expression emerges after Reynolds averaging:

$$S_{R_{ijp}} = \frac{\alpha\rho_p}{\tau_p}\left(2\overline{u}_i\left(\overline{u}_j - \overline{u}_{pj}\right) + 2\overline{u}_j\left(\overline{u}_i - \overline{u}_{pi}\right) + 2\overline{u'_{pi}u'_{pj}} - \overline{u'_iu'_{pj}} - \overline{u'_ju'_{pi}}\right) \tag{131}$$

For the normal stresses this expression always assumes a large positive value and hence this term will act to enhance the kinetic energy while the other terms contain correlations of the fluctuating particle velocity which are small in comparison. For the derivation of the new model in the RSM framework the momentum source term, equation (127), is split into two expressions corresponding to two different mechanisms:

$$S_{upi} = S_{upi,1} + S_{upi,2} = \frac{\alpha\rho_p}{\tau_p}\left(u_{pi} - \overline{u}_i\right) + \frac{\alpha\rho_p}{\tau_p}\left(\overline{u}_i - u_i\right) \tag{132}$$

For the derivation of the new model the consistent approach is applied on the first term while the standard approach is applied on the last term. This yields the following source term for the new model to the Reynolds stress equations:

$$S_{R_{ijp}} = \frac{\alpha\rho_p}{\tau_p}\left(2\overline{u}_i\overline{u}_j + 2\overline{u}_{pi}\overline{u}_{pj} - 2\overline{u}_i\overline{u}_{pj} - 2\overline{u}_j\overline{u}_{pi} + 2\overline{u'_{pi}u'_{pj}} - 2\overline{u'_iu'_j}\right) \tag{133}$$

Again it can be realized that this expression can be obtained simply by adding the standard expression and the consistent expression. This expression thus contains mechanisms which can both attenuate and augment the turbulence.
To find the source term to the dissipation rate transport equation it is customary to assume proportionality with the turbulent kinetic energy:

$$S_{\varepsilon p} = C_{\varepsilon 3}\frac{1}{2}\frac{\varepsilon}{k}S_{R_{iip}} \tag{134}$$

where summation in the repeated index *i* is implicit. The constant of proportionality $C_{\varepsilon 3}$ depends on the model used and it is most likely not universal. For the standard method $C_{\varepsilon 3} = 1.1$ while for the consistent method a value of 1.8 is suggested. For the new model a value of 1.0 is recommended.

Appendix G: Evaluation of velocity correlations

In this appendix the relative magnitude of the correlations which exists in particle-fluid flow are evaluated by an analytical approach and by the use of DNS data for decaying turbulence. This analysis is a recap of analysis's which can be found in Elghobashi (1994), M.F. Ligthstone's PhD thesis (Lightstone 1992), S. Hodgson's MSc thesis (Hodgson 1999) and the ongoing work of PhD student C. Strutt, (Strutt 2008). The correlations in question are $\overline{u_i'^2}$, $\overline{u_{pi}'^2}$ and $\overline{u_i' u_{pi}'}$ which all can be found in different evaluations of the source term to the k-equation due to the presence of particles.

From Elghobashi (1994)

The relative magnitude of the second order correlation:

$$\overline{u_i'\left(u_{pi}' - u_i'\right)} \tag{135}$$

which describes the effect of the particles on the *k*-equation using the standard approach are evaluated by imagining different scenarios:

a) The fluid and particles velocities have, on average, the same sign but the fluid velocity u_i' are larger than the particle velocity u_{pi}'. Since the correlation $\overline{u_i' u_{pi}'}$ is smaller than the $\overline{u_i'^2}$ the effect of the particles, equation (135), would be to act as extra dissipation. Similarly it is also possible to state that the correlation $\overline{u_{pi}'^2}$ would be smaller than both $\overline{u_i' u_{pi}'}$ and $\overline{u_i'^2}$ for this scenario.

b) The fluid and particles velocities have, on average, different signs. Here equation (135) would be negative regardless of the magnitudes of the correlations. The particle autocorrelation would similar to the fluid auto correlation, on a average basis, always be positive.

c) The fluid and particles velocities have, on average, the same sign but the particle velocity u_{pi}' is larger than the fluid velocity u_i'. This would result in the correlation $\overline{u_i' u_{pi}'}$ being larger than the fluid autocorrelation $\overline{u_i'^2}$ and that the expression (135) acting as a source of turbulent kinetic energy. The particle autocorrelation would for this scenario be the larger of the correlations.

The scenarios a) and b) are typical of what would be expected for stationary, homogeneous turbulence where the motion of the particles is independent of the initial conditions of the particles. Here, the motion of large particles would be little affected by the turbulent eddies and thus $\overline{u_i'^2} > \overline{u_{pi}'^2}$. While on the other hand the motion of small particles would be greatly affected by the turbulent eddies, they are still required to be accelerated by the eddies and thus $\overline{u_i'^2} > \overline{u_{pi}'^2}$.
Scenario c) requires that the particles are dragging the fluid along which only can be achieved by prescribing special initial conditions for the particles or fluid. For example, DNS studies have shown that for decaying turbulence it is possible that u_i' and u_{pi}' have the same sign and that $\overline{u_i' u_{pi}'}$ are larger than $\overline{u_i'^2}$.

From Lightstone (1992)

The particle autocorrelation can be related to the fluid autocorrelation by integrating the particle equation of motion and utilizing the definition of the fluid autocorrelation function. For the case of stationary homogeneous isotropic turbulence, by subtracting the instantaneous particle equation with the time averaged, the particle equation of motion can be expressed as:

$$\frac{du_p'}{dt} + \beta u_p' = \beta u' \tag{136}$$

where β is the inverse of the particle response time. For simplicity the interfacial forces are expressed solely by the drag force.

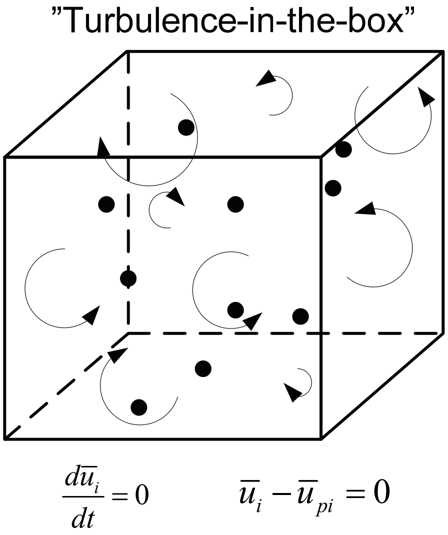

Figure 92: “Turbulence-in-the box”. In the absence of gravity and mean flow particles are only affected by the turbulent eddies and momentum are exchanged through the interfacial forces.

Assuming that the particle is released from rest, the particle equation of motion can be multiplied by $e^{\beta t}$ and integrated to give:

$$u'_p(t) = e^{-\beta t}\beta\int_0^t u'(\xi)e^{\beta\xi}d\xi \tag{137}$$

By squaring both sides and performing time averaging the particle autocorrelation can be found as:

$$\overline{u'^2_p(t)} = e^{-2\beta t}\beta^2\int_0^t\int_0^t \overline{u'(\xi_1)u'(\xi_2)}e^{\beta(\xi_1+\xi_2)}d\xi_1 d\xi_2 \tag{138}$$

By realizing that the fluid autocorrelation function, along the particle path, can be expressed as an exponential function:

$$R(\xi_2-\xi_1) = \frac{\overline{u'(\xi_1)u'(\xi_2)}}{\overline{u'^2}} = e^{-\alpha|\xi_2-\xi_1|} \tag{139}$$

it is possible to reduce the particle autocorrelation to the following:

$$\overline{u'^2_p(t)} = e^{-2\beta t}\beta^2 u'^2\int_0^t\int_0^t e^{-\alpha|\xi_2-\xi_1|}e^{\beta(\xi_1+\xi_2)}d\xi_1 d\xi_2 \tag{140}$$

The constant α is the inverse of the integral time scale of the turbulence. Performing the integration and evaluating the expression as $t \to \infty$ yields the following result:

$$\lim_{t\to\infty} \overline{u_p'^2} = \left(\frac{\beta}{a+\beta}\right)\overline{u'^2} \tag{141}$$

Which states that $\overline{u_i'^2} > \overline{u_{pi}'^2}$ for stationary and homogeneous turbulence.

From Hodgson (1999)

Utilizing a similar approach as above the correlation $\overline{u_i'u_{pi}'}$ can be related to the particle autocorrelation. Multiplying equation (137) with $u'(t)$ and performing time averaging yields:

$$\overline{u'(t)u_p'(t)} = e^{-\beta t}\beta\int_0^t \overline{u'(t)u'(\xi)}e^{\beta\xi}d\xi \tag{142}$$

By utilizing equation (139) this can be reduced to:

$$\overline{u'(t)u_p'(t)} = e^{-\beta t}\beta\overline{u'^2}\int_0^t e^{-a(t-\xi)}e^{\beta\xi}d\xi \tag{143}$$

Performing the integration and evaluating the expression as $t \to \infty$ yields the following result:

$$\lim_{t\to\infty} \overline{u'u_p'} = \left(\frac{\beta}{a+\beta}\right)\overline{u'^2} \tag{144}$$

which is the same as was found for the particle autocorrelation. Thus $\overline{u'u_p'} = \overline{u_p'^2}$ for stationary and homogeneous turbulence. Also note that equation (144) can be derived by taking the fluctuating particle velocity, equation (136), multiplying both side with by u_{pi}', noting that:

$$u_{pi}'\frac{du_{pi}'}{dt} = 0.5\frac{du_{pi}'^2}{dt} \tag{145}$$

perform time averaging and taking the limit as $t \to \infty$

From Strutt (2008)

Particles are released from rest in a DNS simulation of decaying isotropic turbulence. This serves as a test of the results contained in equation (141) and (144). In DNS simulations the correlations $\overline{u_i'^2}$ and $\overline{u_{pi}'^2}$ as well as the mean square fluctuating relative velocity $\overline{u_{rel}'^2}$ are given directly. The correlation $\overline{u_i'u_{pi}'}$ can be found by considering the relation:

$$\overline{u_{rel}'^2} = \overline{\left(u_i' - u_{pi}'\right)^2} = \overline{u_i'^2} + \overline{u_{pi}'^2} - 2\overline{u_i'u_{pi}'} \tag{146}$$

DNS simulation has been performed for the case of solid glass particles released into an air flow with a velocity equal to the fluid velocity. Time was taken for the particles to adjust to the turbulence. The virtual release point was considered when the particles were found to be independent of their initial conditions and the particle-fluid correlations statistic were recorded after that point. This is basically a replication the DNS simulation performed by Elghobashi and Truesdell (1992) which again is a replication of the experiment by Snyder and Lumley (1977). Figure 93 shows that the correlation $\overline{u'u_p'}$ is similar to $\overline{u_p'^2}$ as $t \to \infty$.

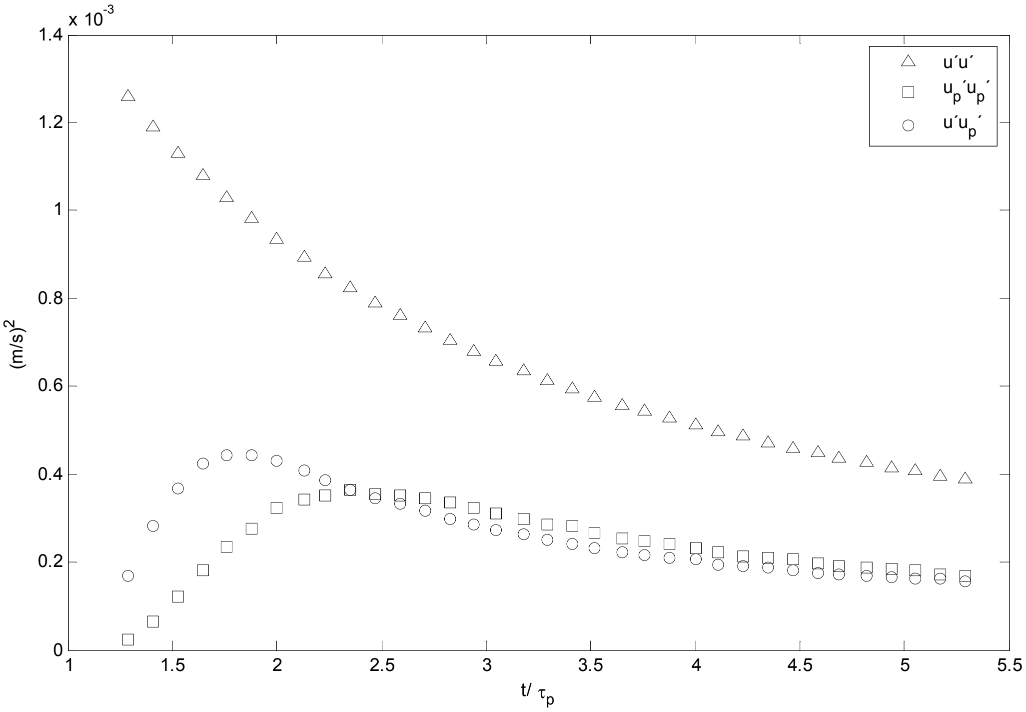

Figure 93: DNS of particle released in isotropic, homogeneous decaying turbulence τ_p/τ_t=0.44.

Appendix H: Combustion modeling

Combustion involves coupling of turbulent fluid flow, heat transfer, and chemical reactions in addition to the handling of combusting particles. Combustion processes are governed by Eulerian transport equations to describe the convection and dissipation of combustion species and heat transfer with additional models for radiation heat transfer and chemical reactions. This makes CFD a natural choice for combustion modeling and applications for the modeling of pulverized coal combustion have become industrial standard. Usually only the most important species and reactions are incorporated into CFD simulations compared to actual combustion.

Chemical reactions of the gas phase

The chemical composition of straw is in terms of an ultimate and a proximate analysis supplied by the boiler manufacturer Burmeister Wain Energy (BWE):

Table 17: Chemical composition of straw:

Ultimate analysis		Proximate analysis		
mass % wet		mass %	wet	dry
C	40.10%	Volatiles	72.0%	80.0%
H	5.24%	Ash	4.5%	5.0%
O	38.99%	Moisture	10.0%	0.0%
N	1.00%	Char	13.5%	15.0%
S	0.20%			
Ash	4.5%	LHV	15000 kJ/kg	
Moisture	9.97%			

Combustion reactions can be simplified to a single global process, where the reaction between fuel and oxygen is complete and all reactions are converted to products. This stoichiometric reaction can be written for straw combustion as:

$$aC + bCH_xO_y + cO_2 + fH_2O \rightarrow dCO_2 + eH_2O \tag{147}$$

where C denotes the char, CH_xO_y denotes the volatiles and H_2O denotes the moisture present in the straw.

For 1kg of fuel the number of moles in equation (147), molar masses, and enthalpy of formations is given in Table 18:

Table 18: Properties of reactions

number of moles		Molar mass		ΔH [J/kmol]		CH_xO_y	
a	11.26mol	C	12.0115	C,O_2	0	x	2.24911
b	23.12mol	H	1.00797	CO_2	-3.93E08	y	1.05379
c	37.97 mol	O	15.9994	H_2O (g)	-2.42E08		
d	34.38mol	N	14.0067	H_2O (l)	-2.86E08		
e	31.54mol	CH_xO_y	31.1383	CH_xO_y	-1.98E08		
f	5.54mol						

For maximum load the burner settings are specified as:

Table 19: Burner settings

	Flow	Temperature
Primary air	4.01 kg/s	323K
Secondary air	1.61 kg/s	593K
Tertiary air	3.76 kg/s	593K
Core air	0.15 kg/s	593K
Total air	9.53 kg/s	593K
Fuel	1.82 kg/s	
excess air ratio, λ	1.1	
A/F – PA	2.2	
A/F – Total	5.2	
heating value	27.300 kJ/s	

For the description of the composition of the continuous phase inside the combusting flow domain the so-called species transport model in Fluent are used. The local mass fraction of each species, Y_i, is solved using transport equations:

$$\frac{\partial}{\partial t}\rho Y_i + \nabla \cdot \rho u_i Y_i = -\nabla \cdot J_i + R_i + S_i \tag{148}$$

where J_i is the diffusion flux of species i due to concentration gradients, R_i is the net rate of production of species i by chemical reaction and S_i is the rate of creation by addition from the dispersed phase. For turbulent flows the mass diffusion is calculated as:

$$J_i = \left(\rho D_{i,m} + \frac{\mu_t}{Sc_t} \right) \nabla Y_i \tag{149}$$

where $D_{i,m}$ is the mass diffusion coefficient for species i and Sc_t is the turbulent Schmidt number. By default the turbulent Schmidt number is set to 0.7. The net rate of production of species i, R_i, is calculated used the Finite rate/Eddy dissipation model described below. For the present simulation the following reactions are considered:

$$CHxOy + 0.54O_2 \rightarrow CO + 1.12H_2O \tag{150}$$

$$CO + 0.5O_2 \rightarrow CO_2 \tag{151}$$

This is also known as a two step reaction scheme. Volatiles, released from particles during devolatilization, are entered as a source term in the continuous phase equation for the species transport of CH_yO_x. This specie reacts with oxygen, entered in the flow domain from boundary conditions, to form CO and H_2O. Next, the CO is reacted with O_2 for a complete combustion. If the concentration of more species is desired they need to be entered as additional transport equations and appropriate reaction schemes need to be specified. At the same time more sophisticated turbulence chemistry interaction models should also be applied to accurately model the detailed chemical mechanisms.

Turbulence - chemistry interaction

Chemical reaction follows the same laws whether the flow is laminar or turbulent. The difference is that the physical flow properties changes and influences the combustion. Most gaseous fuels are fast burning which imply that the overall reaction rate is limited by turbulent mixing. The complex, often unknown, chemical reactions are neglected and the net production rate of species i, R_i, is given by the smaller value of the expression:

$$R_{fuel} = A\rho \frac{\varepsilon}{k} \cdot \min\left(Y_{fuel}, \frac{1}{r} Y_{O_2}, B \frac{1}{1+r} Y_{prod} \right) \tag{152}$$

Where A and B are constants (often $A=4$, $B=0.5$) and r is the fuel/oxygen relationship in reaction (147) and (148). This is known as the eddy-dissipation model which is attributed to the work of Magnussen and Hjertager (1976). The chemical reaction rate is governed by the large-eddy mixing time scale ($\tau_e=k/\varepsilon$). Combustion proceeds whenever turbulence is present and is limited by the lack of fuel, oxygen or products. For pre-mixed flames, such as that resulting from suspension firing, this causes the reactants to unrealistically burn as soon as they enter the computational domain, upstream of the flame stabilizer. This is countered by calculating the laminar Arrhenius reaction rate. For reactions (147) and (148) the laminar Arrhenius reaction rate are given as:

$$R_{CO} = k_{CO} C_{CO} C_{O_2}^{0.25} C_{H_2O}^{0.5}, \qquad k_{CO} = 2.239 \times 10^{12} \exp\left(\frac{1.7 \times 10^8}{RT_{gas}} \right) \tag{153}$$

$$R_{CH_xO_y} = k_{CH_xO_y} C_{CH_xO_y}^{0.1} C_{O_2}^{1.65}, \qquad k_{CH_xO_y} = 5.62 \times 10^9 \exp\left(\frac{1.256 \times 10^8}{RT_{gas}} \right) \tag{154}$$

The net reaction rate is taken as the minimum of Arrhenius and eddy-dissipation reaction rate. In practice, the Arrhenius rate acts as a kinetic switch, preventing reaction before the flame holder. Once the flame is ignited, the eddy-dissipation rate is generally smaller than the Arrhenius rate, and reactions are mixing-limited.

Particle combustion

The combustion of a particle is progressed stepwise by the activation of different modes of heating/combustion by the fulfillment of certain conditions to the particle temperature or mass. An overview of the particle combustion modes used for the present investigation is shown in Table 20.

Table 20: Overview of particle combustion modes

	Conditions	Particle composition at activation
Inert heating/cooling	$T_p < T_{vap}$	volatiles/char/ash
Devolatilisation	$T_p \geq T_{vap}$ $m_p > \left(1 - f_{v,0}\right) m_{p,0}$	volatiles/char/ash
Char combustion	$m_p \leq \left(1 - f_{v,0}\right) m_{p,0}$ $m_p > \left(1 - f_{v,0} - f_{comb}\right) m_{p,0}$	char/ash
Inert heating/cooling	$m_p \leq \left(1 - f_{v,0} - f_{comb}\right) m_{p,0}$	ash

As the particle enters the computation domain its current temperature, T_p, is below the temperature for which devolatillization can proceed, the vaporization temperature T_{vap}, and the particle is heated through convection and radiation heat transfer. When the particle temperature exceeds the vaporization temperature the devolatilization model is initiated. Devolatilization continues until all volatile matter is released, i.e. the current particle mass, m_p, is below the initial particle mass, $m_{p,0}$, minus the volatile fraction, $f_{v,0}$. Char combustion ensues and continues until all char is reacted, i.e. the current particle mass is below the initial mass minus the volatile fraction and the char fraction, f_{comp}. After all combustibles have been evolved from the particle it reverts to inert heating/cooling. At anytime during the combustion process the particle may escape through the outlet. Thus the fraction of unburnt volatiles and char at the outlet may be determined. For all cases all volatile matter has been released before the outlet and only the unburnt char fraction is noted. A particles trajectory is progressed via specification of a limited number of particle time steps. If the particle has not escaped though the outlet before its time is out it is removed from the simulation and the trajectory is recorded as incomplete. Typically this happens when a particle is caught in a recirculation zone. The number of particle time steps for each particle trajectory has been set such that all incomplete particle trajectories represents ash particles for which all volatile matter and char have been evolved. The moisture present in the straw particles is assumed to be evaporated in the mill/fuel pipe before entry into the computational regime. Thus the moisture fraction has been subtracted in the fuel mass flow and is entered in the air mass flow rate as water vapor. Clearly this assumption is more valid for the coal combustion case due to the higher milling air temperature (Coal – 300°C; Straw – 80°C) and due to the lower particle size (Coal – $d_{p,ave}$=60μm; Straw – $d_{p,ave}$=300μm). In Fluent it is possible to include in vaporization process using the so-called wet combustion model. This models the moisture fraction as an addition water film on the particle surface which is to be evaporated before devolatilization can proceed. This is viewed as being unrealistic (Eriksson 2009) and this model has not been used for the base case simulation. The used particle combustion procedure is valid if the particle in question can be assumed to be lumped. Lumped particle analysis assumes that the heat conduction internally in the particle is much greater than the heat convected to the particle. Thus, for lumped particle analysis the particle internal temperature is assumed to be uniform. For a very large particle all three modes of combustion might proceed at the same time in different layers of the particle due to the existence of an internal temperature gradient. To model internal gradients using Fluent, requires a complete reformulation of the particle combustion procedure which is beyond the scope of this thesis.

The particle heat balance during combustion can be stated as:

$$\underbrace{m_p c_p \frac{dT_p}{dt}}_{Accumulation} = \underbrace{hA_p\left(T_\infty - T_p\right)}_{Convention} + \underbrace{A_p\varepsilon_p\sigma\left(\theta_R^4 - T_p^4\right)}_{Radiation} - \underbrace{\frac{dm_p}{dt}h_{fg}}_{Evaporation} - \underbrace{f_h\frac{dm_p}{dt}H_{reac}}_{Surface\ reaction} \qquad (155)$$

where m_p is the particle mass, c_p the particle heat capacity coefficient, T_p particle temperature, h convective heat transfer, A_p particle surface area, T_∞ local fluid temperature at particle position, ε particle emissivity, σ Stefan–Boltzmann constant, θ_R the radiation temperature, h_{fg} the latent heat, H_{reac} the heat released by the surface reaction and f_h is the fraction heat produced by surface reactions which is absorbed by the particle directly. f_h is set to 1.0 since the burnout product is CO (Fluent 2006). The evaporation and surface reaction term is only active during respectively devolatilization and char combustion modes. The effect of non-sphericity has only been implemented by enhancement of the particle surface area compared to that of a volume equivalent sphere with same diameter.

Devolatilization is modeled using a single kinetic rate which assumes that the devolatilization rate is first order dependent of the amount of volatiles remaining in the particle:

$$\frac{dm_p}{dt} = k\left(m_p - \left(1 - f_{v,0}\right)\right), \qquad k = A\exp\left(\frac{E}{RT_{gas}}\right) \qquad (156)$$

where A is the pre-exponential factor and E is the activation energy. During devolatilization the particle diameter changes due to the pressure of the escaping gasses as they diffuse through the pores of the particle. The particle swelling is governed by the swelling coefficient, C_{sw}, which denotes the increase in diameter at the end of devolatilization. Thus $C_{sw}<1$ indicate a decrease in diameter whereas $C_{sw}>1$ indicates a increase in diameter. The following relationship relates the particle diameter to the devolatilization process:

$$\frac{d_p}{d_{p,0}} = 1 + \left(C_{sw} - 1\right)\frac{m_{p,0} - m_p}{f_{v,0} m_{p,0}} \tag{157}$$

where $d_{p,0}$ is the initial particle diameter and the ratio $m_{p,0}\text{-}m_p/f_{v,0}m_{p,0}$ is the fraction of volatiles left.

Char combustion is modeled as a single surface reaction which is limited by the availability of oxygen at the particle surface. This is known as the diffusion limited surface reaction rate model in Fluent. The char reaction can be stated as:

$$C + 0.5O_2 \rightarrow CO \tag{158}$$

The reaction proceeds at a rate which is determined by the diffusion of oxygen to the surface of the particle:

$$\frac{dm_p}{dt} = -4\pi d_p D_{i,m} \frac{Y_{ox} T_{\infty} \rho}{0.5\left(T_p + T_{\infty}\right)} \tag{159}$$

The diffusion limited rate model assumes that the diameter of the particle does not change during the combustion. This result is a porous particle since the effective density decreases due to the decrease in particle mass. Note that several other models for both devolatilization and char combustion exist.

Radiation modeling

Heat transfer in the continuous phase is the result of the combined effect of conduction, convection and radiation. The conductive and convective heat transfer modes are solved for by the solution of a transport equation for the enthalpy distribution due to fluid flow. This is commonly known as the energy equation and can be stated as:

$$\underbrace{\frac{\partial}{\partial t}\rho h}_{accumulation} + \underbrace{\frac{\partial}{\partial x_i}\rho u_i h}_{convection} = \underbrace{\frac{\partial}{\partial x_i}\left(\frac{\mu}{\Pr}\frac{\partial h}{\partial x_i} + \mu\frac{1}{Sc} - \frac{1}{\Pr}\sum_{k=1}^{N} h_k \frac{\partial Y_k}{\partial x_i}\right)}_{diffusion:\ enthalpy\ gradient\ +\ species\ concentration\ gradients} + \underbrace{\frac{\partial p}{\partial x_i}}_{pressure} + \underbrace{S_{rad}}_{radiation} \tag{160}$$

where h is the enthalpy, *Pr* is the mixture Prandtl number, *Sc* is the Schmidt number and S_{rad} is the radiation loss or gain. Here the index *k* is used for the species and the summation is carried out over all *N* species considered in the chosen reaction mechanism. The third mode of energy transfer, radiation, is caused by the emission/absorption of electromagnetic waves/photons which is dependent of the temperature and species composition of the gas. The net radiative heat flux at a point is the difference between the incident radiative heat flux and the outgoing radiative heat flux. To obtain the net radiative heat flux it is thus necessary to integrate the radiation intensity over all possible directions. This is usually done by consideration of a unit sphere as illustrated in Figure 94.

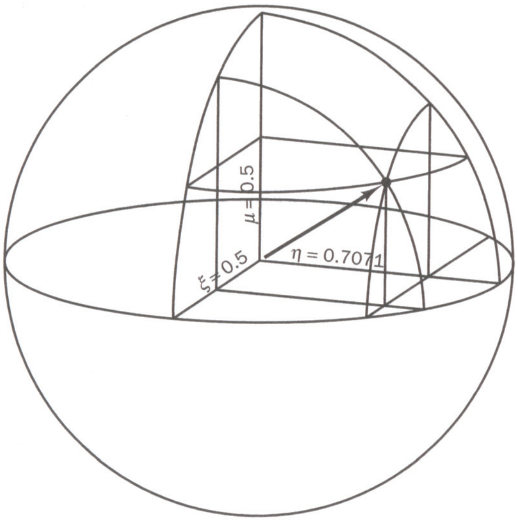

Figure 94: Discrete ordinates in one-eighth of a sphere (Versteeg and Malalasekara 2007).

The discrete ordinates (DO) radiation model solves the radiative transfer equation for a finite number of discrete solid angles, each associated with a vector direction, ***s*,** fixed in the global Cartesian system (*x,y,z*):

$$\frac{dI(\mathbf{r},\mathbf{s}_i)}{ds} = \kappa I_b(\mathbf{r}) - \beta I(\mathbf{r},\mathbf{s}_i) + \frac{\sigma_s}{4\pi}\sum_{j=i}^{n} w_j I_{-}(\mathbf{s}_j)\Phi(\mathbf{s}_i,\mathbf{s}_j) \qquad (161)$$

where $I(\mathbf{r},s_i)$ is the radiation intensity at a given location indicated by position vector $\mathbf{r}$, in the direction $\mathbf{s}_i$. I_b is the black-body intensity, κ is the absorption coefficient, σ_s is the scattering coefficient, β is the extinction coefficient $(\beta = \kappa + \sigma_s)$, w_j are quadrature weights associated with the directions $\mathbf{s}_j$, I_{-} is the incident radiation and Φ is the scattering phase function (Modest, 2003). Each octant of the angular space is discretised into $N_\theta \times N_\phi$ solid angles. For the present work two theta and phi divisions are specified for the angular discretization resulting in a total of 24 directions per unit sphere. The scattering coefficient and the scattering phase function depends on the size, concentration, shape and material characteristics of the particles in the fluid. All the radiative properties generally also have a complex wavelength dependence. The effect of particles is included by modification of the scattering coefficient and inclusion of an additional emission term. Absorption coefficients are calculated by the Weighted Sum of Gray Gas Model (WSGGM) which assigns appropriate weights to account for windows in the radiation spectra for different species. Further information can be found in the Fluent User Guide (Fluent, 2006)

Appendix I: Principles of a low NOx burner

The purpose of a burner is to combine fuel and air to initiate and sustain the combustion process. The main functions that a burner must address is fuel injection, air introduction and flame stabilization. Burners are generally classified by the amount of nitrogen oxide (NOx) emissions they produce: conventional burners, low-NOx burners and ultra-low-NOx burners (Baukal, 2004).

Conventional burners are designed to premix air and fuel as fast as possible in order to achieve a short and stable flame which is tolerant to rapid changes in firing rate and excess air. The drawback of such designs is that the intensity of the combustion produces high thermal NOx emissions and the rapid fuel-air mixing also does not retard fuel NOx formation.

Figure 95: Picture of a low NOx burner (Christensen 2006).

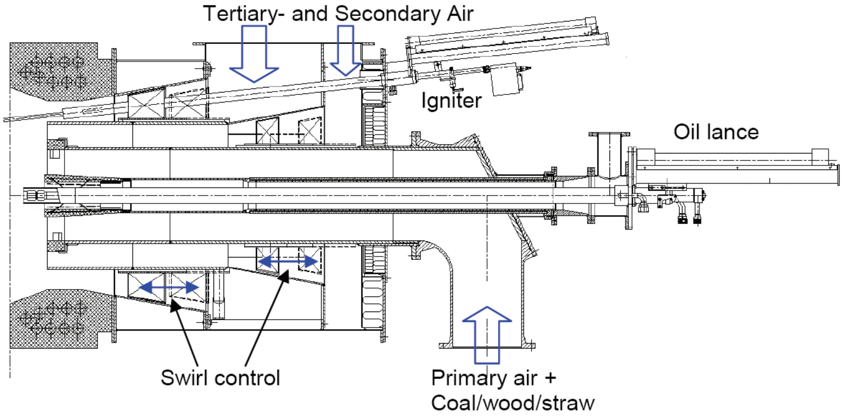

Figure 96: Schematics of a low NOx burner (Gjernes 2006)

Low-NOx burners are designed to minimize the NOx emissions by staging the air: Burners separate air into two or more streams creating a stratified flame structure with a fuel-rich zone close to the burner and fuel-lean zones further from the burner. Both fuel-rich and fuel-lean zones combust at lower peak temperature resulting in lower thermal NOx formation. In addition, the fuel-rich zone in the front part of the flame also reduces the conversion of fuel-bound nitrogen to NOx and thereby leads to lower fuel NOx formation. Although, the increase in sub-stoichiometric zones in the flame increases the prompt NOx formation, this is offset by the large decreases in thermal and fuel NOx formation. The delayed mixing of fuel and air also leads to an increase in flame lengths; up to 50% longer compared to conventional burners of the same heat input. Most burners employ guiding vanes in the primary air nozzle to impart angular momentum and create a small rotational vortex in the front of the burner. This entrains a portion of fuel, creating a combustion zone immediately in front of the vanes which act stabilize the flame and mount it to the burner. These guiding vanes are also known as flame holders or flame stabilizers. These ensure the maintenance of a flammable mixture over a broad range of burner throat velocities and fuel injection rates, and keep the burner operating reliably, even at extremely low flame temperatures. To achieve complete fuel burnout at minimum excess air, the burner design must provide for fuel-lean zones to directly interact with the center fuel-rich sections. This is accomplished by introduction of the secondary air where the majority of the combustion air is introduced (65 to 90%). The secondary air passes through adjustable guiding vanes which act to swirl to the air and can induce a substantial tangential velocity component to the secondary air. The amount of swirl introduced helps to determine the shape of the flame. A high swirl setting results in a short and wide flame whereas a low swirl setting results in a longer flame. To increase the flexibility of combustion staging and flame shaping capabilities, some low-NOx burner designs are equipped with a tertiary air injection. The tertiary air, which can be swirled or completely axial, is mixed in the furnace with the combustion gases to achieve complete fuel burnout.

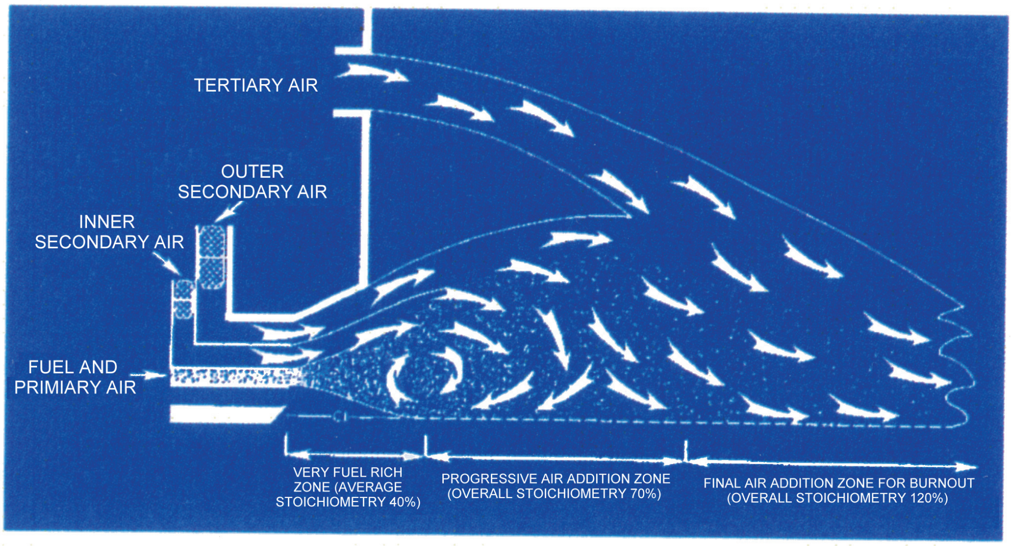

Figure 97: Air staging and combustion zones (Dam-Johansen 2006).

The amount of air used in the tertiary zone can range from 10 to 15%. However, more tertiary air flow will increase the flame length because it adds an additional delay to the combustion process. Ultra low NOx burners use additional initiatives to further reduce NOx emissions. Thermal NOx can be further reduced by flue gas recirculation (FGR) or steam injection. However, the prompt NOx created in the fuel-rich zone still remains. Thus the main feature of ultralow NOx burners is to avoid fuel-rich regions and lower the flame temperature further to reduce thermal NOx to the desired level. This can be done by premixing the fuel with 80% to 100% of the oxygen needed or by rapid mix burners. However, the designs of ultra low NOx burners are often limited in their turn-down ratio due to the risk of flashback.

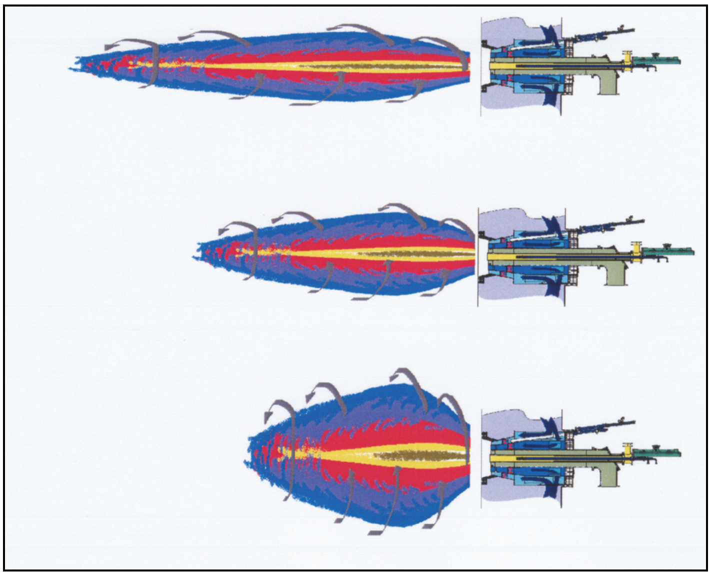

Figure 98: Influence of swirl on flame shape (Christensen 2006).

Appendix J: Implementation of source code in Fluent

Fluent provides several routes for implementation of custom field functions and boundary conditions into the actual code via the GUI. However, the most general and versatile method is to write a piece of custom code in the program language which is native to the Fluent solver and splice it together with the fluent code. In Fluent terminology this custom code is known as a User Defined Function (UDF) and allows the possibility to access and modify the flow variables at each node. As such a UDF can be used to define custom boundary conditions, material properties, and source terms for the transport equations, as well as specify customized model parameters (e.g., Discrete Phase Model (DPM), multiphase models), initialize a solution, or enhance post-processing. UDFs are written in the C programming language using any text editor and the source code file is saved with a .c extension (e.g., myudf.c). UDFs are defined using so-called DEFINE macros which are custom C functions provided by Fluent. A header file, udf.h, contained in the default fluent directory is placed in the beginning of each UDF to provided access to the DEFINE macros and other Fluent-provided macros and functions to be included during the compilation process. All values which are passed between the solver and the UDF are specified in SI units and source terms are to be defined in the for generation rate per volume. For example, a source term for the continuity equation would have units of $kg \cdot m^{-3} \cdot s^{-1}$. Once defined, a UDF are to be compiled in Fluent. In the compiling process a shared object code library is first built and is then loaded into Fluent by a process called dynamic loading. Once compiled the UDF functions become visible and selectable in the graphics panels, and can be hooked to a solver by choosing the function name in the appropriate panel. In Figure 99 is shown an illustration of the solution procedure for the used solver with the UDF interaction included. UDFs are called at predetermined times in the solution process. DEFINE_SOURCE UDFs are evaluated whenever the associated transport equation is updated.

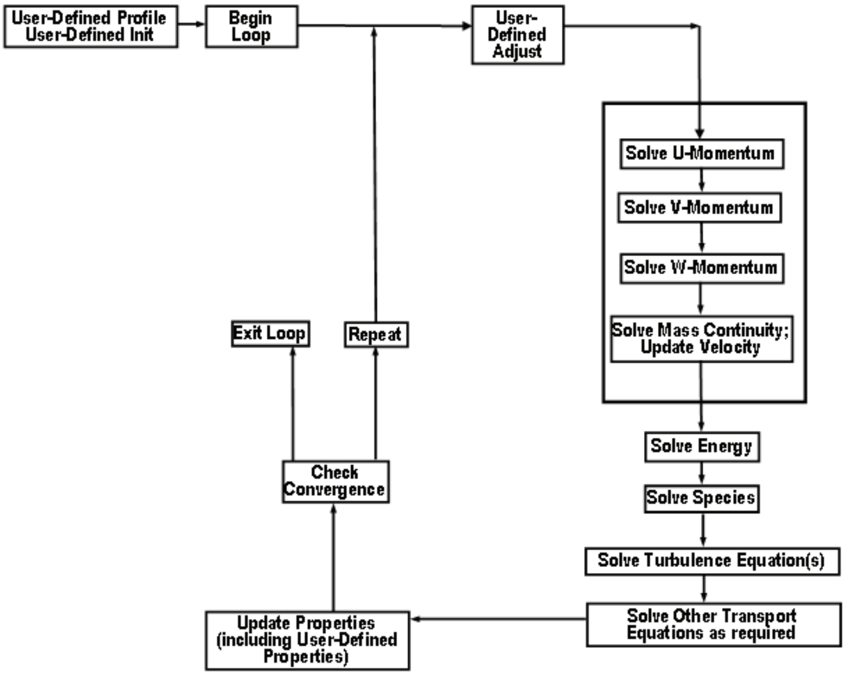

Figure 99: Solution Procedure for the Pressure-Based Segregated Solver (Fluent 2006)

The DEFINE_SOURCE macro is used to specify custom source terms for the different types of solved transport equations. The DEFINE_SOURCE macro and it arguments are stated in the following way:

$$\text{DEFINE\_SOURCE(name, c, t, dS, eqn)} \tag{162}$$

The argument name indicate the name of the UDF, and is supplied by the user, c is the index which identifies the cell on which the source term is to de applied and t is similarly a pointer to the cell tread. Both are automatically passed by the fluent solver as it loops over all the cells in the domain in which it is applied. The definition of the DEFINE_SOURCE macro contains a cell loop thus it is only necessary to define the actual source term which is to be implemented in the transport equation. The argument dS is an array that contains the derivative of the source term with respect to the dependent variable of the transport equation. If the source term contains derivative this argument may be used to linearize the source term to enhance the stability of the solver. The argument eqn is an integer number to specify the number of equations. The function returns a real number specified with the RETURN argument at the end of the UDF.

It is prudent to note at UDF's are not optimized coding in the same way as the inherent models used in the solver. Thus depending on the sophistication of UDF the implementation of custom source terms will be more computational expensive then the base coding.

Strategies to calculate the slip velocity in Fluent

There are two main strategies concerning the use of the particle velocity which is included in the source term. One deals with the direct acquisition of the particle velocity at each cell while the other assumes that the particles are traveling at terminal velocity and deduce the particle velocity in relation to the mean fluid velocity. As is shown below both methods have its strong and weak features. Firstly, it is important to note that there is no standard methodology implemented in fluent to acquire the Lagrangian particle quantities at each cell of the Eulerian discretised fluid domain. As default, only the mass concentration is stored as a variable in addition to the momentum coupling which is implemented in code.

To obtain the particle velocity together with the particle density and diameter for non-uniform particle distributions for each particle at each cell it is necessary to implement an acquisition routine using UDF's. As can be seen in the source code below a routine which first creates memory to store the particle variables and then loops over all cell particle in each cell and over all cells in the domain to calculate the particle source term for the k and ε transport equations have been implemented. The function returns the mass weighted mean of the source term calculated from the properties of each individual particle present in the cell. A more obvious method would be to first calculate the mean of the particle velocity and a single source term using only mean values however this method would neglect the influence of the fluctuating particle velocity. This routine thus uses the instantaneous velocity directly in the calculations and uses that:

$$\overline{\left(\bar{u}_i - u_{pi}\right)}^2 = \left|\bar{u}_i - \bar{u}_{pi}\right|^2 + \overline{u'_{pi}u'_{pi}} \tag{163}$$

The advantages using this method compared to relying on the terminal velocity is obviously the possibility to acquire all terms directly rather then model or neglecting some terms. This method also enables dealing correctly with multiple particle sizes and properties which likely have different concentration profiles.

For many flows it is acceptable to use the terminal velocity of a freely falling particle as the relative velocity between the fluid and the particle. For a general flow the smaller the particle the faster will the particle be able to respond the sudden velocity difference, from the particle point of view, and the better will this approximation be. However, for large particles in flows with high strain regions, in developing flows or in flows with influential boundary conditions using such an approach can cause significant discrepancies. The advantage using the terminal velocity is that this is much less computational intensive and much simple to implement than sampling the particle velocity by looping over all particles in all cells in the domain. Furthermore, for Fluent it is necessary to use the so-called unsteady particle treatment when looping over the particles while using the terminal velocity it is possible to use the so-called steady particle treatment which again decreases the simulation time.

Actual Source code

The following paragraphs contain the UDF source code used to implement the new model in Fluent. Text wrapped with /* */ contains comments to the code.

```
#include "udf.h"    /*   header file which enables DEFINE macros and other Fluent-provided macros */


DEFINE_SOURCE(k_new_model_all_terms,c,t,dS,eqn)  /* source term for the k equation */
{

  Domain *d=Get_Domain(1);  /* domain used in the particle loop.  this should be the fluid domain , change
index if necessary*/

  Particle *p; /* particle index to be used in particle loop */

  double umean[3],vmean[3], mass_mean, dp, vrel, rhop; /* declaration of variables */
  double Skp,Sep,t_p,t_V,f,rep,aaa, muc, rhoc, tedc, tkec,v_mean[3];
  int i;  /* index used in for loops  */
  #define g 9.8         /* gravity constant */
  #define ce3 1.0    /* proportionality constant */

  Alloc_Storage_Vars(d, SV_DPM_PARTICLE_BIN, SV_NULL); /* memory is allocated for the particles
which are to be bined in each cell */

bin_particles_in_cells(d); /*  particles are bined in each cell of the fluid domain */

            begin_particle_cell_loop(p, c, t) /* loops over all particle p which are contained in each cell c  */
            {

                        for(i=0;i<3;i++)   /*  instantaneous particle velocity ( started using the mean velocity but
switch to used to the instantaneous velocity to include all as prescribed in the definition of the new model but
did not update the variable name) */
                        {vmean[i] = p->state.V[i];
                        }

                        umean[0] = C_U(c,t);  /*  mean fluid u velocity at center of cell*/
                        umean[1] = C_V(c,t);  /*  mean fluid v velocity at center of cell */
                        umean[2] = C_W(c,t); /*  mean fluid w velocity at center of cell */
                        rhop = p->state.rho;   /*  individual particle density */
                        dp = p->state.diam;    /*  individual particle diameter */
                        rhoc = C_R(c,t);         /*  fluid density at center of cell */
                        muc = C_MU_L(c,t);  /*  fluid  dynamic viscosity at center of cell */
                        tkec = C_K(c,t);          /*  fluid turbulent kinetic energy at center of cell */
                        tedc = C_D(c,t);          /*  fluid dissipation rate at center of cell */

                        vrel=sqrt(pow((umean[0]-vmean[0]),2)+pow((umean[1]-vmean[1]),2)+pow((umean[2]-
vmean[2]),2)); /* calculation of slip velocity using the instantaneous particle velocity and the fluid mean velocity!
*/

                        rep=dp*vrel*rhoc/muc;                         /*  particle reynolds number*/

                        f= 1+0.15*pow(rep,0.687);                      /*Sciller and Naumann drag correction at higher
re numbers - rep<800 only */

                        t_V=((dp*dp)*rhop)/(18*muc);             /* particle time constant */

                        t_p=t_V/f;                                     /* particle response time */
```

```
                mass_mean +=p->state.mass; /* += indicate summation of contribution from each
particle, here summation of particle mass */

                aaa += ((vrel*vrel-2*tkec)*C_DPMS_CONCENTRATION(c,t)/t_p)*p->state.mass;   /*
summation of source term from each particle multiplied with the particle mass */

                Skp = aaa/mass_mean; /*mass weigthed mean of the source contribution from each
particle stream*/

        }
        end_particle_cell_loop(p, c, t)  /* terminate particle loop */

        Free_Storage_Vars(d, SV_DPM_PARTICLE_BIN, SV_NULL); /*  release allocated memory*/

        return Skp; /* source of turbulent kinetic energy which is returned to the solve */

} /*end source term loop */



DEFINE_SOURCE(e_new_model_all_terms,c,t,dS,eqn)  /* source term for the ε equation, since this is
basically the same as for the k equation this part of the code has not been commented. It was found to be
necessary to perform the particle loop for both the k and ε equation to get the code to work */
{

 Domain *d=Get_Domain(1);
 Particle *p;

 int i;
 double umean[3],vmean[3], mass_mean, dp, vrel, rhop;
 #define g 9.8
 #define ce3 1.0

 double Skp,Sep,t_p,t_V,f,rep,aaa, muc, rhoc, tedc, tkec,v_mean[3];

        Alloc_Storage_Vars(d, SV_DPM_PARTICLE_BIN, SV_NULL);

        bin_particles_in_cells(d);

        begin_particle_cell_loop(p, c, t)
        {

                for(i=0;i<3;i++)
                {vmean[i] = p->state.V[i];
                }
                umean[0] = C_U(c,t);
                umean[1] = C_V(c,t);
                umean[2] = C_W(c,t);
                rhop = p->state.rho;
                dp = p->state.diam;
                rhoc = C_R(c,t);
                muc = C_MU_L(c,t);
                tkec = C_K(c,t);
                tedc = C_D(c,t);

                vrel=sqrt(pow((umean[0]-vmean[0]),2)+pow((umean[1]-vmean[1]),2)+pow((umean[2]-
vmean[2]),2));

                rep=dp*vrel*rhoc/muc;
```

```
        f= 1+0.15*pow(rep,0.687);

        t_V=((dp*dp)*rhop)/(18*muc);

        t_p=t_V/f;

        mass_mean += p->state.mass;

        aaa   +=   (ce3*(vrel*vrel-2*tkec)*C_DPMS_CONCENTRATION(c,t)/t_p)*tedc/tkec*p-
>state.mass;

        Sep = aaa/mass_mean;

    }
    end_particle_cell_loop(p, c, t)

    Free_Storage_Vars(d, SV_DPM_PARTICLE_BIN, SV_NULL); /*  release allocated memory*/

        return Sep;
}
```

Appendix K: Principles of Laser Doppler Anemometry

The following appendix has been written and is currently used as an educational note at the engineering educations at AAU. The term Laser Doppler Velocimetry is used in this note whereas in the rest of the thesis the term Laser Doppler Anemometry is used. These different notations deal with exactly the same technique and are used in replacement of one another.

A brief introduction to Laser Doppler Velocimetry

by Matthias Mandø
Institute of Energy Technology, Aalborg University
email: mma@iet.aau.dk

Table of contents:

Acknowledgement

This document is indented as a brief introduction to the basic principles associated with Laser Doppler Velocimetry (LDV). Worked examples for the calculation of important parameters are available in the back of this note. Additional information can be found in Albrect et al. (2003), which is regarded as the most exhaustive work to date on LDV and in the BSA Flow Software manual which contain detailed instructions to the practical use of the LDV system. This note has taken inspiration from a similar introduction note by Meyer (2004) and the reference guide provided by Dantec Dynamics A/S. The author is also grateful for the comments provided by associated professor Henrik Sørensen, Aalborg University.

M.Mandø, Institute of Energy Technology, July 2008

Introduction

Laser Doppler Velocimetry (LDV) uses the scattered light from small tracer particles, which have been deliberately added to the flow, to measure the flow velocity. The LDV technique was first demonstrated in the early sixties after the advent of the laser and came into wide spread use in the 1970s. Today, LDV is regarded as a mature technique where commercial systems with easy setup and operation are available for purchase. LDV systems are only rarely seen in the process industry but have found a home in many research and development departments. The advantages of LDV compared to other measurement techniques can be summarized as follows:

- Non-intrusiveness
- Directional sensitivity
- High spatial and temporal resolution
- Independent of pressure and temperature

Besides the addition of small tracer particles the only thing which is required for measurement using LDV is optical access. By the use of up to three overlapping measurement volumes using laser light with different wavelength all velocity components can be determined unambiguously. LDV can be applied to reacting multiphase flows to provide point measurements suitable to use as validation for computational methods without risking the destruction of the probe or disturbing the flow field. The size of the measuring volume can be from about 20 μm to several mm and measurements can be sampled with an average sampling rate of up to an order of 100 kHz depending on the setup. Although for practical measurements the acquisition rate should be limited by the particles ability to follow the flow. Velocities up to 1000 m/s can be measured from distances ranging from 1 mm to 2 m. LDV can provide both one-time statistics such as calculation of the ensample mean and standard deviance as well as two-time statistics including spectral analysis.

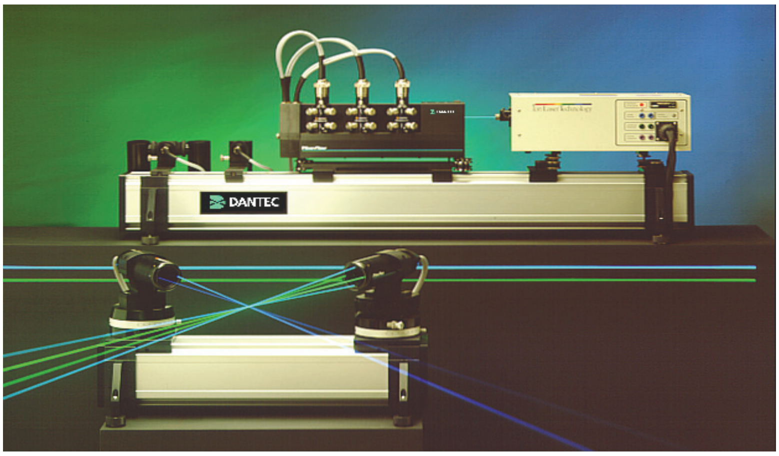

Figure 1: Commercial 3-component LDV system from Dantec Dynamics A/S

Laser Safety

LDV measurements involve the use of class 3 or 4 lasers which can pose significant danger if handled incorrectly. To be allowed to handle laser equipment at Aalborg University it is required that a laser safety course has been passed. Below follows some general guidelines which always should be respected while in the lab.

NEVER look directly into a laser beam or expose your skin to laser light. Any eye damage is permanent and cannot be mended with time. Also, be aware of reflections. As a general precaution, any reflections should be shielded so that they do not exit from the measurement area. This can be done with thick black cloth or black cardboard screens. Appropriate eye goggles can be worn for additional safety, however they do not permit you to see the laser beam; sometimes goggles are useful - sometimes not! Similarly, the laser beam and possible reflections can be seen more clearly in a dark room, however, the darkness also dilate the pupils and thus increases the risk of eye damage. During alignment use low intensity laser beams and remove reflecting metal, such as rings, watches and bracelets from your hands. Arrange your equipment safely so that it can not be knocked over and make sure that there are no loose wires lying on the ground. Keep out of the way of traversing equipment and make sure that the probe can move to the end positions without obstructions. When the laser equipment is in use, appropriate warning signs should be placed on the entrance to the laboratory. Additional markings such as blinking lights and chains may used to secure the laboratory while in use. When leaving the room use the shutter or turn of the laser.

Figure 2: Common Laser warning markers.

The Doppler Effect

The Doppler Effect can be stated as the change in frequency and wavelength of a wave received by a stationary observer from a moving emitter. In LDV the laser emits light with a given wavelength towards the moving tracer particle. The light scattered by the particle has a different frequency due to the motion of the particle; the so-called Doppler shift. The Doppler shift depends on the velocity of the moving particle and on the angle between the incident and scattered light. The Doppler Effect is illustrated in Figure 3.

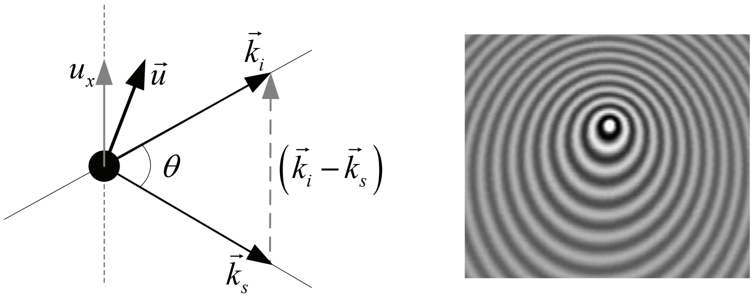

Figure 3: Doppler effect for a particle with velocity u hit by a light beam with wave vector k_i. The scattered light in the direction of the detector is denoted with the wave vector k_s. On the right is shown a source of waves (the scattering from a moving particle) moving upwards. The frequency is higher on the top, and lower on the bottom.

Incident light with the wave vector k_i hits the particle which emits scattered light with wave vector k_s. A wave vector has the same direction as the light and the length $k=2\pi/\lambda$ where λ is the wavelength of the light. It can be shown that the difference in frequency between the emitted light and the received light, the Doppler shift f_D, is:

$$f_D = \frac{1}{\lambda_i} \vec{u} \cdot \left(\vec{k}_i - \vec{k}_s\right) \tag{1}$$

Since the frequency of the light is much greater than the frequency of the Doppler shift the latter can be calculated as:

$$f_D = \frac{2u_x}{\lambda_i} \sin\left(\frac{\theta}{2}\right) \tag{2}$$

where θ is the angle between the emitted light and the scattered light received at the detector. As indicated in Figure 3 the velocity of the particle is proportional to the Doppler shift. Since the Doppler shift is much smaller than the frequency of the light it is difficult to resolve directly. Practical LDV systems are therefore based on a dual-beam principle where the light collected at the receiver is a mixture of two different Doppler shifted light signals. Figure 4 shows the principle of the dual-beam setup.

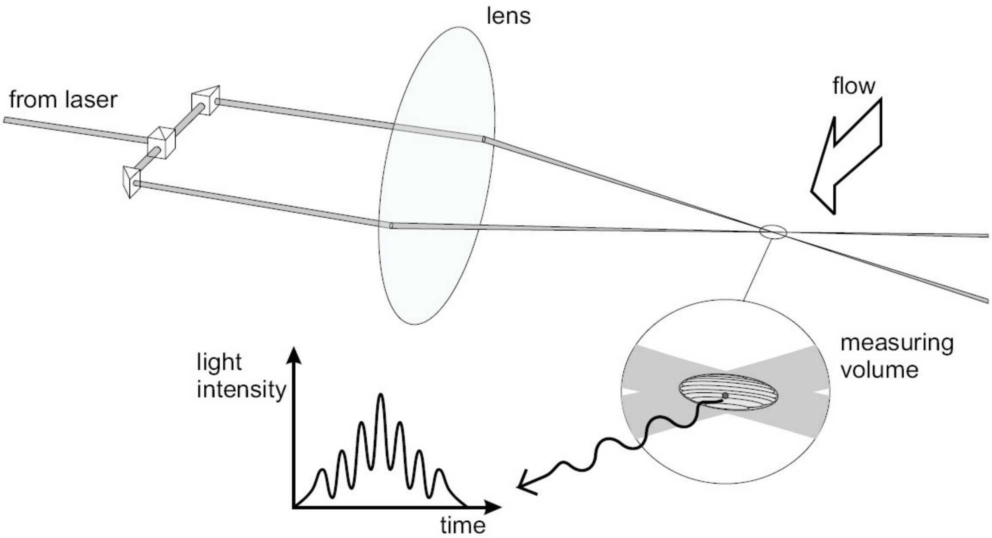

Figure 4: The dual-beam principle. From (Meyer 2004).

At the intersection between the two laser beams an interference pattern will form. The pattern consists of planes with high intensity and planes with low intensity as shown in Figure 5. These alternating planes are also known as fringes. A particle passing through the fringe pattern will emit scattered light with a frequency proportional to the distance between the fringes and the velocity u_x of the particle. The fringe model is the most intuitive way for explaining the dual-beam principle but it cannot explain e.g. multiple particle detection. For a more thorough explanation the reader is referred to Albrect et al. (2003)

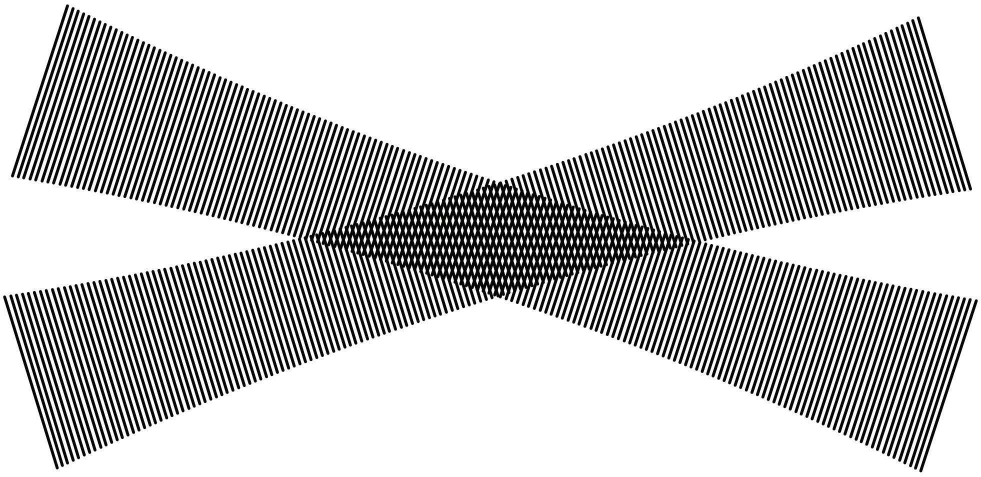

Figure 5: Fringes from in the intersection between two coherent laser beams.

Optical Parameters

The distance between the fringes δ_f can be determined by the angle between the two beams and the wavelength of the of the coherent laser light λ:

$$\delta_f = \frac{\lambda}{2\sin\left(\theta/2\right)} \tag{3}$$

The particle velocity normal to the plane of the fringes u_x can then be found from the relation:

$$u_x = \delta_f f_D \tag{4}$$

which is the same result as obtained in equation (2).

It is often useful to determine the physical extent of the measurement volume formed by the intersecting laser beams. The measurement volume is ellipsoidal in shape and has a Gaussian intensity distribution in all 3 dimensions. The thickness of the laser beam and the measurement volume is defined by there borders where the intensity is $I=1/e^2$ (≈ 14%) of full intensity. When a laser beam is focused by a lens with a focal length F the minimum beam thickness, the beam waist, is found at the focal point of the lens:

$$d_f = \frac{4}{\pi}\frac{F\lambda}{ED_L} \tag{5}$$

where D_L is the initial thickness of the laser beam and E is the beam expansion factor. Similarly the dimensions of the measurement volume can be found from the relations:

$$d_x = \frac{d_f}{\cos\left(\theta/2\right)}, \qquad d_y = d_f, \qquad d_z = \frac{d_f}{\sin\left(\theta/2\right)} \tag{6}$$

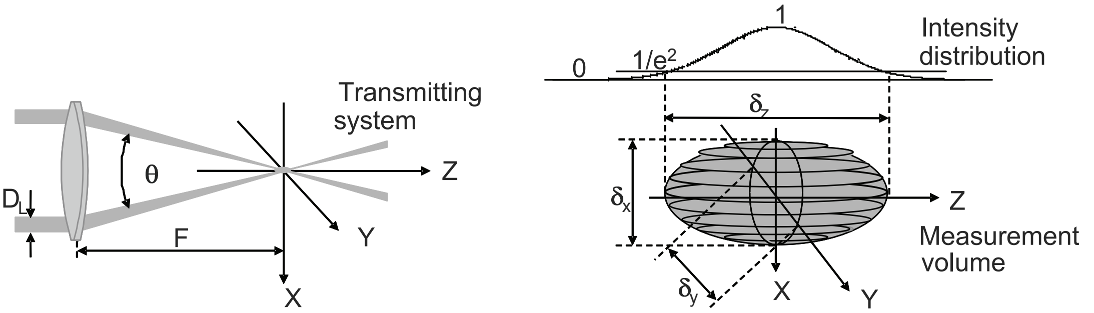

Figure 6: The measurement volume and its dimensions. From (Dantec, 2000).

Tracer Particles

It is important to realize that the LDV technique does not measure the velocity of the flow but the velocity of small particles or bubbles dispersed in the flow. Thus it is of prime interest that the particles are able to follow the flow. A parameter for a particles ability to follow the flow can be derived from the equation of motion for a single particle. If only Stokes drag is considered, i.e. $Re_p<1$, this can be expressed as:

$$\frac{dv}{dt}=\frac{1}{\tau_V}(u-v), \qquad \tau_V=\frac{(\rho_p-\rho)d_p^2}{18\mu} \tag{7}$$

where τ_V is the particle momentum response time. If this ordinary differential equation is solved for constant fluid velocity u and an initial particle velocity of zero the following result is obtained:

$$v=u\left(1-e^{-t/\tau_V}\right) \tag{8}$$

which states that the momentum response time is the time required for the particle to reach 63% (*e-1/e*) of the fluid velocity. The response time for a 2 μm oil particle in air τ_V is about 10 μs. Thus, it is desired of a tracer particle that its density match that of the fluid and that it is as small as possible. The other main quality of a tracer particle is its ability to scatter light efficiently. This means that the particle should be as large as possible and have a reflective index very different from the fluids. Notice that these desired properties are often in conflict as can be in Figure 7. The desired properties of tracer particles can be summed up as follows (Dantec, 2000):

- Able to follow the flow
- Good light scatterers
- Conveniently generated
- Cheap
- Non-toxic, non-corrosive, non-abrasive
- Non-volatile, slow to evaporate
- Chemically inactive
- Clean
- Homogeneous size distribution

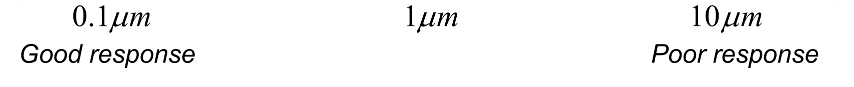

Figure 7: Prosperities of heavy particles in air for variable particle size.

Table 1: Properties of typical tracer particles

Particles in air			
type	Size [μm]	Density [kg/m^3]	Comments
glycerine, oil droplets	1 – 3	800	Generated by atomization
smoke	0.1 – 1	1500	low light scatter efficiency
TiO_2/Al_2O_3	0.5 – 2	3500	for high temperature flames
micro-balloons	30 – 100	30	efficient light scatter
Helium soap bubbles	1000 – 3000	1.2	neutrally buoyant
Particles in water			
Polymer beads	5-100	1050	can be made fluorescent
hollow glass spheres	10-30	1000	efficient light scatter
gas bubbles	50-1000	~1	easy removal of seeding

Table 1 summarizes the properties of the most commonly used particles. Seeding generators and tracer particles are commercially available from specialized vendors e.g. Dantec Dynamics A/S.

The most common tracer particles used for air or gas flows are small droplets made by atomization of glycerine or various organic oils. The small size and narrow size distribution gives excellent flow tracking capabilities for most air flows. These tracer particles are non-volatile, non-toxic and do not evaporate, however, given time, these droplets will adhere to exposed surfaces, which much be cleaned regularly for optimal optical access. For high temperature applications more expensive metal oxides such as TiO_2 or Al_2O_3 particles are often used. Alternatively, soot particles naturally formed in combustion processes can be used providing that the light intensity is sufficient. For applications where a high light scattering efficiency are desired micro-balloons, made of expanded plastic, or alternatively helium filled soap bubbles can be used. Both types can be made nearly neutrally buoyant but practical problem concerning generation, handling and removal have made them less popular.

For water or liquid flows there are fewer restrictions on the size since many particles are naturally buoyant in water. Tracer particle made from polystyrene or latex can be manufactured with a narrow size distribution but tend to be expensive. Hollow glass spheres are also a very common tracer particle and offer high light scatter efficiency. Alternatively, particles can be coated with silver to improve the scatter efficiency. Gas bubbles can be generated locally in the water and do not stay permanently in the water. Generally gas bubbles need to be small to avoid problem with flows tracking.

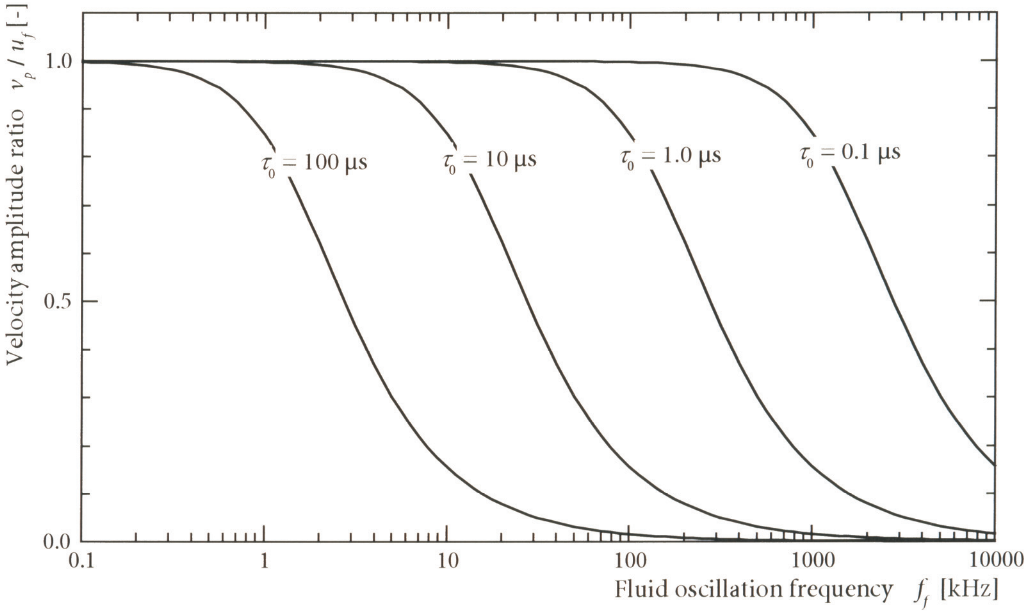

Figure 8: Particle response for particles in air. From (Albrect et al. 2003).

The particle equation of motion can also be solved for an oscillating fluid velocity to mimic the particle response in turbulence. Figure 8 shows the ability of different particles in air to follow the flow. Commonly a particle response parameter of $v_p/u_f =0.99$ is used to calculate the cutoff frequency for which particles are no longer considered to be able to follow the flow. For large density ratios the cutoff frequency can be calculated from the following expression:

$$f_c = \frac{1}{\tau_V}\frac{1}{2\pi}\sqrt{\frac{1}{\left(v_p/u_f\right)^2}-1} \tag{9}$$

The Stokes number is also often used to evaluate the particle ability to follow the flow. The Stokes number is related to the particle response time as:

$$St = \frac{\tau_V}{\tau_F} \tag{10}$$

where τ_F is a characteristic time scale related to the flow. For the flow through a venturi the characteristic time may be expressed as: $\tau_F=D_T/U$ where D_T is the throat diameter and U is the flow velocity. If St << 1, the response time of the particle is much smaller then the characteristic time of the flow and the particle is able to follow the flow. If St >>1 the particle is not able to follow the flow and will only be little affected by the passage through the venturi.

Light Scattering

A measure of the light scattering capability of particles is the scattering cross-section C_s, which is defined as the ratio of the total scattered power P_s to the intensity of the laser light I_0 incident on the particle:

$$C_s = P_s / I_0 \tag{11}$$

Table 2 shows the variation of C_s for different sizes of particles. It is clear that there is a large difference in the light scattering properties of molecules and different sizes of tracer particles. Small changes in the particle size can cause large variations in the light received.

Table 2: The scattering cross-section as a function of the particle size. From (Melling 1997)

Diameter d_p	Scattering cross section: C_s	
Molecule		$\approx 10^{-33}$ m^2
1 μm	$C_s \approx (d_p/\lambda)^4$	$\approx 10^{-12}$ m^2
10 μm	$C_s \approx (d_p/\lambda)^2$	$\approx 10^{-9}$ m^2

Figure 9 illustrates the light pattern scattered by different sizes of transparent spherical particles. For larger particles the scattered light forms a highly complex pattern known as Lorentz-Mie scattering. It is clear that the intensity of the light in the forward direction is about two orders of magnitude larger than the intensity in other directions. The intensity is smallest for scattered light perpendicular to the direction of the laser beam, i.e. side scatter. It is also clear that there can be a large variation in intensity even for small change in the scattering angle.

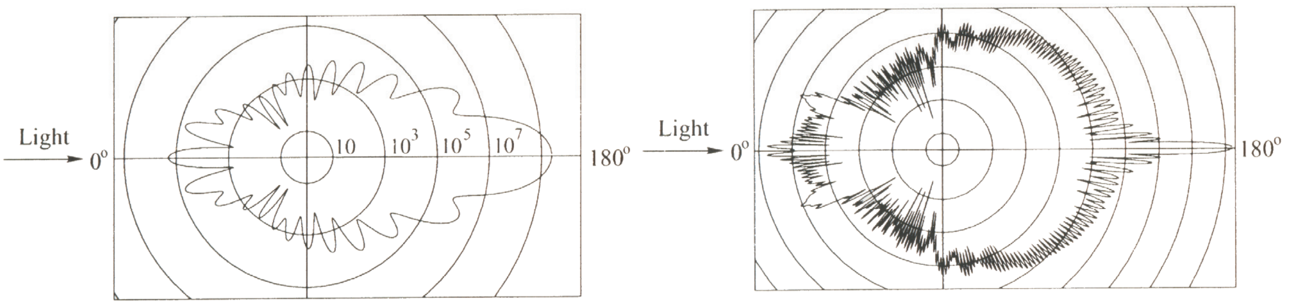

Figure 9: Polar distribution of the scattered light intensity for a 1 μm (left) and 10 μm (right) oil particle in air with a wavelength λ = 532 nm according to Mie's theory. From (Raffel et al. 1998).

System Configuration

It is possible to configure the LDV system in a back-scatter mode, a forward-scatter mode or a side-scatter (off-axis) mode. Forward- and backward-scattering modes are shown in Figure 10. The most common configuration is the backscatter mode which allows the integration of receiving and transmitting optics in a single housing. This means that no additional alignment is necessary, however, backward scatter also have the lower intensity leading to a lower signal–to–noise ratio than forward scattering. Forward scattering is used for applications where it is difficult to get a “good” signal. Typical application may include combusting flows, which has a large noise level combined with low scatter efficiency; high-speed flows, which require small tracer particles which only stay in the measurement volume for a short time; transient phenomenon, such as shock waves which require a high data rate to resolve the shock front. Side scattering or off-axis scattering is used to reduce the size of the effective measuring volume as indicated on Figure 11. Signals form tracer particles passing at the ends of the measurement volume are out of focus and only contribute to the background noise. This reduces the inherent sensitivity to velocity gradients which is located inside the measurement volume. However, side-scatter suffers from a low intensity of scattered light and requires separate receiving and transmitting housing.

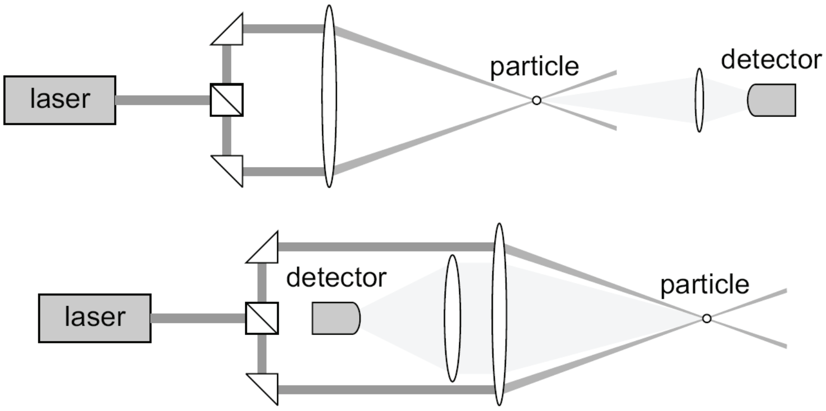

Figure 10: Dual-beam LDV system configuration for detection of forward (top) and backward (bottom) scattered light. From (Meyer 2004).

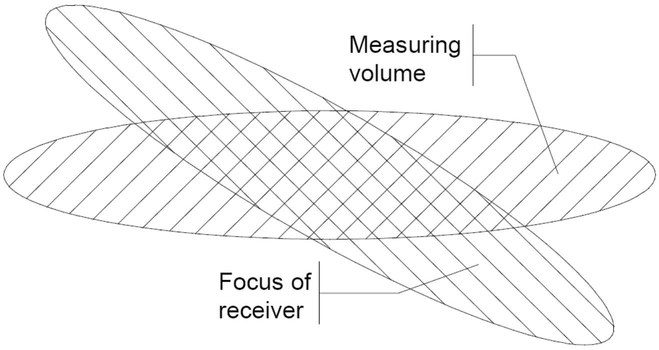

Figure 11: Effective measurement volume for off-axis scattering. From (Dantec 2000).

Components

A practical LDV system makes use of optical fibers to easy align and contain the laser beam. The laser beam can also be used directly or manipulated using highly polished mirrors if the power of the laser beam exceeds the specifications of the optical fiber. In addition, a number of components in used to manipulate and condition the laser beam received from the laser. An overview of the components of a practical LDV system is shown in Figure 12. The optical probe can be mounted on a traversing system which allows systematic measurements of the flow region.

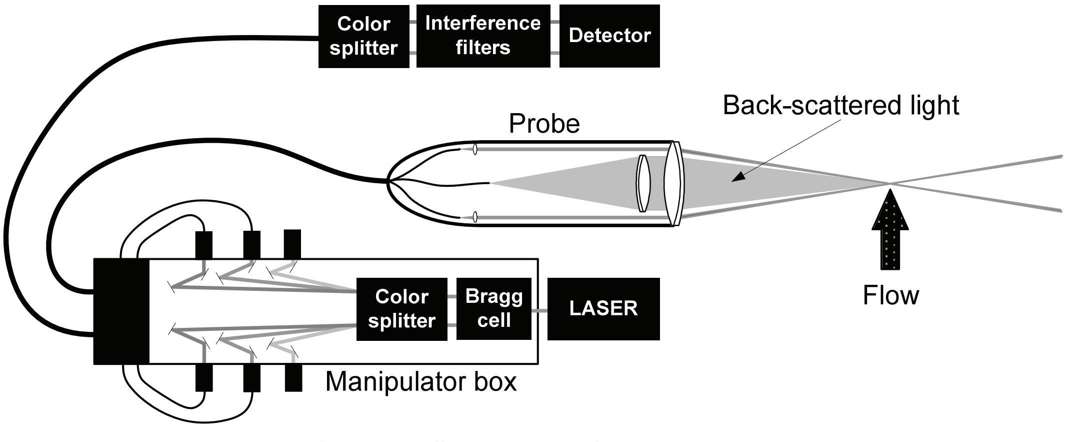

Figure 12: Components of a LDV system.

Laser

Light Amplification and Simulation of Emitted Radiation, or LASER, generates a high focused high intensity light beam with a number of properties which make it suitable for optical measurements. The laser, which can be seen in Figure 13, consists of gain medium, a gas or a solid, which is stimulated with a flash lamp or DC current to emit light which only contain one or a few wavelengths.

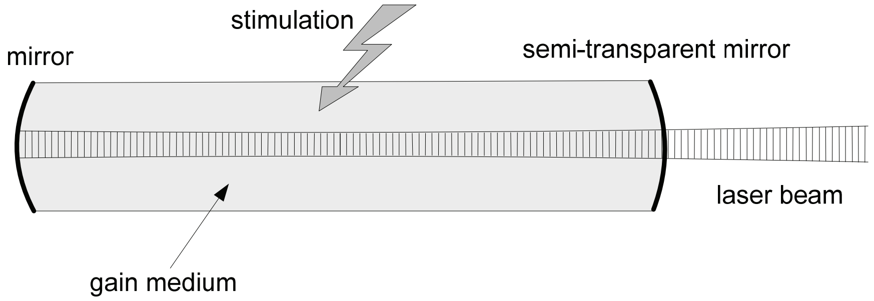

Figure 13: Schematics of a laser.

Laser light is coherent which means that it is in phase with itself and is thus able to make interference. Different types of lasers emit radiation in different wavelengths. Additional color filters and color splitters can be used to further control the wave length. In Table 3 is shown the wave length contained in the laser beam from an Argon, Ar^+, gas laser.

Table 3: Properties of an argon laser.

color:	Wave length:
violet	476.5 nm
blue	488 nm
green	514.5 nm

Bragg cell

The configuration described by Figure 4 cannot distinguish between particles traveling with or against the main flow and is thus only capable of detecting the magnitude of the flow and not the sign. Using a Bragg cell the frequency of a laser beam is shifted. The interference pattern formed by the intersection of a shifted and non-shifted laser beam is no longer stationary but moves with a velocity equal to the fringe spacing multiplied with the frequency shift. As shown in Figure 14 it is thus possible to determine the velocity unambiguously.

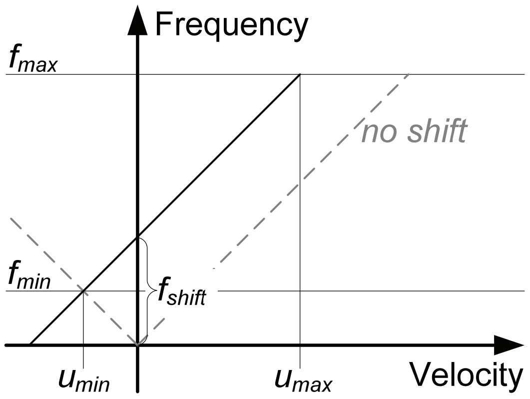

Figure 14: Frequency shift.

Figure 15 illustrates the principle of a Bragg cell. A Bragg cell consists of a crystal in which pressure pulses are transmitted. This generates a periodic moving pattern of high and low density which causes fluctuations in the refractive index of the crystal. A laser beam passing through the Bragg cell is partly refracted yielding an undisturbed beam and a beam with a frequency shift equal to the frequency of the pressure pulses. By adjusting the intensity of the pressure pulses and the tilt angle of the Bragg cell the intensity of the undisturbed and refracted beam can be balanced. Thus the Bragg cell itself acts as a beam splitter. The velocity of the tracer particle can be found by subtracting the Bragg cell shift frequency from the Doppler frequency in equation (4).

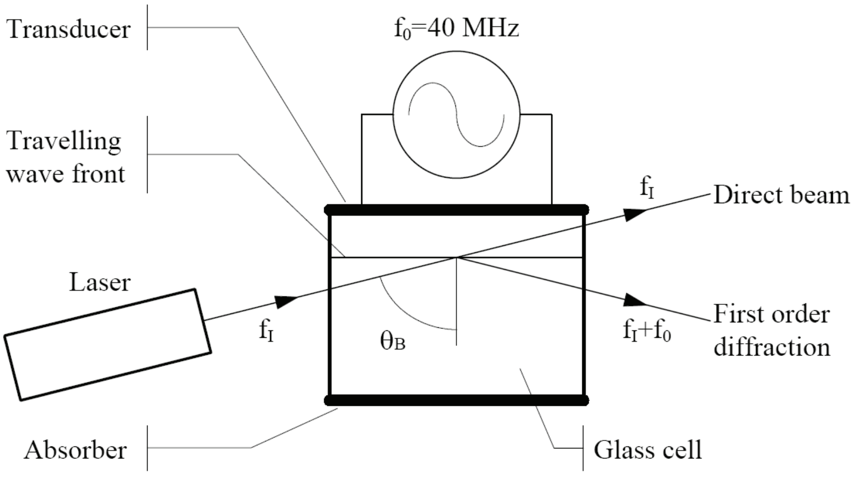

Figure 15: Principles of a Bragg cell. From (Dantec 2000).

Color splitter

A color splitter is basically a prism, separating the different wavelengths contained in the laser beam.

Manipulator box

In addition to the Bragg cell and the color-splitter the manipulator box holds a number of mirrors and fiber-manipulators which all can be adjusted for optimal alignment of the original laser beam with the optical fibers.

Probe

The optical probe is a housing which holds the transmitting and receiving optics. A single probe can handle up to 4 beams which allow the measurement of two velocity components. The third velocity component can be obtained using a second probe intersecting the measurement volume at different angle as seen in Figure 1. This requires careful alignment of the two probes. To distinguish between the velocity components beams of different wavelength are used. The received light will later pass through a second color splitter which separates the signals before they are sent to a burst detector.

Beam expander

A beam expander is a combination of lenses which can be mounted in front of the probe. It converts the beams exiting of the probe to beams of greater width. According to equation (5), providing that the focal length is unchanged, this will decrease the size of the measurement volume. Since the beams are focused into a narrower volume this also increases the light intensity and the aperture, the receiving lens, is able to pick up move of the scattered light, increasing the signal-to-noise ratio.

Interference filters

Interference filters are used along with digital filters in the signal processing unit to condition the signal received from the probe. An interference filter is an optical filter which only transmits a part of the wavelengths contained in the signal and thus act as a band pass filter.

Detector

The measurement of the velocity of a particle moving though the measurement volume is carried out in a dedicated signal processing unit. This contains an integrated photomultiplier, which converts the light signal into electrical current, and equipment to further process the signal. Figure 16 shows the principles of a photomultiplier.

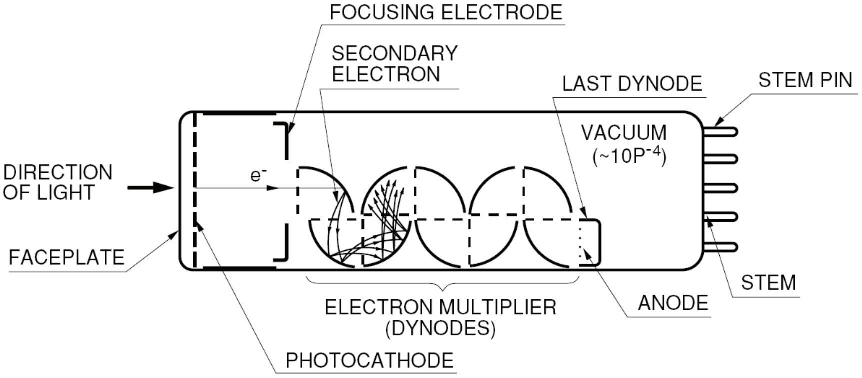

Figure 16: Sketch of a photomultiplier tube.

Light passing into the photomultiplier excites electrons in the photocathode so that electrons are emitted into a vacuum. This is also known as the external photoelectric effect. The electrons are accelerated due to the high voltage between the cathode and anode and focused by the focusing electrode. The electrons are successively multiplied as they hit the dynodes by means of secondary electron emission. The multiplied electrons are finally collected by the anode where they are turned into a current with a magnitude in the order of one μA. The applied voltage is used to adjust the amplification of the signal and is typically set around 1000 V.

Signal Processing

The signal caused by the passage of a particle is only fund in short “bursts” while the current from the photomultiplier also contains noise from undesired light reaching the detector and quantum processes occurring inside the photomultiplier. The signal processing thus involves several steps:

- Amplifying the signal using a gain parameter
- Conditioning of the signal using bandwidth filters
- Detection of the burst and burst length
- Validation of the burst according to noise level
- Conversion from Doppler frequency to velocity using an FFT algorithm

The performance of a LDV system is optimized by proper selection of laser power, tracer particle concentration, photomultiplier high voltage, signal gain, velocity range (bandwidth), minimum and maximum burst length and validation criteria. Note that by improper selection of any of these parameters it is possible to acquire both bogus signals but also not acquiring any signals at all.

High voltage

Increasing the high voltage applied on the photomultiplier increases the amplification of the signal but will also increase the noise. If possible, an alternative is to increase the light received by the photomultiplier by increasing the power of the laser, changing the particle type or changing the configuration of the system. As a first test a high voltage of 1000 V is a good choice. Depending on the initial data rate and validation percentage recorded the voltage can be increased to increase the data rate or decreased to increase the validation acceptance. The typical range of the high voltage is 700 – 1400 V.

Signal gain

Similarly to adjusting the high voltage the signal can be amplified by adjusting the internal gain in the signal processor. This also amplifies any noise present in the signal. The effective gain is thus a combination of the high voltage and the signal gain. In practice the signal gain is kept default level and the total gain is adjusted using the high voltage.

Velocity range

Setting the velocity range affects both the resolution of the signal and sensitivity to noise. Thus it is desired to select a velocity range which as narrowly resolves the range of velocities. The appropriate velocity range can be selected from viewing a histogram of the recorded velocities. A correctly recorded histogram should be Gaussian in appearance. Selecting a too narrow or wrongly placed velocity range will cause validated velocities to be rejected. Usually the velocity range is only resolved using 8 bits meaning that selecting a too wide range decreases the resolution. Also, a single wrongly recorded sample which is located far from the mean will have a great impact on the measured spread, thus increasing the sensitivity to noise.

Burst length

On average much less than one particle is present in the measurement volume and the signal is considered as a burst type Doppler signal. Since the signal from the photomultiplier contains noise at similar frequency as the Doppler signal it is necessary to positively identify each signal as originating from a tracer particle. The sensitivity to noise is reduced by using a three-level detection scheme to determine the signal gate for which frequency analyze is performed. Drawing A in Figure 17 shows that the gate period starts at a positive crossing of level 2 and stops at a negative crossing of level 2. Hence, the measurement volume is symmetrical. It should be pointed out that the signal must cross level 3 (drawing C in Figure 17) for a burst to be accepted. Also, the signal must cross level 1 before a new measurement can start (drawing D in Figure 17). Drawing B in Figure 17 shows that the gate period is not much affected by noise, since multiple crossings of level 2 are ignored as long as levels 3 or 1 are not crossed. The burst length is specified as the "burst bandwidth frequency" and should be proportional to the inverse of the average particle transit time. Usually the default value provided is used. Note that this value is automatically changed according to the setting of the velocity range. Also note that it is not possible to change the trigger levels for burst detection.

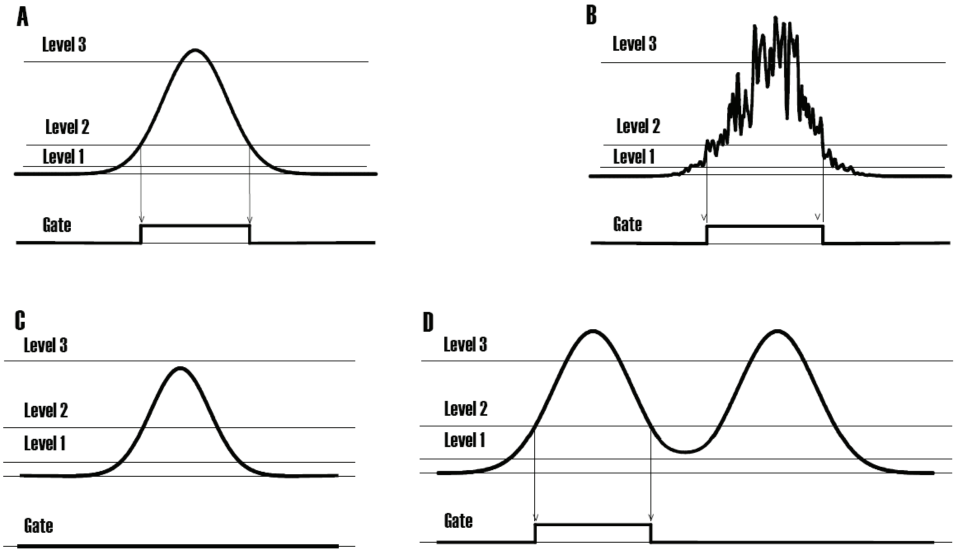

Figure 17: Triggering of gate pulse: A: principle, B: noisy signal, C: inadequate noise amplitude, D: missing crossing of level 1 between two bursts. From (Dantec, 2000).

Validation

To distinguish between burst originating from a particle and the inherent noise it is necessary to determine if the signal is trustworthy. This is usually done by comparing the estimated Signal to Noise Ratio, SNR, with a predefined acceptance value. The SNR may be defined by the ratio of the power of the signal fluctuations, σ_S^2, to the power of the noise fluctuations, σ_N^2, expressed in decibels:

$$SNR/_{dB} = +10\log\left(\frac{\sigma_S^2}{\sigma_N^2}\right) \tag{12}$$

Note that the SNR estimate may vary according to the estimator which is used and that the threshold ratio may differ greatly from system to system. The SNR validation level can be selected between -6 dB and +3 dB. The higher SNR validation level is set the less signals will be accepted but these will be more trustworthy. The default SNR validation level is 0 dB. Although it is possible to set SNR validation for both the u and v velocity component it is recommended that SNR validation is only used for one component. It is also possible to switch off SNR validation altogether. The percentage of signals which passes the test can be used as a measure for the quality of the signal. A high quality signal will thus have a 100% validation. However, for most measurements a validation level of 90% (or lower) is acceptable. The best method to evaluate the results is to use knowledge of the flow to see if the measured values match the expected e.g. mean velocity, turbulence intensity, zero velocity at no slip walls, recirculation zones, etc. For non-periodic flows the distribution of velocities should approach a Gaussian (normal) distribution. This can be evaluated by computing a histogram of the velocity samples.

Statistics

LDV records a sample each time a particle passes through the measurement volume. The particles are swept though the volume at uneven time intervals yielding a signal which is neither continuous nor periodic. Furthermore, during periods of higher velocity, a larger volume of fluid is swept through the measuring volume, and consequently a greater number of velocity samples will be recorded. This has some important consequences when calculating the statistics of the flow. The LDV system can be run in two modes: Burst mode which samples all signals and dead time mode, for which it is possible to set a minimum time between each successive sample. It is clear that burst mode acquires significant more samples than dead-time mode, however, the calculated mean will be biased towards a higher mean velocity. To compensate for that LDV-measurements, especially in highly turbulent flows, tend to contain more samples of fast particles than slow ones, a special weighting factor η_i can be used:

$$\eta_i = t_i \Big/ \sum_{i=1}^{n} t_i \qquad (13)$$

where t_i is the transit time of the i'th particle crossing the measuring volume. This bias correction is especially important when calculating one-time statistics from a data set recorded in burst mode which is done if the data set is also to be used for spectral analysis.

When calculating one-time statistics it is desired that the samples are independent of one another. In turbulence measurements, this is usually done by ensuring that the time between two samples are at least twice the integral time scale of the flow. The integral time scale of the flow can be estimated by calculating the autocorrelation when in burst mode. Note that when acquiring independent samples in dead time mode the difference between the weighting factor corresponding to normal arithmetic mean: *1/n* and the bias corrected one is often negligible. Table 4 shows some often used one-time statistics.

Table 4: Important one time statistics

Mean	$\overline{u} = \sum_{i=1}^{n} \eta_i u_i$	(14)
RMS	$\sigma = \sqrt{\sum_{i=1}^{n} \eta_i (u_i - \overline{u})^2}$	(15)
Turbulence intensity	$I = \sigma / \overline{u}$	(16)
Cross-moment	$\overline{uv} - \overline{u} \cdot \overline{v} = \sum_{i=1}^{n} \eta_i \left(u_i - \overline{u}\right)\left(v_i - \overline{v}\right)$	(17)

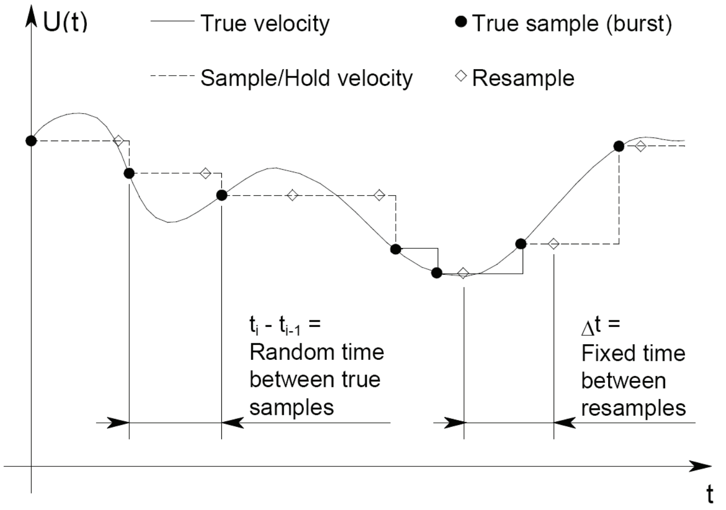

Figure 18: Random sampling, sample/hold and resampling. From (Dantec 2000).

Calculations of the frequency domain e.g. the spectrum of turbulence, is usually done using a FFT algorithm. These require periodic samples which makes it especially challenging when it is to be applied on LDV data sets. To overcome this, the acquired signal is resampled using a so-called sample-and-hold technique. Figure 18 illustrates the principle of the sample-and-hold technique. The velocity signal is recreated by assuming that velocity is constant between two samples. This recreated signal is then resampled at regular time intervals to provide time series suitable for FFT analysis. Note that if two samples are further apart than the time between resamples the first sample will be resampled several times. If two samples are closer together than the time between resamples information will be lost. To avoid loss of information the resampling frequency should be larger than the mean sampling frequency. This however will increase the total amount of data significantly while only adding little new information. Typically a resampling frequency between 2 and 10 times the mean sample frequency is used. For calculation of spectra the sample-and-hold technique is also known to introduce additional white noise, so-called step noise, over the entire range of frequencies. However more important, the sample-and-hold technique acts as a first-order low pass filter attenuating frequencies above $\dot{n}/2\pi$, where $\dot{n}$ is the mean data rate. Figure 19 shows the power spectrum of turbulence measured with a mean data rate of 9.2 kHz. The spectrum estimate above the cut-off frequency will be attenuated with slope of -2 which easily can be confused with the Kolmogorov -5/3 law for the inertial subrange.

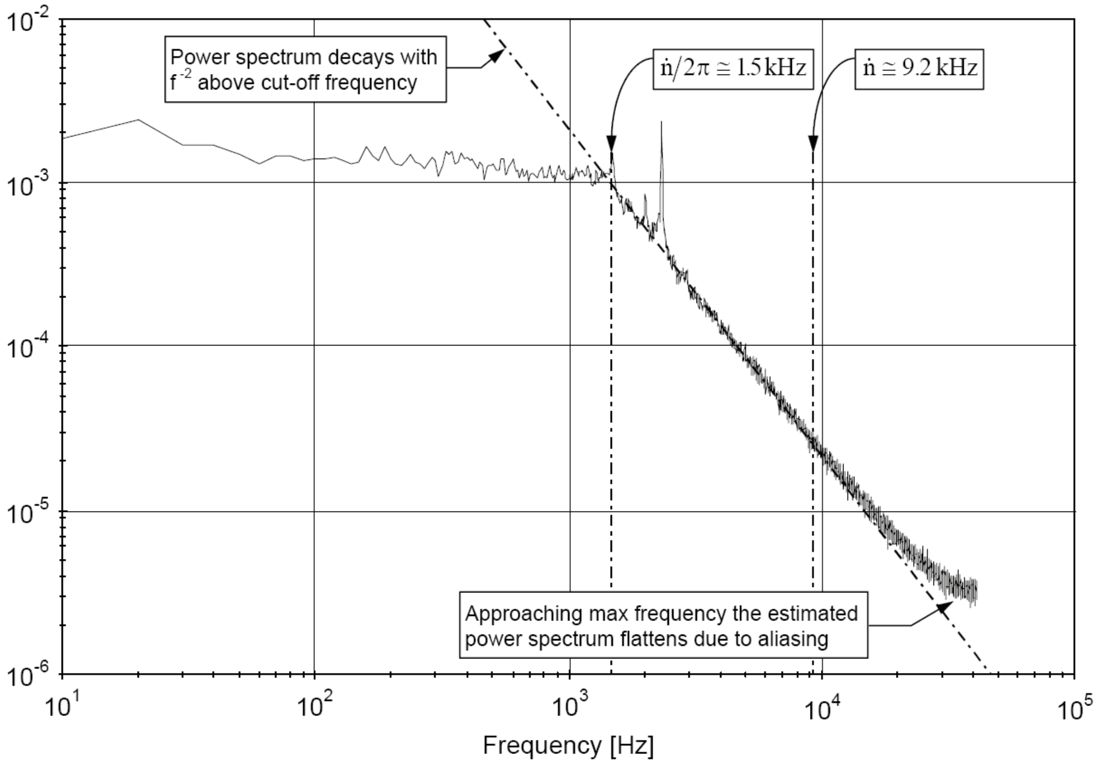

Figure 19: The 'Sample-and-hold' technique act as a low-pass-filter attenuating the spectrum. From (Dantec 2000).

Example 1: Resolution of Turbulent Scales

The LDV equipment found in the Laser Laboratory of the Institute of Energy Technology, Aalborg University is used to measure the velocity statistics of a turbulent air flow with a turbulence Reynolds number of $Re_\lambda \approx 90$ and integral length scale $l_e \approx 25mm$. Is it possible to resolve all turbulent scales?

Turbulence consists of length and time scales ranging from large, slow turbulent eddies the size of the flow geometry to small eddies with length and time scales limited by the dissipative action of viscosity. The turbulence Reynolds number Re_λ is often used to characterize grid turbulence and l_e is considered to be the length scale characterizing the large energy containing eddies. The smallest scales of turbulence are the Kolmogorov scales:

$$\eta_K = \left(\frac{\nu^3}{\varepsilon}\right)^{1/4}, \qquad \tau_K = \sqrt{\frac{\nu}{\varepsilon}}, \qquad \upsilon_K = \left(\nu\varepsilon\right)^{1/4} \tag{18}$$

It is possible to determine the dissipation rate ε directly using the LDV equipment providing that the Taylors hypothesis is valid and is the turbulence can be assumed to be homogeneous. However, for this example we use the knowledge which is given to determine ε. From dimensional analysis we know that:

$$\mathrm{Re}_\lambda = \left(\frac{20}{3}\mathrm{Re}_{l_e}\right)^{1/2}, \qquad \mathrm{Re}_{l_e} = \frac{k^{1/2} l_e}{\nu}, \qquad l_e = \frac{k^{3/2}}{\varepsilon} \tag{19}$$

where k is the turbulent kinetic energy and Re_{le} is the turbulence Reynolds number based on l_e. Hence:

$$\begin{aligned} & air \rightarrow \nu = 1.5E-5m\cdot s \\ & \varepsilon = \left(\frac{3}{20}\frac{\mathrm{Re}_\lambda^2\,\nu}{l_e^{4/3}}\right)^3 = 15\frac{m^2}{s^3} \\ & \eta_K = \left(\frac{\nu^3}{\varepsilon}\right)^{1/4} = 120\mu m \\ & \tau_K = \sqrt{\frac{\nu}{\varepsilon}} = 0.001s \\ & \frac{1}{\tau_K} = 1000Hz \end{aligned} \tag{20}$$

According to the Nyquist sampling criteria to resolve the smallest turbulent scales we need to sample with at least 2 kHz and the measuring volume should be at smaller than 60 μm. The actual sampling rate depends on several parameters e.g. the amount of seeding, the flow velocity and the setup of the burst analyzer. Knowing these parameters it is possible to calculate the maximum resolvable frequency. In practical terms the actual sampling frequency depends to a large degree on the skill of the operator. Previous experiments using the LDV equipment on this type of flow have yielded sampling rates in excess of 20 kHz.

The available equipment encompass lenses of different focal length e.g. *F*=150mm and *F*=400mm. The integral length scale length scale given corresponds to that which is found for fully developed turbulent flow along the centerline in a 250mm wide duct, which suggests that it is necessary to use the 400mm lens. At present time there is no beam expander available which means that the beam expansion ratio can be set equal to one. The wavelength of the laser beam can be seen in Table 3. From a two component setup typically the green and the blue beam are used. The initial beam diameter can be acquired from the laser specifications; for the present laser the beam thickness is 1mm. The angle between the two beams is found from the geometry of the setup, Figure 6:

$$\tan\left(\frac{\theta}{2}\right)=\frac{D_{lens}}{2F}=\frac{40}{2\cdot 400} \quad\Rightarrow\quad \frac{\theta}{2}=2.86^{\circ} \tag{21}$$

where D_{lens} is the diameter of the lens corresponding to the length between the beams in the lens plane. The size of the measuring volume can be found using equation (5) and (6):

$$\begin{aligned} d_f &= d_y = \frac{4}{\pi}\frac{F\lambda}{ED_L}=\frac{4}{\pi}\frac{0.4m\cdot 514.5E-9m}{1\cdot 0.001m}=262\mu m \\ d_x &= \frac{d_f}{\cos(\theta/2)}=262\mu m \\ d_z &= \frac{d_f}{\sin(\theta/2)}=5.25mm \end{aligned} \tag{22}$$

If can be seen that the length of the measuring volume in the z direction (coordinates according to Figure 6) is 20 times larger than the other dimensions. It can be seen that the actual measuring volume in the x-direction is greater than the Kolmogorov scales but smaller than the large energy containing eddies. Thus, the present setup is not able to resolve the entire spectrum of turbulence. Using the present setup it is still possible to acquire one-time statistics and some of the two-time statistics, e.g. autocorrelations, providing that Taylors hypothesis is valid.

Figure 20 shows the longitudinal (x-direction) spectrum obtained for the present flow. The spectrum has been normalized using the usual quantities and the initial frequency spectrum (units 1/s) has been converted to a wave number spectrum, *k,* (units 1/m). It can be seen that the present setup is not able to resolve the smallest scales of turbulence. The divergence from the benchmark spectrum occurs at around kη_K =0.3 which corresponds to 3.3·η_K or 400μm. This is in accordance with the resolution which is expected from the initial calculations of the measurement volume. Using the present setup it is possible to resolve the largest scales and most of the inertial sub-range. Notice that to resolve the entire spectrum the required resolution is actually more like ¼η_K or in this case 30 μm since the dissipative scales extend beyond the Kolmogorov scales.

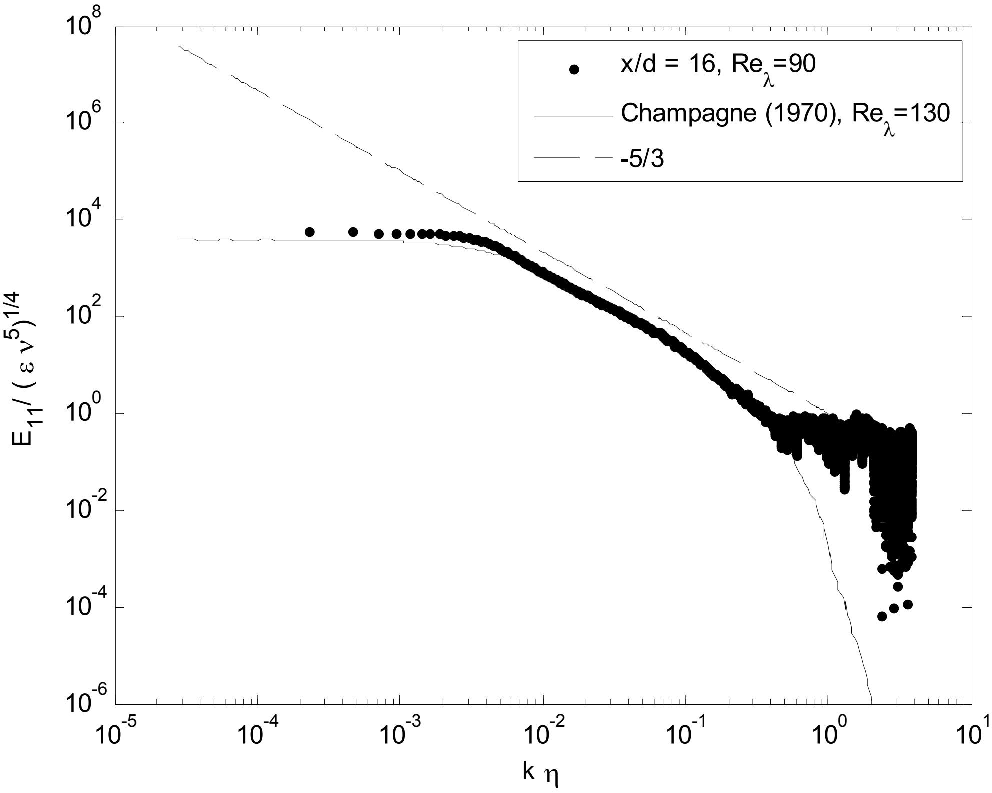

Figure 20: Normalized longitudinal spectrum measured with the IET laser equipment for the present flow compared with the hotwire measurements of Champagne (1970) and Kolmogorovs -5/3 law for the inertial subrange.

Example 2: Tracer Particle Response

For the flow in Example 1 small oil droplets are used as tracer particles. Are these able to follow the turbulent eddies?

According to Table 1 oil droplets have a maximum diameter of about 3 μm and a density of about 800 kg/m3. By substitution into equation (7) the particle response can be calculated to:

$$\tau_V = \frac{\left(\rho_p - \rho\right) d_p^2}{18\mu} = \frac{800 \cdot \left(3E-6\right)^2}{18 \cdot 1.8E-5} = 22\mu s \tag{23}$$

Using the Kolmogorov time scale as the characteristic time of the flow the Stokes number can be calculated as:

$$St = \frac{\tau_V}{\tau_K} = \frac{22E-6}{1E-3} = 0.022 \tag{24}$$

Since St<< 1 this suggests that the particles are capable of following the smallest scale of turbulence present in the flow. However, this criterion is based on a response time for when the particle velocity is equal to 63% of the fluid velocity. For the more strict criteria of 99% the cutoff frequency can be found from equation (9):

$$f_c = \frac{1}{\tau_V}\frac{1}{2\pi}\sqrt{\frac{1}{\left(v_p/u_f\right)^2} - 1} = \frac{1}{22E-6}\frac{1}{2\pi}\sqrt{\frac{1}{\left(0.99\right)^2} - 1} = 1031Hz \tag{25}$$

The frequency of the smallest scales of turbulence was previously found to be 1000Hz which means that the tracer particles are just capable of following the turbulent eddies.

Example 3: Velocity Range Resolution

The LDV equipment is used to measure the velocity statistics of a turbulent air flow with a known mean velocity of 3m/s and a RMS velocity of 0.7m/s. Account for the accuracy of the measurements and possible sources of error?

Turbulence can be simulated numerically by assuming that it follows a Gaussian distribution. Note that is requires that the samples are independent of one another and thus the calculations presented below assumes that the velocity measurements are made in dead-time mode with sufficient time between samples, e.g. twice the integral time scale. Bias corrected measurements made in burst mode can be used to calculate a mean but since the samples are not independent of each other more samples, compared to the number of samples made in dead-time mode, are required. Additionally it is not possible to calculate the accuracy since the theory used assumes that the samples are independent of each other. When calculating statistics from a number of samples we distinguish between the true mean, $\overline{\mu}$ and the sample mean $\overline{X}$. The error that the sample mean is not equal to the true mean can be estimated by the following expression:

$$e^2 = \frac{2}{n} \tag{26}$$

where *n* is the number of samples. This expression is shown in Figure 21.

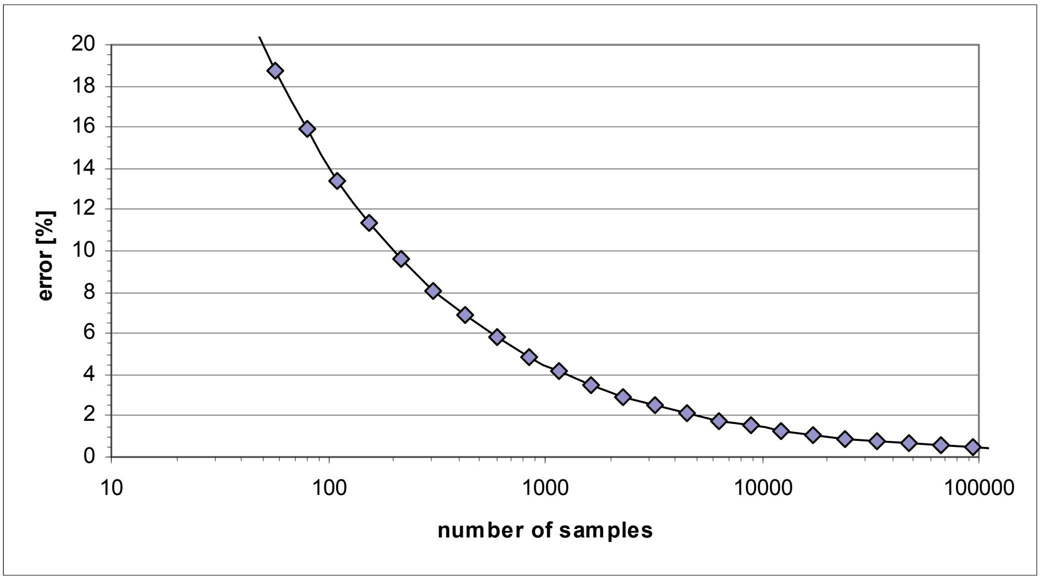

Figure 21: The error on the sample mean to the true mean depending on the number of samples.

It can be seen that for an acceptable error of 10 % 200 samples are required while an acceptable error of 2 % requires 5000 samples. An often used acceptable accuracy is 4 % which corresponds to 1250 samples.

A confidence interval, which expresses an interval where there is a 95% change that the true mean lies within, can be calculated using the sample mean and sample RMS, equation (14) and (15), as:

$$\overline{\mu} = \overline{X} \pm \frac{\sigma z}{\sqrt{n}} \tag{27}$$

where z for a normal distribution is equal to 1.96. Thus if 1250 samples are used for the turbulent flow with mean 3 m/s and RMS 0.7 m/s the confidence interval is:

$$\overline{\mu} = \overline{X} \pm \frac{\sigma z}{\sqrt{n}} = 3 \pm \frac{0.7 \cdot 1.96}{\sqrt{1250}} = 3 \pm 0.03 \text{ m/s} \tag{28}$$

In turbulence measurements the RMS velocity is equally important to the mean. Expression (26) can be seen to express the error for both the mean and the RMS velocity for a limited number of samples. Thus for very accurate measurements of turbulence it is not unseen to have several hundred thousand samples.

The AD-converter in the LDV system has a 8-bit resolution. It is possible to select between different velocity ranges (corresponding to a specific bandwidth of the input filter) depending on the flow:

Table 5: Properties of the input filter.

bandwith (MHz)	velocity range (m/s)	resolution (m/s)
0.12	-0.14 to 0.43	0.0022
0.4	-0.48 to 1.4	0.0073
1.2	-1.4 to 4.3	0.022
4	-4.8 to 14	0.073
12	-14 to 43	0.22
36	-29 to 143	0.67

The minimum velocity range required to resolve the flow might be expressed as the mean plus/minus 3 times the RMS. For the present flow this corresponds to a velocity range between 0.9 to 5.1 m/s. Thus the velocity range of -4.8 to 14 m/s should be chosen. Notice that if the range -1.4 to 4.3 m/s is chosen the distribution will appear Gaussian since only a few procent of the samples will be located outside of the velocity range. Choosing the wrong velocity range will in this case bias the mean towards lower velocities. The resolution error or the AD-conversion error for the sample mean can be calculated as:

$$e = \frac{resolution}{mean} = \frac{0.073}{3} \cdot 100\% = 2.4\% \tag{29}$$

If the widest velocity range is used for the present flow the resolution error would be over 20%. The resolution error is symmetrical over the sample mean this means that given enough samples the sample mean will approach the true mean. For calculation of the accuracy of the sample mean compared to the true mean only the estimate in equation (26) or the confidence interval, equation (27), should be included. Also, any instrumental error which is symmetrical over the mean should not be considered when calculating the total accuracy of the mean.

It is good practice that the number of significant digits of reported values expresses the accuracy to the system. Thus, when reporting measurements the author should be aware that the accuracy is always implicitly reported by the number significant digits. The LDV system can be set up to output the result with a large number of significant digits. Thus it is important to note that this is not an expression of the accuracy of the measurement. In Figure 22 a sample histogram is shown. Notice the division of the x-axis which represents the recorded velocity of individual samples.

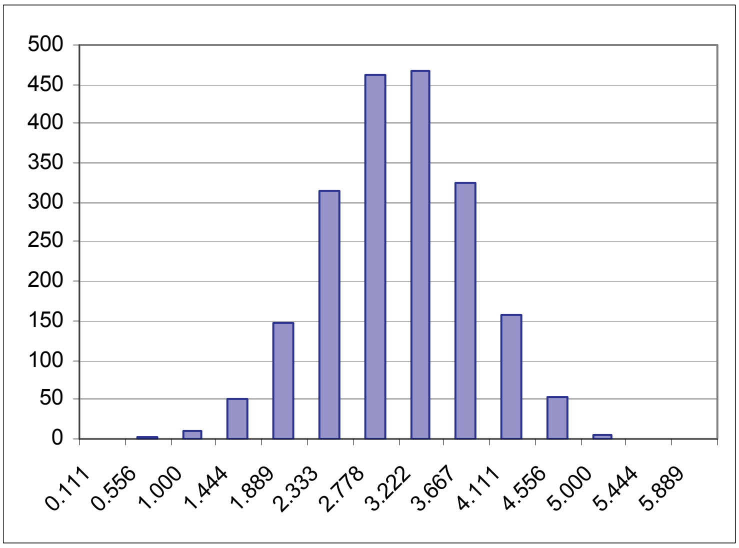

Figure 22: A sample histogram. Notice that the velocity samples are put in discrete bins which correspond to the resolution of the measurement.

An important parameter for turbulence is the turbulence intensity, equation (16), which is composed of both the mean and the RMS velocity. Similar to the sample mean the sample RMS is also associated with an error. This error will be in the same order as the estimate in equation (26). An estimate of the total error associated with the turbulence intensity would thus be twice this estimate. However, the resolution error associated with sample RMS velocity is not symmetrical meaning that it will not be insignificant for infinite number of samples. The influence of resolution on the calculation of the RMS velocity and the turbulence intensity can be obtained by simulating a Gaussian signal with mean 3 and RMS 0.7. This can be simulated a sufficient number of times to eliminate the influence of a limited number of samples. Here we are interested in showing the difference between the estimate based on unlimited resolution and an estimate which is based on varying degree of resolution.

The error for this experiment is calculated as:

$$\frac{I_{\text{limited resolution}} - I_{\text{unlimited resolution}}}{I_{\text{unlimited resolution}}} \cdot 100\%, \qquad I = \frac{\sigma}{\overline{X}} \tag{30}$$

For the case of an infinite number of samples the turbulence intensity for unlimited resolution could be replaced with the true turbulence intensity. The result of this experiment is shown in Figure 23. The resolution is in this case indicated by the approximate number of bins required to resolve the Gaussian velocity distribution. Notice that the numerator in equation (30) is not in absolute values. Thus it can be realized that resolution error will always tend to increase the RMS velocity and the turbulence intensity. This can be related to the placement of values in discrete bins which alters the distribution compared to a distribution with unlimited resolution. Whereas the calculation of the sample mean given enough samples will approach the true mean, the RMS velocity based on limited resolution will always be calculated larger than the true RMS no matter the amount of samples. It can be seen that the error diminishes quickly as the resolution is increased.

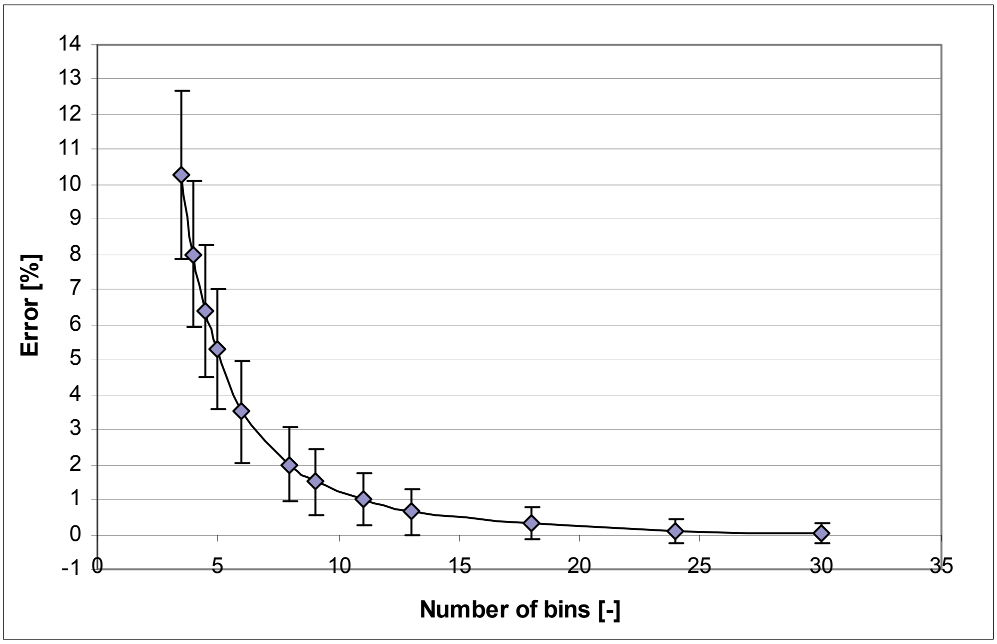

Figure 23: Error on the turbulence intensity. This error will always act to increase the turbulence intensity. The error-bars denote the spread of the simulations.

For the present experiment the number of bins is roughly equal to 3-4 times the RMS velocity divided by the resolution. Hence for the present flow the velocity range is resolved with approximately $3 \cdot 0.7/0.73=29$ bins. This corresponds to a resolution error for the RMS velocity and the turbulence intensity of less than 0.02%. If the widest velocity range was used the number of bins would be around 4 and the resolution error would be 8 %.

Bibliography

Abbas, T., Costen, P., Kandamby, N.H., Lockwood, F.C. & Ou, J.J. 1994, "The Influence of Burner Injection Mode on Pulverized Coal and Biomass Cofired Flames", *Combustion and Flame,* vol. 99, no. 3-4, pp. 617-625.

Albrecht, H.E., Borys, M., Damaschke, N. & Tropea, C. 2003, *Laser Doppler and Phase Doppler Measurement Tecniques,* Springer.

Allen, T. 1981, *Particle size measurement,* Chapman & Hall.

Backreedy, R.I., Fletcher, L.M., Jones, J.M., Ma, L., Pourkashanian, M. & Williams, A. 2005, "Co-firing pulverised coal and biomass: a modeling approach", *Proceedings of the Combustion Institute,* vol. 30, pp. 2955-2964.

Ballester, J., Barroso, J., Cerecedo, L.M. & Ichaso, R. 2005, "Comparative study of semi-industrial-scale flames of pulverized coals and biomass", *Combustion and Flame,* vol. 141, no. 3, pp. 204-215.

Barlow, R.S. & Morrison, C.Q. 1990, "2-Phase Velocity-Measurements in Dense Particle-Laden Jets", *Experiments in Fluids,* vol. 9, no. 1-2, pp. 93-104.

Battista, J.J., Hughes, E.E. & Tillman, D.A. 2000, "Biomass cofiring at Seward Station", *Biomass & Bioenergy,* vol. 19, no. 6, pp. 419-427.

Baukal, C.E. (ed) 2003, *Industrial burners handbook*, CRC Press.

Baxter, L. 2005, "Biomass-coal co-combustion: opportunity for affordable renewable energy", *Fuel,* vol. 84, no. 10, pp. 1295-1302.

Beer, J.M. & Chigier, N.A. 1972, *Combustion Aerodynamics,* Applied Science Publishers.

Bernstein, O. & Shapiro, M. 1994, "Direct determination of the orientation distribution function of cylindrical particles immersed in laminar and turbulent shear flows", *Journal of Aerosol Science,* vol. 25, no. 1, pp. 113-136.

Bharadwaj, A., Baxter, L.L. & Robinson, A.L. 2004, "Effects of intraparticle heat and mass transfer on biomass devolatilization: Experimental results and model predictions", *Energy & Fuels,* vol. 18, no. 4, pp. 1021-1031.

Bilanski, W.K. & Lal, R. 1965, "Behavior of Treshed Materials in an Verical Wind Tunnel", *Transactions of the ASAE,* vol. 8, pp. 411-416.

Black, D.L. & McQuay, M.Q. 2001, "Laser-based particle measurements of spherical and nonspherical particles", *International Journal of Multiphase Flow,* vol. 27, no. 8, pp. 1333-1362.

Black, D.L., McQuay, M.Q. & Bonin, M.P. 1996, "Laser-based techniques for particle-size measurement: A review of sizing methods and their industrial applications", *Progress in Energy and Combustion Science,* vol. 22, no. 3, pp. 267-306.

Boulet, P. & Moissette, S. 2002, "Influence of the particle-turbulence modulation modelling in the simulation of a non-isothermal gas-solid flow", *International Journal of Heat and Mass Transfer,* vol. 45, no. 20, pp. 4201-4216.

Boussinesq, J. 1877, "Theorie de l'Ecoulement Tourbillant"*, Mem. Presentes par Divers Savants Acad. Sci. Inst. Fr.*, vol. 23, no. 8, pp. 46-50.

Brenner, H. 1964, "The Stokes Resistance of a Slightly Deformed Sphere", *Chemical Engineering Science,* vol. 19, no. 8, pp. 519-539.

Brenner, H. 1964, "The Stokes Resistance of an Arbitrary Particle .2. an Extension", *Chemical Engineering Science,* vol. 19, no. 9, pp. 599-629.

Brenner, H. 1964, "The Stokes Resistance of an Arbitrary Particle .3. Shear Fields", *Chemical Engineering Science,* vol. 19, no. 9, pp. 631-651.

Brenner, H. 1964, "The Stokes Resistance of an Arbitrary Particle .4. Arbitrary Fields of Flow", *Chemical Engineering Science,* vol. 19, no. 10, pp. 703-727.

Brenner, H. & Condiff, D.W. 1972, "Transport Mechanics in Systems of Orientable Particles .3. Arbitrary Particles", *Journal of colloid and interface science,* vol. 41, no. 2, pp. 228-&.

Calabrese, R.V. & Middleman, S. 1979, "Dispersion of Discrete Particles in a Turbulent Fluid Field", *AICHE Journal,* vol. 25, no. 6, pp. 1025-1035.

Carlsson, A. 2007, *Orientation of fibres in suspensions flowing over a solid surface*, licentiate thesis, Royal Institute of Technology, Stockholm.

Cenedese, A., Romano, G.P. & Defelice, F. 1991, "Experimental Testing of Taylor Hypothesis by LDA in Highly Turbulent-Flow", *Experiments in Fluids,* vol. 11, no. 6, pp. 351-358.

Champagne, F.H., Harris, V.G. & Corrsin, S. 1970, "Experiments on nearly Homogeneous Turbulent Shear Flow", *Journal of Fluid Mechanics,* vol. 41, pp. 81-139.

Chen, C.P. & Wood, P.E. 1985, "A Turbulence Closure-Model for Dilute Gas-Particle Flows", *Canadian Journal of Chemical Engineering,* vol. 63, no. 3, pp. 349-360.

Chhabra, R.P., Agarwal, L. & Sinha, N.K. 1999, "Drag on non-spherical particles: an evaluation of available methods", *Powder Technology,* vol. 101, no. 3, pp. 288-295.

Christensen, M.S. 2006, *Kulfyringsteknologi*, Presentation of Combustion Technology edn.

Christiansen, E.B. & Barker, D.H. 1965, "Effect of shape and density on free settling of particles at high Reynolds number", *AICHE journal,* vol. 11, no. 1, pp. 145.

Clift, R., Grace, R. & Weber, M.E. 2005, *Bubbles, drops, and particles,* Dover Publications, Inc., Mineola, New York.

Crowe, C.T. 2000, "On models for turbulence modulation in fluid-particle flows", *International Journal of Multiphase Flow,* vol. 26, no. 5, pp. 719-727.

Crowe, C.T., Sharma, M.P. & Stock, D.E. 1977, "Particle-Source in Cell (PSI-Cell) Model for Gas-Droplet Flows", *Journal of Fluids Engineering-Transactions of the ASME,* vol. 99, no. 2, pp. 325-332.

Crowe, C.T., Sommerfeld, M. & Tsuji, Y. 1998, *Multiphase flows with droplets and particles,* CRC Press, Boca Raton, Florida.

Cui, H.P. & Grace, J.R. 2007, "Fluidization of biomass particles: A review of experimental multiphase flow aspects", *Chemical Engineering Science,* vol. 62, no. 1-2, pp. 45-55.

Curtis, J.S. & van Wachem, B. 2004, "Modeling particle-laden flows: A research outlook", *AICHE Journal,* vol. 50, no. 11, pp. 2638-2645.

Dam-Johansen, K. 2006, *Fyrrumsprocesser*, Presentation of Combustion Technology

Damstedt, B., Pederson, J.M., Hansen, D., Knighton, T., Jones, J., Christensen, C., Baxter, L. & Tree, D. 2007, "Biomass cofiring impacts on flame structure and emissions", *Proceedings of the Combustion Institute,* vol. 31, pp. 2813-2820.

Dantec 2000, *BSA/FVA Flow Software Installation & User's guide*, Dantec Measurement Technology A/S, Technical manual.

Demirbas, A. 2004, "Combustion characteristics of different biomass fuels", *Progress in Energy and Combustion Science,* vol. 30, no. 2, pp. 219-230.

Di Blasi, C. 2008, "Modeling chemical and physical processes of wood and biomass pyrolysis", *Progress in Energy and Combustion Science,* vol. 34, no. 1, pp. 47-90.

Ding, E.J. & Aidun, C.K. 2000, "The dynamics and scaling law for particles suspended in shear flow with inertia", *Journal of Fluid Mechanics,* vol. 423, pp. 317-344.

Elfasakhany, A. 2005, *Modeling of Pulverised Wood Flames*, Ph.D. thesis, Lund University.

Elfasakhany, A. & Bai, X.S. 2006, "Modelling of pulverised wood combustion: a comparison of different models", *Progress in computational fluid dynamics,* vol. 6, no. 4-5, pp. 188.

Elfasakhany, A., Klason, T. & Bai, X.S. 2008, "Modelling of pulverised wood combustion using a functional group model", *Combustion Theory and Modelling,* vol. 12, no. 5, pp. 883-904.

Elghobashi, S. 1994, "On Predicting Particle-Laden Turbulent Flows", *Applied Scientific Research,* vol. 52, no. 4, pp. 309-329.

Energistyrelsen 2008, *Energi i Danmark,* Energy statistics from the Danish ministery of Climate and Energy.

Energistyrelsen 2002, *Wood for Energy Production*, Publication from the Center for Biomass Technology.

Eriksson, J. 2009, *Personal communication.*

Esteban, L.S. & Carrasco, J.E. 2006, "Evaluation of different strategies for pulverization of forest biomasses", *Powder Technology,* vol. 166, no. 3, pp. 139-151.

Evald, A. & Witt, J. 2006, *Biomass CHP best practice guide,* publication from the Altener project: "Bio-CHP - European Biomass CHP in Practice".

Fan, F.G. & Ahmadi, G. 2000, "Wall deposition of small ellipsoids from turbulent air flows - A Brownian dynamics simulation", *Journal of Aerosol Science,* vol. 31, no. 10, pp. 1205-1229.

Fan, F.G. & Ahmadi, G. 1995, "Dispersion of Ellipsoidal Particles in an Isotropic Pseudo-Turbulent Flow-Field", *Journal of Fluids Engineering-Transactions of the Asme,* vol. 117, no. 1, pp. 154-161.

Fan, J.R., Zhao, H. & Jin, J. 1996, "Two-phase velocity measurements in particle-laden coaxial jets", *Chemical Engineering Journal,* vol. 63, no. 1, pp. 11-17.

Field, S.B., Klaus, M., Moore, M.G. & Nori, F. 1997, "Chaotic dynamics of falling disks", *Nature,* vol. 388, no. 6639, pp. 252-254.

Fisher, M.J. & Davies, P.O.A. 1964, "Correlation Measurements in a Non-Frozen Pattern of Turbulence", *Journal of Fluid Mechanics,* vol. 18, no. 1, pp. 97-116.

Fleckhaus, D., Hishida, K. & Maeda, M. 1987, "Effect of Laden Solid Particles on the Turbulent-Flow Structure of a Round Free Jet", *Experiments in Fluids,* vol. 5, no. 5, pp. 323-333.

Fluent Inc. 2006, *Fluent 6.3 User's guide*.

Founti, M., Achimastos, T. & Klipfel, A. 1999, "Effects of increasing particle loading in an axisymmetric, vertical, liquid-solid sudden expansion flow", *Journal of Fluids Engineering-Transactions of the ASME,* vol. 121, no. 1, pp. 171-178.

Frank, T., Schade, K.P. & Petrak, D. 1993, "Numerical-Simulation and Experimental Investigation of a Gas Solid 2-Phase Flow in a Horizontal Channel", *International Journal of Multiphase Flow,* vol. 19, no. 1, pp. 187-198.

Gallily, I. & Cohen, A. 1979, "On the orderly nature of the motion of nonspherical aerosol particles. II. Inertial collision between a spherical large droplet and an axially symmetrical elongated particle", *Journal of colloid and interface science,* vol. 68, no. 2, pp. 338-356.

Ganser, G.H. 1993, "A Rational Approach to Drag Prediction of Spherical and Nonspherical Particles", *Powder Technology,* vol. 77, no. 2, pp. 143-152.

Gavze, E. 1990, "The accelerated motion of rigid bodies in non-steady stokes flow", *International Journal of Multiphase Flow,* vol. 16, no. 1, pp. 153-166.

Geiss, S., Dreizler, A., Stojanovic, Z., Chrigui, M., Sadiki, A. & Janicka, J. 2004, "Investigation of turbulence modification in a non-reactive two-phase flow", *Experiments in Fluids,* vol. 36, no. 2, pp. 344-354.

Gera, D., Mathur, M.P., Freeman, M.C. & Robinson, A. 2002, "Effect of large aspect ratio of biomass particles on carbon burnout in a utility boiler", *Energy & Fuels,* vol. 16, no. 6, pp. 1523-1532.

Gillandt, I., Fritsching, U. & Bauckhage, K. 2001, "Measurement of phase interaction in dispersed gas", *International Journal of Multiphase Flow,* vol. 27, no. 8, pp. 1313-1332.

Gjernes, E. 2006, "Fuel flexibility at Amager unit 1 using pulverized fuels", *Presented at Power-Gen Europe, Cologne, Germany*.

Goldstein, H. 1980, *Classical Mechanics,* Addison-Wesley Press.

Gore, R.A. & Crowe, C.T. 1989, "Effect of Particle-Size on Modulating Turbulent Intensity", *International Journal of Multiphase Flow,* vol. 15, no. 2, pp. 279-285.

Gouesbet, G. & Berlemont, A. 1999, "Eulerian and Lagrangian approaches for predicting the behaviour of discrete particles in turbulent flows", *Progress in Energy and Combustion Science,* vol. 25, no. 2, pp. 133-159.

Govan, A.H., Hewitt, G.F. & Ngan, C.F. 1989, "Particle Motion in a Turbulent Pipe-Flow", *International Journal of Multiphase Flow,* vol. 15, no. 3, pp. 471-481.

Govan, A.H., Hewitt, G.F. & Terry, J.W. 1990, "Axial-View Measurements of Particle Motion in a Turbulent Pipe-Flow", *Particle & Particle Systems Characterization,* vol. 7, no. 2, pp. 60-69.

Hadinoto, K., Jones, E.N., Yurteri, C. & Curtis, J.S. 2005, "Reynolds number dependence of gas-phase turbulence in gas-particle flows", *International Journal of Multiphase Flow,* vol. 31, no. 4, pp. 416-434.

Haider, A. & Levenspiel, O. 1989, "Drag Coefficient and Terminal Velocity of Spherical and Nonspherical Particles", *Powder Technology,* vol. 58, no. 1, pp. 63-70.

Happel, J. & Brenner, H. 1965, *Low Reynold's Number Hydrodynamics,* Prentice-Hall, Englewood Cliffs.

Harper, E.Y. & Chang, I.D. 1968, "Maximum Dissipation Resulting from Lift in a Slow Viscous Shear Flow", *Journal of Fluid Mechanics,* vol. 33, pp. 209-&.

Hennick, E.A. & Lightstone, M.F. 2000, "A comparison of stochastic separated flow models for particle dispersion in turbulent flows", *Energy & Fuels,* vol. 14, no. 1, pp. 95-103.

Hetsroni, G. 1989, "Particles Turbulence Interaction", *International Journal of Multiphase Flow,* vol. 15, no. 5, pp. 735-746.

Hilpert, H., Maier, J., Scheurer, W. & Hein, K.R.G. 2006, *Status report on firing secondary fuels in Europe*, International Flame Research Foundation.

Hinze, J.O. 1975, *Turbulence,* second edn, McGraw-Hill.

Hodgson, S. 1999, , MSc thesis, University of Toronto.

Hoerner, J.F. 1965, *Fluid-dynamics drag,* Hoerner Fluid Dynamics (Published by the author).

Holm, J.K., Sørensen, L.H., Henriksen, U., Hjuler, K., Simonsen, K. & Berg, M. 2006, *Fuel preparation and characterization - Part of the PSO project: Biomass dust firing*.

Hoogwijk, M., Faaij, A., van den Broek, R., Berndes, G., Gielen, D. & Turkenburg, W. 2003, "Exploration of the ranges of the global potential of biomass for energy", *Biomass and Bioenergy,* vol. 25, no. 2, pp. 119-133.

Hughes, P.C. 1986, *Spacecraft Attitude Dynamics,* Wiley.

Hussein, H.J., Capp, S.P. & George, W.K. 1994, "Velocity-Measurements in a High-Reynolds-Number, Momentum-Conserving, Axisymmetrical, Turbulent Jet", *Journal of Fluid Mechanics,* vol. 258, pp. 31-75.

Hutchinson, P., Hewitt, G.F. & Dukler, A.E. 1971, "Deposition of Liquid Or Solid Dispersions from Turbulent Gas Stream - Stochastic Model", *Chemical Engineering Science,* vol. 26, no. 3, pp. 419.

Hwang, G.J. & Shen, H.H. 1993, "Fluctuation Energy Equations for Turbulent Fluid Solid Flows", *International Journal of Multiphase Flow,* vol. 19, no. 5, pp. 887-895.

Hwang, W. & Eaton, J.K. 2006, "Turbulence attenuation by small particles in the absence of gravity", *International Journal of Multiphase Flow,* vol. 32, no. 12, pp. 1386-1396.

Hwang, W.T. & Eaton, J.K. 2006, "Homogeneous and isotropic turbulence modulation by small heavy (St similar to 50) particles", *Journal of Fluid Mechanics,* vol. 564, pp. 361-393.

IEA 2008, *Key world energy statistics*, Energy statistics for the International Energy Agency.

IEA 2006, *Co-utilisation of Biomass with Fossil Fuels*, Publication from the International Energy Agency.

Jeffery, G.B. 1922, "The Motion of Ellipsoidal Particles Immersed in a Viscous Fluid", *Proceedings of the Royal Society of London.Series A, Containing Papers of a Mathematical and Physical Character,* vol. 102, no. 715, pp. 161-179.

Jou, B.H., Sheen, H.J. & Lee, Y.T. 1993, "Particle Mass Loading Effect on a 2-Phase Turbulent Downward Jet Flow", *Particle & Particle Systems Characterization,* vol. 10, no. 4, pp. 173-181.

Kankkunen, A., Miikkulainen, P., Jarvinen, M. & Fogelholm, C.J. 2005, "Shape characteristics of non-spherical black liquor droplets", *Pulp & Paper-Canada,* vol. 106, no. 12, pp. 71-74.

Karnis, A., Goldsmit.Hl & Mason, S.G. 1966, "Flow of Suspensions through Tubes .V. Inertial Effects", *Canadian Journal of Chemical Engineering,* vol. 44, no. 4, pp. 181.

Karnis, A., Mason, S.G. & Goldsmith, H.L. 1963, "Axial Migration of Particles in Poiseuille Flow", *Nature,* vol. 200, no. 490, pp. 159.

Kaspers, G. 1982, "Dynamics and Measurement of Smokes. I Size Characterization of Nonspherical Particles", *Aerosol science and technology,* vol. 1, no. 2, pp. 187-199.

Kenning, V.M. 1996, *Self-induced turbulence in soild-liquid flow*, Washington State University.

Kenning, V.M. & Crowe, C.T. 1997, "On the effect of particles on carrier phase turbulence in gas-particle flows", *International Journal of Multiphase Flow,* vol. 23, no. 2, pp. 403-408.

Kharaz, A.H., Gorham, D.A. & Salman, A.D. 2001, "An experimental study of the elastic rebound of spheres", *Powder Technology,* vol. 120, no. 3, pp. 281-291.

Klett, J.D. 1995, "Orientation Model for Particles in Turbulence", *Journal of the Atmospheric Sciences,* vol. 52, no. 12, pp. 2276-2285.

Kulick, J.D., Fessler, J.R. & Eaton, J.K. 1994, "Particle Response and Turbulence Modification in Fully-Developed Channel Flow", *Journal of Fluid Mechanics,* vol. 277, pp. 109-134.

Lain, S. & Sommerfeld, M. 2008, "Euler/Lagrange computations of pneumatic conveying in a horizontal channel with different wall roughness", *Powder Technology,* vol. 184, no. 1, pp. 76-88.

Lain, S. & Sommerfeld, M. 2003, "Turbulence modulation in dispersed two-phase flow laden with solids from a Lagrangian perspective", *International Journal of Heat and Fluid Flow,* vol. 24, no. 4, pp. 616-625.

Lanzetta, M. & Di Blasi, C. 1998, "Pyrolysis kinetics of wheat and corn straw", *Journal of Analytical and Applied Pyrolysis,* vol. 44, no. 2, pp. 181-192.

Launder, B.E. & Spalding, D.B. 1972, *Mathematical models of Turbulence,* Academic Press.

Lawrence, C.J. & Weinbaum, S. 1988, "The Unsteady Force on a Body at Low Reynolds-Number - the Axisymmetric Motion of a Spheroid", *Journal of Fluid Mechanics,* vol. 189, pp. 463-489.

Lawrence, C.J. & Weinbaum, S. 1986, "The Force on an Axisymmetrical Body in Linearized, Time-Dependent Motion - a New Memory Term", *Journal of Fluid Mechanics,* vol. 171, pp. 209-218.

Lazaro, B.J. & Lasheras, J.C. 1989, "Particle Dispersion in a Turbulent, Plane, Free Shear-Layer", *Physics of Fluids A-Fluid Dynamics,* vol. 1, no. 6, pp. 1035-1044.

Leal, L.G. 1980, "Particle Motions in a Viscous Fluid", *Annual Review of Fluid Mechanics,* vol. 12, no. 1, pp. 435-476.

Lee, S.L. & Durst, F. 1982, "On the Motion of Particles in Turbulent Duct Flows", *International Journal of Multiphase Flow,* vol. 8, no. 2, pp. 125-146.

Li, A. & Ahmadi, G. 1992, "Dispersion and Deposition of Spherical-Particles from Point Sources in a Turbulent Channel Flow", *Aerosol Science and Technology,* vol. 16, no. 4, pp. 209-226.

Lightstone, M.F. 1992, PhD Thesis, University of Waterloo.

Lightstone, M.F. & Hodgson, S.M. 2004, "Turbulence modulation in gas-particle flows: A comparison of selected models", *Canadian Journal of Chemical Engineering,* vol. 82, no. 2, pp. 209-219.

Lokare, S.S., Dunaway, J.D., Moulton, D., Rogers, D., Tree, D.R. & Baxter, L.L. 2006, "Investigation of ash deposition rates for a suite of biomass fuels and fuel blends", *Energy & Fuels,* vol. 20, no. 3, pp. 1008-1014.

Losenno, C.G.R. 2004, *An investigation of irregular particles in free-fall*, PhD thesis, University of Edinburgh.

Lu, H., Robert, W., Peirce, G., Ripa, B. & Baxter, L.L. 2008, "Comprehensive study of Biomass particle combustion", *Energy & Fuels,* vol. 22, no. 4, pp. 2826-2839.

Luo, K., Fan, J.R. & Cen, K. 2005, "Modulations on turbulent characteristics by dispersed particles in gas-solid jets", *Proceedings of the Royal Society A-Mathematical Physical and Engineering Sciences,* vol. 461, no. 2062, pp. 3279-3295.

Luo, K., Fan, J.R. & Cen, K.F. 2004, "DNS of the turbulence modulation by dispersed particles in compressible spatially developing two-phase jets", *Progress in Natural Science,* vol. 14, no. 9, pp. 817-821.

Ma, L., Jones, J.M., Pourkashanian, M. & Williams, A. 2007, "Modelling the combustion of pulverized biomass in an industrial combustion test furnace", *Fuel,* vol. 86, no. 12-13, pp. 1959-1965.

Magnus, G. 1861, "A Note on the Rotary Motion of the Liquid Jet", *Annalen der Physik und Chemie,* vol. 63, pp. 363-365.

Magnussen, B.F. & Hjertager, B.H. 1976, "On the mathematical modeling Turbulent Combustion with Special Emphasis on Soot formation and combustion", *Proceedings of the Combustion Institute*, vol. 16, pp. 719-729.

Mandø, M., Lightstone, M.F., Rosendahl, L., Yin, C. & Sørensen, H. 2009, "Turbulence modulation in dilute particle-laden flow", *International Journal of Heat and Fluid Flow,* vol. 30, pp. 331-338.

Maxey, M.R. & Riley, J.J. 1983, "Equation of Motion for a Small Rigid Sphere in a Nonuniform Flow", *Physics of Fluids,* vol. 26, no. 4, pp. 883-889.

Mckay, G., Murphy, W.R. & Hillis, M. 1988, "Settling Characteristics of Disks and Cylinders", *Chemical Engineering Research & Design,* vol. 66, no. 1, pp. 107-112.

Melling, A. 1997, "Tracer particles and seeding for particle image velocimetry", *Measurement Science & Technology,* vol. 8, pp. 1406-1416.

Meyer, K.E. 2004, *LDV and optical flow measurements*, Technical University of Denmark, Internal report.

Michaelides, E.E. 1997, "Review - The transient equation of motion for particles, bubbles, and droplets", *Journal of Fluids Engineering-Transactions of the Asme,* vol. 119, no. 2, pp. 233-247.

Militzer, J., Kan, J.M., Hamdullahpur, F., Amyotte, P.R. & Al Taweel, A.M. 1989, "Drag coefficient for axisymmetric flow around individual spheroidal particles", *Powder Technology,* vol. 57, no. 3, pp. 193-195.

Modarress, D., Tan, H. & Elghobashi, S. 1984, "2-Component LDA Measurement in a 2-Phase Turbulent Jet", *AIAA Journal,* vol. 22, no. 5, pp. 624-630.

Modarress, D., Wuerer, J. & Elghobashi, S. 1982, "An experimental study of a round two-phase jet", .

Modest, M.F. 2003, *Radiative Heat Transfer,* Academic Press.

Mohanarangam, K. & Tu, J.Y. 2007, "Two-fluid model for particle-turbulence interaction in a backward-facing step", *AICHE Journal,* vol. 53, no. 9, pp. 2254-2264.

Nikolaisen, L., Jensen, T.N., Hjuler, K., Busk, J., Junker, H., Sander, B., Baxter, L. & Bloch, L. 2002, *Quality Characteristics of Biofuel Pellets,* Danish Technological Institute.

Nussbaumer, T. 2003, "Combustion and co-combustion of biomass: fundamentals, technologies, and primary measures for emission reduction", *Energy & Fuels,* vol. 17, no. 6, pp. 1510-1521.

Olson, J.A. 2001, "The motion of fibres in turbulent flow, stochastic simulation of isotropic homogeneous turbulence", *International Journal of Multiphase Flow,* vol. 27, no. 12, pp. 2083-2103.

Olson, J.A., Frigaard, I., Chan, C. & Hämäläinen, J.P. 2004, "Modeling a turbulent fibre suspension flowing in a planar contraction: The one-dimensional headbox", *International Journal of Multiphase Flow,* vol. 30, no. 1, pp. 51-66.

Panchapakesan, N.R. & Lumley, J.L. 1993, "Turbulence Measurements in Axisymmetrical Jets of Air and Helium .1. Air-Jet", *Journal of Fluid Mechanics,* vol. 246, pp. 197-223.

Paschkewitz, J.S., Dubief, Y., Dimitropoulos, C.D., Shaqfeh, E.S.G. & Moin, P. 2004, "Numerical simulation of turbulent drag reduction using rigid fibres", *Journal of Fluid Mechanics,* vol. 518, pp. 281-317.

Poiseuille, J.L.M. 1841, "Recherches sur le Mouvement du Sang dans les Vein Capillaires", *Mémoires de l'Académie Royale des Sciences,* vol. 7, pp. 105-175.

Pope, S.B. 2000, *Turbulent Flows,* Cambridge University Press, Cambridge.

Powers, M.C. 1953, "A new roundness scale for sedimentary particles", *Journal of sedimentary petrology,* vol. 23, pp. 117-119.

Prandtl, L. 1925, "Bericht uber die Entstehung der Turbulenz", *Zeitschrift fur Angewandte Mathematik und Mechanik,* vol. 5, pp. 136-139.

Prevost, F., Boree, J., Nuglisch, H.J. & Charnay, G. 1996, "Measurements of fluid/particle correlated motion in the far field of an axisymmetric jet", *International Journal of Multiphase Flow,* vol. 22, no. 4, pp. 685-701.

Prins, M.F., Ptasinski, K.J., Janssen, F.J.J.G. 2007, "From coal to biomass gasification: Comparison of thermodynamic efficiency", *Energy,* vol. 32, no. 7, pp. 1248-1259.

Qi, D.W. 2006, "Direct simulations of flexible cylindrical fiber suspensions in finite Reynolds number flows", *Journal of Chemical Physics,* vol. 125, no. 11.

Qi, D.W. 2005, "Many-particle interactions in Couette flows", *Progress in Computational Fluid Dynamics,* vol. 5, no. 1-2, pp. 104-109.

Qi, D.W. 2001, "Simulations of fluidization of cylindrical multiparticles in a three-dimensional space", *International Journal of Multiphase Flow,* vol. 27, no. 1, pp. 107-118.

Qi, D.W. 2000, "Lattice-Boltzmann simulations of fluidization of rectangular particles", *International Journal of Multiphase Flow,* vol. 26, no. 3, pp. 421-433.

Qi, D.W. 1999, "Lattice-Boltzmann simulations of particles in non-zero-Reynolds-number flows", *Journal of Fluid Mechanics,* vol. 385, pp. 41-62.

Qi, D.W. 1997, "Non-spheric colloidal suspensions in three-dimensional space", *International Journal of Modern Physics C,* vol. 8, no. 4, pp. 985-997.

Qi, D.W. & Luo, L.S. 2003, "Rotational and orientational behaviour of three-dimensional spheroidal particles in Couette flows", *Journal of Fluid Mechanics,* vol. 477, pp. 201-213.

Raffel, M., Willert, C. & Kompenhans, J. 1998, *Particle Image Velocimetry - a practical guide,* Springer.

Rosendahl, L.A. 1998, *Extending the modelling framework for gas-particle systems*, PhD thesis, Aalborg University.

Rosendahl, L. 2000, "Using a multi-parameter particle shape description to predict the motion of non-spherical particle shapes in swirling flow", *Applied Mathematical Modelling,* vol. 24, no. 1, pp. 11-25.

Rosendahl, L.A., Yin, C., Kær, S.K., Friborg, K. & Overgaard, P. 2007, "Physical characterization of biomass fuels prepared for suspension firing in utility boilers for CFD modelling", *Biomass and Bioenergy,* vol. 31, no. 5, pp. 318-325.

Saffman, P.G. 1965, "Lift on a Small Sphere in a Slow Shear Flow", *Journal of Fluid Mechanics,* vol. 22, pp. 385.

Schiller, L. & Naumann, A. 1933, "Fundamental calculations in gravitational processing", *Zeitschrift Des Vereines Deutscher Ingenieure,* vol. 77, pp. 318-320.

Sheen, H.J., Jou, B.H. & Lee, Y.T. 1994, "Effect of Particle-Size on a 2-Phase Turbulent Jet", *Experimental Thermal and Fluid Science,* vol. 8, no. 4, pp. 315-327.

Shin, H. & Maxey, M.R. 1997, "Chaotic motion of nonspherical particles settling in a cellular flow field", *Physical Review E,* vol. 56, no. 5, pp. 5431-5444.

Shirolkar, J.S., Coimbra, C.F.M. & Queiroz McQuay, M. 1996, "Fundamental aspects of modeling turbulent particle dispersion in dilute flows", *Progress in Energy and Combustion Science,* vol. 22, no. 4, pp. 363-399.

Shuen, J.S., Solomon, A.S.P., Zhang, Q.F. & Faeth, G.M. 1985, "Structure of Particle-Laden Jets - Measurements and Predictions", *AIAA Journal,* vol. 23, no. 3, pp. 396-404.

Smeets, E.M.W., Faaij, A.P.C., Lewandowski, I.M. & Turkenburg, W.C. 2007, "A bottom-up assessment and review of global bio-energy potentials to 2050", *Progress in Energy and Combustion Science,* vol. 33, no. 1, pp. 56-106.

Sommerfeld, M. 2003, "Analysis of collision effects for turbulent gas-particle flow in a horizontal channel: Part 1. Particle transport", *International Journal of Multiphase Flow,* vol. 29, no. 4, pp. 675-699.

Sommerfeld, M. 1994, *Modellierung und numeriske Berechnung von Partikelbeladenen turbulenten Stromung mit Hilfe des Euler/Lagrange Verfahrens*, Habilitationsschift, University of Erlangen-Nuernburg.

Sommerfeld, M. 1992, "Modeling of Particle Wall Collisions in Confined Gas Particle Flows", *International Journal of Multiphase Flow,* vol. 18, no. 6, pp. 905-926.

Sommerfeld, M. & Huber, N. 1999, "Experimental analysis and modelling of particle-wall collisions", *International Journal of Multiphase Flow,* vol. 25, no. 6-7, pp. 1457-1489.

Sommerfeld, M. & Kussin, J. 2004, "Wall roughness effects on pneumatic conveying of spherical particles in a narrow horizontal channel", *Powder Technology,* vol. 142, no. 2-3, pp. 180-192.

Sommerfeld, M. & Kussin, J. 2003, "Analysis of collision effects for turbulent gas-particle flow in a horizontal channel. Part II. Integral properties and validation", *International Journal of Multiphase Flow,* vol. 29, no. 4, pp. 701-718.

Sommerfeld, M., van Wachem, B. & Oliemans, R. (eds) 2007, *Best Practice Guidelines - on Computational Multiphase Dynamics for turbulent dispersed multiphase flows*, Version 16-oct-07 edn, ERCOFTAC Special Interest Group on "Dispersed Turbulent Multi-Phase Flow".

Squires, K.D. & Eaton, J.K. 1992, "On the modelling of particle-laden turbulent flows", *Proc. 6th Workshop on Two-phase Flow Predictions*.

Stringham, G.E., Simons, D.B. & Guy, H.P. 1969, "The behaviour of large particles falling in quiescent liquids.", *Prof. Pap. US Geol. Surv.,* vol. 562-C, pp. C1-C36.

Strutt, C. 2008, *Personal communication*.

Sun, L., Lin, J., WU, F. & Chen, Y. 2004, "Effect of non-spherical particles on the fluid turbulence in a particulate pipe flow", *Journal of Hydrodynamics, Ser.B,* vol. 16, no. 6, pp. 721-729.

Sørensen, H. 2005, *"Experimental Investigation of Non-Spherical Particle Aerodynamics",* Ph.D. thesis, Aalborg University.

Tang, L., Crowe, C.T., Chung, J.N. & Troutt, T.R. 1992, "Self-organizing particle dispersion mechanisme in free shear flows", *Physics of Fluids A,* vol. 4, pp. 2244.

Taylor, G.I. 1938, "The Spectrum of Turbulence", *Proceedings of the Royal Society of London. Series A,* vol. 164, no. 919, pp. 476-490.

Taylor, G.I. 1915, "Eddy motion in the atmosphere", *Philosophical Transactions of the London Mathematical Society, Series A,* vol. 215, pp. 1.

Tennekes, H. & Lumley, J.L. 1972, *A First Course in Turbulence,* The MIT Press, Cambridge, Massachusetts.

Thompson, T.L. & Clark, N.N. 1991, "A holistic approach to particle drag prediction", *Powder Technology,* vol. 67, no. 1, pp. 57-66.

Tsuji, Y., Morikawa, Y. & Shiomi, H. 1984, "LDV Measurements of an Air Solid 2-Phase Flow in a Vertical Pipe", *Journal of Fluid Mechanics,* vol. 139, no. FEB, pp. 417-434.

Tsuji, Y., Morikawa, Y., Tanaka, T., Karimine, K. & Nishida, S. 1988, "Measurement of an Axisymmetric Jet Laden with Coarse Particles", *International Journal of Multiphase Flow,* vol. 14, no. 5, pp. 565-574.

Tsuji, Y. 2007, "Multi-scale modeling of dense phase gas–particle flow", *Chemical Engineering Science,* vol. 62, no. 13, pp. 3410-3418.

Tu, J.Y. & Fletcher, C.A.J. 1994, "An Improved Model for Particulate Turbulence Modulation in Confined 2-Phase Flows", *International Communications in Heat and Mass Transfer,* vol. 21, no. 6, pp. 775-783.

Versteeg, H. & Malalasekera, W. 2007, *An Introduction to Computational Fluid Dynamics,* 2nd edn, Prentice Hall.

Vreman, A.W. 2007, "Turbulence characteristics of particle-laden pipe flow", *Journal of Fluid Mechanics,* vol. 584, pp. 235-279.

Wadell, H. 1934, "The coefficient of resistance as a function of Reynolds number for solids of various shapes", *Journal of the Franklin Institute,* vol. 217, no. 4, pp. 459-490.

White, F.M. 1991, *Viscous fliud flow,* Second edn, McGraw-Hill.

Wilcox, D.C. 2002, *Turbulence Modeling for CFD,* DCW Industries.

Williams, A., Pourkashanian, M. & Jones, J.M. 2001, "Combustion of pulverised coal and biomass", *Progress in Energy and Combustion Science,* vol. 27, no. 6, pp. 587-610.

Willmarth, W.W., Hawk, N.E. & Harvey, R.L. 1964, "Steady and Unsteady Motions and Wakes of Freely Falling Disks", *Physics of Fluids,* vol. 7, no. 2, pp. 197-208.

Wolf, J., Bindraban, P.S., Luijten, J.C. & Vleeshouwers, L.M. 2003, "Exploratory study on the land area required for global food supply and the potential global production of bioenergy", *Agricultural Systems,* vol. 76, no. 3, pp. 841-861.

Wu, C., Tree, D. & Baxter, L. 2007, "Reactivity of NH3 and HCN during low-grade fuel combustion in a swirling flow burner", *Proceedings of the Combustion Institute,* vol. 31, no. 2, pp. 2787-2794.

Wygnanski, I. & Fiedler, H. 1969, "Some Measurements in Self-Preserving Jet", *Journal of Fluid Mechanics,* vol. 38, pp. 577-612.

Yan, F., Lightstone, M.F. & Wood, P.E. 2007, "Numerical study on turbulence modulation in gas-particle flows", *Heat and Mass Transfer,* vol. 43, no. 3, pp. 243-253.

Yan, F., Lightstone, M.F. & Wood, P.E. 2006, "A mathematical model of turbulence modulation in particle-laden pipe flows", *International Journal of Computational Fluid Dynamics,* vol. 20, no. 1, pp. 37-44.

Yang, Y.B., Ryu, C., Khor, A., Yates, N.E., Sharifi, V.N. & Swithenbank, J. 2005, "Effect of fuel properties on biomass combustion. Part II. Modelling approach - identification of the controlling factors", *Fuel,* vol. 84, no. 16, pp. 2116-2130.

Yarin, L.P. & Hetsroni, G. 1994, "Turbulence Intensity in Dilute 2-Phase Flows .1. Effect of Particle-Size Distribution on the Turbulence of the Carrier Fluid", *International Journal of Multiphase Flow,* vol. 20, no. 1, pp. 1-15.

Yarin, L.P. & Hetsroni, G. 1994, "Turbulence Intensity in Dilute 2-Phase Flows .2. Temperature-Fluctuations in Particle-Laden Dilute Flows", *International Journal of Multiphase Flow,* vol. 20, no. 1, pp. 17-25.

Yarin, L.P. & Hetsroni, G. 1994, "Turbulence Intensity in Dilute 2-Phase Flows .3. the Particles-Turbulence Interaction in Dilute 2-Phase Flow", *International Journal of Multiphase Flow,* vol. 20, no. 1, pp. 27-44.

Ye, T.H., Azevedo, J., Costa, M. & Semiao, V. 2004, "CO-COMBUSTION of pulverized coal, pine shells, and textile wastes in a propane-fired furnace: Measurements and predictions", *Combustion Science and Technology,* vol. 176, no. 12, pp. 2071-2104.

Yin, C.G., Rosendahl, L., Kaer, S.K. & Condra, T.J. 2004, "Use of numerical modeling in design for co-firing biomass in wall-fired burners", *Chemical Engineering Science,* vol. 59, no. 16, pp. 3281-3292.

Yin, C.G., Rosendahl, L., Kaer, S.K. & Sorensen, H. 2003, "Modelling the motion of cylindrical particles in a nonuniform flow", *Chemical Engineering Science,* vol. 58, no. 15, pp. 3489-3498.

Yuan, Z. & Michaelides, E.E. 1992, "Turbulence Modulation in Particulate Flows - a Theoretical Approach", *International Journal of Multiphase Flow,* vol. 18, no. 5, pp. 779-785.

Zhang, L.X., Lin, J.Z. & Chan, T.L. 2005, "Orientation distribution of cylindrical particles suspended in a turbulent pipe flow", *Physics of Fluids,* vol. 17, no. 9.

Zhang, L.X., Lin, J.Z. & Zhang, W.F. 2006, "Theoretical model of particle orientation distribution function in a cylindrical particle suspension subject to turbulent shear flow", *Progress in Natural Science,* vol. 16, no. 1, pp. 16-20.

Zhou, H., Jensen, A.D., Glarborg, P., Jensen, P.A. & Kavaliauskas, A. 2005, "Numerical modeling of straw combustion in a fixed bed", *Fuel,* vol. 84, no. 4, pp. 389-403.